# LEVEL STRUCTURE OF $^{191}$Ir AND $^{193}$Ir

# LEVEL STRUCTURE OF $^{191}$Ir AND $^{193}$Ir

by

ROBERT H. PRICE, B.Sc.

A Thesis
Submitted to the Faculty of Graduate Studies
in Partial Fulfilment of the Requirements
for the Degree
Doctor of Philosophy

McMaster University
March, 1971

DOCTOR OF PHILOSOPHY (1971)
(Physics)

McMASTER UNIVERSITY
Hamilton, Ontario

TITLE: Level Structure of $^{191}$Ir and $^{193}$Ir

AUTHOR: Robert H. Price, B.Sc. (University of Victoria)

SUPERVISOR: Professor M. W. Johns

NUMBER OF PAGES: viii, 254

SCOPE AND CONTENTS:

A variety of experiments has been performed in order to establish and identify the states in $^{191}$Ir and $^{193}$Ir. From radioactive decay, the energies and intensities of the gamma rays and internal conversion electrons have been measured with high precision using Ge(Li) detectors and the Chalk River $\pi\sqrt{2}$ spectrometer. A series of gamma-gamma coincidence experiments were performed using Ge(Li) detectors. The gamma rays following Coulomb excitation of $^{191}$Ir and $^{193}$Ir were also measured with Ge(Li) detectors. In addition, ($^{3}$He,d) and ($\alpha$,t) transfer reactions were performed and the reaction products analyzed by means of an Enge split-pole spectrograph. From these data, the energies, spins, parities and spectroscopic factors for the states in $^{191}$Ir and $^{193}$Ir have been established and interpreted in terms of the Nilsson model with band mixing.

# ACKNOWLEDGEMENTS

The author expresses sincere gratitude to his research supervisor, Professor M. W. Johns, for his guidance during the early period of the work, for useful discussions and assistance with the data analysis in the final stage, and for continued interest in the problem throughout the course of the investigation. Appreciation is also expressed to the other members of the author's supervisory committee, Dr. R. H. Tomlinson and Dr. J. A. Cameron, as well as Dr. D. G. Burke who kindly substituted for Dr. Cameron during a sabbatical leave, for their interest and comments.

It has been a pleasure to be associated with the beta ray spectroscopy group during my stay at McMaster. The fellowship provided by this group, in addition to the general assistance, interesting discussions and noon hour card games, will be long remembered.

The author is indebted to many other members of the McMaster physics community for the valuable aid and discussions which they have so generously provided. Special thanks are due to Mr. J. C. Tippett for providing the DWBA programs, Mr. R. A. O'Neil for the particle spectra fitting program, Mr. R. G. H. Robertson for discussions regarding the spectroscopic factors, and to Drs. A. B. Volkov and R. G. Summers-Gill for many enlightening discussions involving the theoretical aspects of the work.

The co-operation provided by the staff of the McMaster reactor, the tandem accelerator laboratory and the computing centre has been essential to these experiments and is gratefully acknowledged.

I am indebted to Dr. W. P. Alford for making available the excellent facilities of the Nuclear Structure Laboratory at the University of Rochester and the accelerator staff for their capable operation of the machine.

Appreciation is also expressed to Drs. J. S. Geiger and R. L. Graham of the Nuclear Research Laboratory at Chalk River for making available their large $\pi\sqrt{2}$ beta ray spectrometer and for useful discussions. The technical assistance of Mrs. J. Merrit, Mr. W. Perry, Mr. L. Smith and Mr. R. Walker is gratefully acknowledged.

The financial support provided by the Government of Ontario and the National Research Council of Canada for these studies is acknowledged with gratitude.

The ability of Mrs. Susan Anderson to decipher the scribblings of "second worst writer in the department" and formulate them into the present manuscript is not only noteworthy, but much appreciated.

Finally, I wish to thank my wife, whom I met and married during my graduate years at McMaster, not only for the understanding attitude which she has displayed during these first years of marriage, but also for preparing most of the drawings used in this manuscript.

# TABLE OF CONTENTS

CHAPTER I NUCLEAR MODELS

CHAPTER II EMBELLISHMENTS TO THE MODELS

CHAPTER VI EXPERIMENTAL PROCEDURES AND ANALYSIS

CHAPTER VII THE DECAY OF $^{193}$Os

CHAPTER VIII THE DECAY OF $^{191}$Pt

CHAPTER IX ($^3$He,d) AND ($\alpha$,t) REACTIONS ON $^{190}$Os AND $^{192}$Os

# CHAPTER I

# NUCLEAR MODELS

## Introduction

The development of a general theory of the nucleus remains an unsolved problem in nuclear physics. As a result, physicists use models to provide an explanation of the observed nuclear properties. The successful nuclear model must be able to predict the features which characterize a nuclear state -- namely the energy, spin, parity and the electric and magnetic moments. In addition to these properties of the stationary state, the model should be able to predict the transition rates between nuclear states in an adequate fashion. Since these are rather sensitive to the details of the nuclear wave function, their prediction provides a very exacting test of a model.

At present, no single model exists which predicts all the observed nuclear properties. However different models have been proposed which give reasonably adequate discriptions of the observed phenomena for different classes of nuclei. For this purpose, nuclei can be loosely divided into two classes: those which possess spherical equilibrium shapes and those which exhibit permanent deformations. Spherical nuclei are best described by the shell model and collective vibrations whereas deformed nuclei are best considered in terms of the Nilsson model and collective motions. Although the underlying assumptions in these various models differ considerably, an effort will be made to relate these assumptions to the basic features of the nuclear interaction. When viewed in this manner, the various models become logical extensions of one another as the effects of the nuclear force are modified by changing the number of nucleons.

## A. Models Describing Near-Spherical Nuclei

### 1.1 Shell Model

The shell model assumes that each nucleon moves in a static central potential $V(r)$ created by the averaged interaction between the other nucleons. The potential is supposed to have much the same shape as the charge density. In a central potential such as this, the orbital angular momentum is a constant of motion designated by $\ell$. For each quantum number $\ell$ a series of energy levels occur which can be distinguished by the quantum number $n$ which gives the number of nodes (including the origin) of the radial wave function.

If a relatively large gap appears in the level spacing, then "closed shell" effects are expected when all the levels up to this gap have been filled. The experimental data indicate that the special stability associated with these shell closures occur at the "magic numbers" 2, 8, 20, 50, 82 and 126.

However any reasonable form for the central potential fails to reproduce these magic numbers. Mayer (1949, 1950) and Haxel, Jensen and Suess (1949, 1950) overcame this difficulty by postulating a strong coupling between the spin of a nucleon and its orbital angular momentum. The potential then takes the form

$$V = V(r) - f(r)\ \vec{\ell}\cdot\vec{s} \qquad f(r) > 0.$$

The effect of the spin-orbit term is to split each level into two states corresponding to the two possible values of j which may be formed from each $\vec{\ell}$-value. The states with $j = \ell-1/2$ are raised from their original position while the states with $j = \ell+1/2$ are depressed by an equal amount. The magnitude of the splitting increases with the value of $\vec{\ell}$, thereby depressing the levels with high angular momentum down to the next shell. The closing of the major shells can then be made to occur for nucleon numbers which correspond to the observed magic numbers.

Figure 1.1 shows the ordering of the shell model levels appropriate for protons, with each level labelled by $n\ \ell\ j$. The parity of the levels is given by $(-)^{\ell}$. The interaction strengths have been empirically adjusted to provide the experimentally observed level ordering (Mayer and Jensen (1966)). The number of nucleons of a specific type in each $(n\ \ell\ j)$ level is restricted to $2j + 1$ by the Pauli exclusion principle.

## 1.2 Extreme Single-Particle Model

The simplest form of the shell model is the extreme single-particle model in which it is assumed that the proton and neutron states fill independently. That is to say, the state into which a

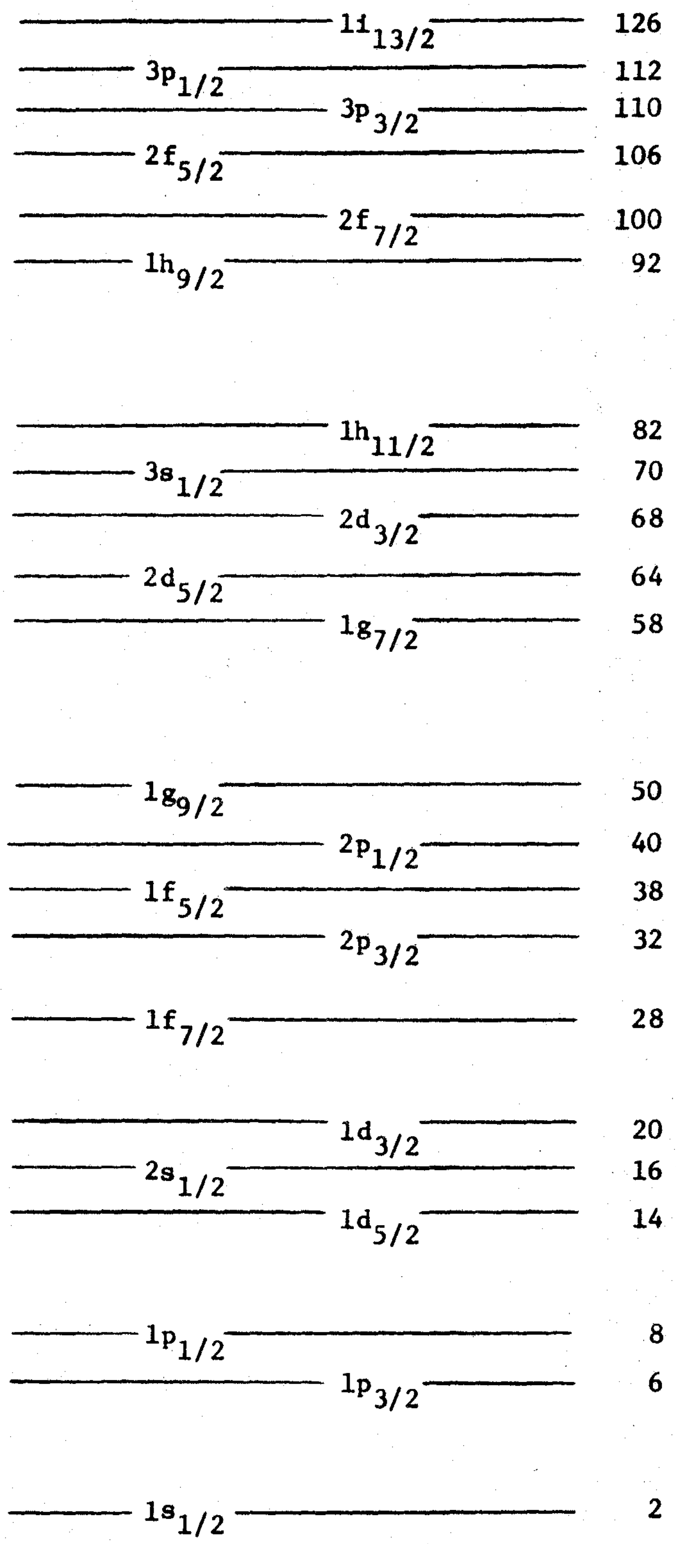

Figure 1.1 Shell model energy levels for protons.

given proton goes is independent of the number of neutrons in the nucleus and vice versa. Furthermore the nucleons are supposed (in the ground state) to have dynamically paired motions so that the nuclear properties are dictated only by the last unpaired nucleon, whenever it is present.

For even-even nuclei in the ground state, this simple model predicts that the protons and neutrons will separately couple pair-wise to zero spin. Such a configuration will be symmetric with respect to the pair-wise exchange of all space coordinates and hence will exhibit positive parity. Thus the model predicts the experimentally observed fact that all even-even nuclei have 0+ ground states. For odd-A nuclei, the spin and parity characteristics of the ground state will be given by that of the last unpaired particle. The model is unable to provide unique spin and parity assignments for odd-odd nuclei.

Excited states are formed by promoting one or more nucleons into higher-lying levels. The simplest type of intrinsic excitation which can occur for an even-even nucleus is that of promoting a single nucleon into a higher shell. This gives rise to a so-called particle-hole excitation. The particle and hole may couple their individual j-vectors in a variety of ways but since there is nothing to indicate which of the possible resultants has lowest energy, the ordering of the resulting excited states remains ambiguous. However the model (along with the exclusion principle) does predict the number of states expected and the accompanying spin and parity assignments. In addition to one particle - one hole excitations, it is possible to raise a pair of particles (still coupled to 0+) into a higher-lying state. An even more remote possibility is that of two particle - two hole excitations or in general many particle - many hole excitations. Excitations of this type, however, are not likely to be observed among the low-lying nuclear states.

The excited states of odd-A nuclei are more readily predicted by the extreme single-particle model. The lowest lying intrinsic excitations are generally due to promoting the unpaired particle into an unoccupied state. In addition, particles lying below the Fermi surface may be promoted to the surface to pair-off with the previously unpaired nucleon. In this case the excitation energy creates a vacancy or hole below the Fermi surface. For either of the above excitations, the spin and parity of the resulting nuclear state are those appropriate to the unpaired particle or hole.

The extreme single-particle model may also be used to provide estimates of the differential cross section for reactions involving the direct transfer of nucleons. This reaction cross section is proportional to a quantity $S_\ell$ called the spectroscopic factor (see section 4.5). For present purposes, we may think of the spectroscopic factor as measuring that fraction of the wave function resembling a pure shell model state weighted by a statistical factor which expresses the fractional number of equivalent ways of forming the state. The extreme single-particle model predicts that the spectroscopic factor for stripping reactions leading to states in an odd-A nucleus is simply

$$S_\ell = \frac{\text{number of holes in active shell}}{2j + 1}$$

$$= 1 \text{ for stripping into completely empty states.}$$

This follows since in this description, each state is a pure shell model state.

## 1.3 Pairing Energy

The protons are expected to fill the energy states of the nucleus as indicated in figure 1.1 (slight differences occur in the level diagram for neutrons). Experimentally it is observed that "pairing energy" exists between two nucleons in the same shell which manifests itself as an increase in the nuclear binding energy. Furthermore it is found that the pairing energy increases with the j-value of the particles. This provides a mechanism for upsetting the level ordering whenever a high spin state lies slightly above a low spin level, for then it is likely that maximum binding energy will result from pairing particles in the high spin state at the expense of leaving a hole in the low spin state. From figure 1.1 it is seen that the $1h_{11/2}$ level, which is expected to be populated in the iridium isotopes (Z=77), is a likely candidate for exhibiting this type of behaviour.

## 1.4 Single-Particle Model

A more realistic approach to the shell model would be to consider only those nucleons in filled shells to be inert and to take into account the internucleon forces between all remaining particles. This forms the single-particle model. With such a model the nuclear properties are due to the "loose" particles outside closed shells. It is assumed that the interactions between these loose particles do not perturb them appreciably from the single particle orbits described by the quantum numbers (n, ℓ, j). This is equivalent to ignoring any correlations (such as formation of clusters) in the motion of the particles.

The interaction potential between the various extra-core nucleons is not the same as that for a two-particle system. A large part of the actual interaction is accounted for by the shell model potential, which represents the average effect of all the other nucleons on any one nucleon. In practice the residual interaction is approximated by a simple analytic form with adjustable parameters.

The procedure employed in a single-particle model calculation is to consider all possible couplings of the extra-core nucleons. Ideally all shells beyond the core should be considered in the calculation. However shells lying at high excitations may be safely excluded from the calculation with little effect upon the energies of the lower states. In a realistic calculation, the complexity of the problem quickly limits the actual number of shells which may be successfully employed. The matrix elements between all possible states (formed from the various couplings) must then be calculated and the resulting matrix diagonalized to obtain the energy spectrum. The corresponding wave functions indicate that the resulting states are described by a linear combination of the product wave functions of the (n, ℓ, j) states used. This procedure admixes other states into the wave function and consequently is termed configuration mixing. If the calculation confines the nucleons to a single $(n, \ell, j)$ state, then obviously no configuration mixing occurs.

The lowest energy level resulting from a single-particle model calculation will be the ground state while the remaining levels yield the excited states. Clearly the details of such a calculation will depend upon the specific nucleus under consideration along with the specific assumptions imposed. However some general remarks may be offered. In the first place, it is found that the lowest state formed by coupling an even number of neutrons or protons in the same j-shell is $J = 0$. Secondly, the lowest state formed when coupling an odd number of these particles is $J = j$. Here then is the reason why the extreme single-particle model predicts the correct angular momentum values.

The stripping spectroscopic factor for the formation of states in an odd-A nucleus is predicted by the single-particle model to be

$$S_\ell = \frac{\text{number of holes in active shell}}{2j + 1} [\sum_i \beta_i]^2$$

where $\beta_i$ are the amplitudes of the various single-particle components mixed into the wave function (the index i only runs over the components having $j = J_f$).

## 1.5 General Remarks

We have seen that the shell model describes the nuclear force by means of an "average" spherical potential. This average shell model potential represents the long range (of the order of a few fm) nuclear force and can be generalized by replacing it with a multipole expansion

$$V(\vec{r}_1\ \vec{r}_2) = \sum_k V_k(r_1\ r_2)P_k(\cos\ \theta_{12}).$$

The monopole term (k = 0) provides the dominant contribution and is responsible for the spherical part of the shell-model potential. The dipole term represents a center of mass oscillation and is therefore non-physical. This term also gives rise to motion in which the neutrons are displaced relative to the protons (the so-called "giant electric dipole resonance") which need not be considered here. Thus one expects the quadrupole term in the expansion to be the most important contribution not already included in the spherical shell model potential. This quadrupole term has profound effects. For nuclei in the regions of doubly magic shells, the quadrupole force is weak. Its effect is to weaken the resistance of the nucleus towards quadrupole distortion, and as a consequence, low-frequency vibrations in the nuclear shape occur. Thus vibrations of a collective character are expected to occur in addition to the intrinsic shell model transitions to make up the low energy spectrum of spherical nuclei. The section immediately following deals with such vibrations. As more and more nucleons are added, the strength of the quadrupole interaction quickly increases. Finally for sufficiently many particles outside of closed shells, the force becomes great enough to align the individual nucleon orbits so that a stable ellipsoidal field results. Then the nuclei exhibit permanent deformation. Nuclei of this type will be discussed later in the chapter.

Finally it will be remarked that higher multipole interactions give rise to additional effects, such as octupole and higher order vibrations.

## 1.6 Vibrations

As noted above, vibrations occur in the absence of field producing forces. The tendency will be for the nucleons -- more specifically, nucleon pairs since the pairing force is operative--to undergo independent and incoherent fluctuations away from spherical symmetry. However, due to the long range nuclear forces, the fluctuations of one pair will perturb the average nuclear field thereby inducing coherent fluctuations of all the other pairs. The induced fluctuations in turn act back on the first pair, changing its motion. In this manner a large amplitude oscillation involving the coherent motion of several nucleons may be established. The corresponding vibrational states may thus be considered as due to combinations of several particle -- more properly, quasi-particle -- excitations.

The vibrational model treats the core of the nucleus as an incompressible fluid, thereby suppressing all details of the particle structure. The vibrational excitation modes are characterized by angular momentum and z-component quantum numbers $\lambda$ and $\mu$. The surface of the vibrating nucleus can be described in terms of the coordinates of vibration $\alpha_{\lambda\mu}$ -- which are complicated functions of the nucleon coordinates -- as follows (Bohr (1952))

$$R = R_o[1+\sum_{\lambda}\sum_{\mu=-\lambda}^{\lambda} \alpha_{\lambda\mu}\, Y_{\lambda}^{\mu}(\theta,\phi)]$$

where $R_o$ is the equilibrium radius and $Y_\lambda^\mu$ the spherical hormonic of order $\lambda$, $\mu$. $\theta$ and $\phi$ are polar angles with respect to a fixed frame of reference.

If the nuclear oscillations are considered to be harmonic (deformation extending to equal distances on both sides of the equilibrium position) and of small amplitude the Hamiltonian may be written

$$H_{vib} = \sum_{\lambda} \sum_{\mu=-\lambda}^{\lambda} [1/2\ \beta_\lambda |\overset{o}{\alpha}_{\lambda\mu}|^2 + 1/2\ C_\lambda\ |\alpha_{\lambda\mu}|^2].$$

The first term represents the kinetic energy while the remaining term expresses the potential energy. The vibrational motion is that of a surface wave going around the nucleus and $\beta_\lambda$ is associated with the mass transported by this wave. The parameter $C_\lambda$ is a measure of the nuclear deformability. Specific assumptions about the details of the nucleon motions are necessary in order to estimate $\beta_\lambda$ and $C_\lambda$. Calculations assuming the nucleus to behave as irrotational flow of an incompressible fluid are presented by Bohr and Mottelson (1953), however $\beta_\lambda$ and $C_\lambda$ are generally regarded as parameters of the model. Each mode of vibration $\lambda$ has associated with it the frequency

$$\omega_\lambda = \sqrt{\frac{C_\lambda}{\beta_\lambda}} \quad .$$

The resulting spectrum will be that of a harmonic oscillator; in other words, the excitation energies are multiples of $\hbar\omega_\lambda$.

$$E \sim \sum_{\lambda} n_{\lambda} \hbar\omega_{\lambda}.$$

The integer $n_{\lambda}$ is referred to as the number of phonons (of order $\lambda$) in the excited state. Phonons of type $\lambda$ are characterized by angular momentum quantum number $\lambda$ and parity $(-)^{\lambda}$. The oscillations under consideration result from the quadrupole force and consequently are described by $\lambda = 2$ phonons. Vibrational modes involving $\lambda = 0$ and $\lambda = 1$ describe density and center of mass oscillations respectively and do not occur. Octupole ($\lambda = 3$), hexadecapole ($\lambda = 4$) and higher order oscillations are also permitted but identification of transitions having $\lambda > 3$ is very rare. Figure 1.2 indicates the expected vibrational spectrum. The multiplets formed by a coupling of several phonons are degenerate for an ideal harmonic oscillator, but this degeneracy is removed for any real nucleus.

The vibrational spectrum for an even-even nucleus consists of the states indicated in Figure 1.2 superimposed upon the 0+ ground state configuration. The characteristic feature of such a spectrum is the existence of a 2, 4, 0+ multiplet of states at about twice the energy of the first excited 2+ state. It perhaps should be remarked that there are relatively few vibrational nuclei for which the entire triplet of states is experimentally observed.

For an odd-A nucleus, vibrational spectra can be built on the intrinsic states. The combination of a particle state of angular momentum j and a vibrational state of angular momentum $R_{\lambda}$ gives rise to an approximately degenerate multiplet of $2j + 1$ or $2R_{\lambda}+1$ states (whichever is smaller) having angular momenta values $J = R_{\lambda}+j$,

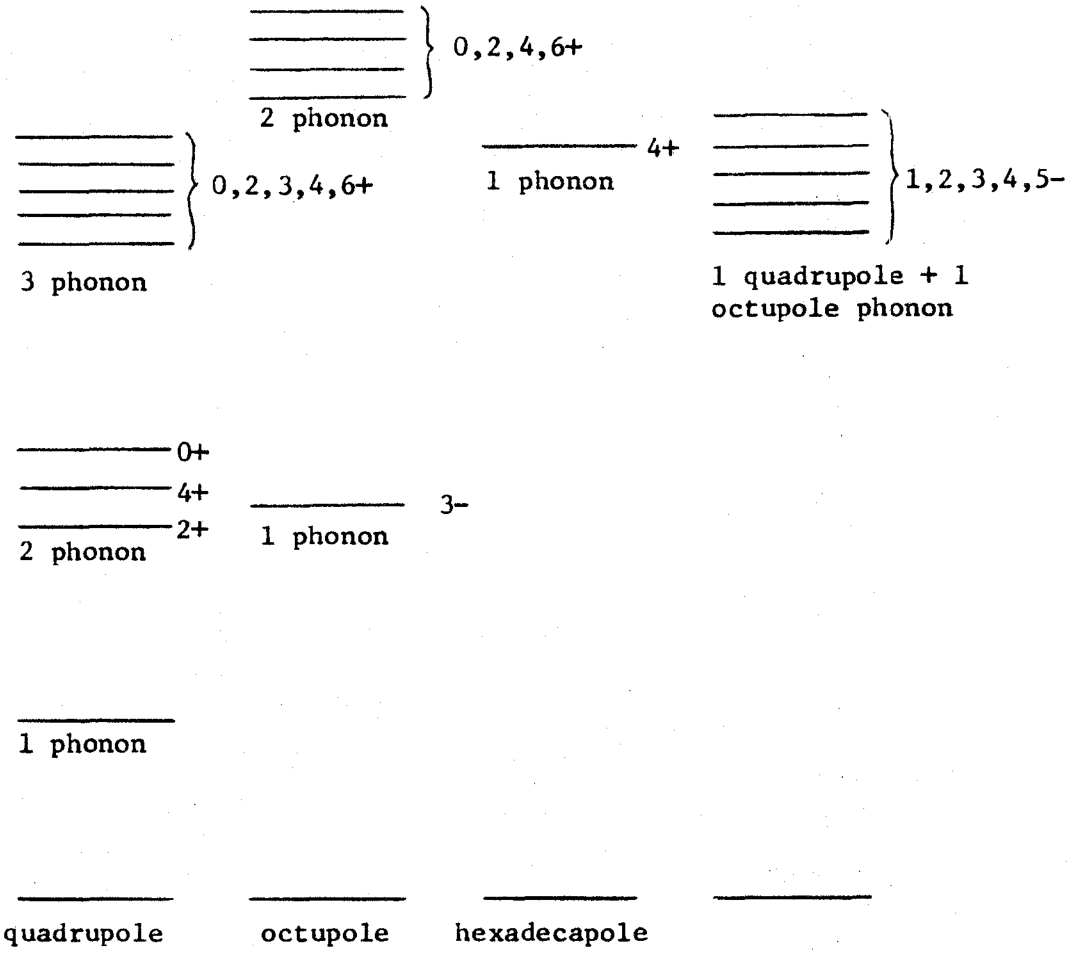

Figure 1.2 Vibrational energy spectrum.

$R_\lambda+j-1$ ----- $|R_\lambda-j|$. The energy of the multiplet relative to the intrinsic state will be approximately equal to the phonon energy for the neighbouring even-even nuclei. In practice it is only useful to consider couplings of the low-lying 2+ quadrupole vibration with the low-lying intrinsic states.

Vibrational states are a co-operative phenomenon involving many nucleons and therefore are not expected to be populated by reactions which involve the direct transfer of a single nucleon. However exceptional situations may arise. For an even-even nucleus, the vibrational state may be considered as a superposition of various two quasi-particle states. With the transfer of a single nucleon, it then becomes possible to populate specific components of these vibrations. Therefore whenever these particular components of the vibration occur with appreciable amplitude, that vibrational state may be populated (Burke et al (1966)).

## 1.7 Core Excitation Model

De-Shalit (1961) has proposed an alternative picture of the vibrational model as applied to odd-A nuclei. Rather than considering the coupling of phonons with the particle states, the core excitation model couples a collective excitation of the core to the odd nucleon. The principal assumption is that the core excitation can be identified with the corresponding core excitation (2+ first excited state) in the neighbouring even-even nucleus. The model need then make no assumptions about the nature of this core state. Obviously this model must predict the same features as the vibrational description since both treatments are representative of the same physical situation.

The coupling of the particle state of angular momentum j with the 2+ core state leads to a multiplet of states with angular momenta values $J = j+2, j+1, ---- |j-2|$. Furthermore the center of gravity of this multiplet is expected to correspond to the energy of the 2+ core state in the neighbouring even-even nucleus, so that

$$\frac{\sum_J (2J+1)\, E(J)}{\sum_J (2J+1)} \sim E_{core}$$

where $E(J)$ is the energy of the multiplet member J and $E_{core}$ is the energy of the core state in the neighbouring nucleus.

It is usual to denote the wave functions of the core excitation states by $| J_c j, J >$ where $J_c$ is the angular momentum of the core, j is that of the odd particle and J is the total angular momentum.

## 1.8 Deformed Nuclei

For nuclei containing many particles outside of closed shells, the quadrupole force is strong enough to produce a permanent deformation of the nucleus and consequently the quadrupole force is most appropriately treated as a field. This is done by using a deformed potential in place of the spherical shell model potential. Calculations employing an axially symmetric potential were first performed by Nilsson (1955) and are generally referred to as the Nilsson model. Calculations using a non-axially symmetric potential have also been carried out (Newton (1960), Hecht and Satchler (1962)). In addition to the intrinsic particle motions described by these models, collective motions involving many nucleons may occur which give rise to vibrations and rotations of the nucleus.

## B. Models Describing Axially Symmetric (Deformed) Nuclei

### 1.9 Nilsson Model

The Nilsson model employs the same procedure as used for the shell model. That is, each nucleon is assumed to move in some average potential generated by the interactions between all the other nucleons. Having specified the form of the potential, some convenient basis of representation is chosen and the Hamiltonian diagonalized in this representation. For the Nilsson calculation, the potential is assumed to be axially symmetric and of the form

$$V = V(r) + C\,\vec{\ell}\cdot\vec{s} + D\,\vec{\ell}\cdot\vec{\ell}$$

where the $\vec{\ell}\cdot\vec{s}$ term is the usual spin-orbit term required to give the correct shell closures. The $\vec{\ell}\cdot\vec{\ell}$ term is necessary to obtain the correct energy scale (its effect is to depress the high angular momentum states). C and D are adjustable parameters which must be chosen so as to reproduce the shell model ordering in the limit of spherical symmetry. The usual treatment assumes a cylindrically symmetric harmonic oscillator potential for V(r) (Nilsson (1955), Chi (1967)),

$$V(r) = \frac{1}{2} m\omega_o^2 r^2 \; [\; 1 - 2\beta Y_2^o(\theta, \phi) \;]$$

where $\omega_o$ is the oscillator constant which is expected to vary as

$$\hbar\omega_o \underset{-}{\sim} 41 \; A^{-1/3} \text{ MeV}.$$

The quantity $\beta$ is a measure of the deformation and is related to the conventional deformation parameter $\delta = \frac{\Delta R}{R}$ by

$$\delta = \frac{3}{4} \sqrt{\frac{5}{\pi}} \; \beta \underset{-}{\sim} 0.95\beta$$

with positive $\delta$ corresponding to a prolate shape and negative values to an oblate shape. The calculations are carried out in terms of the parameters $\kappa$ and $\mu$ which are defined by

$$\kappa \equiv - \frac{C}{2\hbar\omega_o}$$

$$\mu \equiv \frac{2D}{C}$$

For a particle moving in a deformed potential, $\vec{\ell}\cdot\vec{\ell}$ and $\vec{j}\cdot\vec{j}$ are no longer constants of the motion. Consequently if we use a representation involving spherical base vectors, the wave function describing the particle will consist of a linear combination of $(\ell, j)$ terms. For an axially symmetric potential, the projection of $\vec{j}$ along the nuclear symmetry axis is a constant of motion designated by $\Omega$. Furthermore we denote by $\Lambda$ and $\Sigma$ the respective projections of $\vec{\ell}$ and $\vec{s}$ along the symmetry axis. The relationship between these

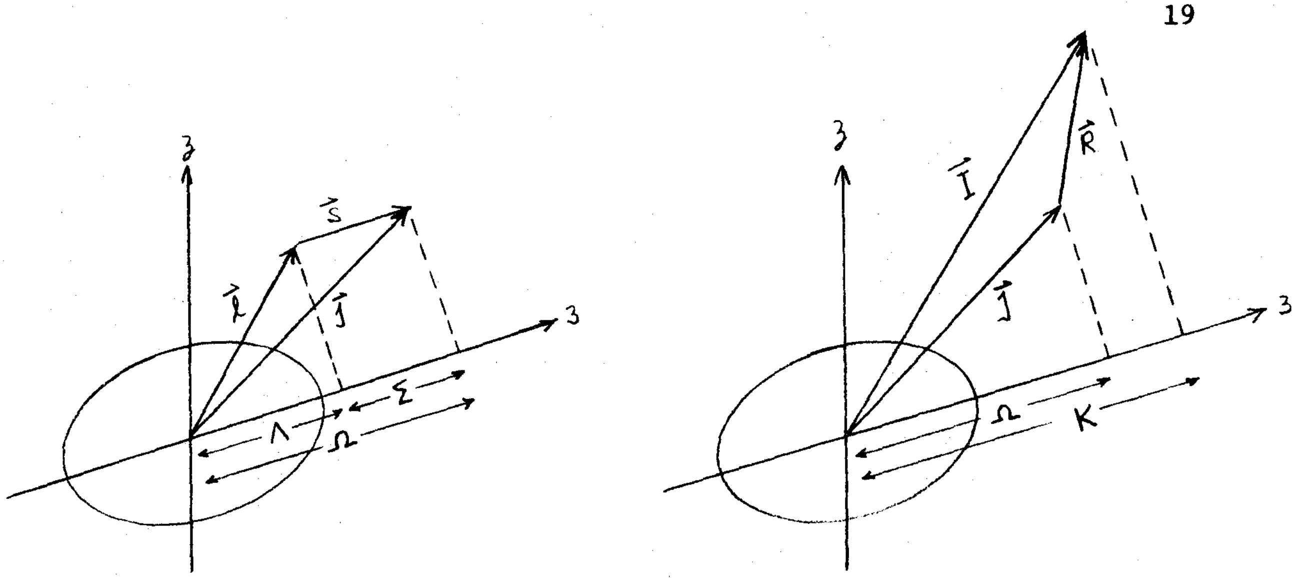

(a) (b)

Figure 1.3 Quantum numbers appropriate to deformed nuclei for (a) the intrinsic particle motion, (b) rotations coupled to the particle motion.

various quantum numbers is shown in figure 1.3(a).

The total number of oscillator quanta N may be regarded as the other constant of motion. Strictly speaking, non-zero matrix elements arise between states having N differing by an even integer, thereby mixing states of different N to some extent. Since these off-diagonal elements generally connect states with widely separated energies, the overlap integral is small and negligible mixing is expected. However there are cases where $\Delta N = 2$ mixing will be significant. These can be seen on the Nilsson diagram of Figure 1.4 where the 1/2 + [660] and 1/2 + [400] orbitals cross and also at the crossing of the 3/2 + [651] and 3/2 + [402] orbitals. Recent studies have confirmed the importance of $\Delta N = 2$ mixing for these regions in odd-neutron nuclei (Borggreen et al (1969), Lovhoiden et al (1970)). Since the 3/2 + [402] and 1/2 + [400] orbitals form the ground and first excited states in the odd-A iridium nuclei, $\Delta N = 2$ mixing may

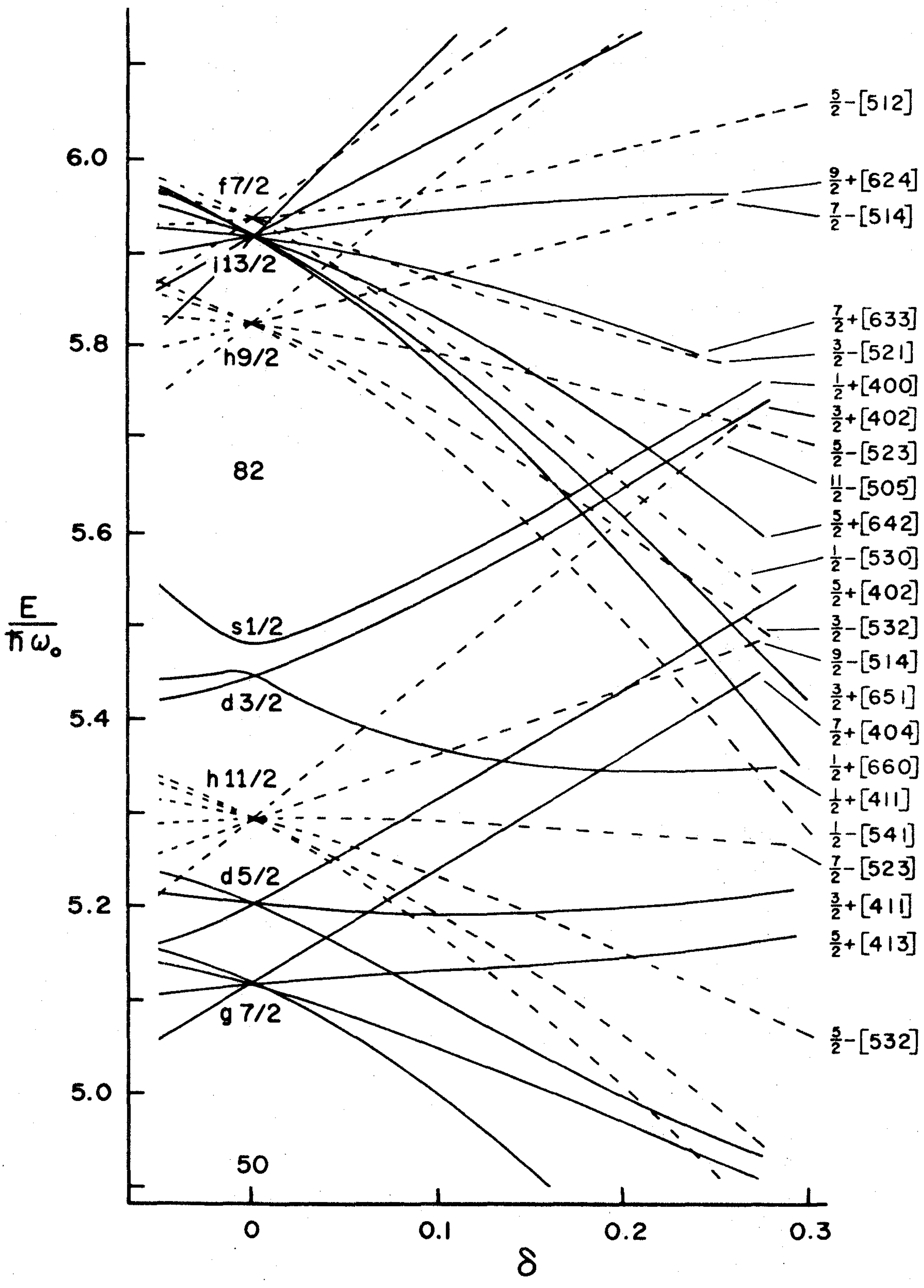

**Figure 1.4** Nilsson energy levels for protons.

play a role in the interpretation of these spectra.

A convenient representation chosen by Chi (1967) uses the isotropic harmonic oscillator eigenvectors as the set of base vectors. This spherical basis may be represented by $|N\ell j\Omega\rangle$. Then the Nilsson wave functions can be written

$$|EN\Omega\rangle = \sum_{j} c_{j\ell\Omega}|N\ell j\Omega\rangle.$$

The representation originally used by Nilsson uses $|N\ell\Lambda\Sigma\rangle$ as basis vectors. Then

$$|EN\Omega\rangle = \sum_{\ell\ \Lambda} a_{\ell\Lambda\Omega}|N\ell\Lambda\Sigma\rangle$$

with the relationship between these representations given by

$$a_{\ell\Lambda} = \sum_{j} c_{j\ell} \langle \ell s\Lambda\Sigma|j\Omega\rangle$$

where the subscript $\Omega$ has been suppressed since it is a good quantum number.

Since the Hamiltonian depends upon the deformation $\delta$, the energy of each state is a function of the deformation. For very large deformations, the number of oscillator quanta parallel to the symmetry axis, $n_3$, and the orbital angular momentum projection, $\Lambda$, become good quantum numbers. These asymptotic quantum numbers may therefore be used to label the levels. The proton levels appropriate for $Z \sim 77$ are shown in Figure 1.4 where the states are labelled by the value of $\Omega$, the parity and the triad $[Nn_3\Lambda]$. The parity of each level is given by $(-)^N$. As the deformation is applied, the shell model states are split into components characterized by $\Omega$. Each of these resulting energy orbitals is doubly degenerate corresponding to two states of $\pm\,\Omega$. As a result, two nucleons of a specific type may be placed in each Nilsson level.

For even-even nuclei, the ground state corresponds to a configuration in which all particles are filling paired orbitals $(\Omega, -\Omega)$. Positive parity results for this symmetric configuration and therefore all deformed even-even nuclei are predicted to have $K = \Omega = 0+$ ground states. Odd-A nuclei contain a single nucleon outside of filled $(\Omega, -\Omega)$ orbitals so that the spin and parity of the ground state is determined by that of the unpaired nucleon.

The excited states are formed by promoting nucleons into higher energy orbitals in a similar fashion as discussed for the shell model.

The Nilsson model predicts that the spectroscopic factor for stripping a nucleon into an even-even target is

$$S_\ell = \frac{2}{2I_f+1}\, c_{j\ell}^2$$

since $c_{j\ell}$ gives the amplitude of shell model state present in the Nilsson wave function.

## 1.10 Vibrations of Deformed Nuclei

Collective nuclear vibrations have already been discussed for spherical nuclei. A rather similar approach applies to the deformed case. However the phonon angular momentum $\lambda$ is no longer a good quantum number, although it is still useful for classification of the vibrations. Instead the projection of the phonon angular momentum on the nuclear symmetry axis, $\nu$, is conserved. Since deformed nuclei may undergo rotations as well as vibrations, the nuclear shape is described by

$$R = R_o \left[ 1 + \sum_{\lambda} \sum_{\nu=-\lambda}^{\lambda} a_{\lambda\nu} Y_{\lambda}^{\nu} (\theta',\phi') \right]$$

where $a_{\lambda\nu}$ are the coordinates relative to a rotating set of axes fixed to the nucleus. $\theta'$ and $\phi'$ are polar angles with respect to the nucleus fixed coordinate system. The corresponding Hamiltonian is

$$H_{coll} = \sum_{\lambda} \sum_{\nu=-\lambda}^{\lambda} \left[ 1/2\, B_{\lambda\nu} |\dot{a}_{\lambda\nu}|^2 + 1/2\, C_{\lambda\nu} |a_{\lambda\nu}|^2 \right].$$

Each mode of vibration $\lambda$ has associated with it the frequencies

$$\omega_{\lambda\nu} = \sqrt{\frac{C_{\lambda\nu}}{B_{\lambda\nu}}} \; .$$

Thus the vibrational modes corresponding to different $\nu$ values are no longer degenerate as they were in the spherical case.

For quadrupole vibrations, only $a_{20}$ and $a_{22} = a_{2-2}$ are non-vanishing since $a_{21}$ and $a_{2-1}$ manifest themselves in the form of rotational motion. Thus the allowed (quadrupole) frequencies become

$$\omega_{20} = \sqrt{\frac{C_{20}}{B_{20}}}$$

$$\omega_{22} = \sqrt{\frac{C_{22}}{B_{22}}}$$

These describe the so-called $\beta$ and $\gamma$ oscillations. This terminology results from expressing the quantities $a_{20}$, $a_{22}$ in terms of an elongation parameter $\beta$ and an axial-asymmetry angle $\gamma$ as follows

$$a_{20} = \beta \cos \gamma$$

$$a_{22} = a_{2-2} = \frac{1}{\sqrt{2}} \beta \sin \gamma \, .$$

The parameters $\beta$ and $\gamma$ are physically significant. $\beta$ represents the total deformation of the nucleus (related to $\delta$ by $\beta = \frac{4}{3}\sqrt{\frac{\pi}{5}}\ \delta$). The angle $\gamma$ is related to how the deformation is oriented in space. $\gamma = 0$ corresponds to a prolate spheroid while $\gamma = \pi$ corresponds to one of oblate shape. For other values of $\gamma$ which are multiples of $\frac{\pi}{3}$ spheroidal symmetries result along the other axes. Since the labelling of the nuclear fixed axes is arbitrary, these can all be described by $\gamma = 0$ or $\pi/3$ depending on whether the nucleus is prolate or oblate. If $\gamma$ is not a multiple of $\pi/3$, the nuclear shape is an ellipsoid having three unequal axes.

From the above considerations, two distinct vibrational modes occur. In the first, $\gamma$ remains at its equilibrium value (0 for prolate nuclei) while $\beta$ oscillates about its equilibrium deformation. These $\beta$ vibrations are associated with $\nu = 0$ and preserve the symmetry axis. For the second mode of vibration, $\beta$ remains fixed while $\gamma$ oscillates through $\gamma = 0$ (or $\pi$). These $\gamma$ vibrations have $|\nu| = 2$ and the nucleus loses its axial symmetry.

Octupole vibrations may also occur at low excitations. Such vibrations have $|\nu| = 0, 1, 2, 3$ although for the mostpart only $\nu = 0$ components are observed experimentally. There has been no experimental identification of the multiple phonon states which may be expected at higher excitations. Figure 1.5 indicates the vibrational states expected for a deformed nucleus. Rotational bands are also indicated (as dotted lines) since they inevitably accompany states of deformed nuclei.

For an even-even nucleus, the vibrational spectrum simply consists of the states of Figure 1.5 superimposed upon the 0+ ground state. For an odd-A nucleus, the vibrational excitations are built on intrinsic states. The combination of a particle state of angular momentum component $K_o$ with a vibrational motion characterized by $\nu$ couples to form states with angular momentum components $K = |K_o \pm \nu|$. Thus a single $\beta$ and two $\gamma$ vibrational states, as well as octupole states, are expected to be built upon the intrinsic state. The vibrational energy should be approximately equal to the corresponding vibrational energy in the neighbouring even-even nuclei.

## 1.11 Rotations

The distribution of particles which comprises a deformed nucleus may gradually change by altering its orientation in space while maintaining a fixed shape. When this happens the nucleus appears

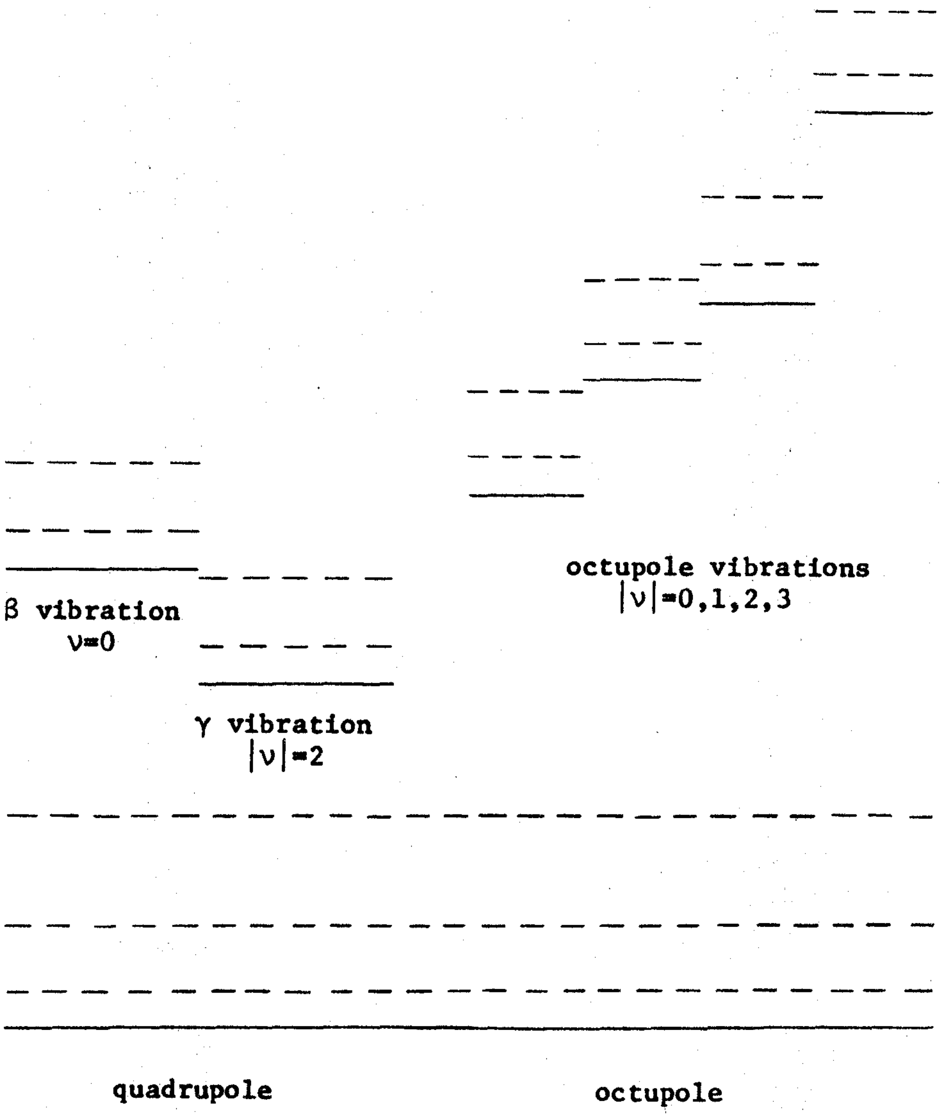

Figure 1.5 Vibrational energy spectrum for a deformed nucleus.

to be rotating.

The Hamiltonian for such a system is

$$H_{coll} = H_{vib} + \sum_{k=1}^{3} \frac{I_k^2}{2\mathcal{J}_k}$$

where $I_k$ is the component of the angular momentum along the nucleus fixed k axis and $\mathcal{J}_k$ is the moment of inertia about the same axis. In general no component $I_k$ is a constant of motion. The wave function for the system may be written as a linear combination of rotational $\mathcal{D}^I$ functions (Bohr (1952))

$$\Psi = f^I(\beta) \sum_{K=-I}^{I} g_K^I(\gamma) \mathcal{D}_{MK}^I$$

where $f^I(\beta)$ depends upon the $\beta$ vibrations and $g_K^I(\gamma)$ involves $\gamma$ vibrations. The condition that the wave function be invariant with respect to the choice of body-fixed axes restricts the summation to even values of K. Thus the wave function becomes

$$\Psi = f^I(\beta) \sum_{K=0}^{I}{}' g_K^I(\gamma) \; |IMK>_{\pm} \qquad K \text{ even.}$$

Since the nucleus possesses reflection symmetry, the rotational wave function is

$$|IMK>_{\pm} = \sqrt{\frac{2I+1}{16\pi^2(1+\delta_{K,0})}} \left(\mathcal{D}_{MK}^I \pm (-)^{I+K} \mathcal{D}_{M-K}^I\right) \qquad 1.1$$

where the ± denotes the parity of the wave function.

If the nucleus has an axis of symmetry (generally denoted as the 3-axis) then the component of angular momentum along that axis $I_3$ is a constant of motion which is specified by the quantum number K. For this case the wave function becomes

$$\Psi = f^I(\beta)\ g_K^I(\gamma)\ |\ IMK >$$

and the motion is seen to be separable into vibrational and rotational parts. The rotational energy is given by

$$E^I_{rot} = <IMK|\ \sum_{k=1}^{3} \frac{I_k^2}{2\mathcal{I}_k}\ |\ IMK > = \frac{\hbar^2}{2\mathcal{I}_1}\ [I(I+1)-K^2] + \frac{\hbar^2}{2\mathcal{I}_3}\ K^2$$

Because of axial symmetry, there can be no component of angular momentum along the 3-axis and therefore K = 0. Then the rotational energy is

$$E^I_{rot} = \frac{\hbar^2}{2\mathcal{I}}\ I(I+1).$$

The only positive parity states allowed are those of even I since the wave function 1.1 vanishes for odd I if K = 0. The ground states and $\beta$ vibrations ($K = \nu = 0$) of even-even nuclei exhibit axial symmetry with K = 0 and consequently rotational bands built upon these states contain only even I members. Equation 1.1 similarly restricts negative parity K = 0 states to odd I members. Octupole vibrations of the $K = \nu = 0$ type display this type of rotational spectrum. For non-zero K, all values of I are allowed. $\gamma$ vibrations have K = 2 and hence their band structure includes all I members.

We have ignored any coupling between the collective motion and the intrinsic coordinates. Consequently the forgoing is only applicable when the intrinsic angular momentum is zero, as in the case of even-even nuclei. We now consider the rotational motion of odd-A nuclei. The Hamiltonian need now be written

$$H = H_{\text{intrinsic}} + \sum_{k=1}^{3} \frac{R_k^2}{2\mathcal{I}_k}$$

where $R_k$ is the component of the rotational angular momentum along the k axis. The total angular momentum $\vec{I}$ is composed of the rotational angular momentum of the core $\vec{R}$ coupled with the angular momentum of the intrinsic particle motion $\vec{j}$

$$\vec{I} = \vec{R} + \vec{j}.$$

Figure 1.3(b) indicates the relationships between the various angular momenta. If we assume axial symmetry, the Hamiltonian is readily expressed as

$$H = H_{\text{intrinsic}} + \frac{\hbar^2}{2\mathcal{I}}[I(I+1)-2K^2] - \frac{\hbar^2}{2\mathcal{I}}(I_+J_-+I_-J_+) + \frac{\hbar^2}{2\mathcal{I}}\hat{j}^2 . \qquad 1.2$$

The last term contains only particle coordinates and can be absorbed in the intrinsic Hamiltonian. The term containing the operators $(J_+J_-+J_-J_+)$ couples the rotational and intrinsic particle angular momenta and is generally abbreviated RPC. Classically when a particle moves relative to a rotating set of axes (such as those fixed in the earth) the particle is subject to a Coriolis force which is directed at right angles to its motion. The RPC term has the same origin as the Coriolis force and is often referred to as Coriolis coupling. The operators $I_{\pm}$ in the Coriolis term have non-zero matrix elements only between states which differ by one unit in K. Thus RPC mixes K to some extent. However states of different K represent different particle states and therefore if the rotational spacing is small compared with the particle-excitation energies, the Coriolis term may be ignored. It should be noted that often this condition is not fulfilled.

The wave function corresponding to the Hamiltonian 1.2 is

$$\Psi = \sqrt{\frac{2I+1}{16\pi^2}}\ \phi(\beta,\gamma)\ (\mathcal{D}^{I}_{MK}\ \chi_K \pm (-)^{I-1/2}\mathcal{D}^{I}_{M-K}\ \chi_{-K}) \qquad 1.3$$

where $\phi(\beta,\gamma)$ represents vibrations in $\beta$ and $\gamma$ while $\chi_{\pm K}$ describes the motion of the particle. Notice that the wave function is composed of functions having both $\pm$ K. This means that for the special case of K = 1/2 bands, the RPC term is able to connect the K = $\pm$ 1/2 components and cannot be neglected. The RPC energy is

$$< \Psi \mid \frac{\hbar^2}{2\mathcal{J}} (I_+J_- + I_-J_+) \mid \Psi > = \frac{\hbar^2}{2\mathcal{J}} a(-)^{I+1/2}\ (I+i)$$

where a, called the decoupling parameter, is given by

$$a = \sum_j (-)^{j-1/2} (j+1/2)\, c_{j\ell}^2 \; .$$

A decoupling parameter of $a = 0$ indicates complete decoupling of the rotational and particle motions. The remainder of the rotational energy is

$$E_{rot}^{I} = \frac{\hbar^2}{2\mathcal{J}} [I(I+1) - 2K^2] \; .$$

Thus the solution to the total Hamiltonian 1.2 may be written

$$E = E_o + \frac{\hbar^2}{2\mathcal{J}} [I(I+1) - 2K^2 + \delta_{K,1/2}\, a\, (-)^{I+1/2} (I+1/2)] \; .$$

A rotational band of this form will be built upon each particle state with all values of $I \geq K$ permitted. For axially symmetric nuclei, the collective angular momentum $\vec{R}$ has no component along the 3-axis. Then K is entirely due to the particle angular momentum so that $K = \Omega$.

## C. Models Describing Non-Axially Symmetric Nuclei

### 1.12 Intrinsic States of an Asymmetric Nucleus

The previous discussion assumed that nuclei which exhibit permanent deformation also possess an axis of symmetry. The experimental data support this assumption for the low-lying states of a large number of deformed nuclei. However it is not clear that axial symmetry holds for the higher excitations. Moreover nuclei in the areas of transition between the highly deformed and spherical regions are likely to deviate from axial symmetry, even in their ground states. For such nuclei, it may be necessary to invoke models involving non-axial symmetry.

The intrinsic states of a non-axially symmetric nucleus may be found by employing a potential of corresponding shape. A procedure similar to that used in the Nilsson calculation is followed. Hecht and Satchler (1962) have performed the calculation using an asymmetric harmonic oscillator potential of the form

$$V(r) = \frac{1}{2} m \left(\omega_x x^2 + \omega_y y^2 + \omega_z z^2\right)$$

where $\omega_k = \omega_o(\beta,\gamma)\left[1+\sqrt{5/4\pi}\ \beta \cos\left(\gamma-\frac{2}{3}\pi k\right)\right]^{-1}$ $(k = 1,2,3=x,y,z)$.

The diagonalization of the Hamiltonian is carried out in a representation which uses angular momentum eigenfunctions in pseudo-space as basis vectors. However to first order, this representation is equivalent to the usual $|N\ell j\Omega>$ representation. The resulting wave functions are

$$|ENI> = \sum_{j\Omega} c_{j\ell\Omega}\ |N\ell j\Omega>$$

where the values of $\Omega$ are restricted to.... -11/2, -7/2, -3/2, 1/2, 5/2, 9/2, 13/2.... by the ellipsoidal symmetry. We see that for non-axial symmetry, $\Omega$ is no longer a good quantum number. The wave functions can also be expressed in the $|N\ell\Lambda\Sigma>$ representation in which case the Nilsson expansion coefficients $a_{\ell\Lambda\Omega}$ are given in terms of the $c_{j\ell\Omega}$ through

$$a_{\ell\Lambda\Omega} = \sum_j c_{j\ell\Omega} \langle \ell\ 1/2\ \Lambda\ \Sigma |\ j\Omega \rangle .$$

The energy of the states is now a function of the asymmetry parameter $\gamma$ as well as the deformation $\beta$. Figure 1.6 shows the proton levels for $Z \sim 77$ for values of $\gamma$ of 15° and 30°. The levels are labelled by the number of the odd nucleon occupying the state for small deformation $\beta$. In order to give some idea of the possible rotational bands which can be built on these particle states, the spin of the lowest rotational level when $\beta = 0.3$ ($-0.2$ for $\beta < 0$) is also indicated on the orbitals. Note that since levels with different $\Omega$ interact with each other, levels of the same parity cannot cross. The states $\sum_{j\Omega} c_{j\ell\Omega}\chi^j_\Omega$ and $\sum_{j\Omega} c_{j\ell-\Omega}\chi^j_{-\Omega}$ are degenerate and thus two nucleons of a given type may occupy each orbital.

As an illustrative example, we may consider the particle state 79 which is expected to form the ground state of the iridium isotopes. In the prolate symmetric rotor limit, $\beta > 0$, $\gamma = 0°$, this is the pure 3/2 + [402] state. In the oblate symmetric rotor limit, $\beta < 0$, $\gamma = 0°$, or what is equivalent, $\beta > 0$, $\gamma = 60°$, this becomes pure 1/2 + [400] state. The ground state thus changes from an $I = 3/2+$ to an $I = 1/2+$ state between $\gamma$ of 0° and 60°. It is a feature of the model that $I = 1/2+$ ground states become very common for large asymmetry.

The spectroscopic factor for stripping a nucleon into an

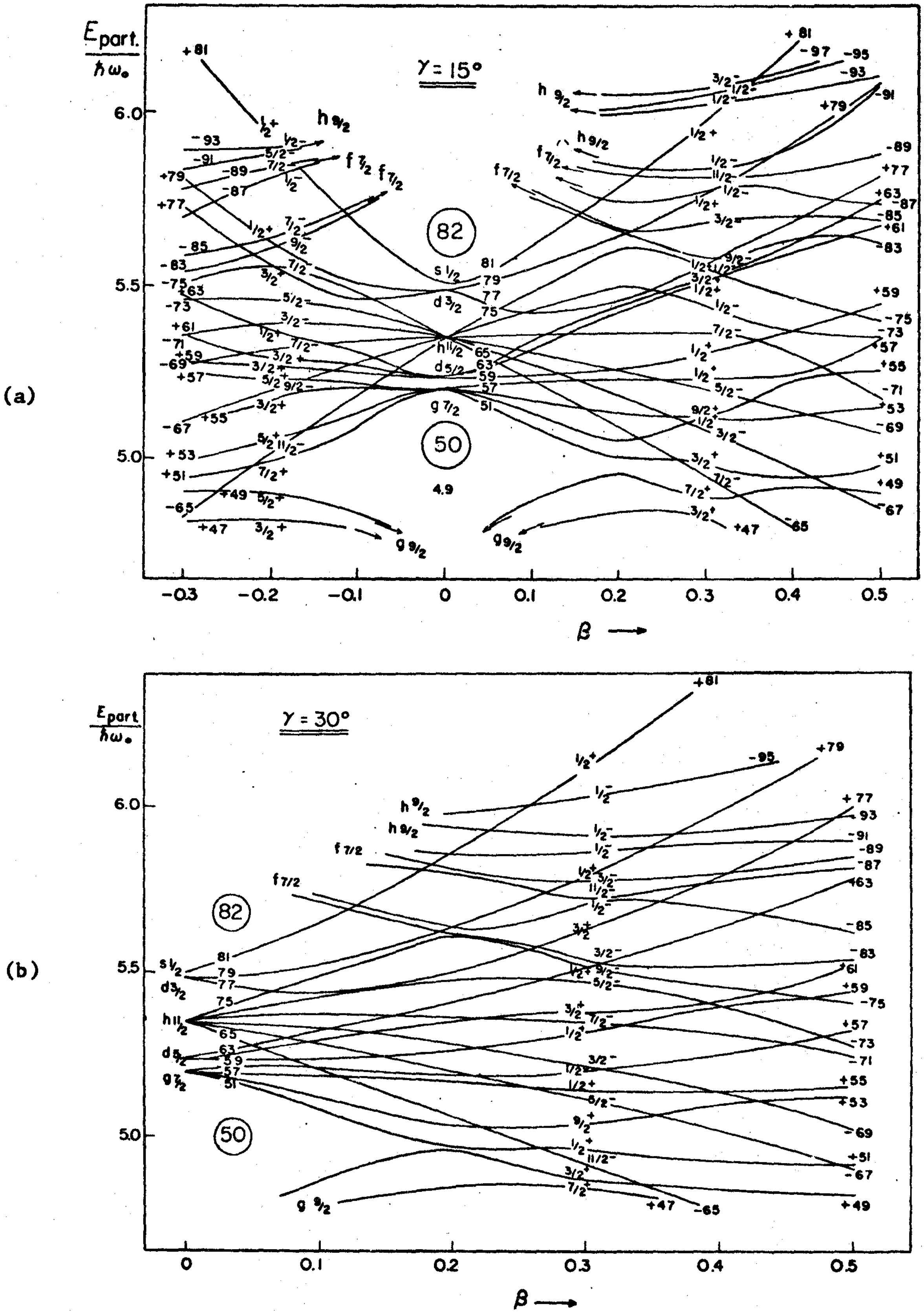

Figure 1.6 Proton levels of an asymmetric nucleus for (a) γ = 15°, (b) γ = 30°. [From Hecht and Satchler (1962)]

even-even target to form states in an asymmetric nucleus is

$$S_\ell = \frac{2I_i+1}{2I_f+1} \left\{ \sum_{K_i}{}' \sum_{K_f}{}' g^A_{K_i} g^{A+1}_{K_f} [c_{j\ell(K_f-K_i)} < I_i\; j\; K_i\; K_f-K_i \,|\, I_f\; K_f > \right.$$

$$\left. + (-)^{I_i} c_{j\ell(K_f+K_i)} < I_i\; j\; -K_i\; K_f+K_i \,|\, I_f\; K_f > ] \right\}^2$$

where the summation over $K_i$ includes only positive (including zero) even values of $K_i$. $K_f$ is summed over the values ... -7/2, -3/2, 1/2, 5/2, 9/2, ... The coefficients $g_K$ which determine the K-admixtures are to be determined from the solution of the rotational problem, as discussed in the following section.

## 1.13 Rotations of an Asymmetric Nucleus

The rotational levels of an unsymmetric even-even nucleus are obtained from the Hamiltonian

$$H_{rot} = \sum_{k=1}^{3} \frac{I_k^2}{2\mathcal{I}_k}$$

by using three unequal moments of inertia. The deviation of the nucleus from axial symmetry is expressed by the parameter $\gamma$ which varies between 0 and $\pi/3$. The moments of inertia are related to this parameter by the relation (Bohr (1952))

$$\mathcal{I}_k = 4B\beta^2 \sin^2 (\gamma - k \frac{2\pi}{3})$$

where B and $\beta$ are the mass and deformation parameters previously encountered.

Since there is no axis of symmetry, K is no longer a good quantum number and the wave function is written as a linear combination of K values

$$\Psi = \sum_{K}{}' \, g_K^I \, (\beta,\gamma) \mid IMK >. \qquad 1.4$$

For given I, K runs over all even integers less than or equal to I (except for odd I, K = 0 is excluded). The rotational energy is obtained by diagonalizing the matrix

$$< IMK \mid \sum_{k=1}^{3} \frac{I_k^2}{2\mathscr{I}_k} \mid IMK > \qquad 1.5$$

for each value of I. The coefficients $g_K$ can then be obtained by substituting the rotational eigenvalues into the system of linear equations resulting from the eigenvalue equation*. The number of states resulting with given I will equal the number of K values

---

*Diagonalization of 1.5 provides the eigenvalue solutions to the set of linear equations $\sum_i \{<IMK(j) \mid H_{rot} \mid IMK(i)> - E\delta_{ij}\} \, g_i = 0$ which result from the eigenvalue equation $H_{rot}\Psi = E\Psi$. The eigenvalues can then be substituted, one at a time, back into this system of linear equations to yield the coefficients $g_i$ appropriate to each eigenvalue.

included in the summation 1.4 (i.e. the order of the matrix). We therefore obtain one 0+ state, no 1+ state, two 2+ states, one 3+ state, three 4+ states, two 5+ states, and so on. The energies of the 2+ and 3+ states are (Davydov and Filippov (1958))

$$E^{2+}_{rot} = \frac{\hbar^2}{4B\beta^2} \frac{9(1 \pm \sqrt{1-8/9 \sin^2 3\gamma)}}{\sin^2 3\gamma}$$

$$E^{3+}_{rot} = \frac{\hbar^2}{4B\beta^2} \frac{18}{\sin^2 3\gamma} .$$

Note that $E^{2+} + E^{2'+} = E^{3+}$. This provides a quick test for the validity of the asymmetric rotor model. Moreover from the ratio $E^{2+}/E^{2'+}$ the value of $\gamma$ can be experimentally deduced.

Figure 1.7 shows the rotational energy levels for an asymmetric nucleus. For $\gamma = 0$ the spectrum is identical to that of an axially symmetric nucleus. The violation of axial symmetry leads to a slight increase in these energies (corresponding to a decrease in the effective moment of inertia) and the appearance of new energy levels. Although K is not a good quantum number, it is found that there is only a small admixture if $\gamma$ is not too large. The lowest energy levels for each I are predominantly K = 0 for all values of $\gamma$.

The rotational motion of non-axially symmetric odd-A nuclei is described by the Hamiltonian

$$H_{rot} = \sum_{k=1}^{3} \frac{R_k^2}{2\mathcal{J}_k}$$

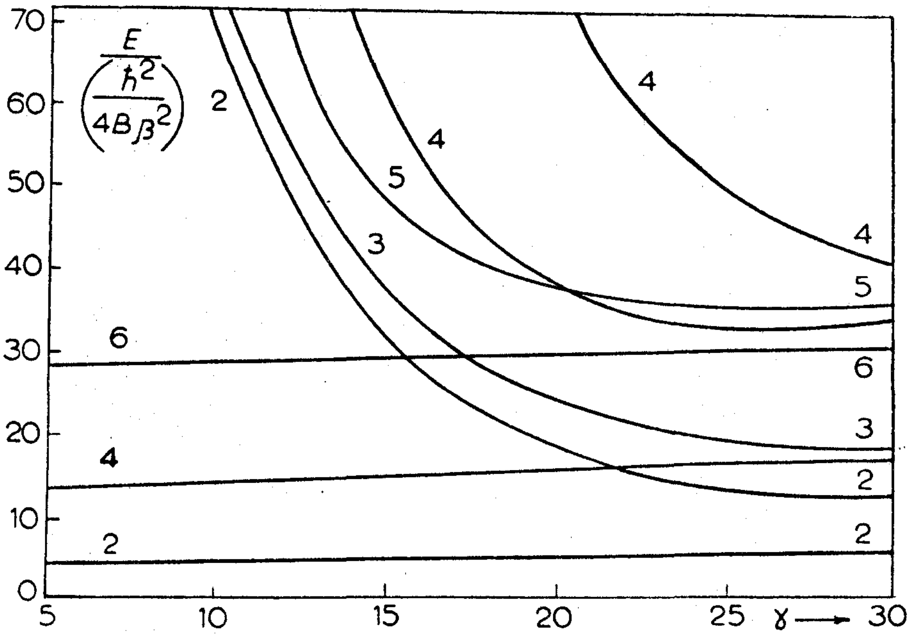

Figure 1.7 Rotational levels for an asymmetric nucleus. [From Davydov and Fillippov (1958)]

where the rotational angular momentum of the core $\vec{R}$ couples with the angular momentum of the odd particle $\vec{j}$ to yield the total angular momentum $\vec{I}$. The corresponding wave function may be expressed as the following linear combination (Hecht and Satchler (1962))

$$\Psi = \sum_K{}'' g_K \sqrt{\frac{2I+1}{16\pi^2}} \left( \mathfrak{D}^I_{MK} \chi_\nu \pm (-)^{I-1/2} \mathfrak{D}^I_{M-K} \chi_{-\nu} \right)$$

where the intrinsic state is described by $\chi_\nu = \sum_{j\Omega} c_{j\ell\Omega} |N\ell j\Omega>$ . The double prime on the summation is to remind us that the summation over both K and $\Omega$ is restricted to ... -7/2, -3/2, 1/2, 5/2, 9/2,.... In the axially symmetric limit, K is a good quantum number and all but one of the coefficients, $g_K$, go to zero. Similarly only one $\Omega$ remains and we then have $K = \Omega$.

The rotational spectrum is obtained by diagonalizing the Hamiltonian for each value of I. For given I there result I + 1/2 states corresponding to the I + 1/2 possible values of K. To illustrate the rather complicated dependence of the rotational energy upon the odd nucleon, the energy of the diagonal I = 1/2 state may be written as (Hecht and Satchler (1962))

$$\mathcal{E}_{rot} = -\frac{1}{2} \left(\frac{\hbar^2}{2\mathcal{I}_1} + \frac{\hbar^2}{2\mathcal{I}_2}\right) (a+b) - \frac{1}{2} \left(\frac{\hbar^2}{2\mathcal{I}_1} - \frac{\hbar^2}{2\mathcal{I}_2}\right) c + \frac{\hbar^2}{2\mathcal{I}_3} <K_R^2>$$

$$+ \left(\frac{\hbar^2}{2\mathcal{I}_1} + \frac{\hbar^2}{2\mathcal{I}_2}\right) d + \left(\frac{\hbar^2}{2\mathcal{I}_1} - \frac{\hbar^2}{2\mathcal{I}_2}\right) e$$

where the quantities a+b, c, d, e and $<K_R^2>$ depend upon the state of the odd nucleon. The parameter a + b plays the role of the decoupling parameter and is given by

$$a+b = \sum_{j\Omega}{}' c_{j\Omega}\, c_{j-(\Omega-1)} (-)^{j-1/2} \sqrt{(j+\Omega)(j-\Omega+1)} \quad .$$

The remaining parameters have the values

$$c = \sum_{j\Omega}{}' c_{j\Omega}\, c_{j-(\Omega+1)} (-)^{j-1/2} \sqrt{(j-\Omega)\ (j+\Omega+1)}$$

$$d = \frac{1}{2} \sum_{j\Omega}{}' c_{j\Omega}^2\ [j(j+1)-\Omega^2 + 1/2]$$

$$e = \frac{1}{2} \sum_{j\Omega}{}' c_{j\Omega}\, c_{j\Omega-2} \sqrt{(j+\Omega)\ (j-\Omega+1)\ (j+\Omega-1)\ (j-\Omega+2)}$$

$$\langle K_R^2 \rangle = \sum_{j\Omega}{}' c_{j\Omega}^2\ (K-\Omega)^2 \quad .$$

These quantities have been written explicitly since they will be encountered again when discussing electromagnetic properties.

Figure 1.8 shows the rotational energy levels based upon the particle state 79 for β values of 0.2 and 0.3. It may be recalled that this state is expected to form the ground state in the iridium isotopes. The low-lying levels are seen to take on the appearance of two overlapping band systems.

In concluding this section it will be remarked that the asymmetric rotor model is very similar to the symmetric rotor model plus vibrations. The additional rotational states which are formed

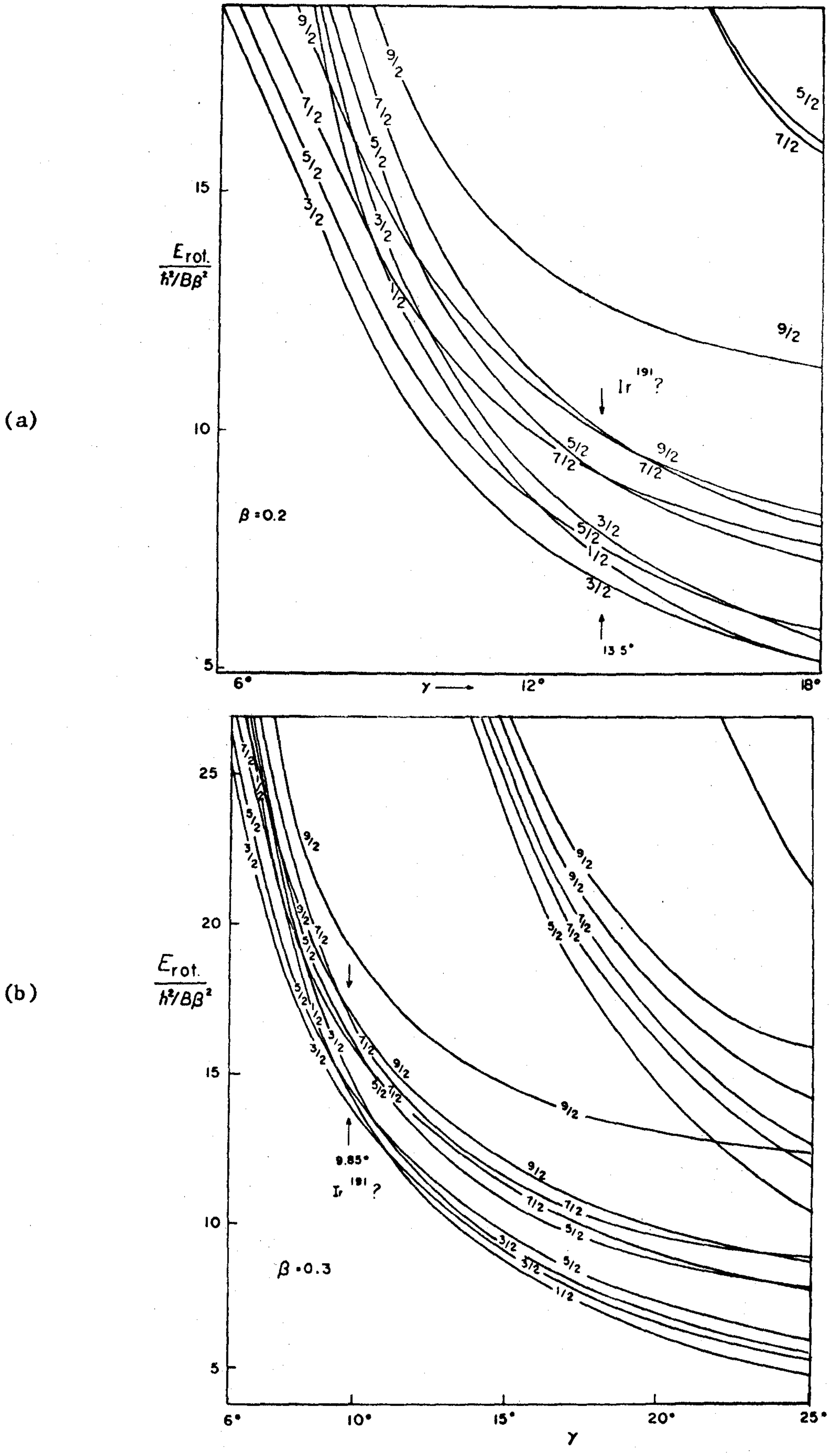

Figure 1.8 Rotational levels based on the asymmetric particle state 79 for (a) $\beta = 0.2$, (b) $\beta = 0.3$. [From Hecht and Satchler (1962)]

in the asymmetric description replace vibrational states of the axially symmetric model. Such correspondence is expected since a rotor with fixed asymmetry $\gamma_o$ is physically quite similar to a nucleus oscillating about axial symmetry with an rms value $\gamma_o$. Probably a combination of the two models allowing vibrations about nonzero equilibrium values of $\gamma$ would provide the most realistic description.

# CHAPTER II

# EMBELLISHMENTS TO THE MODELS

## Introduction

It is realized that the various models of the nucleus are highly simplified representations of the true physical situation. The models attempt only to describe the dominant features of the nuclear interaction and purposely neglect remaining minor contributions. Often it is possible to obtain an improved description of the nuclear properties by refining the models to include some of the effects which are normally neglected. These embellishments to the models form the subject of the present chapter.

## 2.1 Pairing

It is realized that when a self-consistent single-particle potential has been established, it does not precisely represent the whole nuclear interaction and some of the two-nucleon forces remain unaccounted for. It appears that among these presumably weak remnants there is a particularly strong interaction between two nucleons having time-reversed orbitals (i.e. nucleons which have identical quantum numbers except for the sign of their spin projections on a given axis). Direct evidence for this argument is provided by the fact that the lowest state of any even-even nucleus has $J = 0$. That only interactions between pairs of particles in the same state are important implies that the residual force responsible for pair-correlations is of very short range. The two interacting particles are able to move throughout the volume of the nucleus, but in a correlated manner. This correlation appreciably alters the wave function so that the resulting pair state contains a mixture of various single-particle states in comparable proportions.

The pairing formalism is most easily discussed in the language of second-quantization. We may write a shell model state $\psi_{jm}$ as $a^{+}_{jm}\,|0>$ where $a^{+}_{jm}$ defines a creation operator operating on the vacuum $|0>$ and creating a particle in the shell model orbit (jm). Similarly a destruction operator $a_{jm}$ may be defined which destroys a particle in an orbit (jm). The force acting between the particle pairs can then be represented by (Bardeen et al (1957))

$$V_{pair} = -G \Sigma\, a^{+}_{jm}\, a^{+}_{j-m}\, a_{j'm'}\, a_{j'-m'}$$

where the summation is confined to a few oscillator shells. Note that only correlations between particles in the same state (i.e. same j, opposite m) are included. This expression is associated with the destruction of one pair (in state $j' \pm m'$) and the creation of another ($j \pm m$). The quantity G is a measure of the strength of the pairing force. Explicitly it represents matrix elements of the form $<jm\ j-m|V_{pair}|j'm'\ j'-m'>$. Although this overlap integral becomes smaller as the orbitals become less similar, it is assumed these matrix elements are constant when pairs from only a few oscillator shells are included.

Let us generalize the notation by writing the states (jm) and (j-m) as ν+ and ν-. The procedure is then representative for both spherical and deformed nuclear states. The solution for the ground state was originally proposed by Bardeen, Cooper and Schrieffer (1957) to treat the superconductor problem. The same solution was introduced into nuclear physics to describe, the ground state wave function of an even-even nucleus by Bohr, Mottelson and Pines (1958)

$$|0>_{BCS} = \prod_{\nu} (U_{\nu}+V_{\nu}\ a^{+}_{\nu+}\ a^{+}_{\nu-})\ |0>. \qquad 2.1$$

From the solution, we see that there is a probability amplitude $U_{\nu}$ that the state ν is unoccupied by a pair of particles, and an amplitude $V_{\nu}$ that it is occupied. This implies

$$U^2_{\nu} + V^2_{\nu} = 1$$

and also that the total number of particles is

$$n = \sum_{\nu} 2\Omega_{\nu}\ V^2_{\nu}$$

where $\Omega_{\nu}$ is the number of pairs able to occupy the state $\nu(\Omega_{\nu} = 1$ or $j+1/2$ depending whether the Nilsson model or shell model is assumed). It is seen from 2.1 that the ground state wave function contains a mixture of various single-particle states and that the particles occupy these single-particle states only in pairs. Thus a single-particle level $\nu$ is either completely empty, and this occurs with the probability $U_\nu^2$, or filled with a pair, for which case the probability is $V_\nu^2$. The probabilities $U_\nu^2$ and $V_\nu^2$ are given by

$$U_\nu^2 = \frac{1}{2} \left| 1 + \frac{\varepsilon_\nu - \lambda}{\sqrt{(\varepsilon_\nu - \lambda)^2 + \Delta^2}} \right|$$

$$V_\nu^2 = \frac{1}{2} \left| 1 - \frac{\varepsilon_\nu - \lambda}{\sqrt{(\varepsilon_\nu - \lambda)^2 + \Delta^2}} \right|$$

where $\varepsilon_\nu$ is the single-particle energy ignoring the pairing force. The average Fermi level $\lambda$ is the energy up to which would be filled in the absence of pairing while the gap parameter $\Delta = G \sum_\nu \Omega_\nu U_\nu V_\nu$ provides a measure of the strength of the pairing.

If there is no pairing force, then $\Delta$ vanishes and $U_\nu$ and $V_\nu$ become 0 and 1 respectively if $\varepsilon_\nu < \lambda$, and 1 and 0 if $\varepsilon_\nu > \lambda$. In other words, all states below the Fermi level $\lambda$ are completely occupied while those states above the Fermi level are completely vacant. This situation is indicated in Figure 2.1(a). The presence of the pairing force causes a "smearing" of the Fermi level as shown in Figure 2.1(b). The high and low energy states are still almost completely empty or filled, but states near the Fermi surface are only partially occupied. The inflection point of the level population curve is determined by the value of $\lambda$ while the diffuseness of the Fermi surface is measured by the parameter $\Delta$.

Before we can discuss excited states, the quasi-particle concept must be introduced (Bogoliubov (1958), Valatin (1958)). The

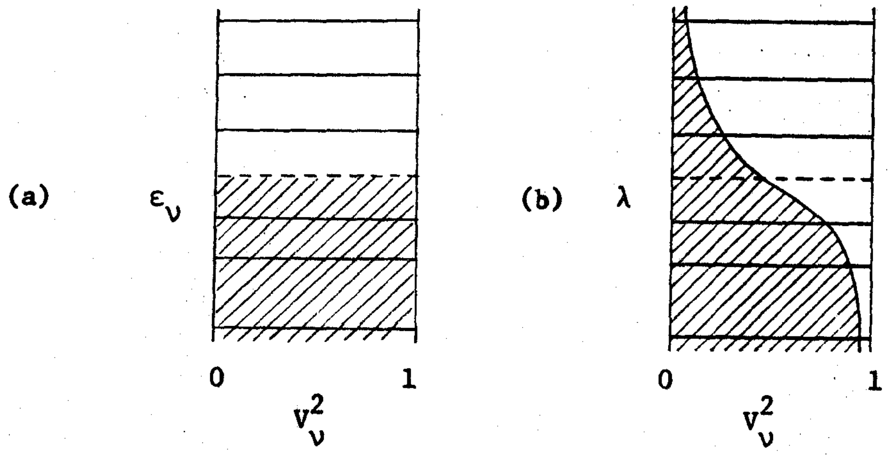

Figure 2.1 The pair population $V_\nu^2$ for the single-particle levels $\varepsilon_\nu$ (a) when no pairing force is present (i.e. $\Delta = 0$), (b) with pairing included.

ground state wave function $|0\rangle_{BCS}$ is defined to be the quasi-particle vacuum $|\tilde{0}\rangle$. All excitations are then obtained by operating on $|\tilde{0}\rangle$ with the following quasi-particle operators

$$\alpha^+_{\nu+} = U_\nu \, a^+_{\nu+} - V_\nu \, a_{\nu-}$$

$$\alpha^+_{\nu-} = U_\nu \, a^+_{\nu-} + V_\nu \, a_{\nu+}.$$

The first of these creates a quasi-particle with spin up while the second creates the quasi-particle with spin down. Thus the even-even system is transformed into its neighbouring odd nucleus by the application of one of these operators. The created quasi-particle has the properties of a particle to the extent that the level $\nu$ was empty (in the even-even system) and the properties of a hole with opposite angular momentum to the extent that the level in question was already occupied.

The energy of the one quasi-particle state is

$$E_\nu = \sqrt{(\varepsilon_\nu - \lambda)^2 + \Delta^2}\ .$$

Obviously, one-quasi-particle states of the form $\alpha^+_\nu\,|\tilde{0}>$ occur as the ground state and as low-lying excitations in odd nuclei, never in even ones. The energy difference between one-quasi-particle excitations is simply $E_\nu - E_{\nu'}$, which leads to a compression of the low energy spectrum relative to the single-particle picture. For an even-even nucleus, the lowest excited states are the two-quasi-particle states $\alpha^+_\nu\,\alpha^+_{\nu'}\,|\tilde{0}>$. Since usually $|\varepsilon_\nu - \lambda| << \Delta$ for the lowest odd state, these two-quasi-particle states correspond to an energy $E_\nu + E_{\nu'} \overset{>}{\sim} 2\Delta$. This provides the energy gap observed in all even-even nuclei.

The gap parameter $\Delta$ can be obtained from the even-odd mass difference in adjacent nuclei. For proton states, the value of the gap parameter is

$$2\Delta \sim S_p(Z,N) - \frac{S_p(Z-1,N) + S_p(Z+1,N)}{2}$$

where $S_p$ are proton separation energies. For $^{191}$Ir and $^{193}$Ir, the values of $\Delta$ required are those appropriate to the corresponding quasi-particle vacuum states $^{190}$Os and $^{192}$Os. A value of $\Delta = 950$ keV is estimated for these nuclei.

## 2.2 Coupling of Intrinsic and Collective Motions

It has been seen that nuclear models provide a description of the nucleus in terms of either intrinsic motions involving a few loose particles, or collective motions involving many nucleons. For the most part it was assumed that these motions were decoupled -- i.e. that the vibrations, rotations and intrinsic states could be treated independently. Unfortunately, such is not really the case.

It is helpful to visualize the intrinsic and collective coupling. Imagine at any instant in time that the nucleons form some asymmetric pattern in space. Because the surface is distorted at this moment, the potential "felt" by a particle is not spherically symmetric. If the distortion lasts for a few nucleon periods, the particles find themselves moving in orbits appropriate to an aspherical shell-model potential with the resulting particle motion tending to preserve the nuclear shape. This gives rise a slow change in the spatial pattern, producing a surface effect to which the particle motion is clearly coupled.

When the coupling is very weak, the particles have no directional correlation and the resultant average shape is spherical. Thus nearly spherical nuclei experience only weak coupling between the intrinsic and vibrational motions. For strong coupling, however, the nuclear surface acquires directional correlation thereby giving rise to permanent deformation. Consequently deformed nuclei exhibit strong coupling between the intrinsic and vibrational or rotational motions.

Since the bulk of the nucleons are unable to contribute to intrinsic excitations, they may be considered to form a core. Then we need only consider the extra-core nucleons as valid contributors to the coupling between the intrinsic and collective motions. Often only one extra-core nucleon provides an adequate description of the intrinsic states.

For spherical nuclei, the coupling between intrinsic and vibrational motions is weak and may be satisfactorily treated by perturbation techniques. It is found that the main effect of such coupling is to remove the degeneracy of the vibrational multiplets. The treatment of weak coupling closely parallels that of the intermediate coupling situation which is discussed below.

The coupling between the intrinsic and vibrational or rotational motions for deformed nuclei is strong. Such strong coupling implies that the precession frequency of the particle is large compared to the collective frequencies of the system. This fact provided the basis for writing the wave function 1.3 in its separable form. Hence strong coupling was implicit in the discussion of rotational levels for odd-A nuclei. As was seen at that time, the coupling produced the RPC term which gives rise to band mixing between states having $\Delta K = 1$. Band mixing calculations are currently popular and accordingly we devote the next section to their discussion. In addition to RPC, there exists a vibration-rotation interaction which is generally small. Such coupling depends on $\hat{I}^2$ and can be calculated from second order perturbation theory to introduce a correction term of the form

$$-B[I(I+1) + \delta_{K1/2}\, a^{I+1/2}\, (I+1/2)]^2$$

to the rotational spectrum.

For nuclei in the regions of transition between the spherical and highly deformed nuclei, an intermediate coupling situation prevails and the situation is more complex. The wave function may be expressed as (Bohr and Mottelson (1953))

$$\Psi = \sum_{jNR} a_{NR} \mid j;\ NR;\ JM> \qquad 2.2$$

where j is the particle angular momentum, N is the number of phonons (each of angular momentum λ) and R is the angular momentum of the core. J and M denote the total angular momentum and its z-component. Care must be taken that the expansion includes enough phonon states to give an adequate description of the nuclear state in this intermediate coupling region. In the absence of coupling, the ground state is given by $|j;\ 00;\ J=j,\ M>$. The interaction energy may be represented by (Choudhury (1954))

$$H_{int} = -k \sum_{\mu} \alpha_{\lambda\mu}\, Y_{\lambda}^{\mu}\, (\theta,\phi)$$

where k measures the coupling strength. The coupling energy is obtained upon diagonalizing this Hamiltonian. The results indicate that the degeneracy of the vibrational multiplet is split apart as the coupling strength k is applied. This is illustrated in figure

2.2 for the case of quadrupole oscillations (with up to 3 phonons) coupled to a single $j = 5/2$ particle. When more than one intrinsic state is involved, the dominant effect of the interaction is to mix one-phonon states based upon the intrinsic states $j'$ into the particle states $j$. Only states which obey $|j-j'| \leq \lambda$ are permitted to mix. Furthermore, appreciable mixing only occurs for those states close in energy.

In principle, if enough phonon states are included in the expansion 2.2 then the technique can be extended into the strong coupling region of deformation. Such calculations are impractical with present techniques. It is, however, illustrative to compare the energy levels obtained from the intermediate coupling and strong coupling treatments. Figure 2.3 indicates the excited states formed by coupling a $j = 5/2$ particle to the $2^+$ collective core as a function of the coupling strength. For very weak coupling, the vibrational states are nearly degenerate but this degeneracy is quickly removed as the intermediate coupling treatment is applied. When the coupling strength is sufficiently strong that the strong coupling solution applies, the states can be characterized as rotational and vibrational. The gap between the regions of validity of the two methods of treatment is indicated by the dotted interpolations in the figure.

## 2.3 Band Mixing

The mixing of states due to RPC will now be discussed. The Coriolis interaction is of the form (Kerman (1956))

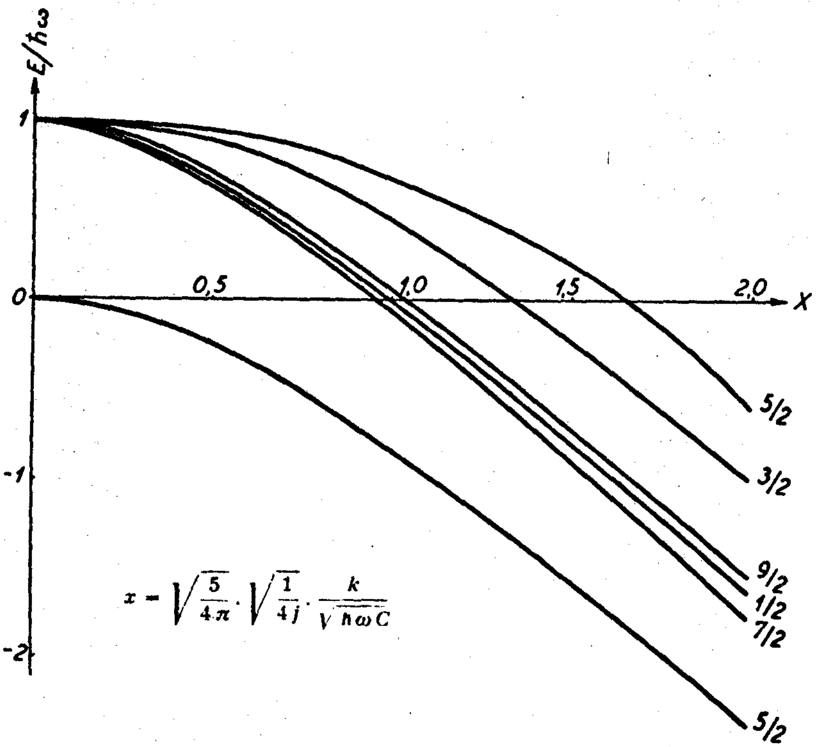

Figure 2.2 Energy of the states formed by the coupling of a quadrupole vibration to a j=5/2 particle as a function of coupling strength. The lower curve represents the ground state of the system. [From Choudhury (1954)]

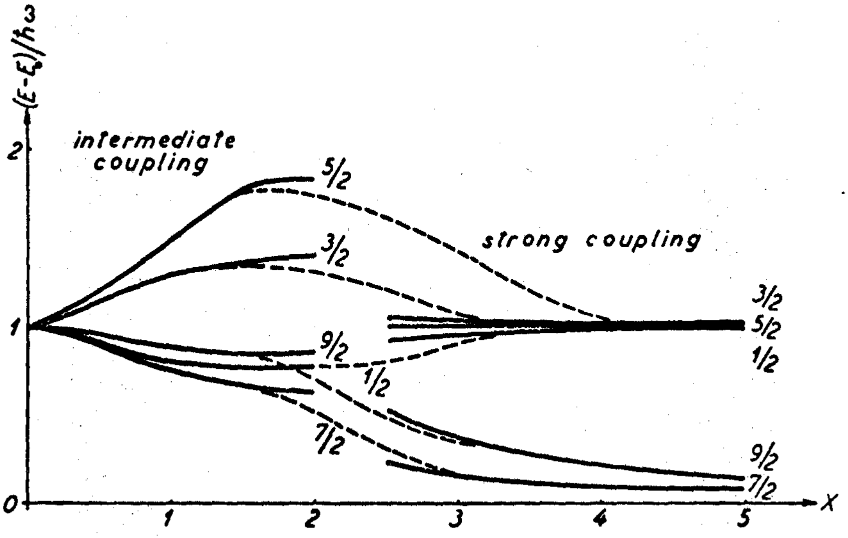

Figure 2.3 A comparison between the energy levels obtained from the intermediate coupling and strong coupling treatments. [From Choudhury (1954)]

$$\mathrm{RPC} = -\frac{\hbar^2}{2\mathcal{J}}\,(I_+J_- + I_-J_+)$$

which may be readily seen to couple states for which $\Delta K = 1$. In addition, states having $K = 1/2$ will couple together though the +K and -K interaction. The Coriolis matrix elements connecting bands with K and K + 1 are

$$\langle\mathrm{RPC}\rangle = -\frac{\hbar^2}{2\mathcal{J}}\,\Big(\sum_j c^{K}_{j\ell}\, c^{K+1}_{j\ell}\,\sqrt{(j-K)(j+K+1)}\;\Big)$$

$$\times\;(U_K\, U_{K+1} + V_K\, V_{K+1})\;\sqrt{(I-K)(I+K+1)}$$

where pairing has been included. Generally these matrix elements are somewhat larger than experiments would indicate so that it is customary to use an attenuated inertial parameter instead of $\frac{\hbar^2}{2\mathcal{J}}$.

The band mixing procedure consists of diagonalizing the matrix consisting of unperturbed energies and Coriolis interactions as the diagonal and off-diagonal terms respectively. As an example, the $5/2^+$ [642], $3/2^+$ [651] and $1/2^+$ [660] bands are coupled through the Coriolis interaction by diagonalizing the matrix

$$\begin{pmatrix} E_{642} & \langle\mathrm{RPC}\rangle & 0 \\ \langle\mathrm{RPC}\rangle & E_{651} & \langle\mathrm{RPC}\rangle \\ 0 & \langle\mathrm{RPC}\rangle & E_{660} \end{pmatrix}$$

for various values of I. The eigenvalues of this matrix are the perturbed energies of the states while the eigenvectors give the amplitude of the mixing. The wave function for the mixed state becomes

$$\chi = \sum_i a_i \chi_i^K$$

where the pure Nilsson states $\chi_i^K$ occur with corresponding amplitudes $a_i$.

If the mixing involves states originating from the same shell state, the Coriolis interaction "drains" the spectroscopic factor strength into the lowest of the interacting levels. For Coriolis mixed bands, the stripping spectroscopic factor (for an even-even target) becomes

$$S_\ell = \frac{2}{2I_f + 1} \left[ \sum_i a_i c^i_{j\ell} U_i \right]^2$$

where pairing has been included. The summation only includes components for which $j = I_f$.

## 2.4 $\Delta N = 2$ Mixing

It has already been remarked that $\Delta N = 2$ mixing will be significant in the regions of crossing between the $1/2^+$ [660] and $1/2^+$ [400] orbitals and between the $3/2^+$ [651] and $3/2^+$ [402] orbitals. It is to be noticed that the intersecting orbitals approach each other rather steeply and hence the mixing should only be appreciable within a very narrow deformation interval ($\Delta\delta \sim .01$), although zero-point fluctuations of the nuclear shape are expected to broaden this interval to some extent.

Matrix elements involving the $\Delta N = 2$ coupling energy have been evaluated by Nilsson (1955). However, recent experiments (Tjom and Elbek (1967)) indicate that these matrix elements are much too small. By using a deformed Woods-Saxon potential, Andersen (1968) has been able to calculate $\Delta N = 2$ matrix elements which are in good agreement with the experimental values.

## 2.5 Pairing Plus Quadrupole Model

Kisslinger and Sorensen (1963) have carried out calculations which explicitly include both the short range pairing and long range quadrupole forces. By adjusting the strengths of these interactions and using the shell model single-particle energies, they have been able to successfully reproduce many of the nuclear properties for a wide variety of different nuclei. Naturally such a procedure involving so few parameters cannot be expected to reproduce the properties of any particular nucleus as successfully as the individual models. However the fact that the general trends of the observed energy spacings, static moments and transition probabilities are reproduced for a wide variety of nuclei encompassing both the deformed and spherical mass regions is a significant accomplishment. Such success tends to validate the phenomological description of the residual interaction as consisting of short range pairing and long range (predominantly) quadrupole forces.

# CHAPTER III

# ELECTROMAGNETIC PROPERTIES OF THE MODELS

## Introduction

Transition probabilities provide information concerning the matrix elements $<f|O_{\lambda\mu}|i>$ connecting the states of a nucleus. These quantities are rather sensitive to the details of the nuclear wave function and therefore their prediction provides a more stringent test for any nuclear model than does the prediction of gross properties, such as energies or spins. Indeed, the main drawback of such a test is that the transition rates are far too sensitive to the fine details of the wave function so that slight admixtures are able to appreciably alter the rate. Unfortunately the crude forms in which the models of the nucleus presently exist cannot be expected to predict all the admixtures which arise in real nuclei from the complex nature of their nucleonic motions. The problem is circumvented to some extent by describing these transition probabilities in terms of a relatively small number of parameters. Such an approach, while not altogether satisfactory, provides a more realistic basis than calculations based entirely on oversimplified and general assumptions. Often the model can be subjected to a further test by comparing the experimental values of these parameters to the values expected on the basis of the zero-parameter model.

## 3.1 The Electromagnetic Operators

The reduced transition probability $B(\sigma\lambda)$ is defined to be (Preston (1962))

$$B(\sigma\lambda,\ J_i \to J_f) = \frac{1}{2J_i+1} \sum_{M_i M_f} |\langle f | O_{\lambda\mu} | i \rangle|^2$$

Defined in this manner, the $B(\sigma\lambda)$ is independent of the orientation of either the initial or the final nucleus. The magnetic and electric multipole operators for particle transitions may be written as

$$M_{\lambda\mu} = \mu_o \sum_p \left(g_s \vec{s} + \frac{2}{\lambda+1} g_\ell \vec{\ell}\right) \cdot \vec{\nabla}_p\, r_p^\lambda\, Y_\lambda^\mu \qquad 3.1$$

$$Q_{\lambda\mu} = \sum_p e_p^{eff}\, r_p^\lambda\, Y_\lambda^\mu \qquad 3.2$$

where the sum is taken only over the particles involved in the transition. $\mu_o$ is the nuclear magneton $\frac{e\hbar}{2m_p c}$ and $e_p^{eff}$ is the effective charge of the nucleon while $g_s$ and $g_\ell$ are the spin and orbital g-factors.

The collective motion of the nucleus is treated by means of the collective magnetic and electric multipole operators

$$M_{\lambda\mu} = \mu_o \frac{2}{\lambda+1} g_c \int \vec{\mathbb{R}}\,(\vec{r}) \cdot \vec{\nabla}\, r^\lambda\, Y_\lambda^\mu\, d\tau \qquad 3.3$$

$$Q_{\lambda\mu} = \frac{3}{4\pi} Ze\, R_o^\lambda\, \alpha_{\lambda\mu}^* \qquad 3.4$$

where $\alpha_{\lambda\mu}$ are the collective variables determining the deformed surface. $g_c$ is the collective g-factor and $\vec{\mathcal{R}}\ (\vec{r})$ is the collective angular momentum density. For $\lambda = 1$, the integral occuring in Eq. 3.3 reduces to the core angular momentum operator $\vec{R}$. In the sections to follow we restrict the discussion to M1 and E2 type transitions.

## 3.2 Extreme Single-Particle Model

In the case of the extreme single-particle model, the properties of the nucleus are attributed to the last unpaired particle. Consequently the sums in Eqs. 3.1 and 3.2 reduce to a single term. Assuming that the radial wave functions are constant over the nuclear volume, the transition probabilities for such single-particle transitions are (Preston (1962))

$$T_W\ (E\lambda) = \frac{2(\lambda+1)}{\lambda[(2\lambda+1)!!]^2} \left(\frac{3}{\lambda+3}\right)^2 \frac{e^2}{\hbar c} \left(\frac{\omega R}{c}\right)^{2\lambda} \omega \qquad 3.5$$

$$T_W\ (M\lambda) = \frac{2(\lambda+1)}{\lambda[(2\lambda+1)!!]^2} \quad 10 \left(\frac{3}{\lambda+3}\right)^2 \frac{e^2}{\hbar c} \left(\frac{\hbar/mc}{R}\right)^2 \left(\frac{\omega R}{c}\right)^{2\lambda} \omega. \qquad 3.6$$

Strictly speaking, the first of these expressions should be multiplied by $\alpha^2\ S(J_i,\lambda,J_f)$ and the second by $S(J_i,\lambda,J_f)$ where S is the statistical factor

$$S(J_i,\lambda,J_f) = (2J_f+1)\ \langle J_i\ \lambda\ 1/2\ -1/2|J_f\ 0\rangle^2$$

while for transitions other than E1, the effective charge $\alpha$ takes the values

$\alpha = 1$ for proton jumps

$= 0$ for neutron jumps.

It has become standard practice to omit S and $\alpha$ since these are the only portions which refer to a specific nucleus. The resulting expressions 3.5 and 3.6, which are universally used for expressing transition rates, are known as the Weisskopf estimates or units. The nuclear radius has arbitrarily been taken as 1.2 $A^{1/3}$ fm which results in the following values for M1 and E2 transitions

$$T_W(M1) = 3.09 \times 10^{13}\ E^3(\text{MeV}) \quad \text{sec}^{-1}$$

$$T_W(E2) = 7.39 \times 10^{7}\ A^{4/3}\ E^5(\text{MeV}) \quad \text{sec}^{-1} .$$

For M$\lambda$ type transitions, the matrix element involving the operator 3.1 contains grad $(r^\lambda\ Y_\lambda^\mu)$ which is a combination of spherical harmonics of order $\lambda$-1. This leads to the general selection rule $\Delta\ell \leq \lambda-1$. Thus M1 transitions are allowed only between states involving the same $\ell$-value; transitions which require a change in $\ell$ are said to be $\Delta\ell$-forbidden. For E$\lambda$ transitions, the operator imposes no such restriction upon $\ell$ (actually the restriction $\Delta\ell \leq \lambda$ exists but violations of this condition are forbidden in any case by angular momentum and parity considerations).

Related to the transition probabilities are the magnetic dipole and electric quadrupole moments of the nucleus. These quantities are measures of the diagonal elements involving the magnetic and electric multipole operators. In the extreme single particle model, the angular momenta and therefore the magnetic moments of the nucleons cancel in pairs so that the overall magnetic moment of the nucleus results only from that of the last odd nucleon. The value of the magnetic moment depends on the value of $J = j$ and is given by the following Schmidt limits

$$j = \ell + 1/2 \qquad \mu = (j-1/2)\ g_\ell + 1/2\ g_s$$

$$j = \ell - 1/2 \qquad \mu = \frac{j}{j+1}\ [(j+3/2)\ g_\ell - 1/2\ g_s]\ .$$

In this extreme single-particle picture, the electric quadrupole moment is also due to the last nucleon and can be expressed as

$$Q_p = -\frac{2J-1}{2(J+1)} \langle r^2 \rangle \qquad \text{for a proton}$$

$$Q_n = \frac{Z}{A^2} Q_p \qquad \text{for a neutron}$$

where $\langle r^2 \rangle$ is the mean square distance of the proton from the nuclear center. The quadrupole moment of the odd neutron is entirely due to the recoil motion of the rest of the nucleus. This model predicts that both the magnetic and electric moments vanish for even-even nuclei.

### 3.3 Vibrational Model

We have seen that the vibrations which a spherical nucleus undergoes are generally of a quadrupole nature. Consequently the gamma ray transitions connecting the vibrational states are restricted to quadrupole type transitions. For this reason, the model predicts that all M1 transitions between different phonon states vanish.

If we consider even-even nuclei, the reduced E2 transition probability between the first vibrational state and the ground state is (Nathan and Nilsson (1966))

$$B(E2;\ n_\lambda=1\rightarrow n_\lambda=0) = (\frac{3}{4\pi}\,Ze\,R_o^2)^2\ \frac{\hbar}{2\sqrt{B_\lambda C_\lambda}} \qquad 3.7$$

where $R_o$ is the equilibrium radius. Vibrational excitations are subject to the harmonic oscillator selection rule $\Delta n_\lambda = \pm 1$ and hence transitions from the $0^+$, $2^+$, $4^+$ triplet to the ground state are forbidden. Furthermore, the intensity rule

$$\sum_f B(E\lambda;\ n_\lambda,\ J_i \rightarrow n_\lambda-1,\ J_f) = n_\lambda\ B(E\lambda;\ n_\lambda=1 \rightarrow n_\lambda=0)$$

predicts that the transition probability between the two-phonon and one-phonon states is twice that for the decay of the one-phonon state.

$$B(E2;\ n_\lambda=2,\ J_i \rightarrow n_\lambda=1,\ J_f) = 2B(E2;\ n_\lambda=1 \rightarrow n_\lambda=0).$$

For odd-A nuclei, the foregoing expressions apply with slight changes due to the increased multiplicity of the phonon states. The reduced E2 transition probability between each of the one-phonon vibrational states and the ground state is equal and given by Eq. 3.7. It is expected that the vibrational parameters $B_\lambda$ and $C_\lambda$ will be similar to those of the neighbouring even-even nuclei so that the B(E2) rate should also be similar. This rate considerably exceeds the single-particle estimate. Two-phonon states may also occur in odd-A nuclei, although their interest is somewhat academic since such states have not been experimentally identified. The selection rule $\Delta n_\lambda = \pm 1$ would forbid transitions from the two-phonon states to the ground state. The intensity rule now predicts that the transition probability from the two-phonon to the one-phonon states should be summed between the one-phonon multiplets such that

$$\sum_f B(E2;\, n_\lambda=2,\, J_i \rightarrow n_\lambda=1,\, J_f) = 2B(E2;\, n_\lambda=1 \rightarrow n_\lambda=0).$$

In addition, the B(E2) strengths from any particular two-phonon state to the various one-phonon states will be proportional to the degeneracy of the final (one-phonon) state.

It should be stressed that the predictions of the vibrational model are based on the assumption that the nucleus describes harmonic oscillations. The assumption of harmonicity is dictated because of the difficulty in including the large number of possible anharmonic terms in a satisfactory manner. Experimentally it is found that the ratios of E2 transition probabilities often deviate by as much as 50% from the predictions of the harmonic approximation.

### 3.4 Core Excitation Model

In the core excitation model, a multiplet of states arises from coupling the odd nucleon to a core excitation, without specifying the nature of this core excitation. It follows that the model predictions are formulated in rather general terms.

The reduced transition probability may be expressed as

$$B(\sigma\lambda) = \frac{1}{2J_i+1} |<f||\Omega^{(\lambda)}||i>|^2$$

where $\Omega^{(\lambda)}$ denotes a multipole operator. For the core excitation model, the reduced matrix element $<f||\Omega^{(\lambda)}||i>$ is given by (de-Shalit (1961))

$$<J_c^f\ j',\ J_f||\Omega_c^{(\lambda)}+\Omega_p^{(\lambda)}||J_c^i\ j,\ J_i> = (-)^{J_c^f+j+J_f} \sqrt{(2J_f+1)(2J_i+1)}$$

$$\times \left[ <J_c^f||\Omega_c^{(\lambda)}||J_c^i> \begin{Bmatrix} J_c^f & J_f & j \\ J_i & J_c^i & \lambda \end{Bmatrix} \right.$$

$$\left. + (-)^{J_i-J_f} <j'||\Omega_p^{(\lambda)}||j> \begin{Bmatrix} j' & J_f & J_c \\ J_i & j & \lambda \end{Bmatrix} \delta_{J_c^f J_c^i} \right] \qquad 3.8$$

The subscripts p and c refer to the particle and core respectively. Usually the states which occur are all based on the same particle state so that $j' = j$. The reduced matrix elements occuring in 3.8 are generally regarded as parameters of the model. However the diagonal elements are related to the static magnetic and electric moments as follows

$$\mu_p = j\ g_p = \sqrt{\frac{j}{(j+1)(2j+1)}}\ <j||\Omega_p^{(1)}||j>$$

$$\mu_c = J_c g_c = \sqrt{\frac{J_c}{(J_c+1)(2J_c+1)}}\ <J_c||\Omega_c^{(1)}||J_c>$$

$$Q_p = \sqrt{\frac{16\pi}{5}} \sqrt{\frac{j(2j-1)}{(j+1)(2j+1)(2j+3)}}\ <j||\Omega_p^{(2)}||j>$$

$$Q_c = \sqrt{\frac{16\pi}{5}} \sqrt{\frac{J_c(2J_c-1)}{(J_c+1)(2J_c+1)(2J_c+3)}}\ <J_c||\Omega_c^{(2)}||J_c> .$$

$g_p$ and $g_c$ are the g-factors appropriate to the particle and the collective core while $Q_p$ and $Q_c$ are the quadrupole moments for the same particle and core states. These quantities are determined if the ground state and neighbouring $2^+$ excited state moments are known.

For E2 transitions from the multiplet $|J_c^i=2\ j,\ J_i>$ to the ground state $|J_c^f=0\ j,\ J_f=j>$, we obtain

$$B(E2) = \frac{1}{5}\ |<0||\Omega_c^{(2)}||2>|^2\ .$$

Therefore the E2 transition rate to the ground state is the same for all members of a multiplet. This is in agreement with the vibrational prediction. Furthermore this value should be similar to that of the neighbouring even-even nucleus, if the core states are equivalent. M1 transitions from the multiplet to the ground state are forbidden by the triangle relationships of the 6-j symbols which also accords with the vibrational model.

It is worth pointing out that admixtures of states are easily handled with the formalism described. These admixtures are often important. Although the model does not predict which mixtures occur, it seems likely that admixtures of nearby states with the same spin should be included.

## 3.5 Nilsson Model

The intrinsic states of an axially symmetric nucleus are described by the Nilsson model. Based upon each of these states, a rotational band sequence occurs so that for a nucleus having axial symmetry, the gamma transitions may involve a change in either the intrinsic state or the rotational state or both. The reduced M1 transition probability for such transitions is given by (Nilsson (1955))

$$B(M1;\ I_i,\ K_i \rightarrow I_f,\ K_f) = \left(\frac{e\hbar}{2mc}\right)^2 \frac{3}{16\pi} \mid M1 \mid^2 \qquad 3.9$$

where $M1 = \Big\{ <I_i\ 1\ K_i\ K_f - K_i | I_f\ K_f>$

$$+\ b_{M1}(K_i,K_f)(-)^{I_f+K_f} <I_i\ 1\ K_i - K_f - K_i | I_f - K_f> \Big\}\ G_{M1}(K_i,K_f)$$

and $b_{M1}$ and $G_{M1}$ are defined by Nilsson (1955). It is usual to regard these quantities as parameters to be fitted. Simplification occurs since $b_{M1}$ is non-zero only when $K_i = 1/2$ and $K_f = 1/2$.

The reduced E2 transition probability is given by

$$B(E2;\ I_i,\ K_i \rightarrow I_f,\ K_f) = e^2 \left(\frac{\hbar}{m\omega_o}\right)^2 \frac{5}{4\pi} \mid E2 \mid^2 \qquad 3.10$$

where $E2 = \Big\{ <I_i\ 2\ K_i\ K_f - K_i | I_f K_f>$

$$+\ b_{E2}(K_i,K_f)(-)^{I_f+K_f} <I_i\ 2\ K_i - K_f - K_i | I_f - K_f> \Big\}\ G_{E2}(K_i,K_f).$$

For cross-band transitions (which involve a change in the intrinsic state), $b_{E2}$ and $G_{E2}$ are regarded as parameters to be fitted. However for in-band transitions, the single-particle effects are small compared to the collective effects so that

$$b_{E2} = 0$$

$$G_{E2} = \frac{Q_o^K}{2\left(\frac{\hbar}{m\omega_o}\right)}$$

where $Q_o^K$ is the intrinsic quadrupole moment.

From the properties of the Clebsch-Gordon coefficients, it may be seen that whenever $\Delta K>\lambda$, the transition probabilities vanish. Thus M1 transitions are only allowed when $\Delta K\leq 1$ and E2 transitions may only occur when $\Delta K\leq 2$; transitions which violate these rules are said to be $\Delta K$-forbidden.

The Nilsson model predicts that the magnetic moment is given by

$$\mu = g_R I + \frac{K^2}{I+1}(g_K-g_R) + \frac{1}{4}\,\frac{2I+1}{I+1}\left[(g_s-g_\ell)(-)^{I-1/2+\ell}\sum_\ell a_{\ell o}^2 + (g_\ell-g_R)(-)^{I-1/2}\,a\right]\delta_{K1/2}$$

where

$$(g_K-g_R) = \frac{1}{2K}(g_s-g_\ell)\sum_\ell (a^2_{\ell\ K-1/2} - a^2_{\ell\ K+1/2}) + (g_\ell-g_R)$$

and $g_s$, $g_\ell$, $g_R$ are the spin, orbital, and collective g-factors. This standard expression may be rearranged into the convenient form

$$\mu = g_R I + \frac{1}{2}\sqrt{\frac{I}{I+1}}\ M1\ .$$

This form for the magnetic moment has the advantage that it enables band mixing to be treated in terms of the parameters appearing in the expression for the transition probability.

If a uniform charge distribution is assumed, the intrinsic quadrupole moment for an axially symmetric nucleus is

$$Q_o \simeq 0.8\ Z\ R_o^2\ \delta\ (1+1/2\delta)$$

where $R_o$ is the mean charge radius of the nucleus.

## 3.6 Band Mixing in the Nilsson Model

Let us denote the pure Nilsson wave functions by $|\psi_j\rangle$. Then when band mixing is included, the wave functions describing the mixed states become

$$|E\ N\ I_i\rangle = \sum_j a_j^{I_i}\ |\psi_j\rangle$$

$$|E\ N\ I_f\rangle \quad \sum_k a_k^{I_f}\ |\psi_k\rangle$$

where $a_j$ is the amplitude with which the Nilsson state $|\psi_j\rangle$ occurs.

The transition probabilities for the mixed states can be expressed as

$$B(M1;\ I_i \rightarrow I_f) = \left(\frac{e\hbar}{2mc}\right)^2 \frac{3}{16\pi} \left[ \sum_{jk} a_j^{I_i}\ a_k^{I_f}\ M1 \right]^2$$

$$B(E2;\ I_i \rightarrow I_f) = e^2 \left(\frac{\hbar}{m\omega_o}\right)^2 \frac{5}{4\pi} \left[\sum_{jk} a_j^{I_i}\, a_k^{I_f}\, E2\right]^2$$

where the quantities M1 and E2 have already been defined. The summations are performed over all components of both the initial and final wave functions. The magnetic moment for a mixed state can be written in the corresponding form

$$\mu = g_R I + \frac{1}{2}\sqrt{\frac{I}{I+1}}\ \sum_{jk} a_j^I\, a_k^I\, M1 \quad .$$

## 3.7 Deformed Vibrational Model

The vibrations which a deformed nucleus undergoes are usually quadrupole type $\beta$ or $\gamma$ oscillations. This restricts transitions involving a change of phonons to pure quadrupole type with the result that all M1 transitions involving different phonon states are forbidden.

For both even-even and odd-A nuclei, the reduced E2 transition probability between the $\beta$ or $\gamma$ vibrational states and the ground state rotational band is (Alder et al (1956))

$$\begin{aligned} &B(E2;\ n_\lambda=1,\ I_i,\ K_i \rightarrow n_\lambda=0,\ I_f,\ K_f) \\ &= \langle I_i\ 2\ K_i\ K_f-K_i | I_f\ K_f\rangle^2 \left(\frac{3}{4\pi} ZeR_o^2\right)^2 \frac{\hbar}{2\sqrt{B_{\lambda\nu}C_{\lambda\nu}}} \end{aligned}$$

where the Clebsch-Gordan coefficient gives the branching ratios to the members of the ground state band. This formula also applies for the inverse process of exciting a rotational band built upon a vibration, such as might be observed in a Coulomb excitation experiment. The harmonic oscillator selection rule $\Delta n_\lambda = \pm 1$ forbids transitions from any two-phonon state to the ground state band. Such vibrations have yet to be experimentally identified in the deformed region.

### 3.8 Rotational Model

For an even-even nucleus, the rotational levels form a $0^+$, $2^+$, $4^+$, ..... sequence of states. The gamma decay then proceeds in cascades of E2 radiation with the reduced transition probability for the I+2→I transition given by (Bohr and Mottelson (1953))

$$B(E2) = \frac{15}{32\pi} e^2 Q_o^2 \frac{(I+1)(I+2)}{(2I+3)(2I+5)} \quad .$$

In an odd-A nucleus, the rotational levels form a sequence with I = K, K+1, K+2, .... For the cross-over transitions I+2→I, the reduced E2 transition probability can be written as

$$B(E2) = \frac{15}{32\pi} e^2 Q_o^2 \frac{(I+1-K)(I+1+K)(I+2-K)(I+2+K)}{(I+1)(2I+3)(I+2)(2I+5)}$$

while for the I+1→I transitions, both E2 and M1 radiations result which are given by

$$B(E2) = \frac{15}{16\pi} e^2 Q_o^2 \frac{K^2(I+1-K)(I+1+K)}{I(I+1)(2I+3)(I+2)}$$

$$B(M1) = \frac{3}{4\pi} \left(\frac{e\hbar}{2mc}\right)^2 (g_K-g_R)^2 \frac{K^2(I+1-K)(I+1+K)}{(I+1)(2I+3)} \quad \text{providing } K \neq 1/2.$$

These expressions for odd-A nuclei result directly from Eqs. 3.9 and 3.10.

It is noticed that the ratios of transition probabilities within a band are independent of the intrinsic structure of the band. This is a mathematical consequence of the fact that the rotational state of the nucleus is changing without altering its intrinsic state.

### 3.9 Asymmetric Rotor Model

It has been seen that the rotational levels of an asymmetric nucleus take on the appearance of overlapping band sequences. The reduced E2 and M1 transition probabilities between these rotational levels have been given by Davydov and Filippov (1958) for an even-even nucleus. The first few values are given by

$$B(E2;\ 2+ \rightarrow 0+) = \frac{e^2Q_o^2}{16\pi}\ \frac{1}{2}\left[1 + \frac{3-2A}{\sqrt{9-8A}}\right]$$

$$B(E2;\ 2'+ \rightarrow 0+) = \frac{e^2Q_o^2}{16\pi}\ \frac{1}{2}\left[1 - \frac{3-2A}{\sqrt{9-8A}}\right]$$

$$B(E2;\ 2'+ \rightarrow 2+) = \frac{e^2Q_o^2}{16\pi}\ \frac{10}{7}\ \frac{A}{9-8A}$$

$$B(M1;\ 2'+ \rightarrow 2+) = \frac{90}{49\pi^2}\ \mu_o g_c^2\ \beta^2\ \frac{A}{9-8A}$$

with $A = \sin^2 3\gamma$

$$Q_o = \frac{3ZeR_o^2\beta}{\sqrt{5\pi}}\ .$$

For an odd-A nucleus, the rotational levels are based upon the particle state in a rather complicated manner. The reduced transition probabilities for transitions $I_i \rightarrow I_f$ between different rotational states based on the same particle excitation are given by (Hecht and Satchler (1962))

$$
\begin{aligned}
B(M1) = \frac{3}{4\pi} \Bigg[ & g_R \sqrt{I_i(I_i+1)}\, \delta_{I_i I_f} \sum_K{}' g_K^i\, g_K^f \\
& + \sum_K{}' g_K^i\, g_K^f \langle I_i\ 1\ K\ 0 | I_f\ K \rangle \{ (g_s - g_\ell) \langle S_o \rangle + (g_\ell - g_R) \langle \Omega \rangle \} \\
& + \sum_K{}' g_K^i\, g_{-(K-1)}^f \langle I_i\ 1\ K\ {-1} | I_f\ K-1 \rangle \frac{(-)^{I_f - 1/2}}{\sqrt{2}} \\
& \qquad \{ (g_s - g_\ell) \langle S_- \rangle + (g_\ell - g_R)(a+b) \} \\
& + \sum_K{}' g_K^i\, g_{-(K+1)}^f \langle I_i\ 1\ K\ 1 | I_f\ K+1 \rangle \frac{(-)^{I_f + 1/2}}{\sqrt{2}} \\
& \qquad \{ (g_s - g_\ell) \langle S_+ \rangle + (g_\ell - g_R)\ c \} \Bigg]^2
\end{aligned}
$$

$$
\begin{aligned}
B(E2) = \frac{5}{16\pi} \Bigg[ & \{ Q_o \cos\gamma + q_o \} \sum_K{}' g_K^i\, g_K^f \langle I_i\ 2\ K\ 0 | I_f\ K \rangle \\
& + \frac{\{ Q_o \sin\gamma + q_2 \}}{\sqrt{2}} \sum_K{}' ( g_K^i\, g_{K-2}^f \langle I_i\ 2\ K\ {-2} | I_f\ K-2 \rangle \\
& + g_K^i\, g_{K+2}^f \langle I_i\ 2\ K\ 2 | I_f\ K+2 \rangle ) \Bigg]^2
\end{aligned}
$$

The coefficients $g_K$ are obtained from the solution of the rotational problem (not to be confused with the g-factors $g_s$, $g_\ell$, $g_R$). Hecht and

Satchler (1962) define the remaining terms although it would appear useful to treat the expressions surrounded by braces { } as parameters of the calculation. This provides five parameters in terms of which all the M1 and E2 transitions must be expressed. In addition, the magnetic and electric quadrupole moments are expressed in terms of these same parameters, although the expressions will not be reproduced here.

### 3.10 Pairing Effects

We shall conclude the chapter by examining the effect that pairing correlations have upon the single-particle transition rates. We recall that a quasi-particle may be considered as a linear combination of a particle and a hole with opposite angular momentum. Since a hole has opposite charge to a particle, quasi-particles near the Fermi surface, which are equally as much holes as particles, will have small electric moments. It is therefore expected that electric transitions between states in the vicinity of the Fermi surface will be strongly hindered. For magnetic properties, the particle-hole character of the quasi-particle is unimportant since, although the hole has opposite charge to the particle, it also travels in the opposite sense. Consequently, we expect magnetic transitions to be independent of the pairing correlations.

The modification of the single-particle transition rates is expressed by a pairing factor

$$F = (U_{\nu'} U_{\nu} - \tau V_{\nu'} V_{\nu})^2$$

where $\tau = -1$ for magnetic multipoles and +1 for electric multipoles. Near the Fermi surface, $U^2$ and $V^2$ are $\sim 0.5$ so that F is small for electric transitions and $\sim 1$ for magnetic transitions.

# CHAPTER IV

# GENERAL CONCEPTS

## Introduction

The various nuclear models and their extensions have had limited success in describing nuclear properties. In order that both the successes and shortcomings of such models may become evident, it is essential that accurate experimental information be available. Clearly then, the need arises to determine the properties of a nucleus.

The assembly of nucleons comprising a nucleus is fully described by a quantum mechanical wave function. The eigenstates of such a wave function are characterized by a set of observable eigenvalues. These include the energy, angular momentum (loosely referred to as "spin") and parity of the assembly. Of all the possible eigenstates for a given system, the one of maximum binding energy is termed the ground state because of its special stability whereas the others are deemed excited states. Any change in the eigenstate of the assembly will be accompanied by appropriate changes in the eigenvalues. Consequently, information about these quantities is often obtained by observing the emissions resulting as the assembly rearranges itself through the various excited states into the maximum stability (ground) state.

A rather limited number of nuclei exist naturally in their excited state since most have been able to decay to an equilibrium state in the time since their creation. In recent years, however, many artificial methods for inducing nuclear excitation have been developed. Capture reactions in which stable isotopes are bombarded by neutrons, protons, alpha particles, etc. have created an enormous range of radioactive isotopes for study. Spellation reactions which "tear apart" the target nucleus also give rise to an extensive variety of non-stable nuclei.

## 4.1 Beta Decay

A nucleus in a highly excited state will usually attempt to minimize its energy by nucleon emission. Often however, the excess energy available forbids such a process and then beta decay is likely to occur. Beta decay may take several forms depending whether the nucleus is neutron or proton rich.

Neutron rich nuclei decay by changing a neutron into a proton and emitting an electron and anti-neutrino from the nucleus. Because the anti-neutrino (and the neutrino) is extremely difficult to detect, experimental studies of the decay process are generally limited to studying the emitted electrons. Because of the statistical sharing of the decay energy between the electron and anti-neutrino, a distribution of electron momenta results with the maximum or "end-point" value corresponding to the case where all the energy is imparted to the electron. A measurement of this end-point energy determines the energy difference between the initial and final nuclear configurations.

Proton rich nuclei may decay by two competing processes. The first of these involves changing a proton into a neutron with the emission of a positron and neutrino. Again the dual lepton emissions result in a continuous distribution of positron momenta being observed up to the well defined end-point energy. The second process is brought about by the capture of an orbital electron, which causes a transmutation of the proton into a neutron with the accompanying emission of a monoenergetic neutrino. In this process, X-rays follow each electron capture as the electron shell vacancy is filled.

Information relating to the spins and parities of the states involved in the beta decay process may be obtained from the observed transition rates for the beta disintegrations. From perturbation theory, the transition probability is

$$T(E) = \frac{2\pi}{\hbar} \mid < \psi_f \mid H_\beta \mid \psi_i > \mid^2 \rho(E) \qquad 4.1$$

where $\psi_i$ and $\psi_f$ represent the initial and final states. $\psi_i$ simply consists of the neutron wave function $\mu_i$ whereas $\psi_f$ involves the product of the proton and lepton wave functions $\mu_f \; \phi_e \; \phi_{\bar{\nu}}$ . $H_\beta$ is the interaction Hamiltonian and $\rho(E)$ is the density of final states. The conditions of Lorentz invariance restrict $H_\beta$ to a combination of five possible forms: the scalar (S), pseudoscalar (P), vector (V), axial vector or pseudovector (A) and tensor (T) interactions. Experiments involving the lepton helicities (Wu et al (1957), Goldhaber et al (1958)) indicate that only the vector and axial vector interactions actually occur in nature. The V interaction (originally used by Fermi) results in the Fermi selection rules while the A interaction yields the Gamow-Teller selection rules. The spin and parity changes resulting from these rules are shown in the following table.

| Type of Transition | Fermi (Vector) | Gamow-Teller (Axial Vector) |
|---|---|---|
| Allowed | $\Delta I=0$ $\Delta\pi$=no | $\Delta I=0,1$ $\Delta\pi$=no<br>(no $0 \to 0$) |
| First Forbidden | $\Delta I=0, 1$ $\Delta\pi$=yes<br>(no $0 \to 0$) | $\Delta I=0,1,2$ $\Delta\pi$=yes<br>no $0 \to 0$<br>$1/2 \to 1/2$<br>$0 \to 1$ |
| Second Forbidden | $\Delta I=0,1,2$ $\Delta\pi$=no | $\Delta I=0,1,2,3$ $\Delta\pi$=no |

Ignoring any possible interactions of the electron and neutrino with the nucleus, the lepton wave functions may be represented by plane waves. The product of these plane waves, which occurs in Eq. 4.1, can be expanded as a series of terms of diminishing magnitude. The dominant term in the expansion then yields an allowed beta spectrum. If this term should vanish (because of non-fulfilment of spin or parity conditions) additional terms in the series must be included until a non-zero probability arises. This results in the so-called forbidden transitions with the degree of forbiddeness specifying the number of vanishing terms. Upon evaluating the density of momentum states, the momentum distribution of the beta particles is found to be

$$N(p)dp = C \mid M_{if} \mid^2 F(Z,E)\ p^2\ (E_o-E)^2\ S_n\ dp \qquad 4.2$$

where C is a constant, $M_{if}$ is the nuclear matrix element, F(Z,E) is the Fermi function which corrects for the Coulomb interaction between the emerging electron and the nucleus, p is the electron momentum, E is the electron energy and $E_o$ is the maximum energy of the emitted electrons. $S_n$ is the shape factor which corrects the expression when higher degrees of forbiddenness are required (n indicates the degree of forbiddenness).

Integrating Eq. 4.2 over all possible momenta results in the total transition probability

$$T = \lambda = \frac{\ln 2}{T_{1/2}} = C \mid M_{if} \mid^2 f_n\ (Z,\ E_o)$$

where $T_{1/2}$ is the half-life for the particular decay mode. The function $f_n = \int F(Z,E)\ p^2\ (E_o-E)^2\ S_n\ dp$ has been tabulated (Feenberg and Trigg (1950)) for the case of allowed decays. Thus the product $f_n\ T_{1/2}$ is inversely proportional to the square of the nuclear matrix element and should be an indicator of the type of transition. Since $S_n$ is not uniquely defined for most forbidden decays, values of $f_o\ T_{1/2}$ are generally quoted. The following table shows typical $\log_{10} f_o\ T_{1/2}$ values for various types of beta transitions.

| Type | $\Delta I$ | $\Delta\pi$ | $\log f_o T_{1/2}$ |
|---|---|---|---|
| Super allowed | 0 | no | 3-4 |
| Allowed | 0,1 | no | 4-6 |
| First Forbidden Non-Unique | 0,1 | yes | 6.5-8.5 |
| First Forbidden Unique | 2 | yes | 8-9 |
| Second Forbidden | 2,3 | no | 11-13 |

It is realized that $\log f_o T_{1/2}$ values are not reliable indicators of the type of beta transition since large variations in the $\log f_o T_{1/2}$ values occur for transitions of a particular type.

## 4.2 Gamma Emission

Immediately following nucleon emission or beta decay, the final nucleus may be left in an excited configuration for which the dominant mode of decay is the emission of electromagnetic radiation. The emission of a gamma ray is accomplished through the interaction of the electromagnetic field with the charges and magnetic moments in the nucleus.

The electromagnetic field surrounding the nucleus is conveniently expressed as an expansion of the vector potential in terms of standing spherical waves. Each such wave has definite angular momentum $\lambda$ and properties corresponding to a classical oscillating $2^{\lambda}$ pole. Emission of the electromagnetic radiation is caused by rearrangement of one or more nucleons whose charges and magnetic moments interact with the surrounding field, thereby producing a perturbation in the field. This perturbation or gamma ray carries angular momentum $\lambda$

with projection $\mu$ and may be classified as either electric ($\tau$ = E) or magnetic ($\tau$ = M) according to the following rules.

| Multipolarity $\sigma\lambda$ | $\Delta I$ | $\Delta\pi$ |
|---|---|---|
| E1 | $\leq 1$ | yes |
| M1 | $\leq 1$ | no |
| E2 | $\leq 2$ | no |
| M2 | $\leq 2$ | yes |
| E3 | $\leq 3$ | yes |
| M3 | $\leq 3$ | no |
| E4 | $\leq 4$ | no |
| M4 | $\leq 4$ | yes |

The initial and final values of the nuclear spin are subject to the vector relation $|I_i - I_f| \leq \lambda \leq I_i + I_f$. Transitions with $\lambda$=0 cannot occur since the photon necessarily carries away at least one unit of angular momentum due to its intrinsic spin.

The probability for a gamma ray transition between an initial and final state is

$$T = \frac{2\pi}{\hbar} \mid <\psi_f \mid H_{int} \mid \psi_i> \mid^2 \rho(E)$$

where $\psi_i$ and $\psi_f$ are the initial and final state wave functions. The interaction $H_{int}$ is that between the nucleus and the surrounding electromagnetic field and is written as a series of multipole operators

$\theta^{\sigma}_{\lambda\mu}$. Since each operator gives rise to a characteristic mode of radiation, it is convenient to treat the operators separately. Furthermore we are not interested in the orientation of either the initial or final angular momenta projections, so we sum over $M_f$ and average over $M_i$. The transition probability then becomes

$$T(\sigma\lambda) = \frac{8\pi\ (\lambda+1)}{\lambda[(2\lambda+1)!!]^2}\ \frac{1}{\hbar}\left(\frac{\omega}{c}\right)^{2\lambda+1}\ B(\sigma\lambda)$$

where $\omega$ and c are the frequency and velocity of the radiation. The reduced transition probability $B(\sigma\lambda)$ is defined by

$$B(\sigma\lambda) = \frac{1}{2I_i+1}\ \sum_{M_iM_f}\ |\ \langle f|\theta_{\lambda\mu}|i\rangle\ |^2 \qquad \mu=M_i-M_f$$

where i and f represent the initial and final nuclear states. Order of magnitude estimates for the multipole matrix elements indicate that electric transitions are faster than magnetic ones for the same multipole order, and that the transition probabilities decrease rapidly as the multipole order increases. Thus one expects possible mixtures of electric and magnetic radiations but with only the lowest multipole orders allowed by angular momentum and parity considerations contributing. In practice, only the M1 + E2 transitions are found to be significantly mixed; almost all other transitions occuring as a single type of radiation.

In decay processes, the measurement of gamma rays provides information relating to the deexciting $B(\sigma\lambda)\downarrow$. Often however, reaction mechanisms may be used to provide direct measurements of the exciting $B(\sigma\lambda)\uparrow$. Since the definition of $B(\sigma\lambda)$ involves a summation over final substates, $B(\sigma\lambda)\downarrow$ and $B(\sigma\lambda)\uparrow$ are not equal, but rather these quantities <u>per magnetic substate</u> are equivalent. Thus the values are proportional to the number of substates available for population as follows

$$\frac{B(\sigma\lambda)\uparrow}{B(\sigma\lambda)\downarrow} = \frac{2I_2 + 1}{2I_1 + 1}$$

where $I_1$ represents the lower spin state and $I_2$ the upper.

The transition probability or decay rate $\lambda$ for a nuclear state gives the probability per second that the state will deexcite. Usually there are several competing modes of deexcitation (i.e. beta disintegration, gamma emission, internal conversion, etc.) and then the total decay rate will be the sum of the individual decay rates

$$\lambda = \sum_i \lambda_i \; .$$

The decay rate $\lambda$ can also be expressed in terms of the mean lifetime $\tau$ and the half-life $T_{1/2}$ for the state as follows

$$\lambda = \frac{1}{\tau} = \frac{\ln 2}{T_{1/2}} \quad .$$

Another measure of the transition strength is provided by the uncertainty principle which relates the decay width $\Gamma$ of the state to the decay rate by

$$\Gamma = \hbar \lambda \quad .$$

## 4.3 Internal Conversion

A mode of decay which always competes with gamma emission is internal conversion. In this process, the excitation energy of the nucleus is transferred by the electromagnetic field to one of atomic electrons. The electron is then ejected from the atom with a kinetic energy equal to the competing gamma energy less the binding energy of the electron. For any given gamma transition, several discrete conversion lines will appear, corresponding to internal conversion of electrons from the K, $L_1$, $L_2$, $L_3$, etc. shells.

The probability for internal conversion emission is given by the transition rate

$$T = \frac{2\pi}{\hbar} \mid \langle\psi_f | H_{int} | \psi_i\rangle \mid^2 \rho(E).$$

The initial and final wave functions, $\psi_i$ and $\psi_f$, involve products of the electronic and nuclear wave functions. $H_{int}$ is the electromagnetic interaction which is written in terms of multipole operators, as in the case of gamma emission.

Provided the electronic wave functions do not penetrate the nucleus, the electronic and nuclear matrix elements may be separated.

The nuclear matrix element will then be exactly that which occurs for gamma emission. It therefore becomes convenient to define the internal conversion coefficient as

$$\mathrm{ICC}_\ell = \frac{\text{probability of internal conversions in the } \ell^{\text{th}} \text{ shell}}{\text{probability of the accompanying gamma emission}} \,.$$

When defined in this manner, the conversion coefficient depends only on the electronic wave functions and hence may be accurately computed. In actual fact, the finite size of the nucleus complicates the situation somewhat because the electrons are able to penetrate into the nucleus. Then the form of the nuclear matrix element is no longer the same as for the corresponding gamma transition, and complete cancellation will not occur. Fortunately, the correction for these penetration effects is small. Recent compilations by Hagar and Seltzer (1968, 1969) express the conversion coefficients in the form

$$\mathrm{ICC} = \alpha[1+A_1\lambda_1+A_2\lambda_1^2+A_3\lambda_2+A_4\lambda_2^2+A_5\lambda_1\lambda_2] \quad \text{for electric multipole}$$

$$\mathrm{ICC} = \beta[1+B_1\lambda+B_2\lambda^2] \quad \text{for magnetic multipoles}$$

where $\alpha$ and $\beta$, the "normal" conversion coefficients, are tabulated in the 1968 reference while the penetration coefficients $A_i$ and $B_i$ are tabulated separately in the 1969 work. The $\lambda$'s involve nuclear matrix elements and may be calculated by assuming a specific model for the nuclear currents. In practice it is found that only a few conversion coefficients clearly exhibit non-vanishing $\lambda$'s.

Since the conversion coefficients depend strongly on the multipolarity of the transition, their determination provides an extremely powerful method for finding the multipolarity of the transition and therefore the spin and parity changes between nuclear levels.

### 4.4 X-Rays and Auger Electrons

Whenever a vacancy is created in an electron shell, such as by orbital electron capture or internal conversion, electrons from higher order shells will attempt to refill the vacancy. In so doing, an amount of energy equal to the difference in the binding energies between the shells involved will be released. If the energy is given off in the form of electromagnetic radiation, the process is termed x-ray emission. Alternatively, the energy may be removed from the atom by ejecting an outer electron, called an Auger electron. The ratio of x-rays to Auger electrons is expressed by a quantity called the fluorescent yield.

### 4.5 Stripping Reactions

Studies of the emissions accompanying nuclear decay provide information about the changes between the various nuclear states. From these observed changes, it is usual to deduce values for the energy, spin, parity, etc. of the actual states of the nucleus. In addition to such indirect approaches, reactions may be used to obtain information directly about the nuclear states. Such information is provided by the class of nuclear reactions known as direct reactions. A direct reaction is one in which the reaction process occurs instantaneously ($\sim 10^{-21}$ sec), thus normally taking place at the nuclear surface. Of particular interest are the single particle transfer "stripping" and "pick-up" reactions. In these reactions, the incident projectile exchanges a single neutron or proton with the target during the collision at the target surface. In stripping, the nucleon is deposited into the target while in pick-up the nucleon is removed. For either case, the outgoing projectile carries with it information about the nuclear interaction involved.

The differential cross section for a stripping reaction can be written (French and Raz (1956))

$$\frac{d\sigma}{d\Omega} = \frac{2I_f+1}{2I_i+1} \sum_{\ell} S_{\ell}\, \phi_{\ell}(\theta) \qquad 4.3$$

where $I_f$ and $I_i$ are the final and initial nuclear spins. $\phi_{\ell}(\theta)$ is the single-particle reaction cross section for orbital angular momentum transfer $\ell$ at angle $\theta$. This quantity can be obtained by means of distorted wave Born approximation (DWBA) calculations (Bassel et al (1962)). The spectroscopic factor $S_{\ell}$ contains the nuclear structure information. The summation over $\ell$ results since several possible $\ell$-values may (for odd-A or odd-odd targets) contribute to the final j-value.

The cross section for a pick-up reaction may be obtained from Eq. 4.3 by the principle of detailed balance. This principle states that for the complementary reactions

$$A + a \rightleftarrows B + b$$

the cross sections are related by

$$\frac{\sigma_{A\to B}}{\sigma_{B\to A}} = \frac{P_b^2\ (2I_B+1)(2I_b+1)}{P_a^2\ (2I_A+1)(2I_a+1)}$$

when the reactions are considered in the center of mass system. The momentum dependence p is included in the DWBA calculations so that the cross section for the pick-up reaction is

$$\frac{d\sigma}{d\Omega} = \frac{2S_i+1}{2S_f+1} \sum_{\ell} S_\ell\ \phi_\ell(\theta) \qquad 4.4$$

where $S_f$ and $S_i$ are the spins of the light and heavy projectiles respectively.*

The spectroscopic factor is defined as the probability that

---

* The adoption of Eq. 4.3 as the definition for the stripping cross section unfortunately leads to an inherent asymmetry between stripping and pick-up reactions. This asymmetry will also be reflected in the spectroscopic factors. For example, when using an even-even target, the shell model spectroscopic factor is $\frac{<\text{holes}>}{2j+1}$ for the stripping reaction but <particles> for the pick-up reaction.

in the initial nuclear state, all but one of the nucleons will find themselves in an arrangement corresponding to the final state (Macfarlane and French (1960)). In other words, it gives the overlap integral between the wave function of the initial nucleus and the final nucleus. It is instructive to compare the spectroscopic factor provided by the shell model to that predicted by the Nilsson model.

Following the notation of Macfarlane and French, we can write the shell model spectroscopic factor for a stripping reaction in its general form

$$S(\rho_3) = n_3 <\rho_3^{n_3} \alpha_3|\rho_3^{n_3-1} \sigma_3'>^2 (2\gamma'+1)(2\alpha_3+1) \begin{Bmatrix} \sigma_3' & \beta' & \gamma' \\ \Gamma & \rho_3 & \alpha_3 \end{Bmatrix}^2 \qquad 4.5$$

where $<\rho_3^{n_3} \alpha_3|\rho_3^{n_3-1} \sigma_3'>$ is a coefficient of fractional parentage. The notation represents the following quantities:

| | |
|---|---|
| $n_3$ | number of equivalent nucleons in the active shell of the heavier nucleus |
| $\rho_3$ | angular momentum of the shell into which stripping is to occur |
| $\alpha_3$ | angular momentum of the particles coupled together in the active shell of the heavier nucleus |
| $\sigma_3'$ | angular momentum of the coupled particles in the active shell of the lighter nucleus |
| $\beta=\beta'$ | angular momentum of the core |
| $\Gamma$ | total angular momentum of the heavier nucleus |
| $\gamma'$ | total angular momentum of the lighter nucleus. |

For the case of interest to us, namely stripping into an even-even target nucleus, we have $\rho_3 = \alpha_3 = \Gamma = j$ and $\sigma_3' = \beta' = \gamma' = 0$ so that

$$S(j) = n_3 < j^{n_3-1} \, j | j^{n_3} \, 0 >^2 \, (2j+1) \left\{ \begin{matrix} 0 & 0 & 0 \\ j & j & j \end{matrix} \right\}^2 .$$

The c.f.p. is given by (de-Shalit and Talmi (1963))

$$< j^{n_3-1} \, j | j^{n_3} \, 0 > = \frac{4j+4-n_3-2T}{2n_3(2j+1)} \quad \text{where } T = \frac{n_3}{2} .$$

Furthermore $(2j+1) \left\{ \begin{matrix} 0 & 0 & 0 \\ j & j & j \end{matrix} \right\}^2$ has the value unity (Rotenberg (1959)). Therefore the spectroscopic factor becomes

$$S(j) = \frac{2j+1 - (n_3-1)}{2j+1}$$

which is simply the fraction of holes in the active shell of the target nucleus.

$$S_\ell = \frac{<\text{holes}>}{2j+1} .$$

A completely empty pure shell model state is thus seen to have a stripping spectroscopic factor $S_\ell = 1$.

If we maintain Eq. 4.3 as the definition for the stripping reaction cross section, then the spectroscopic factor for stripping into a deformed nucleus is (Satchler (1958))

$$S_\ell = \sum_j \theta_{j\ell}^2 \qquad 4.6$$

where $\theta_{j\ell} = g \sqrt{\frac{2I_i+1}{2I_f+1}} \; \langle I_i \; j \pm K_i \mp \Delta K \, | I_f \; K_f \rangle \; c_{j\ell} \; \langle \phi_f | \phi_i \rangle$ .

The $c_{j\ell}$ values are the Nilsson expansion coefficients in terms of shell model states. The factor $\langle \phi_f | \phi_i \rangle$ is the overlap between the initial and final vibrational states (including zero point fluctuations) and is expected to be nearly unity as long as the nuclear deformation does not change greatly. The factor g is $\sqrt{2}$ if either $K_i = 0$ or $K_f = 0$, and unity otherwise.

For stripping into an even-even target nucleus $I_i = K_i = 0$. Furthermore j is restricted to the value $I_f$ so that

$$S_\ell = \frac{2}{2I_f+1} \; c_{j\ell}^2 \; .$$

Thus the stripping cross section to any state measures one particular $c_{j\ell}$ component for that state; namely the component having $j = K_f$. Capture into successive states of a rotational band thereby explores all the various components of the intrinsic wave function.

We may explicitly write the differential cross sections for stripping reactions on even-even target nuclei. The final spin $I_f$ then necessarily equals j and only one $\ell$-value contributes. The cross sections become

$$\text{spherical nuclei} \quad \frac{d\sigma}{d\Omega} = \langle\text{holes}\rangle \; \phi_\ell(\theta)$$

$$\text{deformed nuclei} \quad \frac{d\sigma}{d\Omega} = 2 \; c_{j\ell}^2 \; \phi_\ell(\theta) \quad .$$

No allowance has thus far been made for pairing which gives rise to a "smearing" of the Fermi surface. Such effects are taken into account by introducing a factor $U^2$ which measures the degree of emptiness of the target state (for the spherical case, the emptiness factor is $U^2 \sim \frac{\langle\text{holes}\rangle}{2j+1}$ ). The equations then take the form

$$\text{spherical nuclei} \quad \frac{d\sigma}{d\Omega} = (2j+1)\ \phi_\ell(\theta)\ U^2$$

$$\text{deformed nuclei} \quad \frac{d\sigma}{d\Omega} = 2\ c^2_{j\ell}\ \phi_\ell(\theta)\ U^2\ .$$

We may also consider the corresponding expressions for pick-up reactions. The pick-up cross section is obtained using Eq. 4.4. However the spectroscopic factor is now arrived at by considering the inverse stripping reaction and then applying the general stripping expressions 4.5 or 4.6. It is readily shown that for pick-up from even-even targets

$$\text{spherical nuclei} \quad \frac{d\sigma}{d\Omega} = (2j+1)\ \phi_\ell(\theta)\ V^2$$

$$\text{deformed nuclei} \quad \frac{d\sigma}{d\Omega} = 2\ c^2_{j\ell}\ \phi_\ell(\theta)\ V^2$$

where the projectile spins have been absorbed into the DWBA cross section. Pairing effects are included in the fullness factor $V^2$ (for spherical nuclei $V^2 \sim \frac{\langle\text{particles}\rangle}{2j+1}$ ).

# CHAPTER V

# THE INSTRUMENTS

## 5.1 Germanium Semiconductor Detectors

In its simplest form, a solid state detector consists of an extremely pure crystal of material. When a quantum of radiation is incident upon this detector, it interacts with the valence electrons to produce a trail of electron-hole pairs in the crystal. By applying an electric field, these charge carriers may then be swept from the crystal with the resulting charge pulse proportional to the amount of energy originally deposited by the radiation.

There are practical difficulties with such a detection system. A major problem involves obtaining crystals of the extreme purity and crystal perfection necessary to prevent trapping of the charge carriers. At the present time, only crystals of silicon and germanium can be grown with the necessary perfection and these crystals are semiconductors, whereas the requirements of an electric field for charge collection makes it necessary that the crystal be an insulator. In order to surmount this difficulty, the device is operated as a reverse biased diode with the resulting depletion region providing the necessary increase in resisitivity. If the crystal is to be used for the detection of gamma rays, then a large active volume is required and may be obtained by extending the depletion region by the lithium-drift process.

The usual fabrication procedure for producing a lithium-drifted germanium detector involves diffusing a layer of lithium into one or more surfaces of a crystal of p-type germanium, thereby forming an n-type layer. Lithium is then drifted into the crystal to form a large intrinsic region in which there are no free charge carriers. The crystal thus consists of a p-type layer (the original germanium), an n-type layer (the layer of diffused lithium) and a central intrinsic or depletion region which is the sensitive region of the detector. Electron-hole pairs formed in this region are swept out to produce the charge pulse by applying a reverse bias voltage to the crystal.

The Ge(Li) detector must be kept cool in order to prevent the lithium from drifting out of the intrinsic region. Moreover, the device must be operated at liquid nitrogen temperature in order to eliminate leakage current caused by the thermal generation of charge carriers across the small (0.66 eV) band gap.

In germanium, the formation of each electron-hole pair requires an average of 2.9 eV of energy. Thus it may be estimated that a 662 keV gamma ray will produce about $2.3 \times 10^5$ ion pairs with a statistical fluctuation of $4.8 \times 10^2$ pairs. This corresponds to a resolution of $\sim 3.3$ keV at this energy. However, Fano (1947) has pointed out that whenever the incident radiation is completely stopped in the crystal, the ionizations should not be treated as independent events since an energy exactly equal to the initial energy must be given up. The resulting non-gaussian distribution has a variance which is reduced by a "Fano factor". Present estimates suggest this factor is approximately 0.15 (Camp (1967)).

The pulses of charge produced by the semiconductor detector are small and generally unsuitable for conventional voltage amplification since the resulting voltage signal will depend upon the detector capacitance. This problem is overcome by using a charge sensitive preamplifier which produces an output voltage proportional only to the input charge and independent of the input (detector) capacitance. For optimum noise performance, the preamplifier must be matched to the particular detector with which it is to be used.

The present investigation has employed a variety of Ge(Li) detectors of various sizes and resolutions. The best of these was a thin window Ortec planar detector of 16 mm diameter x 5.5 mm depth coupled to an Ortec 120-1 preamplifier, which provided a resolution of 1.3 keV at 662 keV.

## 5.2 The Multichannel Analyser

Radiation detectors yield voltage pulses whose amplitude is proportional to the energy deposited in the detector and whose frequency of occurrence is related to the intensity of the radiation. To make use of these characteristics, it is necessary to be able to separately scale pulses of differing amplitudes. This task is performed by means of a multichannel analyser.

A principal component of the multichannel analyser is the analogue-to-digital converter (ADC) whose function it is to convert the voltage pulse into a digital number. Present generation ADC's use a Wilkinson type converter which analyzes the pulse by charging a capacitor and then allowing it to linearly discharge. During the discharge interval, oscillator pulses are produced. These oscillator pulses cause an address scalar to advance by the number of pulses in the pulse train thereby generating a number proportional to the amplitude of the input signal. To prevent entry of another signal during analysis of the previous one, a linear gate is used to block the input throughout the analysis time.

Once a number has been set up in the address scalar of the ADC, it is transferred into the address scalar of the other principal component, the memory unit. The contents of core memory corresponding to this generated address is then loaded into the memory register. The register is incremented and its contents then loaded back into memory. Upon completion of the storage cycle, a reset signal allows the linear gate of the ADC to reopen.

The performance of the analyser is determined mainly by the performance of the ADC. In particular the differential non-linearity, which expresses the deviation from linearity as a function of channel number, is determined by the quality of the ramp circuit. In an effort to cancel non-linearities which may occur at the starting end of the capacitor rundown ramp, it is usual to add a small voltage to each input signal and then inhibit the corresponding number of address pulses during the digitization procedure.

The majority of the gamma ray measurements described in the present investigation were taken with a Nuclear Data 161F 4096 channel ADC coupled with a 160 M memory unit. The ADC unit uses a relatively "slow" 16 MHz clock frequency during the capacitor rundown. The differential non-linearity of the system was observed to be less than 3 channels over the region of interest. Measurement of some of the weaker gamma rays required high count rates and were performed with a Nuclear Data 3300 system, utilizing a 50 MHz clock frequency.

## 5.3 Two-Parameter Coincidence Experiments

The gamma-gamma coincidence experiments were performed using the experimental arrangement shown in Fig. 5.1. Pulses from the detectors were shaped to have good timing characteristics by the DDL amplifiers (Canberra model 1411) and then fed into timing single channel analysers (Canberra model 1436). These units generated fast timing markers at the zero-crossing point of each pulse. One of these timing markers was used to start a time-to-amplitude converter (Ortec 437A) while the other provided the stop pulse. The detector with lower efficiency was used to generate the start pulse in order to minimize the number of events having no stop pulse. The output from the TAC then appears as a pulse with amplitude proportional to the time difference between the input pulses. For gamma rays involving prompt cascades, this time difference should simply correspond to the different time delays of the circuitry associated with each detector so that all TAC output pulses might be expected to have

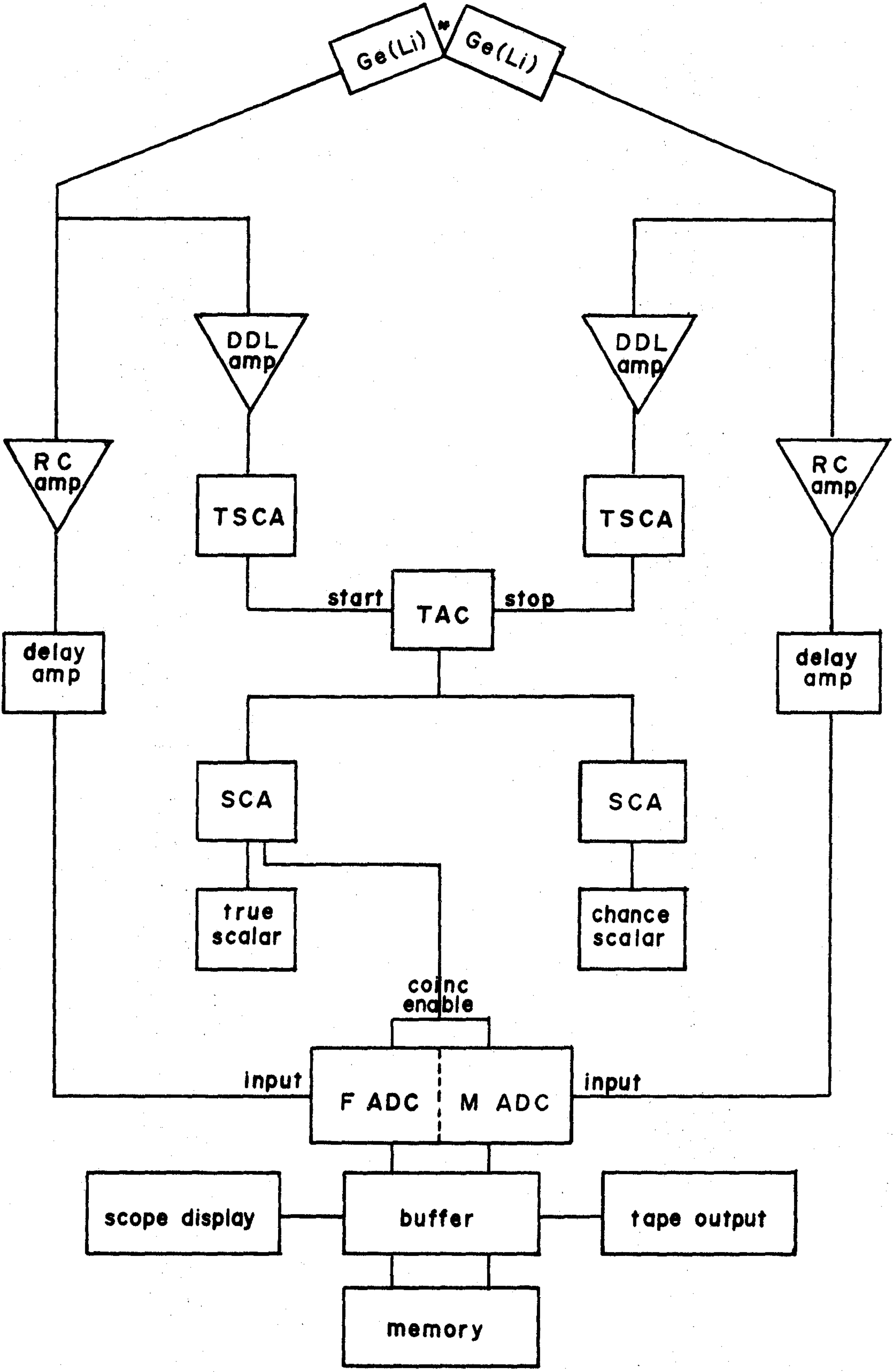

Figure 5.1 Experimental arrangement for the two-parameter coincidence experiments.

constant amplitude. However because of variations in the rise time of the signal (walk), a distribution of TAC output pulses results. Superimposed upon this distribution, there is also a uniform distribution of chance coincidence events. In the present experiments, the TAC spectrum was observed to have a time resolution of $\sim$80 nsec.

In order to evaluate the chance contribution, two single channel analysers (Canberra model 1435) were used to set windows on the TAC spectrum. The "true plus chance" window included essentially all of the time peak to insure that constant coincidence efficiency would prevail. This output was monitored and also used to open the linear gates of the ADC's for the ensuing analysis of the signals. In addition to the "true plus chance" window, a "chance" window of the same width was set off the peak so that the number of chance events could be monitored. The ratio of "true plus chance" events to "chance" events then provided a reliable measure of the number of accidental coincidences.

Low noise amplifiers (Tennelec TC200) were used to shape the linear signals from the detectors. These signals were passed through delay amplifiers (Ortec 427), having unity gain and adjustable delay times, in order to obtain the proper time relationship between the linear signals and the coincidence enable pulse. The signals were then presented to two 4096 channel ADC's for processing.

The memory associated with the ADC's has a capacity of 4096 locations each of which is able to store $2^{18}$ events before overflowing. Since these locations could only provide a 64 x 64 element matrix, while each location could be used to store an 18 bit word, an address-recording procedure was used. The coincidence information was obtained as a 10-bit address from one detector and an 8-bit address from the other thus combining to form an 18-bit word. The address pairs so formed define the coordinates of a two dimensional matrix whose axes represent the energy detected by each detector. The resulting 18-bit words were stored sequentially in the memory locations until 2048 events had been accumulated, at which time the block of 2048 address pairs were dumped onto magnetic tape. The remaining half of the memory was used to display the coincidence projections for monitoring purposes.

At the conclusion of the experiment, the 10-bit x 8-bit addresses were sorted by the McMaster CDC 6400 computer. The number of events occuring in each coordinate of the matrix was tallied and the resulting information outputed in the form of a 1024 x 256 coincidence matrix.

## 5.4 Chalk River $\pi\sqrt{2}$ Spectrometer

Measurements of internal conversion electrons can be used to establish transition energies and multipolarities. Because the conversion process takes place in various electron shells, the resulting electron spectrum is complex and usually requires the use of a detecting device of high resolution. Such a device can be obtained by employing a magnetic field to deflect the electrons in an appropriate manner.

A magnetic field having circular symmetry and a radial field gradient will cause electrons to describe betatron oscillations in both the radial and vertical directions. If the field decreases radially as $\frac{1}{\sqrt{r}}$, then focusing in both dimensions occurs after an angle of $\pi\sqrt{2}$ radians and instruments using this design are termed double focusing $\pi\sqrt{2}$ spectrometers. The Chalk River $\pi\sqrt{2}$ spectrometer (Graham et al (1960)) has a one meter radius and is capable of extremely high resolution (0.01%). In addition, because of the iron-free construction of this instrument, the magnetic field strength is directly proportional to the current in the coils, thereby enabling the electron momenta to be determined with high precision. The $\frac{1}{\sqrt{r}}$ magnetic field shape is provided by the coil arrangement illustrated in Fig. 5.2a. It is interesting that the largest coils have a radius of 200 cm with radial and axial tolerances of only 0.5 mm. The field form resulting from this arrangement is shown in Fig. 5.2b. Since the accuracy of the measurements depends critically on the accuracy with which the earth's field can be compensated, two large sets of degaussing coils are used to provide cancellation of its vertical and north-south components.

In order to realize the inherent precision of the Chalk River instrument, the current through the coils is regulated to better than 1 part in $10^5$. To achieve this stability, the coil current is passed through a precision resistor whose IR drop is compared with a reference potential and the resulting difference signal used to control the feedback circuitry. Measurement of the current is performed by measuring the IR drop across the standard resistor by means of a precision potentiometer.

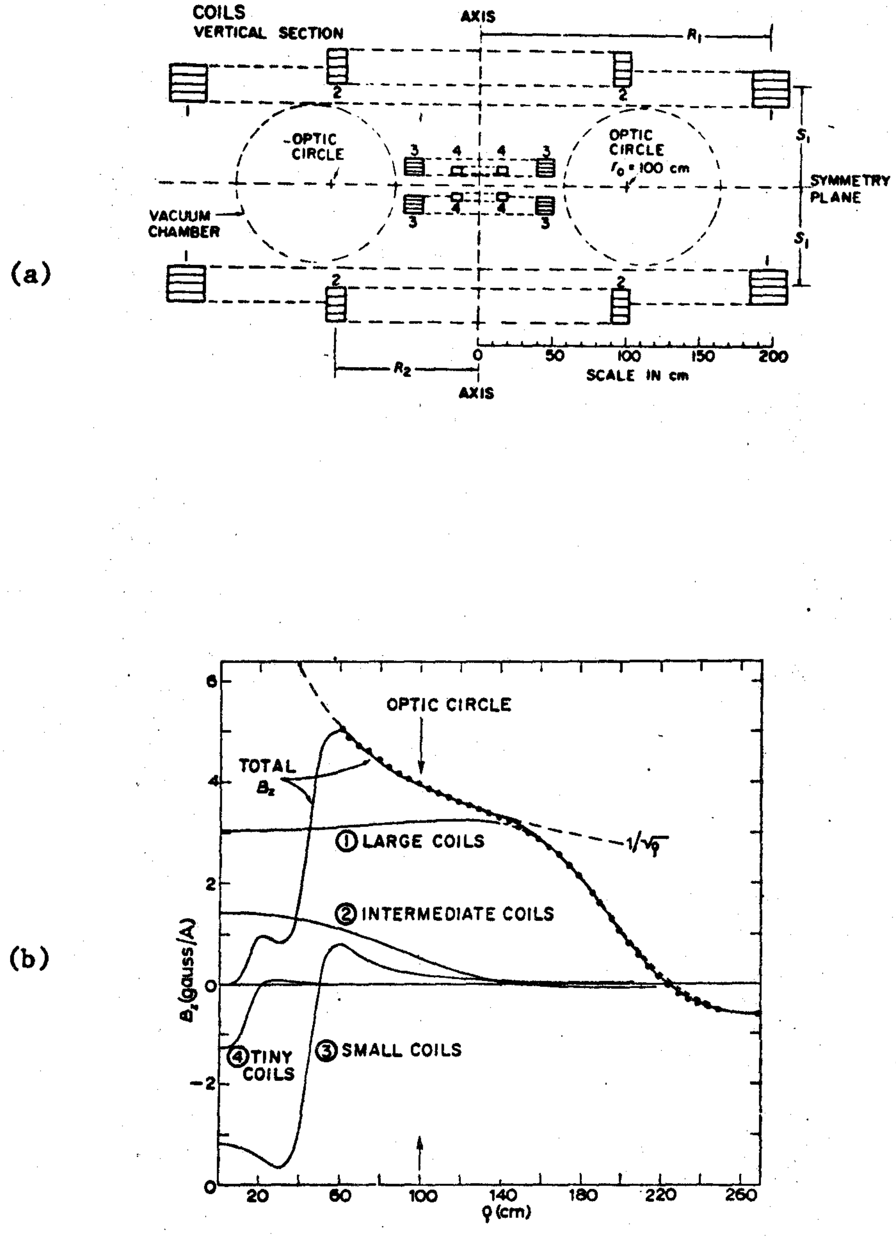

Figure 5.2 (a) Coil arrangement for the Chalk River $\pi\sqrt{2}$ spectrometer.
(b) The resulting $1/\sqrt{r}$ field form. [From Graham et al (1960)]

The reference potentials to which the IR drop is compared are created by a stepping potentiometer which can be programmed to give up to 1000 equally spaced reference voltages in sequence. In the present work, counting periods of 40 sec were used. Upon completion of each counting period, the step location and accumulated counts were outputed, and the stepping potentiometer then advanced to the next preprogrammed setting to restart counting. The unit could be programmed to skip increments and to automatically recycle after completion of a sequence.

An alternative mode of operation could be used for scanning weak peaks whenever background fluctuations posed a problem. In this mode, a Nuclear Data 3300 analyser was used to multi-scale events occuring during repetitive rapid scans of the momentum region. The procedure makes use of separate potentiometers to select the upper and lower reference potentials which correspond to the initial and final channels of the analyser. Having selected these potentials, the analyser is then advanced through its range of channels while generating an analogue voltage proportional to its channel number. The counts recorded at any particular voltage setting are deposited into a corresponding channel. For the present work, the momentum region was divided into 256 channels and the region scanned in 128 sec resulting in a counting time of 0.5 sec per channel per scan. Upon completion of each scan, the scan number and total counts accumulated during the scan were outputed and then the sequence restarted. Often several hundred scans were required in order to build up meaningful statistics. Upon completion of a run, the contents of the 256 channels were dumped onto paper tape for subsequent analysis.

Detection of the electrons was performed by means of a continuous flow proportional counter. Under normal operation, a 1 mg/cm$^2$ Mylar window was used with an atmospheric pressure methane filling. However in order to reduce transmission losses when recording electrons of energy less than 100 keV, the window was replaced with a thinner one ($\sim$ 100 μg/cm$^2$) consisting of 10 to 20 laminated layers of VYNS and the methane filling pressure reduced to a few cm Hg. With the thin window system, it is possible to measure conversion lines down to energies of $\sim$ 3 keV.

## 5.5 Enge Split-Pole Spectrometer

For the analysis of reaction products, a large collecting power is required in addition to the usual desire for high resolution. The need for high collection efficiency is of particular concern for accelerator experiments since machine time is usually limited. The Enge spectrometer (Enge (1964), Spencer and Enge (1967)) combines the inherent high resolution of magnetic analyzing devices with a large collecting power over a broad energy range.

Figure 5.3 shows a top view of the spectrograph which consists of two separate pole pieces enclosed by a current coil. The purpose of the split between the poles is to provide second order double focusing over a large momentum range. Vertical focusing, whose main purpose is to increase the collecting power of the instrument, is

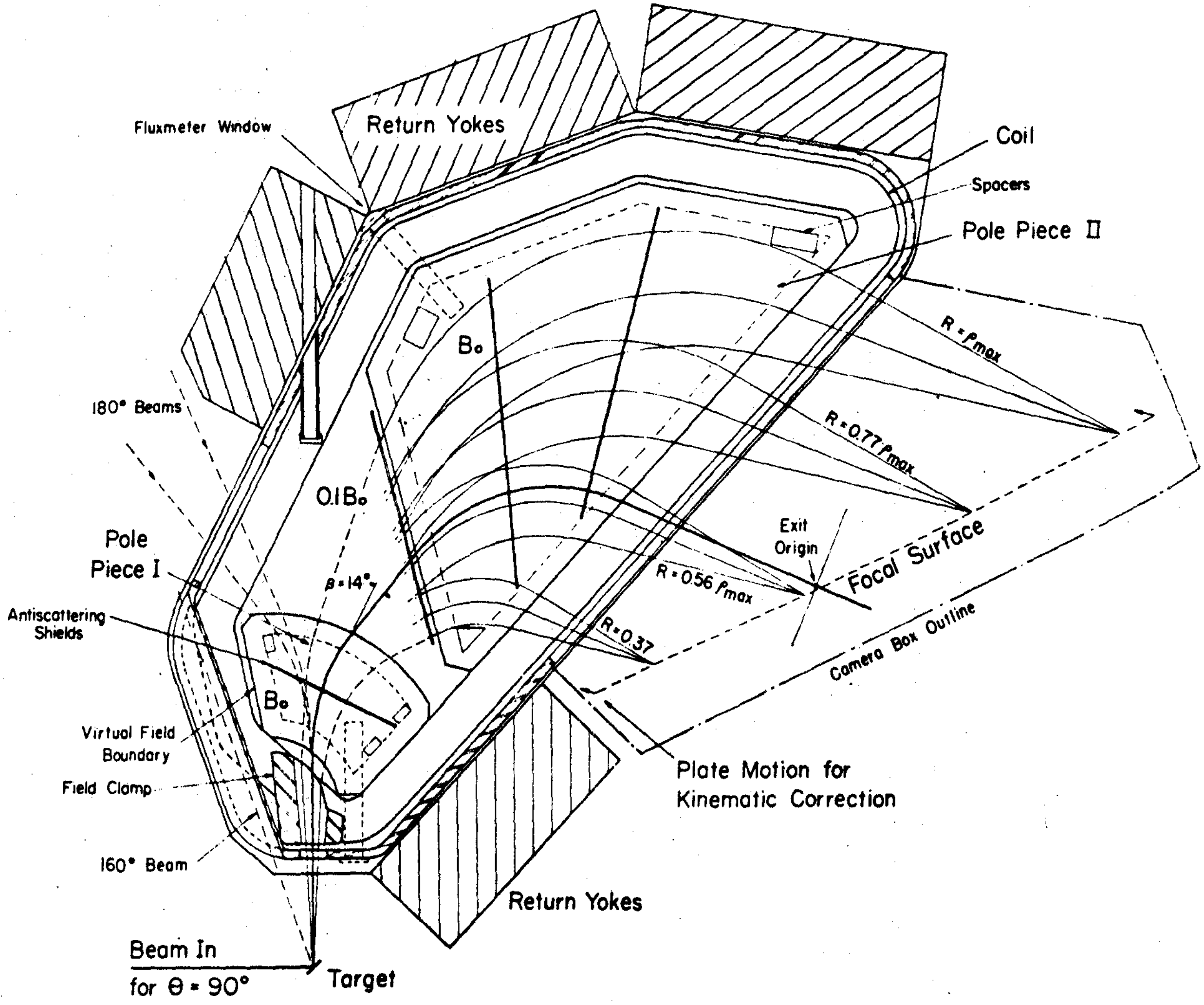

Figure 5.3 Top view of the Enge split-pole spectrograph. [From Spencer and Enge (1967)]

achieved in the fringing-field zones, particularly at the entrance to the first pole gap. The low momentum particles are adequately focused at this gap and the split between the pole pieces is designed mainly to provide additional focusing for the high momentum particles. In this manner, vertical focusing is achieved over a wide range of momenta.

The spectrograph is designed not to interfere with the beam at reaction angles up to θ = 160° and may be operated at solid angles of typically 2-3 msr. Particles which enter the spectrograph are deflected by the field and focused in a plane (labelled as the focal surface in the diagram). For a given field, the effective radius of curvature $\rho$ of the particle trajectory is determined by the charge, mass and energy of particle undergoing analysis. The corresponding position along the focal surface s may be expressed as

$$\rho = a_0 + a_1 s + a_2 s^2 + a_3 s^3 + a_4 s^4 \quad \text{cm}$$

where, for Rochester spectrograph, these coefficients have the values

$a_0 = 93.0179$

$a_1 = -0.416066$

$a_2 = 0.307063 \times 10^{-3}$

$a_3 = 0.250430 \times 10^{-5}$

$a_4 = 0.112131 \times 10^{-7}$ .

Due to the finite acceptance angle of the spectrograph, kinematic effects are expected to shift the position of the focal surface. To overcome these kinematic shifts, provision is made for adjusting the plateholder and the necessary shifts have been listed in the literature (Spencer and Enge (1967)).

The particles were detected by means of nuclear emulsions placed along the focal plane. The emulsions used for the present work were Eastman Kodak NTB nuclear emulsions of thickness 50 μm mounted on glass backings measuring 25 cm in length by 2.5 cm in width. After development, the plates were scanned in 1/4 mm wide strips across the plate with a travelling microscope.

# CHAPTER VI

# EXPERIMENTAL PROCEDURES AND ANALYSIS

## 6.1 The Direct Gamma Ray Measurements

The majority of the direct gamma ray experiments were performed using two Ge(Li) detectors purchased from Nuclear Diodes. The first of these was a thin window planar detector of area 1.5 cm$^2$ and depletion depth 3 mm having a resolution of 1.6 keV at 662 keV. The other detector was an 11 cc coaxial detector with a resolution of 3.2 keV at 1332 keV. In addition, measurements were taken using a thin window Ortec detector of 16 mm diameter x 5.5 mm depth which yielded a resolution of 1.3 keV at 662 keV.

The positions and areas of the full energy peaks were obtained by means of the computer program JAGSPOT. This program, originally developed at the Chalk River Nuclear Laboratory, performs a non-linear least-squares fit to the data in the region of a peak or group of peaks. Each fitting region, which may include up to 6 peaks, is fitted to a function of the form

$$I(x) = \alpha + \beta x + \sum_{i=1}^{\leq 6} I_i \int_{-\infty}^{x_{Pi}} e^{\varepsilon(y-x_{pi})} \, e^{-\delta(x-y)^2} \, dy$$

where $\alpha$, $\beta$, $\delta$, $\varepsilon$, $I_i$, $x_{Pi}$ are parameters of the calculation. The function represents a linear background plus a sum of gaussians (with variance $\frac{1}{2\delta}$ ), each of which is convoluted with an exponential tail (decaying towards $-\infty$ with fall-off rate $\varepsilon$). This functional form simulates the low energy tailing sometimes observed with Ge(Li) detectors. A program option allowed fixing $\delta$ and $\varepsilon$ at values predetermined by a calibration curve obtained from prominent peaks in the spectrum. This procedure proved particularly useful in fitting weak peaks.

The energies of the gamma rays were determined with rather high precision (typically ± 50 eV for well defined peaks) by means of the following procedure. Whenever an energy analysis was to be made, two separate gamma ray spectra were recorded under identical conditions. The first of these, which was counted for the longer period of time, contained only the spectrum of interest while the second spectrum included additional well-known calibration gamma rays. The calibration gamma rays were used to obtain the non-linearity of the system under the conditions of the experiment and to simultaneously establish the energies of the strongest peaks in the unknown spectrum. These non-linearity corrections were then applied to the other spectrum and the energies obtained for the strong peaks used as internal standards to obtain the remainder of the energies.

In order to minimize uncertainties in the peak positions, the data were recorded at high gains (usually 0.10 keV/channel and 0.25 keV/channel). The Nuclear Data 161F analyser used for most of the experiments required quite severe non-linearity corrections of the order of ± 3 channels. In order to accurately establish these corrections, a wide range of standards had to be judiciously chosen over the entire range of the spectrum. The following standards were used for this purpose: $^{241}$Am, $^{57}$Co, $^{139}$Ce, $^{203}$Hg, $^{51}$Cr, $^{198}$Au, $^{22}$Na, $^{207}$Bi, $^{137}$Cs, $^{54}$Mn, $^{88}$Y, $^{65}$Zn, and $^{192}$Ir. With the above procedure it was found that the energies obtained for peaks were nearly always reproduced to within ± 0.05 keV.

The relative intensities of the gamma rays were determined from the measured areas of the full energy peaks. The area associated with the i$^{th}$ gamma ray is

$$N_i = N_o \ (\varepsilon\omega)_i \ I_i$$

where $N_o$ is the source strength, $(\varepsilon\omega)_i$ is the efficiency of the detector for the i$^{th}$ gamma ray and $I_i$ is the intensity of the i$^{th}$ gamma ray. Since the source strength $N_o$ was unknown in these experiments, only relative gamma ray intensities could be extracted.

The intensity measurements were made using three reproducible geometries for which the efficiency as a function of energy had been carefully determined. These efficiency curves were obtained by using a set of IAEA calibrated gamma sources consisting of $^{241}$Am, $^{57}$Co, $^{203}$Hg, $^{22}$Na, $^{137}$Cs, $^{54}$Mn, $^{60}$Co, and $^{88}$Y. In addition, sources of $^{151}$Pm, $^{152}$Eu, $^{134}$Cs, and $^{180m}$Hf for which the relative intensities are well known were used to further define the shape of these curves. The efficiency calibrations were performed for the following geometries:

(1) source 6 cm from a small planar detector

(2) source 2 cm from a small planar detector between which was

placed an absorber composed of 2 mm lead, 1 mm cadmium and 0.5 mm copper

(3) source 5 cm from a 12 cc detector between which was placed the same lead-cadmium-copper absorber.

The efficiency curve for the detector without absorber showed very little scatter with essentially all calibration points falling on a smooth curve. For the geometries with absorber, the scatter in the points became increasing greater at lower energies. For the regions over which the efficiency curves were used, the curves are thought to be accurate to better than 5%.

In order to check for impurity lines, all the intensity measurements were repeated after 2 half-lives and again after 4 half-lives. This established the identity of all but the weakest lines. A similar series of intensity measurements was performed using samples of different enrichments or samples upon which chemical purification had been performed. This check was made to insure that the intensity of the weak lines relative to the stronger lines remained unchanged.

### 6.2 The Gamma-Gamma Coincidence Measurements

The gamma-gamma coincidence experiments were carried out using a 12 cc coaxial detector of resolution 2.4 keV at 1332 keV together with another 37 cc coaxial detector of resolution 2.9 keV. The detectors were located as close as possible but at an angle of 135° to each other. This geometry was chosen in order to minimize back-scattering of gamma rays from one detector into the other and yet still maintain reasonably large solid angles. For the coincidence counting, electroplated sources were mounted in the aperture of an anti-Compton shield and viewed from opposite sides by the two detectors. The data from the coincidence experiments were recorded in the form of a 1024 x 256 channel matrix as discussed in section 5.3.

For both the $^{193}$Os and $^{191}$Pt decay experiments to be described, the windows placed on the TAC spectrum provided resolving times (2τ) of 200 nsec, and by keeping the source strengths low, true to chance ratios of ∿ 40/1 were obtained. However even with this low rate of accidental coincidences, it was found advisable to correct the data for chance coincidences. Since the chance contribution has the same shape as the direct spectra, a chance matrix was generated from the direct spectra recorded in the coincidence geometry. Each element of the chance matrix was formed by taking the product of the corresponding coordinates of the direct spectra and then normalizing the entire matrix to yield the correct total of chance events. This chance matrix was then subtracted from the data matrix to yield the data in its final form.

The coincidence information was extracted from the 1024 x 256 chance-corrected matrix in the following manner. Sums of the coincidence events were first projected onto both axes, and these projections used to select "gates" along the axes. Usually the gates were set along the axis of higher resolution, namely that containing 1024 channels. Each gate was set by selecting several adjacent channels of the projection and summing the spectra in coincidence with each of these channels. The gate was corrected for the underlying Compton distribution by subtracting the content of an equal number of channels, usually chosen half below and half above the selected gate.

The spectra generated by these gates were analyzed to obtain the coincidence probabilities between the gamma rays observed in the gated spectrum and the gating transition. Experimentally, this is obtained from

$$N_{ij} = N_o\ (\varepsilon\omega)_i\ (\varepsilon\omega)_j\ C_{ij}$$

where $N_{ij}$ is the number of coincidence events occuring between the full energy peaks of the $i^{th}$ and $j^{th}$ gamma rays, $(\varepsilon\omega)_i$ and $(\varepsilon\omega)_j$ are the corresponding efficiencies and $C_{ij}$ is the coincidence probability of interest. The source strength $N_o$ was determined by normalizing to a strong cascade for which it was felt that the true coincidence probability was well-known.

The experimental coincidence probabilities can then be compared with those expected from the decay scheme. For a direct cascade involving gamma rays i and j as shown in the accompanying diagram,

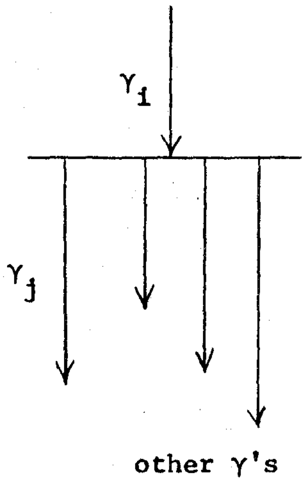

the coincidence probability is defined by

$$C_{ij} = C_{ji} = I_i\ f_j$$

where $I_i$ is the intensity of the incoming gamma ray and $f_j$ is the fraction of the intensity which proceeds through gamma ray j. Clearly this fraction is equal to the intensity of gamma ray j divided by the total intensity (including conversion) deexciting the level. For indirect cascades, the coincidence probability is obtained by similar considerations.

Care must be exercised when analyzing the gated spectra to avoid including spurious peaks as real coincidences. Such peaks may arise from single gamma rays backscattering out of one detector into the other. These peaks are easily recognized since they will only arise in gates which happen to be located at the Compton or backscatter energy of a prominent gamma ray. Moreover the energy of the spurious peak will correspond to the complimentary backscatter or Compton energy of the same gamma ray.

Other spurious peaks were found to result whenever strong triple cascades were present. In these circumstances, all three gamma rays are in coincidence so that two of the gamma rays may be simultaneously detected in one of the detectors, thus giving rise to coincidence summing. The data revealed coincidence summing effects for all the strong triple cascades in both the $^{193}$Os and $^{191}$Pt decays. Estimates of this summing could be made since the number of counts in the sum peak is given by

$$N_{i\ j+k} = N_o\ (\varepsilon\omega)_i\ (\varepsilon\omega)_j\ (\varepsilon\omega)_k\ C_{ijk}$$

where $C_{ijk}$ is the coincidence probability for the triple cascade. Because the absolute efficiencies were not known very accurately for the coincidence geometry, the data were normalized to a prominent sum peak to obtain the absolute efficiency factor. Estimates obtained in this manner agreed very well with the observed effects.

## 6.3 The Internal Conversion Measurements

The internal conversion measurements were performed using the Chalk River large iron-free $\pi\sqrt{2}$ spectrometer after adjusting the degaussing coil currents for cancellation of the external magnetic field. The spectrometer was calibrated using the momentum value of 2222.521 B$\rho$ for the 412 K conversion line of $^{198}$Au (Murray et al (1965)). In both the $^{193}$Os and $^{191}$Pt experiments, this line was measured in the source normal and source inverted positions resulting in a calibration accuracy of 6 parts in $10^5$. The spectrometer was operated at a resolution of 0.05 to 0.15% in momentum, with most of the measurements performed at a resolution of 0.10%.

The observed conversion line shape is asymmetric with a low energy tail caused partly by the focussing properties of the spectrometer and partly by energy degradation in the source. As a result, care must be taken in defining the position of the peak. A useful definition is the "top-peak-center" position which is obtained by drawing a line midway between the high and low energy sides of the peak up until it intersects the top of the peak. This intercept is then taken as the "position" of the peak. An alternative definition chooses the point at which two straight lines fitted to the high and low energy sides of the peak intercept each other as the defining position of the peak. For several of the well defined lines, both procedures were used and found to yield similar values for the peak positions. Although either procedure appeared equally acceptable, the second definition was actually used to obtain the energies reported in these investigations.

Since the spectrometer has a constant momentum resolution $\frac{\Delta p}{p}$, the measured areas of the conversion lines must be divided by the peak momentum (as well as corrected for the scanning increment used) to obtain a true measure of their intensity. For several transitions, L subshell intensity ratios were measured and compared with the theoretical conversion coefficients of Hager and Seltzer (1968) to obtain precise values for the M1 + E2 mixing. These mixing ratios, along with the theoretical conversion coefficients, could then be used to calculate the actual conversion coefficients for the L subshells and thereby establish the relation between the photon and conversion electron scales. The details of the procedure are described more fully with the presentation of the results.

## 6.4 The ($^3$He,d) and ($\alpha$,t) Reaction Measurements

The ($^3$He,d) and ($\alpha$,t) reaction experiments were performed using beams of 28 MeV $^3$He and $^4$He particles obtained from the model MP tandem Van de Graaff accelerator at the University of Rochester Nuclear Structure Research Laboratory. The reaction products were analyzed with an Enge split-pole magnetic spectrograph using a solid angle of 2.29 msr and detected using Kodak NTB nuclear emulsions of thickness 50 μm. The deuteron spectra were recorded with aluminium absorbing foils of thickness 0.032 in placed in front of the emulsions to stop tritons and to intensify the deuteron tracks. Similarly

0.004 in thick aluminium absorbers were used for recording the triton spectra.

Throughout each exposure, the particles elastically scattered through an angle of $\theta = 45°$ were monitored. A 2 mm thick NaI detector, which subtended a solid angle of 0.685 msr at the target, was used for this purpose. The number of counts recorded in the elastic peak, together with the known elastic scattering cross section were later used to convert the intensities of the peaks on the nuclear emulsions into absolute cross sections.

The positions and areas of the peaks in the particle spectra were obtained by means of the computer program SPECTR, originally obtained from the University of Rochester. The fitting regions along with their corresponding backgrounds are inputed into the program which, after subtracting off the specified background, performs a non-linear least-squares fit over these regions to a function of the form

$$I(x) = I\left[ \exp \frac{-(x-x_p)^2\, 4\ell n2}{G^2} + S \exp \frac{-(x-x_p-GG)}{A/\ell n2} \left(1-\exp \frac{-(x-x_p)^2\, 4\ell n2}{GG^2}\right) \right]$$

where A, S, G, GG, I, $x_p$ are parameters of the calculation. The first term represents a gaussian while the remaining term provides an exponential fall-off which is displaced from the main gaussian term and smoothly connected to it by means of a secondary inverted gaussian. Usually all peaks in the spectrum were fitted with fixed parameters of A, S, G and GG obtained from a prominent peak of the spectrum.

The resulting areas were used to obtain the reaction cross sections by comparing the number of reaction events $N_{\text{reaction}}$ to the number of elastically scattered events $N_{\text{elastic}}$. Assuming the target is mono-isotopic, we may write

$$\frac{N_{\text{elastic}}}{N_{\text{reaction}}} = \frac{\Omega_{\text{NaI}} \frac{d\sigma}{d\Omega}_{\text{elastic}}}{\Omega_{\text{magnet}} \frac{d\sigma}{d\Omega}_{\text{reaction}}}$$

where $\Omega_{\text{NaI}}$ and $\Omega_{\text{magnet}}$ are the solid angles subtended by the monitor and the spectrograph. Thus the reaction cross section $\frac{d\sigma}{d\Omega}_{\text{reaction}}$ may be obtained providing the elastic cross section $\frac{d\sigma}{d\Omega}_{\text{elastic}}$ is known.

For low energy ions, the Rutherford scattering formula correctly predicts the elastic cross section. However for the 28 MeV particles used in the present ($^3$He,d) and ($\alpha$,t) experiments, significant deviations may be expected from the classical values due to nuclear effects. Therefore a DWBA analysis has been used to obtain the ratio of elastic to Rutherford cross sections for 28 MeV $^3$He and $^4$He ions. For 45° scattering from osmium targets, these ratios were found to be 0.89 and 1.04 for $^3$He and $^4$He respectively.

## 6.5 Radioactive Source Preparation

Sources of 31 hr $^{193}$Os were prepared by irradiating samples of osmium enriched to 98.7% in $^{192}$Os. The irradiated material was dissolved in aqua regia and distilled as osmium tetroxide into a 5% solution of hydrogen peroxide. This distillation removed any impurities present in the osmium and at the same time trapped the gaseous osmium tetroxide in a convenient form. A drop of sulfuric acid was added and the active hydrogen peroxide solution then distilled into a 20% solution of sodium hydroxide. Heat must be applied rather gently at this stage since it is possible to drive the osmium over so quickly that it is not trapped in the sodium hydroxide. Successful trapping of the osmium is signaled by the sodium hydroxide solution turning yellow. The sodium hydroxide containing the active osmium was then added to an equal volume of plating solution (consisting of 20 g ammonium phosphate, 90 g sodium phosphate and 5 g sodium chloride per litre of solution).

The plating was performed in a lucite cell of a few cc volume with a platinum anode. An opening in the cell base was sealed with 4.5 mg/cm$^2$ copper foil which served as the cathode and source backing. Both the gamma ray and internal conversion sources were prepared in this manner. Using a current of 200 ma, typical plating times ranged from several minutes for the electron sources to several hours for the gamma ray sources.

Preparation of the 3.0 day $^{191}$Pt sources involved irradiating samples of platinum having $^{190}$Pt enrichments of 0.40% and 0.76%. Although no chemical purification was performed on these samples, the irradiated material was dissolved in a small amount of aqua regia. This solution was then added to an equal volume of plating solution (consisting of 16 g ammonium hydrogen phosphate, 4 g sodium chloride, 1.5 g sodium borate and 80 g sodium di-hydrogen phosphate per litre of solution) and the pH adjusted to 5. From this plating bath, sources for both the gamma ray and conversion electron studies were electroplated onto copper foils in the manner already discussed.

The source material of high specific activity required to construct suitably thin conversion electron sources was irradiated in the Chalk River NRU reactor; the material for the sources used in the gamma ray and $\gamma$-$\gamma$ coincidence measurements was activated in the McMaster swimming pool reactor.

### 6.6 Preparation of the Accelerator Targets

For the ($^3$He,d) and ($\alpha$,t) studies, extremely thin and uniform targets are necessary in order to prevent energy straggling of the particles in the target. The preparation of osmium targets presents additional difficulties since this material is refractory as well as having a high melting point (3000° C).

Initially, targets of separated isotope were prepared at the Oak Ridge National Laboratory by "catching" the osmium ions from the mass separator directly onto glass backed carbon foils. Considerable difficulty was experienced in floating these foils off the glass backing as the target material tended to curl upon itself. Tests indicated that negligible osmium was present on those targets which were successfully floated.

Attempts were then made to prepare the osmium targets by electrospraying. The osmium metal was first converted into gaseous osmium tetroxide which was then reduced to form a suspension of osmium dioxide in alcohol. This volatile solution was placed in a capillary tube and sprayed onto a carbon foil by the application of a high potential. The resulting targets of osmium dioxide caused considerable straggling and were not useable.

Successful targets of separated osmium were finally prepared by evaporating the metal onto carbon backings by electron bombardment. About 15 mg of osmium material was placed directly onto the target pan of a Varian electron gun in a vacuum chamber and microscope slides containing 50 $\mu g/cm^2$ carbon foils mounted 7 cm directly above the target material. The chamber was evacuated and the material slowly heated. The current in the electron gun was increased until further increases produced no temperature change. Usually, but not always, the osmium appeared to liquify. Evaporation was continued for 4 hours, after which time uniform targets of thickness $\sim 100$ $\mu g/cm^2$ were obtained. These targets along with their carbon backings were floated off the microscope slides and mounted on target frames for use.

## CHAPTER VII

## THE DECAY OF $^{193}$Os

### 7.1 Previous and Concurrent Work

During the course of this investigation, a considerable number of papers on the decay of $^{193}\mathrm{Os} \rightarrow {}^{193}\mathrm{Ir}$ have been published. Alexander and Ryde (1967) established the doublet character of the 181 keV transition using a bent crystal spectrometer, Metzger (1967) used the techniques of nuclear resonance fluorescence to show that the 558 keV level is a closely spaced doublet, and Atzmony et al (1967) determined the spin of the 73 keV state to be 1/2 using Mossbauer techniques. Several other papers, including Gustafsson et al (1967), Perry amd Murphy (1967), Agin et al (1967), Plajner et al (1967) and Avida et al (1968), appeared at about the same time with incomplete and conflicting assignments.

In the meantime, the results of several years of work carried out in this laboratory were published (Price et al, 1969). This work provided a rather complete set of gamma ray and internal conversion energies and intensities, and reported the results of a series of $\beta$-$\gamma$ and $\gamma$-$\gamma$ coincidence measurements using magnetic spectrometers, together with NaI(Tℓ) and Ge(Li) gamma ray detectors. The discovery of the 142 keV transition, which had previously been unresolved from the very strong 139 keV transition, made it possible to establish the existence of a 219-299-142 keV cascade with a 441 keV crossover and to deduce a decay scheme which was relatively free of ambiguities. The order of this cascade was not certain but on the basis of rather weak evidence, Price et al based it on the ground state with levels at 142, 441 and 660 keV. At about the same time, Bisgard and Hanson (1969) reported decays of the 80 keV isomer of $^{193}$Ir in the $^{193}$Os decay spectrum. A work by the Swedish group of Berg et al (1970) followed which confirmed most of our results but suggested that the order of the triple cascade was reversed and based on the 80 keV isomeric state, with levels at 299, 598 and 740 keV in $^{193}$Ir. Neither Price et al nor Berg et al had been able to document their positions unambiguously.

It was felt that with the significant improvements which had occurred in the Ge(Li) detectors and electronics available to us since our 1969 publication, a re-investigation of the $^{193}$Os decay scheme would be profitable, particularly in light of the questionable positioning of the triple cascade. The gamma ray energies and intensities and the $\gamma$-$\gamma$ coincidence measurements presented in this chapter have resulted from this study. These measurements confirm most of the results which appear in our earlier paper (Price et al (1969)) but are of significatnly higher calibre, and show clearly that the ordering of the 142-299-219 keV cascade suggested by Berg et al is correct. This conclusion was confirmed by the results of the ($^3$He,d) and ($\alpha$,t) reaction data to be described in subsequent chapters of this thesis.

While this thesis was in the writing stage, the results of recent experiments by the Swedish group (Backlin et al (1970)) were published. They showed that the intensity of the 80 keV isomer was consistent with the assumption that the 142-299-219 keV cascade feeds the isomer. Moreover, by using delayed electron-electron coincidence techniques, they showed that the 299 keV transition is followed by the 219 keV transition. As a result of experiments carried out in Stockholm and at McMaster, the spins and parities of the negative parity states at 299, 598, and 740 keV are now solidly established. The question of their interpretation will be discussed later.

## 7.2 The Direct Gamma Ray Spectra

Direct gamma ray spectra of the gamma rays following the decay of $^{193}$Os were taken with the Ge(Li) detectors described in section 6.1. A spectrum obtained with the thin window Ortec planar detector is shown in Fig. 7.1. The upper spectrum in this figure was taken with no absorber while the lower were recorded with a 2 mm lead absorber wrapped in cadmium and copper to remove the lead x-rays. The spectrum is characterized by a large number of close doublets and also shows the Ge(Li) escape peaks characteristic of such small thin-window detectors (Ungrin and Johns (1969)). While the 73 keV line is incompletely resolved from the iridium $K_\beta$ x-rays, it was possible to separate the two by a computer analysis. The spectra show essentially no impurity lines except those arising from the decay of $^{185}$Os. Several of the weaker peaks are shown separately in inserts.

Since the decay of $^{193}$Os results in several strong cascades, coincidence summing is liable to create spurious peaks. The strongest summing peaks may be expected to appear at 518 (299 + 219) and 622 (235 + 387) keV. To insure that the 516 keV peak of Fig 7.1 is not the result of such effects, measurements were made using a series of different geometries. These measurements indicated that summing effects were only important for the large detector, when used in close geometries.

The results of the gamma ray energy measurements are presented in table 7.1. The first column shows the energies derived from the internal conversion data taken on the iron-free $\pi\sqrt{2}$ spectrometer at Chalk River. The second column presents the weighted mean of the energies derived from a large number of Ge(Li) spectra. It is to be emphasized that the Ge(Li) energies have been obtained independently of the $\pi\sqrt{2}$ energies. The agreement between the two sets of results attests to the accuracy of the measurements.

The errors in the energies from internal conversion are compounded of an error of 6 parts in $10^5$ in establishing the calibration and the errors in establishing the individual peak positions. For the photon measurements, peak positions of the well-defined peaks can be extracted to better than 2% of a line width using the program JAGSPOT. The uncertainties in the energies of such peaks reflect mainly the limited accuracy with which the non-linearity corrections can be established.

The gamma ray intensities are presented in column 2 of table 7.4 and have been normalized to a value of 100 for the 460 keV transition. The absolute photon intensities may be obtained from these relative values by using the value of 3.95 emissions per 100 decays

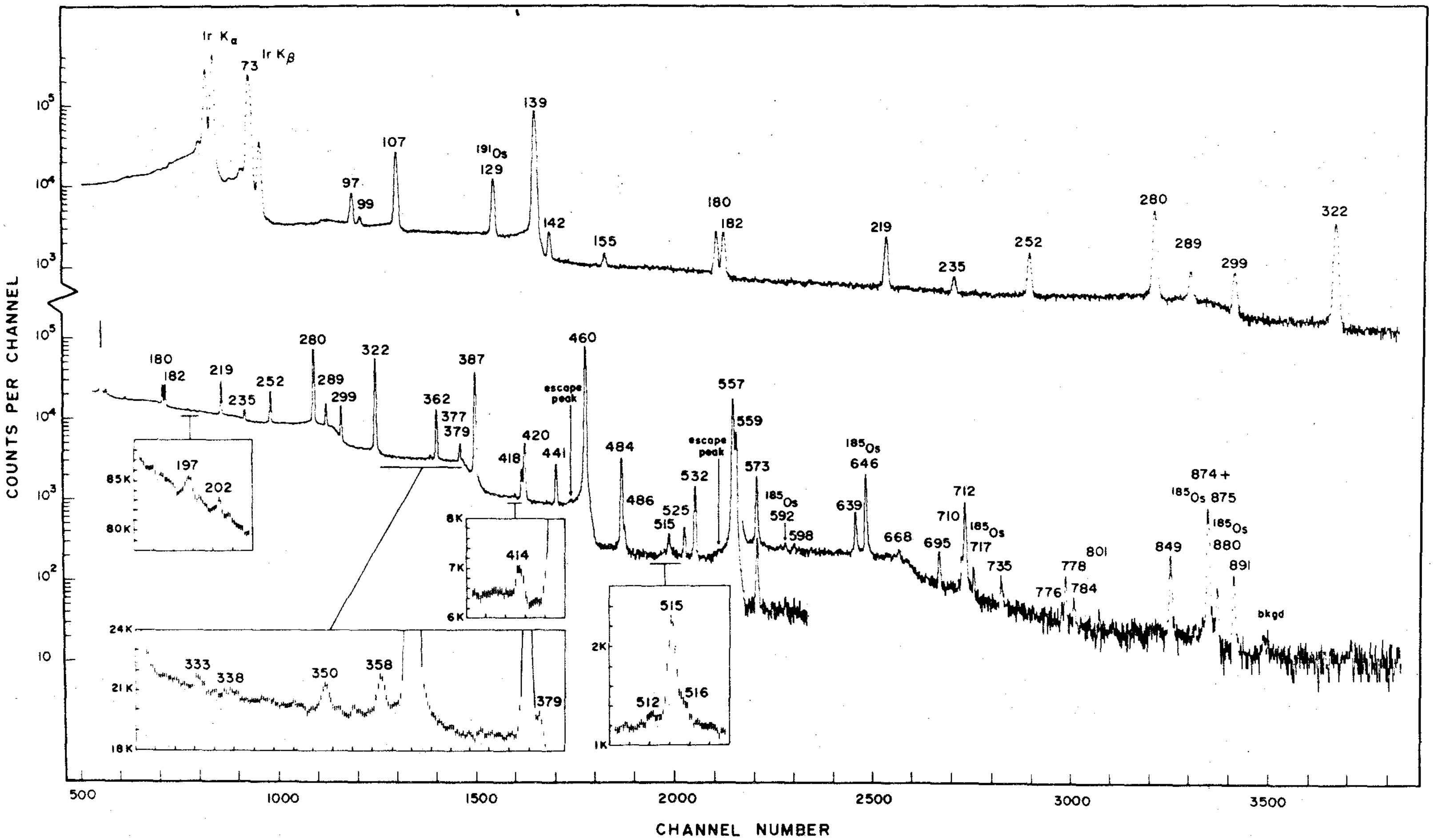

Figure 7.1 The gamma ray spectrum of $^{193}$Os. The upper spectrum was recorded without absorber while the lower were taken with a 2 mm lead absorber.

TABLE 7.1

$^{193}$Ir Gamma Ray Energies

| $\pi\sqrt{2}$ Energy (keV) | Ge(Li) Energy (keV) |
|---|---|
| 73.012 ± 0.007 | 73.08 ± 0.10 |
| 96.82 ± 0.03 | 96.80 ± 0.05 |
| | 98.70 ± 0.08 |
| 106.993 ± 0.010 | 106.96 ± 0.05 |
| 138.892 ± 0.007 | 138.89 ± 0.05 |
| 142.130 ± 0.008 | 142.14 ± 0.05 |
| 154.74 ± 0.03 | 154.78 ± 0.07 |
| 180.03 ± 0.03 | 180.00 ± 0.05 |
| 181.81 ± 0.03 | 181.73 ± 0.05 |
| | 197.4 ± 0.2 |
| | 201.5 ± 0.3 |
| 219.12 ± 0.05 | 219.14 ± 0.05 |
| 234.56 ± 0.10 | 234.58 ± 0.06 |
| 251.62 ± 0.04 | 251.61 ± 0.05 |
| 280.43 ± 0.03 | 280.46 ± 0.05 |
| 288.77 ± 0.05 | 288.82 ± 0.05 |
| 298.87 ± 0.06 | 298.81 ± 0.05 |
| 321.56 ± 0.03 | 321.58 ± 0.05 |
| | 333.3 ± 0.3 |
| | 337.7 ± 0.5 |
| | 350.2 ± 0.2 |
| | 357.7 ± 0.2 |
| 361.79 ± 0.05 | 361.84 ± 0.05 |
| | 377.31 ± 0.07 |
| | 379.04 ± 0.15 |
| 387.44 ± 0.04 | 387.49 ± 0.05 |
| | 413.8 ± 0.2 |
| | 418.35 ± 0.08 |
| 420.30 ± 0.05 | 420.31 ± 0.07 |
| 440.96 ± 0.10 | 440.95 ± 0.05 |
| 460.49 ± 0.03 | 460.50 ± 0.05 |
| 484.27 ± 0.07 | 484.25 ± 0.05 |
| | 486.11 ± 0.15 |
| | 512.3 ± 0.3 |
| | 514.95 ± 0.10 |
| | 516.3 ± 0.4 |
| | 524.98 ± 0.08 |
| | 532.02 ± 0.05 |
| 557.37 ± 0.08 | 557.35 ± 0.08 |
| 559.19 ± 0.10 | 559.26 ± 0.08 |
| | 573.33 ± 0.10 |
| | 598.1 ± 0.3 |
| | 639.09 ± 0.10 |
| | 668.3 ± 0.3 |
| | 695.12 ± 0.10 |
| | 709.93 ± 0.15 |
| | 712.10 ± 0.10 |
| | 735.3 ± 0.3 |
| | 775.9 ± 0.3 |
| | 778.48 ± 0.15 |
| | 784.2 ± 0.2 |
| | 800.9 ± 0.3 |
| | 848.85 ± 0.15 |
| | 874.36 ± 0.15 |
| | 891.26 ± 0.15 |

for the 460 keV transition (Price et al (1969)). The uncertainties in the gamma ray intensities are composed of a statistical error plus allowances for uncertain background subtraction. In addition, an uncertainty of 5% has been arbitrarily added to each measurement to allow for systematic errors in the efficiency curves. This uncertainty corresponds to the maximum deviation expected over the entire range of energies.

## 7.3 The Internal Conversion Results

Typical spectra obtained from a series of sources with the iron free $\pi\sqrt{2}$ spectrometer at Chalk River are presented in Figs. 7.2, 7.3 and 7.4. With each source, the peaks were measured relative to either the L conversion lines of the 139 keV transition, the K line of the 460 keV transition, or both.

For the 73, 107 and 139 keV transitions, precise values of the mixing ratios were obtained from the L subshell ratios. The photon and conversion electron intensity scales were related to each other using the mixing ratio for the 139 keV transition. This mixing ratio was first used to determine the conversion coefficients of the L subshells and these conversion coefficients then employed to establish the relation between the photon and conversion electron scales at 139 keV.

The internal conversion results are summarized in table 7.2. The first column indicates the transition energy and the next five columns present the measured photon and electron intensities. Most of the electron intensities represent a weighted average of several

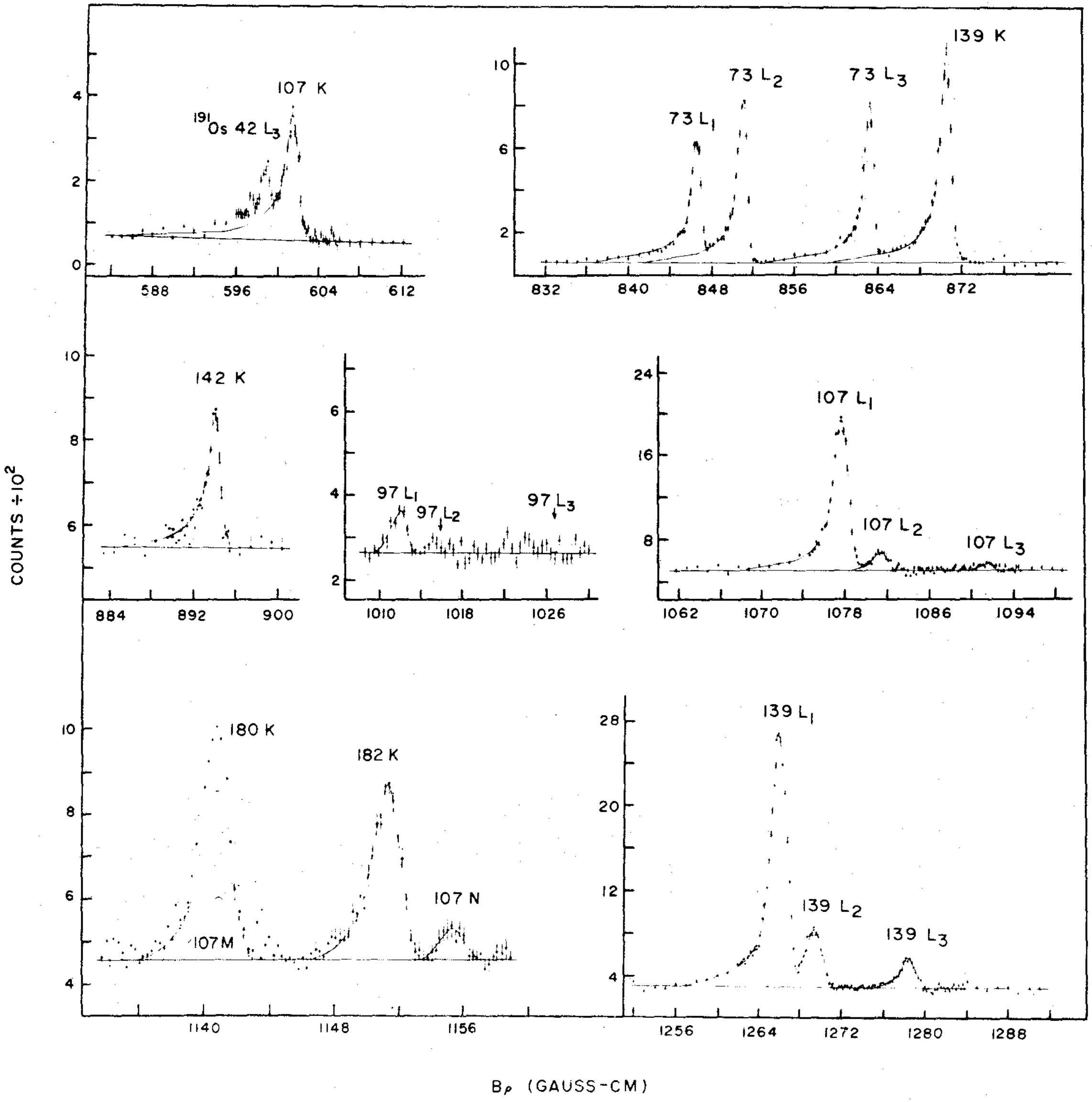

**Figure 7.2** **Portions of the internal conversion spectrum of $^{193}$Os showing the momentum region below 1300 G cm.**

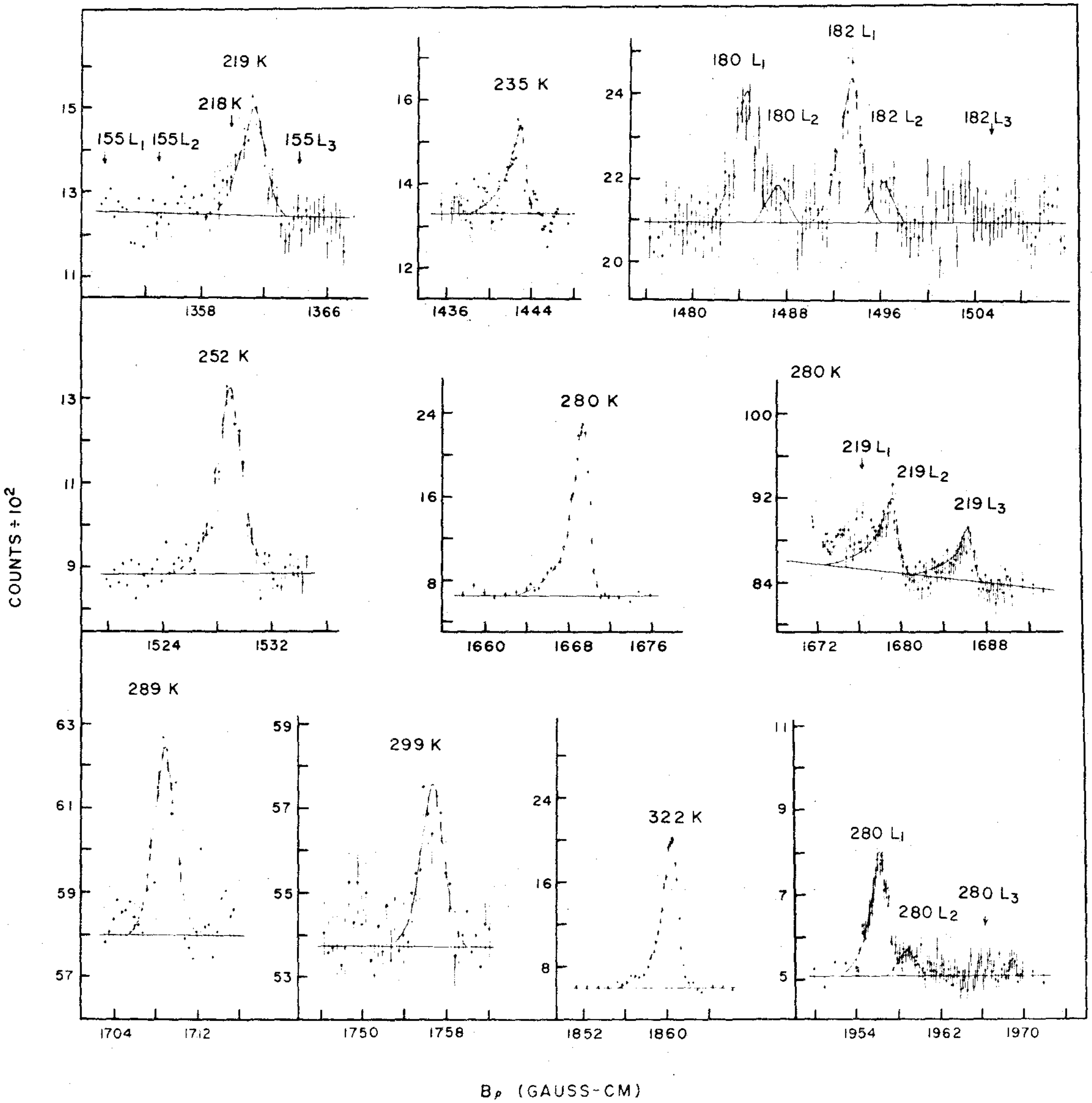

**Figure 7.3** Portions of the internal conversion spectrum of $^{193}$Os showing the momentum region between 1300 and 2000 G cm.

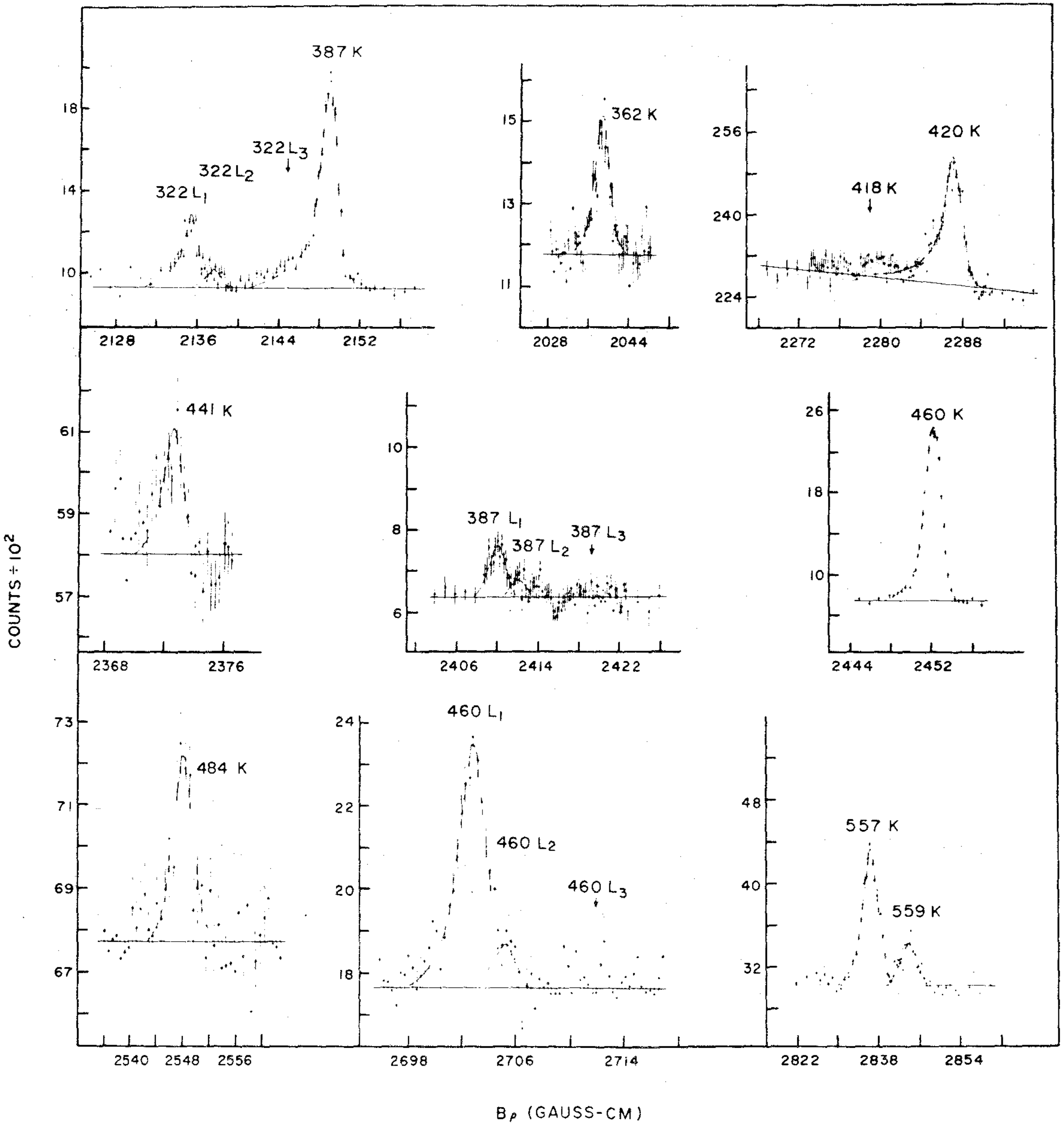

Figure 7.4 Portions of the internal conversion spectrum of $^{193}$Os showing the momentum region above 2000 G cm.

TABLE 7.2

$^{193}$Ir Internal Conversion Intensities and Multipole Assignments

| Transition (keV) | Intensity | | | | | Multipolarity | %E2 |
|---|---|---|---|---|---|---|---|
| | Photon | K | $L_1$ | $L_2$ | $L_3$ | | |
| 73 | 82 ± 12 | | 96.1 ± 1.9 | 132 ± 3 | 126 ± 3 | M1 + E2 | 27.8 ± 1.0 |
| 97 | 2.5 ± 0.2 | | 1.6 ± 0.2 | 0.35 ± 0.09 | 0.15 ± 0.05 | M1 + E2 | 4 ± 2 |
| 107 | 16.1 ± 0.8 | 63 ± 3 | 11.5 ± 0.3 | 1.41 ± 0.14 | 0.49 ± 0.05 | M1 + E2 | 1.7 ± 0.4 |
| 139 | 108 ± 5 | 176 ± 4 | 28.4 ± 0.6 | 6.8 ± 0.3 | 2.41 ± 0.12 | M1 + E2 | 9.1 ± 0.8 |
| 142 | 1.9 ± 0.2 | 2.5 ± 0.3 | | | | M1 + E2 | 37 ± 14 |
| 180 | 4.6 ± 0.5 | 4.0 ± 0.6 | 0.46 ± 0.07 | 0.13 ± 0.04 | 0.07 ± 0.07 | M1 + E2 | 20 ± 8 |
| 182 | 4.9 ± 0.5 | 3.9 ± 0.2 | 0.52 ± 0.08 | 0.11 ± 0.05 | 0.08 ± 0.05 | M1 + E2 | 15 ± 13 |
| 219 | 7.0 ± 0.5 | 0.73 ± 0.15 | <0.12 | 0.27 ± 0.05 | 0.17 ± 0.03 | E2 | >98 |
| 235 | 1.30 ± 0.17 | 0.54 ± 0.11 | | | | M1 + E2 | <40 |
| 252 | 5.5 ± 0.4 | 1.89 ± 0.09 | | | | M1 + E2 | <24 |
| 280 | 31.5 ± 1.6 | 9.43 ± 0.19 | 1.37 ± 0.07 | 0.24 ± 0.05 | <0.07 | M1 + E2 | <10 |
| 289 | 3.6 ± 0.3 | 0.27 ± 0.04 | | | | E2 | >90 |
| 299 | 4.7 ± 0.4 | 0.24 ± 0.04 | | | | E2 | >98 |
| 322 | 32.3 ± 1.6 | 6.83 ± 0.14 | 0.85 ± 0.09 | 0.15 ± 0.07 | 0.12 ± 0.12 | M1 + E2 | <8 |
| 362 | 7.5 ± 0.6 | 1.17 ± 0.12 | | | | M1 + E2 | <8 |
| 387 | 31.9 ± 1.6 | 3.81 ± 0.08 | 0.47 ± 0.07 | 0.11 ± 0.05 | <0.05 | M1 + E2 | <10 |
| 418 | 1.38 ± 0.14 | <0.05 | | | | E2 | >80 |
| 420 | 4.2 ± 0.3 | 0.45 ± 0.04 | | | | M1 + E2 | <8 |
| 441 | 2.32 ± 0.16 | 0.17 ± 0.03 | | | | M1 + E2 | <34 |
| 460 | 100 ± 5 | 6.64 ± 0.13 | 0.98 ± 0.05 | 0.11 ± 0.05 | <0.05 | M1 + E2 | 17 ± 7 |
| 484 | 4.3 ± 0.3 | 0.31 ± 0.05 | | | | M1 + E2 | <12 |
| 557 | 33 ± 3 | 1.82 ± 0.05 | | | | M1 + E2 | <4 |
| 559 | 12.3 ± 1.2 | 0.58 ± 0.05 | | | | M1 + E2 | <20 |

measurements and are all relative to the 460 keV gamma ray intensity. The quoted errors in the electron intensities represent only statistical uncertainties and do not include the uncertainty introduced by the normalization procedure. An additional 5% must be added in quadrature to include this uncertainty when relating these errors to the gamma ray intensities. This uncertainty has been included in arriving at multipolarity and mixing assignments. The transition multipolarities and E2 admixtures as obtained from the theoretical internal conversion coefficients of Hager and Seltzer (1968) are shown in the final columns of table 7.2.

Most of the transitions are observed to be M1 + E2 multipoles with a dominant magnetic dipole component. However, the 73 keV transition clearly contains an appreciable percentage of E2 mixing. The 219, 289 and 299 keV transitions are apparently pure E2 in character. The 418 keV transition appears to be E2 as expected from the decay scheme but the errors are large enough to permit considerable M1 mixing.

## 7.4 The Gamma-Gamma Coincidence Results

The two-parameter gamma-gamma coincidence measurements were taken with the Ge(Li) detectors and the experimental arrangement described in section 6.2. Over a period of a week, 11.32 x $10^6$ coincidence events were recorded at an average (true + chance)/chance rate of 38.5/1. The chance events were removed from the coincidence matrix by the procedure already discussed. The resulting 1024 x 256 channel coincidence matrix was analyzed by setting "gates" along the 1024 dimension and analyzing the corresponding 256 channel spectra. Fig. 7.5 shows the projection of the coincidence events on the 1024 channel axis. This spectrum was used to select the gates for analysis of the data. The set of channels included in a gate is indicated by the markings beneath the labelled peak energy. The sum of the events in these gate channels less the sum of the events in an equal number of near-by but off-peak channels (not shown in Fig. 7.5) represent the true spectrum in coincidence with the gating transition. The coincidence spectra are presented in Figs. 7.6 to 7.11 together with relevent portions of the decay scheme. Since much of the coincidence data provides redundant information, only a selection of data sufficient to justify the proposed decay scheme is presented. To simplify the discussion, each level will be treated in turn.

## The 73 keV Level

No data is specifically presented regarding the 73 keV level since it represents the well-established first excited state of $^{193}$Ir. However several of the gates shown are set on gamma rays which feed into this level and in each instance the associated coincidence spectrum shows prominent 73 keV peaks (i.e. Figs. 7.6b, 7.7c, 7.9b and 7.10f). The 639 and 891 keV gates (Figs. 7.11a and 7.11b) show that these relatively weak gamma rays feed the 73 keV level directly.

## The 139 keV Level

Fig. 7.6a shows the spectrum in coincidence with the 139 keV transition. Most of the peaks present are due to gamma rays which populate this state directly from higher-lying levels as shown in the insert. The peaks at 97, 235 and 252 keV are due to gamma rays which feed the 139 keV state through the 322 keV transition. The 280 keV peak is interesting. This peak indicates the existence of a 41 keV transition between the 180 and 139 keV states. Additional evidence for this transition is provided by the observation of the 139 keV peak in both the 280 and 532 keV gates (Figs. 7.8d and 7.11c). These data indicate a total transition intensity of 1.9 ± 0.5 for the 41 keV transition. Although this transition has not been observed directly, Berg et al (1970) have reported an upper limit of 0.3 for the intensity of the $L_1$ component, in disagreement with the present measurements. However, the electron measurements are seriously impaired in this region due to the 42 keV transition in $^{191}$Os which may account for the observed discrepancy.

The spectra of Figs. 7.11e, 7.11g and 7.11h show clearly that the weak gamma rays of energy 573, 710 and 735 keV all feed the 139 keV state directly. The spectrum of Fig 7.11f indicates that the 668 keV transition also feeds the 139 keV state, thereby defining a level at 807 keV. Since no other support is found for the 807 keV state, it has not been included in the decay scheme of Fig. 7.13.

For several of the strong triple cascades, coincidence summing effects are observed. The coincidence sum peak indicated in Fig 7.6a is due to x-ray + 322 keV summing in one detector in coincidence with the 139 keV transition in the other. Similar effects are noted on several other coincidence spectra.

## The 180 keV Level

The 180 keV state is depopulated by a strong 107 and a weaker

180 keV transition and the spectrum of transitions feeding this state is shown in Fig. 7.6b. This level is directly fed by gamma rays of energies 182, 280, 377, 379, 418, 515, 532, 560 and 784 keV and indirectly by the 97, 235 and 252 keV transitions, all of which appear in Fig. 7.6b. These observations are supported by the spectra in coincidence with the gates set on the higher energy gamma rays in Figs. 7.6d, 7.8d, 7.9d, 7.9e, 7.11c and 7.11d.

### The 358 keV Level

The 358 keV state is well-known from Coulomb excitation (McGowan and Stetson (1958)) but is only weakly populated in the beta decay process. The state is depopulated by the 358 keV ground state transition along with a 219 keV transition and populated by gamma rays of energy 202, 338 and 516 keV. The evidence for these statements is to be found in Figs. 7.6c, 7.6d and 7.6e.

The 107 and 180 keV radiations appearing in Fig. 7.6d are due to coincidences with the 515 keV gating transition. Summing in the gating detector of the 142 and 219 keV radiations from the intense 142-299-219 keV cascade is responsible for the weak 299 keV peak in Fig. 7.6e.

### The 362 keV Level

This level is deexcited by gamma rays of energy 182, 289 and 362 keV and populated by gamma rays of 99, 197, 333, 350, 378 and 512 keV. The spectrum of gamma rays feeding this state is shown in Figs. 7.7c and 7.7f while the spectrum of gamma rays deexciting it is shown in Figs. 7.7a, 7.7b, 7.7d and 7.7e.

For several of the gamma rays, spurious coincidences are observed due to scattering between the detectors. The self-coincidence peak indicated in Fig. 7.7b results from the 874 keV radiation depositing its Compton energy in one detector and backscattering into the other. A region of improper background subtraction, caused by self-coincidences from the 460 keV radiation, is visible in Fig. 7.7c.

### The 460 keV Level

The 460 keV state is depopulated by four strong gamma rays of energies 280, 322, 387 and 460 keV, and populated directly by gamma rays of energy 97, 235, 252 and 414 keV and indirectly by a 155 keV transition. The evidence for the first set of statements is found in Figs. 7.8a, b and c while that for the second set is given in Figs. 7.8d and 7.8e.

### The 557 and 559 keV Levels

The 557 keV state is depopulated by gamma rays of energies 97, 377, 418, 484 and 557 keV and populated by two weak transitions of energy 155 and 317 keV. The 559 keV level is depopulated by gamma rays of energy 197, 202, 379, 420, 486 and 559 keV and is fed by the extremely weak transition of energy 136 keV. By setting gates at 136, 155 and 317 keV on the output of the poorer detector (3.25 keV/channel) and examining the coincidence spectrum in the good detector (0.91 keV/channel), it was evident that the 155 and 317 keV transitions were in coincidence with the 557 keV gamma ray and that the 136 keV transition was in coincidence with the 559 keV gamma ray. This evidence is not presented here although some of the results can be inferred from the spectra of Fig. 7.9. The 155 keV gate (Fig. 7.9a) shows the gamma rays which deexcite the 557 keV level.

The broad gate set on the 556, 557 and 559 keV transitions (Fig. 7.9c) brings up several peaks in the coincidence spectrum. The 155 keV peak arises from the 155-557 keV cascade, the 136 + 139 keV peak is mostly due to a 556-139 keV cascade and partly due to a 136-559 keV cascade and the 317 keV peak is caused by the 317-557 keV cascade. Two other peaks at 181 and 290 keV can also be observed in this spectrum. When gates were set at 181 and 290 keV in the poorer detector and the high resolution spectra examined, both transitions were found to be in coincidence with the 559 keV gamma ray. Because of the poor statistics in the 290 keV peak and since the 181 keV peak is partly due to the 560-180 keV cascade, these transitions cannot be established unambiguously and have not been included in the decay scheme of Fig. 7.13.

There are similar subtleties in the other gates of Fig. 7.9. The statistics in the 484 + 486 keV gate of Fig. 7.9b are too poor to yield much information. The 377 + 378 + 379 keV gate of Fig. 7.9d shows evidence for the 378-289 and 378-362 keV cascades involving the 362 keV level, the 155-377 and 377-107 keV cascades involving the 557 keV level, and the 379-107 keV cascade involving the 559 keV level. In the same way the 418 + 418 + 420 gate of Fig. 7.9e shows peaks corresponding to the 155-418 and 418-139 keV cascades involving the 557 keV state, the 420-139 keV cascade from the 559 keV state and the 418-107 and 418-180 keV cascades involving the 180 keV level.

### The 299, 598 and 740 keV Levels

These states, together with the 80 keV isomeric state, are particularly interesting since they appear to form an independent subsystem of levels which interact only weakly with the remainder of the decay scheme. Because of the weak branching, coincidence data of high quality are necessary to establish the position of this cascade in the decay scheme.

It is clear from the spectra shown in Figs. 7.10a, b, d and e that the 142 and 299 keV transitions are in cascade, that the 441 keV radiation is a crossover, and that the 219 keV gamma ray is in coincidence with all three. The 142-299-219 sequence represents the strongest triple cascade in the $^{193}$Os decay, and accordingly, brings up prominent sum peaks in these spectra. The ordering and positioning of this cascade is determined by the spectra in coincidence with the 598 and 525 keV gates (Figs. 7.10c and 7.10f). These gates show that the 142 keV transition decays through the 598 and 525-73 keV gamma rays in addition to its main 142-299-219 keV cascade. Thus the 142 keV transition necessarily feeds a level at 598 keV while the 299-219 keV cascade populates the 80 keV isomeric state. Confirmation is provided by the 142 keV gate (Fig. 7.10e) which reveals the 598 and 525 keV transitions, along with an additional 418 keV transition, depopulating the 598 keV level.

The spectrum of Fig. 7.10a shows a prominent peak at 778 keV indicating the existence of 778-219 keV coincidences. Similar coincidences arise in the 778 keV gate of Fig. 7.11i. These coincidences were reported in earlier experiments (Price et al (1969)) and establish a level at 1078 keV. Although this provides the only evidence for such a level, the coincidences are quite definite and the 1078 keV level has been incorporated into the decay scheme of Fig. 7.13. Other weak peaks at 202, 338 and 516 keV in Fig. 7.11a arise from coincidences with another 219 keV (358→139) keV) gating transition.

These experiments are completely consistent with the conclusion of Backlin et al (1970) that the intense 142-299-219 keV triple cascade, which involves levels at 740, 598, 299 and 80 keV, feeds the 11.9 day 80 keV isomeric state. In a subsequent chapter, the evidence for these states deduced from ($^3$He,d) and (α,t) reaction studies will be presented.

### The 695, 712, 849, 874, and 964 keV Levels

These levels are securely established by the various coincidence gates already presented and need not be discussed further.

The coincidence data derived from all the gates has been analyzed to yield the coincidence probabilities of table 7.3. The first two columns in this table list the gamma ray pairs, $\gamma_i$ and $\gamma_j$, for which a coincidence probability was determined. The next two columns present the experimental values of $C_{ij}$ and $C_{ji}$ corresponding to whether the gate was set on $\gamma_i$ or $\gamma_j$ respectively and the fifth column tabulates the values of $C_{ij}$ expected on the basis of the proposed decay scheme. The experimental values of $C_{ij}$ and $C_{ji}$ are seen to agree to within ∿10% for well defined peaks.

The large discrepancies (up to ∿30%) between the experimental coincidence probabilities are those deduced from the decay scheme are due to angular correlation effects. The intense 299-219 keV stretched E2 cascade has been corrected for these effects by multiplying its expected $C_{ij}$ value by $W(\theta) = 1 + 0.102\ P_2(\cos\theta) + 0.009\ P_4(\cos\theta) = 1.05$, deduced for the effective angle of 145° at which these experiments were carried out. The experimental $C_{ij}$ values were then normalized

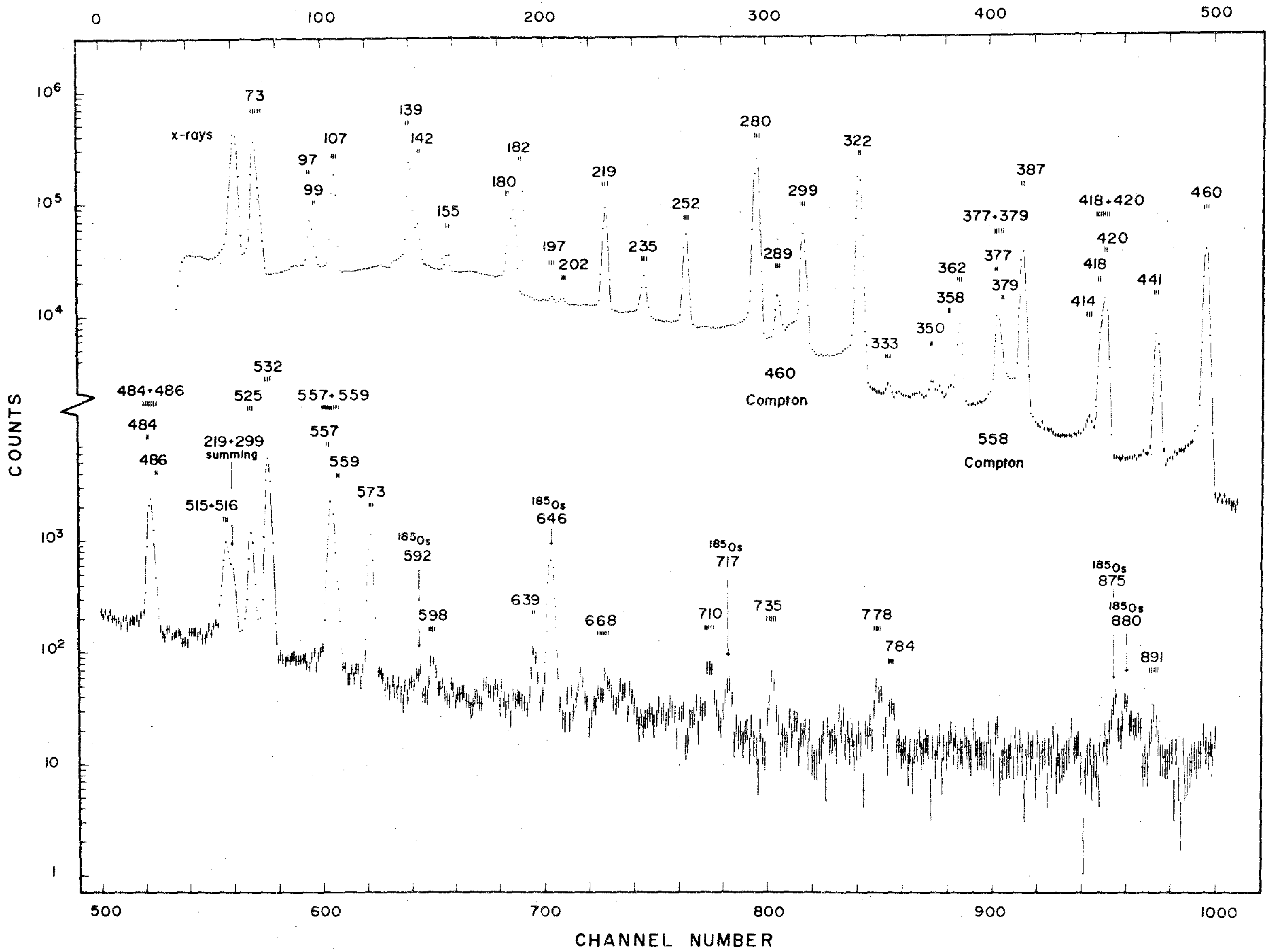

Figure 7.5 The spectrum of $^{193}$Os coincidence events projected onto the high resolution axis. The positions of the gates used in the analysis are indicated.

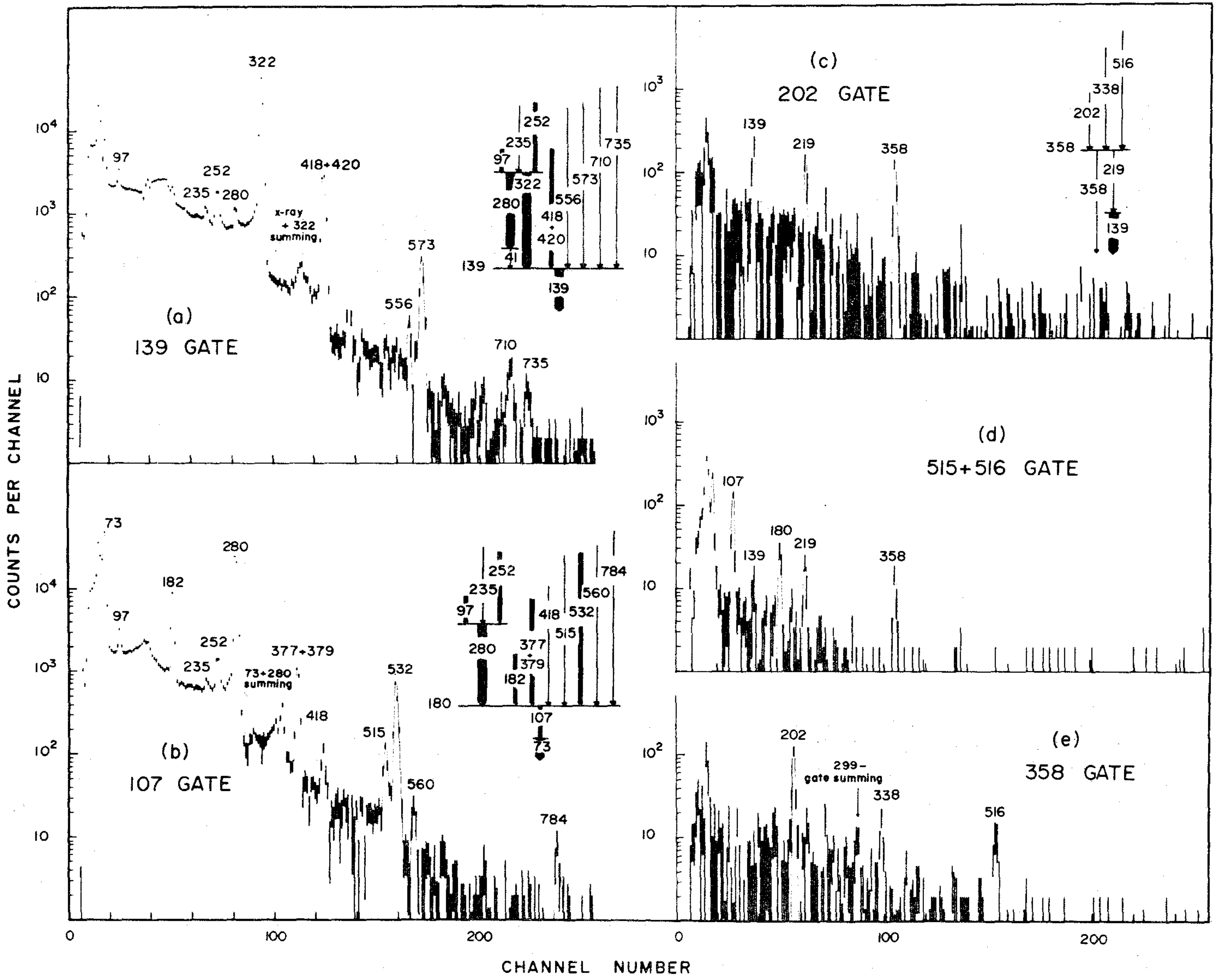

Figure 7.6 Coincidence data associated with the 139, 180 and 358 keV levels.

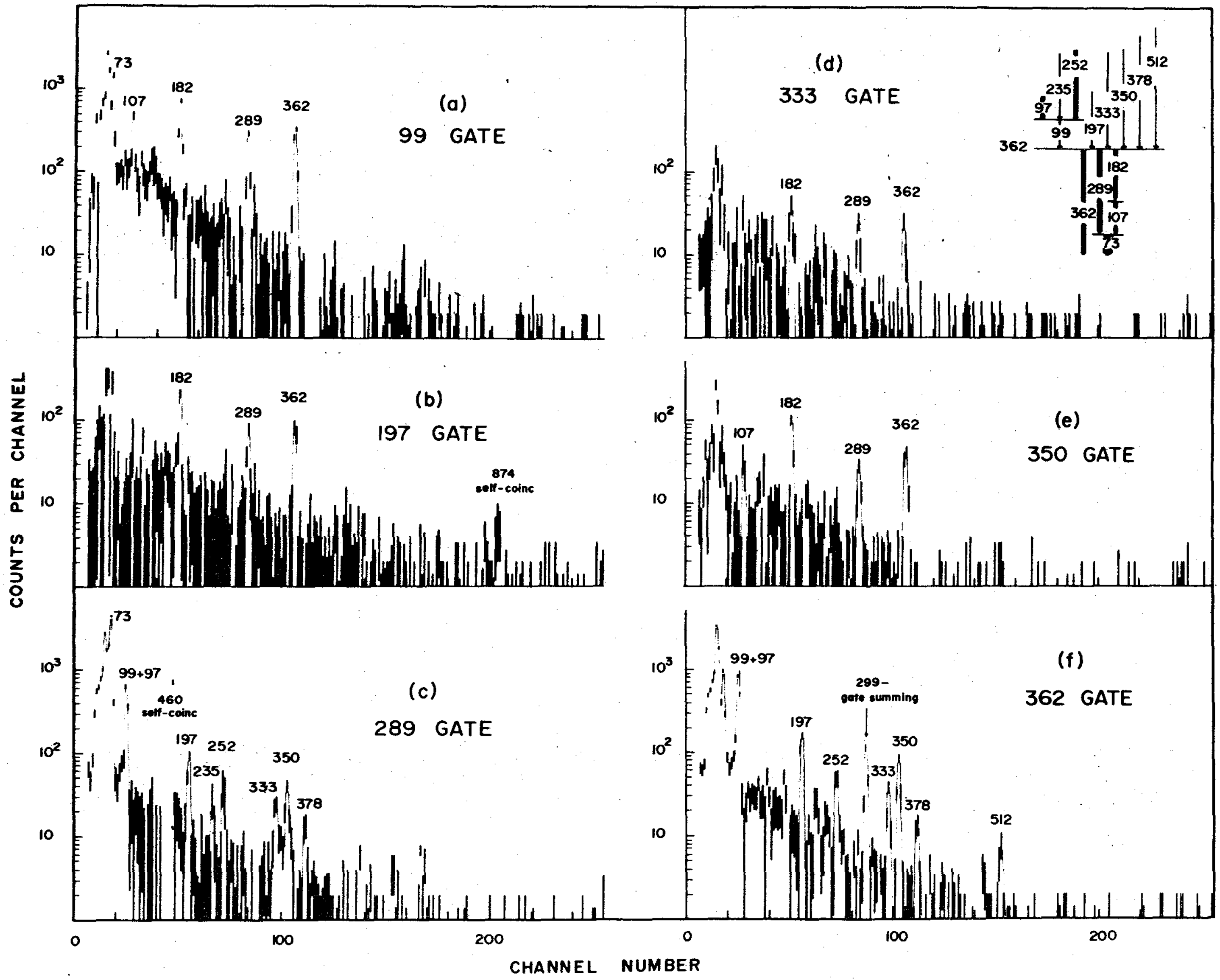

**Figure 7.7** Coincidence data associated with the 362 keV level.

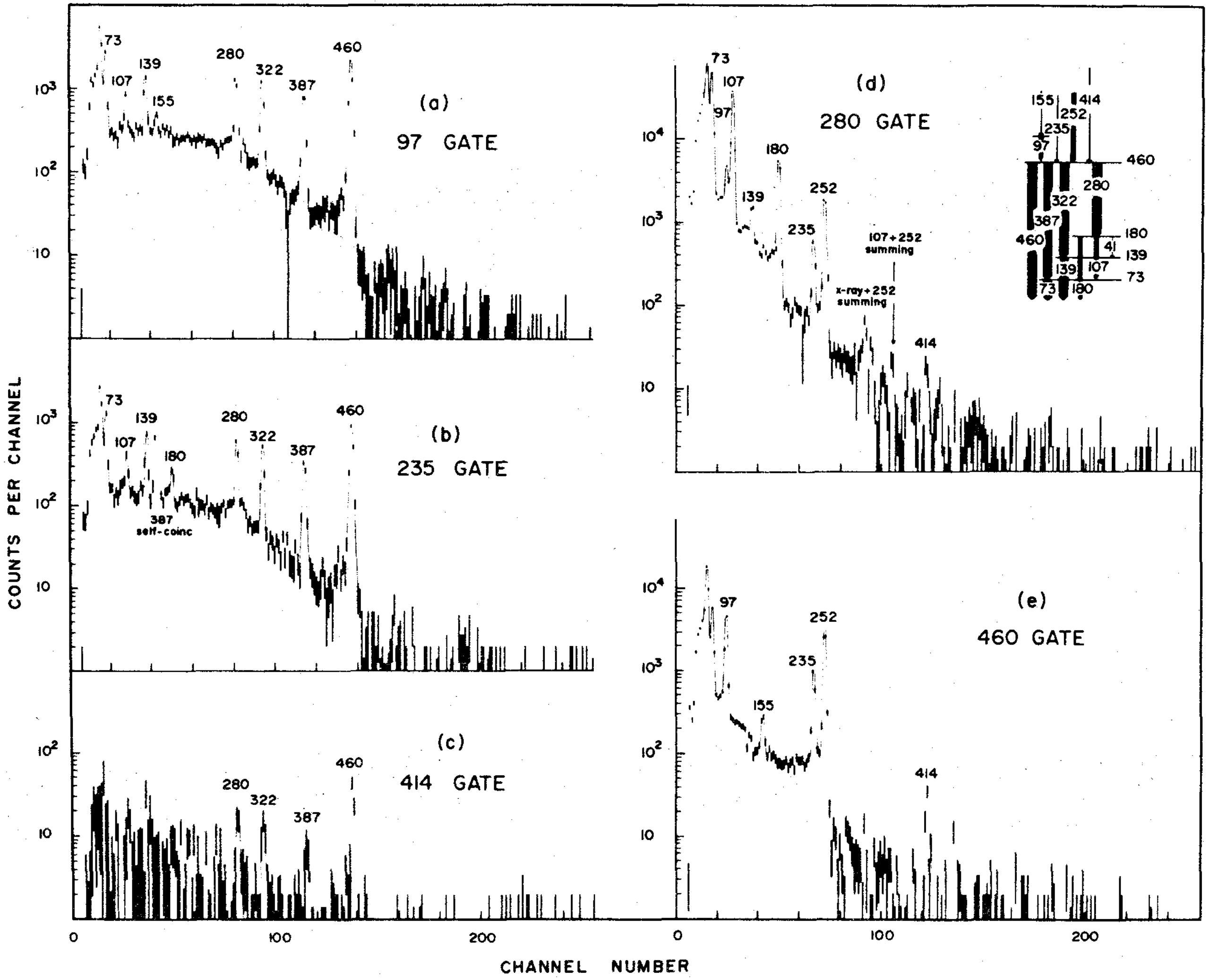

Figure 7.8 Coincidence data associated with the 460 keV level.

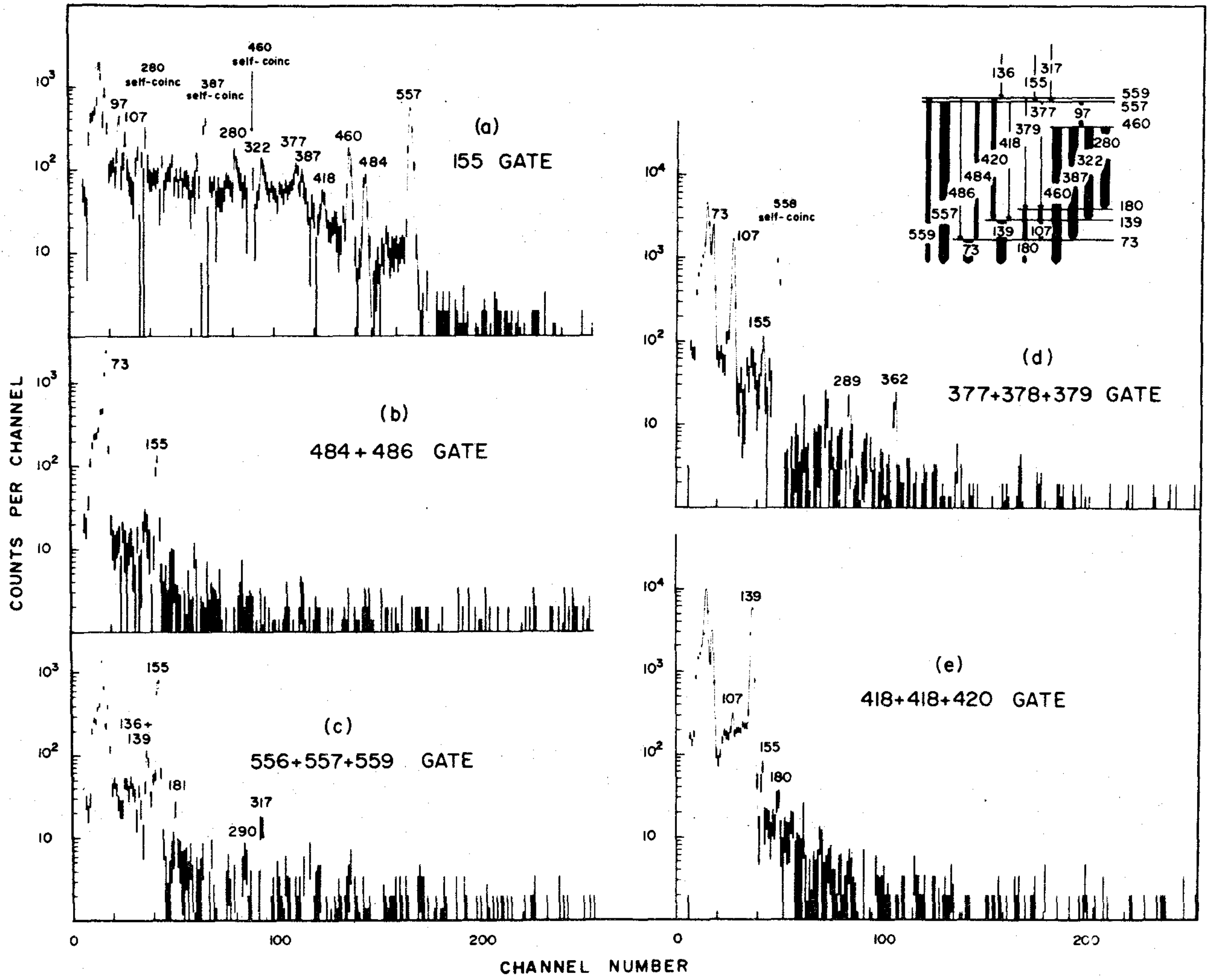

Figure 7.9 Coincidence data associated with the 557 and 559 keV levels.

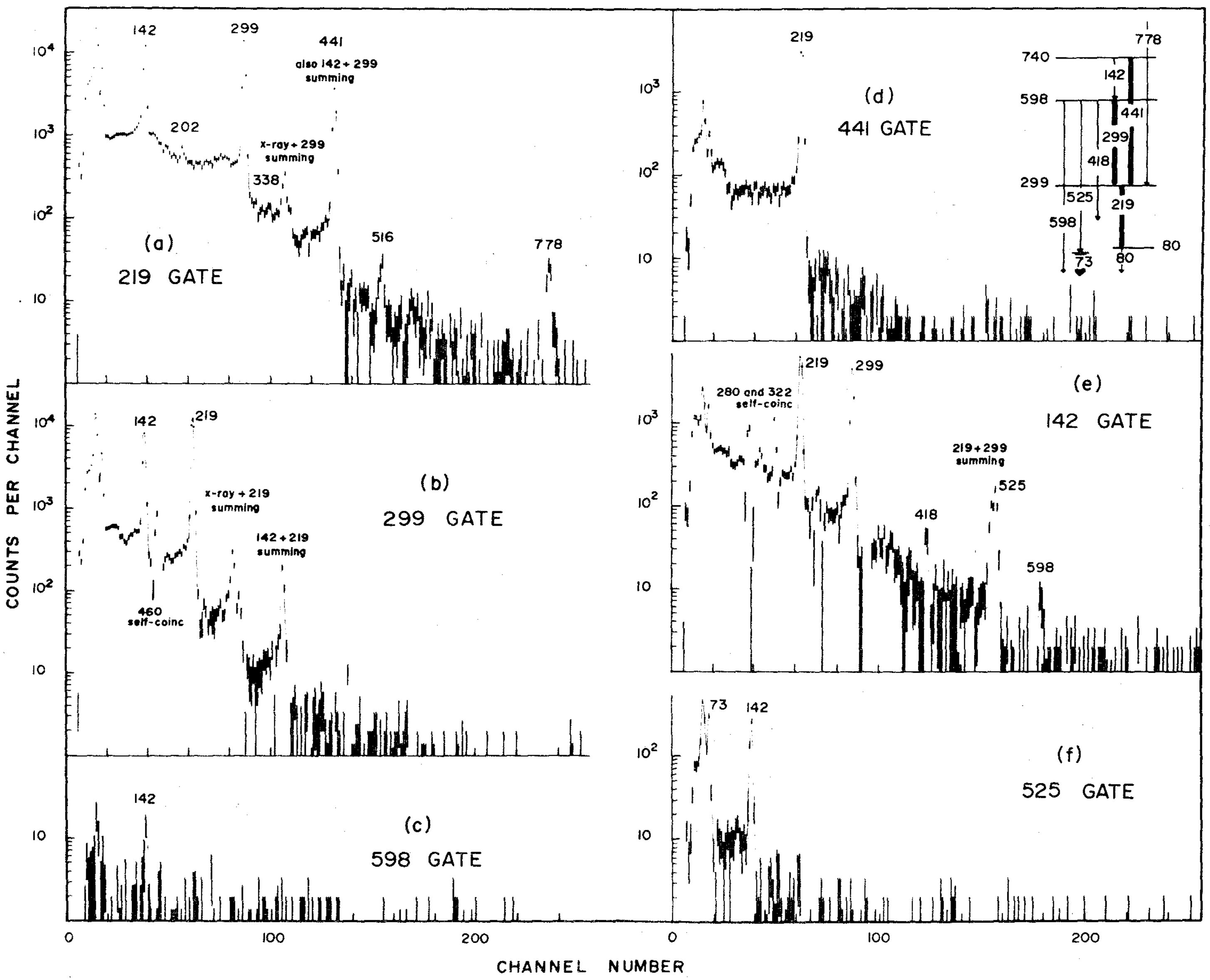

Figure 7.10 Coincidence data associated with the 80, 299, 598 and 740 keV levels.

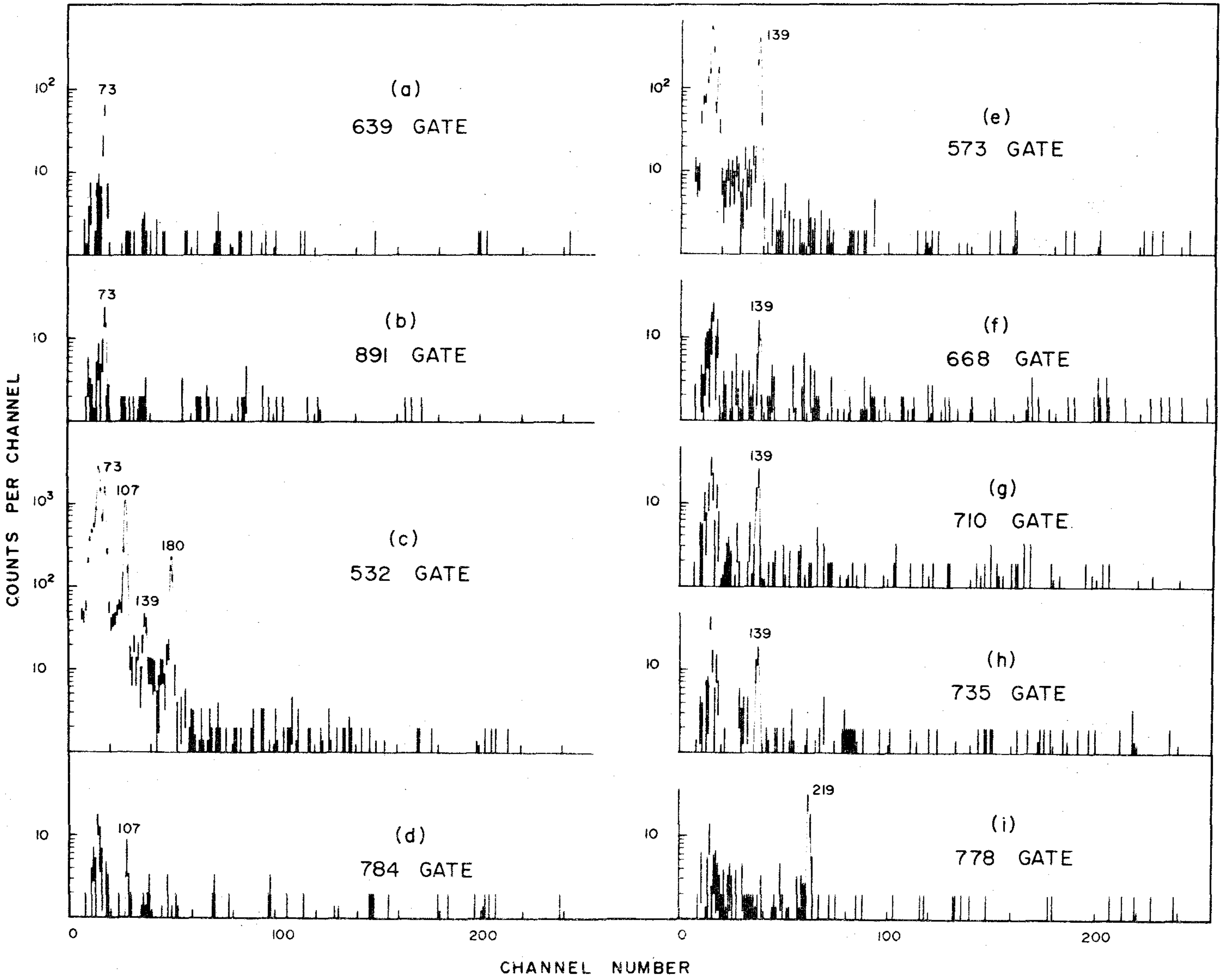

Figure 7.11 Coincidence data associated with various high energy transitions.

TABLE 7.3

$\gamma$-$\gamma$ Coincidence Probabilities in $^{193}$Ir

| $\gamma_i$ | $\gamma_j$ | $C_{ij}$ | $C_{ji}$ | $C_{expected}$ |
|---|---|---|---|---|
| 73 | 97 | 0.22 | 0.07 | 0.10 |
| | 99 | | 0.05 | 0.02 |
| | 107 | 2.74 | 2.04 | 2.10 |
| | 142 | 0.05 | 0.05 | 0.02 |
| | 155 | 0.05 | 0.02 | 0.02 |
| | 182 | 0.57 | 0.60 | 0.58 |
| | 197 | | 0.009 | 0.006 |
| | 235 | 0.08 | 0.05 | 0.09 |
| | 252 | 0.24 | 0.21 | 0.23 |
| | 280 | 3.74 | $3.74^{a)}$ | 3.74 |
| | 289 | 0.50 | 0.48 | 0.47 |
| | 350 | 0.05 | 0.03 | 0.009 |
| | 377 | 0.03 | 0.15 | 0.21 |
| | 379 | | 0.06 | 0.04 |
| | 387 | 4.61 | 4.10 | 4.15 |
| | 414 | | 0.03 | 0.005 |
| | 484 | 0.06 | 0.55 | 0.56 |
| | 486 | | 0.08 | 0.04 |
| | 515 | | 0.03 | 0.03 |
| 73 | 525 | | 0.06 | 0.05 |
| | 532 | 0.30 | 0.23 | 0.25 |
| | 639 | 0.03 | 0.03 | 0.03 |
| | 784 | | 0.011 | 0.002 |
| | 891 | | 0.008 | 0.009 |
| 97 | 99 | 0.008 | 0.004 | 0.005 |
| | 107 | 0.048 | 0.083 | 0.070 |
| | 139 | 0.13 | 0.12 | 0.13 |
| | 155 | 0.021 | 0.021 | 0.030 |
| | 180 | | 0.031 | 0.020 |
| | 280 | 0.28 | 0.56 | 0.34 |
| | 322 | 0.30 | 0.35 | 0.35 |
| | 387 | 0.34 | 0.38 | 0.49 |
| | 460 | 0.99 | 1.18 | 1.08 |
| 99 | 107 | 0.035 | | 0.014 |
| | 182 | 0.12 | 0.13 | 0.09 |
| | 252 | | 0.010 | 0.010 |
| | 289 | 0.083 | 0.099 | 0.066 |
| | 362 | 0.18 | 0.20 | 0.19 |

| $\gamma_i$ | $\gamma_j$ | $C_{ij}$ | $C_{ji}$ | $C_{expected}$ |
|---|---|---|---|---|
| 107 | 155 | | 0.011 | 0.008 |
| | 182 | 0.74 | 0.72 | 0.75 |
| | 197 | | 0.004 | 0.003 |
| | 235 | 0.018 | 0.032 | 0.036 |
| | 252 | 0.14 | 0.13 | 0.15 |
| | 280 | 5.03 | 4.96 | 4.82 (5.12) |
| | 350 | | 0.009 | 0.008 |
| | 377 | 0.30 | 0.28 | 0.28 (0.29) |
| | 379 | | 0.08 | 0.05 |
| | 418 | 0.030 | 0.023 | |
| | 515 | 0.051 | 0.049 | 0.043 |
| | 532 | 0.031 | 0.035 | 0.032 (0.033) |
| | 560 | 0.011 | | |
| | 784 | 0.004 | 0.003 | 0.002 |
| 136 | 559 | 0.008 | 0.007 | |
| 139 | 202 | | 0.012 | 0.009 |
| | 235 | 0.078 | 0.085 | 0.068 |
| | 252 | 0.35 | 0.25 | 0.29 |
| | 280 | 0.14 | 0.21 | |
| | 322 | 14.4 | 13.8 | 9.9 (12.7) |
| | 418 | 1.70 | 0.46 | 0.41 |
| | 420 | | 1.30 | 1.28 (1.20) |
| 139 | 532 | | 0.020 | |
| | 556 | 0.020 | 0.030 | |
| | 573 | 0.19 | 0.20 | 0.15 (0.18) |
| | 668 | 0.008 | 0.006 | 0.006 |
| | 710 | 0.016 | 0.014 | 0.016 |
| | 735 | 0.009 | 0.008 | 0.008 |
| 142 | 219 | 1.39 | 1.40 | 1.61 |
| | 299 | 1.30 | 1.45 | 1.61 |
| | 418 | 0.027 | | |
| | 525 | 0.12 | 0.14 | 0.13 |
| | 598 | 0.007 | 0.007 | 0.006 |
| 155 | 280 | 0.027 | | 0.031 |
| | 322 | 0.025 | 0.025 | 0.032 |
| | 377 | 0.031 | 0.025 | 0.030 |
| | 387 | 0.022 | 0.025 | 0.045 |
| | 418 | 0.018 | 0.015 | 0.019 |
| | 460 | 0.087 | 0.085 | 0.10 |
| | 484 | 0.050 | 0.052 | 0.051 |
| | 557 | 0.32 | 0.36 | 0.40 |
| 180 | 182 | 0.21 | 0.21 | 0.21 |
| | 235 | 0.024 | 0.031 | 0.010 |
| | 252 | 0.055 | 0.049 | 0.043 |

| $\gamma_i$ | $\gamma_j$ | $C_{ij}$ | $C_{ji}$ | $C_{expected}$ |
|---|---|---|---|---|
| 180 | 280 | 1.33 | 1.67 | 1.37 |
| | 377 | 0.17 | 0.080 | 0.079 |
| | 379 | | | 0.015 |
| | 418 | | 0.009 | |
| | 515 | 0.020 | 0.023 | 0.012 |
| | 532 | 0.072 | 0.11 | 0.092 |
| 181 | 559 | $0.007^{b)}$ | $0.009^{b)}$ | |
| 182 | 197 | 0.036 | 0.021 | 0.036 |
| | 333 | 0.014 | 0.015 | 0.015 |
| | 350 | 0.027 | 0.030 | 0.039 |
| 197 | 289 | 0.015 | 0.024 | 0.019 |
| | 362 | 0.027 | 0.056 | 0.040 |
| 202 | 219 | 0.020 | 0.028 | |
| | 357 | 0.036 | 0.071 | 0.029 |
| 219 | 338 | 0.014 | | |
| | 516 | 0.020 | 0.025 | |
| 219 | 299 | $3.92^{c)}$ | $3.96^{c)}$ | 3.75 (3.94) |
| | 441 | 1.90 | 2.11 | 2.32 |
| | 778 | 0.035 | 0.025 | 0.035 |
| 235 | 280 | 0.14 | 0.18 | 0.18 |
| | 289 | | 0.008 | 0.003 |
| 235 | 322 | 0.17 | 0.21 | 0.18 |
| | 387 | 0.17 | 0.23 | 0.18 |
| | 460 | 0.55 | 0.61 | 0.57 |
| 252 | 280 | 0.77 | 0.81 | 0.76 |
| | 289 | | 0.017 | 0.012 |
| | 322 | 0.66 | 0.70 | 0.77 |
| | 362 | | 0.030 | 0.024 |
| | 387 | 0.65 | 0.66 | 0.77 |
| | 460 | 2.02 | 2.47 | 2.41 |
| 280 | 414 | 0.015 | 0.020 | 0.017 |
| 289 | 333 | 0.018 | 0.013 | 0.011 |
| | 350 | 0.028 | 0.024 | 0.028 |
| | 378 | 0.010 | 0.010 | |
| | 512 | 0.004 | 0.005 | 0.006 |
| 290 | 559 | 0.008 | 0.008 | |
| 317 | 557 | 0.014 | 0.014 | |
| 322 | 414 | 0.021 | 0.021 | 0.016 |
| 333 | 362 | 0.020 | 0.028 | 0.023 |
| 338 | 358 | 0.017 | 0.020 | 0.012 |
| 350 | 362 | 0.045 | 0.066 | 0.060 |

| $\gamma_i$ | $\gamma_j$ | $C_{ij}$ | $C_{ji}$ | $C_{expected}$ | $\gamma_i$ | $\gamma_j$ | $C_{ij}$ | $C_{ji}$ | $C_{expected}$ |
|---|---|---|---|---|---|---|---|---|---|
| 358 | 516 | 0.031 | 0.025 | 0.025 | | | | | |
| 362 | 378 | 0.013 | 0.014 | | | | | | |
| | 512 | 0.008 | | 0.013 | | | | | |
| 387 | 414 | 0.018 | 0.013 | 0.017 | | | | | |
| 414 | 460 | 0.063 | 0.050 | 0.052 | | | | | |

[a] Normalized to $C_{ij}$ in order to estimate the x-ray fraction to be removed from the 73 keV peaks.

[b] Includes contribution of 0.003 due to 560-180 keV coincidences.

[c] Mean value of $C_{ij}$ and $C_{ji}$ normalized to $C_{expected}$ after correcting for angular correlation effects.

## TABLE 7.4

### Transitions in $^{193}$Ir Following the Decay of $^{193}$Os

| Transition Energy (keV) | Relative Intensity Photon | Total | Methods of Detection | Classification | $E_{calc}-E_{obs}$ |
|---|---|---|---|---|---|
| 63.28 ± 0.05 | 98 ± 9 | | γ | $K_{\alpha_2}$ | |
| 64.90 ± 0.05 | 160 ± 16 | | γ | $K_{\alpha_1}$ | |
| 73.58 ± 0.10 | 33 ± 5 | | γ | $K_{\beta_1} + K_{\beta_3}$ | |
| 75.63 ± 0.05 | 13 ± 2 | | γ | $K_{\beta_2} + K_{\beta_4}$ | |
| 41[a)] | | 1.9 ± 0.5 | γγ | 180.01 → 138.892 | |
| 73.012 ± 0.007 | 82 ± 12 | 626 ± 83 | γ, ce, γγ | 73.012 → 0 | 0 |
| 80.19[b)] | | | | 80.19 → 0 | |
| 96.82 ± 0.03 | 2.5 ± 0.2 | 19.2 ± 1.5 | γ, ce, γγ | 557.30 → 460.48 | 0 |
| 98.70 ± 0.08 | 0.42 ± 0.06 | 3.1[c)] | γ γγ | 460.48 → 361.81 | -0.03 |
| 106.993 ± 0.010 | 16.1 ± 0.8 | 96 ± 4 | γ, ce, γγ | 180.01 → 73.012 | 0 |
| 136 | 0.011 ± 0.003 | 0.039[c)] | γγ | 695.06 → 559.21 | |
| 138.892 ± 0.007 | 108 ± 5 | 353 ± 13 | γ, ce, γγ | 138.892 → 0 | 0 |
| 142.130 ± 0.008 | 1.9 ± 0.2 | 5.4 ± 0.7 | γ, ce, γγ | 740.20 → 598.04 | +0.03 |
| 154.74 ± 0.03 | 0.76 ± 0.11 | 2.1[c)] | γ, ce, γγ | 712.07 → 557.30 | +0.03 |
| 180.03 ± 0.03 | 4.6 ± 0.5 | 9.3 ± 0.8 | γ, ce, γγ | 180.01 → 0 | -0.02 |
| 181 | 0.008[d)] | | γγ | 740.20 → 559.21 | |
| 181.81 ± 0.03 | 4.9 ± 0.5 | 10.0 ± 0.9 | γ, ce, γγ | 361.81 → 180.01 | -0.01 |
| 197.4 ± 0.2 | 0.12 ± 0.04 | 0.23[c)] | γ γγ | 559.21 → 361.81 | 0 |
| 201.5 ± 0.3 | 0.07 ± 0.04 | 0.13[c)] | γ γγ | 559.21 → 357.7 | +0.01 |
| 219 | 0.22 ± 0.05 | 0.36[c)] | γγ | 357.7 → 138.892 | |
| 219.13 ± 0.05 | 7.0 ± 0.5 | 8.8 ± 0.5 | γ, ce, γγ | 299.32 → 80.19 | 0 |

| Transition Energy (keV) | Relative Intensity Photon | Total | Methods of Detection | Classification | $E_{calc}-E_{obs}$ |
|---|---|---|---|---|---|
| 234.58 ± 0.06 | 1.30 ± 0.17 | 1.9 ± 0.2 | γ, ce, γγ | 695.06 → 460.48 | 0 |
| 251.62 ± 0.04 | 5.5 ± 0.4 | 7.8 ± 0.5 | γ, ce, γγ | 712.07 → 460.48 | -0.03 |
| 280.43 ± 0.03 | 31.5 ± 1.6 | 41.8 ± 1.8 | γ, ce, γγ | 460.48 → 180.01 | +0.04 |
| 288.79 ± 0.05 | 3.6 ± 0.3 | 4.0 ± 0.3 | γ, ce, γγ | 361.81 → 73.012 | +0.01 |
| 290 | 0.012[d)] | | γγ | 848.84 → 559.21 | |
| 298.83 ± 0.05 | 4.7 ± 0.4 | 5.1 ± 0.4 | γ, ce, γγ | 598.04 → 299.32 | -0.11 |
| 317 | 0.026 ± 0.007 | | γγ | 874.36 → 557.30 | |
| 321.56 ± 0.03 | 32.3 ± 1.6 | 39.7 ± 1.7 | γ, ce, γγ | 460.48 → 138.892 | +0.03 |
| 333.3 ± 0.3 | 0.07 ± 0.04 | | γ γγ | 695.06 → 361.81 | -0.05 |
| 337.7 ± 0.5 | 0.03 ± 0.02 | | γ γγ | 695.06 → 357.7 | -0.34 |
| 350.2 ± 0.2 | 0.18 ± 0.06 | | γ γγ | 712.07 → 361.81 | +0.06 |
| 357.7 ± 0.2 | 0.25 ± 0.08 | | γ γγ | 357.7 → 0 | 0 |
| 361.81 ± 0.05 | 7.5 ± 0.6 | 8.8 ± 0.6 | γ, ce, γγ | 361.81 → 0 | 0 |
| 377.31 ± 0.07 | 1.8 ± 0.2 | | γ, ce, γγ | 557.30 → 180.01 | -0.02 |
| 378 | 0.041 ± 0.010 | | γγ | 740.20 → 361.81 | |
| 379.04 ± 0.15 | 0.35 ± 0.09 | | γ γγ | 559.21 → 180.01 | +0.16 |
| 387.46 ± 0.04 | 31.9 ± 1.6 | 36.3 ± 1.6 | γ, ce, γγ | 460.48 → 73.012 | +0.01 |
| 413.8 ± 0.2 | 0.12 ± 0.04 | | γ γγ | 874.36 → 460.48 | +0.08 |
| 418 | 0.18 ± 0.04 | | γγ | 598.04 → 180.01 | |
| 418.35 ± 0.08 | 1.38 ± 0.14 | 1.43 ± 0.14 | γ, ce, γγ | 557.30 → 138.892 | +0.06 |
| 420.30 ± 0.05 | 4.2 ± 0.3 | 4.7 ± 0.3 | γ, ce, γγ | 559.21 → 138.892 | +0.02 |
| 440.95 ± 0.05 | 2.32 ± 0.16 | 2.53 ± 0.16 | γ, ce, γγ | 740.20 → 299.32 | -0.07 |
| 460.49 ± 0.03 | 100 ± 5 | 108 ± 5 | γ, ce, γγ | 460.48 → 0 | -0.01 |

| Transition Energy (keV) | Relative Intensity Photon | Relative Intensity Total | Methods of Detection | Classification | $E_{calc} - E_{obs}$ |
|---|---|---|---|---|---|
| 484.25 ± 0.05 | 4.3 ± 0.3 | 4.6 ± 0.3 | γ, ce, γγ | 557.30 → 73.012 | +0.04 |
| 486.11 ± 0.15 | 0.29 ± 0.14 | | γ γγ | 559.21 → 73.012 | +0.09 |
| 512.3 ± 0.3 | 0.04 ± 0.02 | | γ γγ | 874.36 → 361.81 | +0.25 |
| 514.95 ± 0.10 | 0.28 ± 0.05 | | γ γγ | 695.06 → 180.01 | +0.10 |
| 516.3 ± 0.4 | 0.06 ± 0.03 | | γ γγ | 874.36 → 357.7 | +0.36 |
| 524.98 ± 0.08 | 0.40 ± 0.04 | | γ γγ | 598.04 → 73.012 | +0.05 |
| 532.02 ± 0.05 | 2.10 ± 0.15 | | γ γγ | 712.07 → 180.01 | +0.04 |
| 556 | 0.08 ± 0.02 | | γγ | 695.06 → 138.892 | |
| 557.36 ± 0.08 | 33 ± 3 | 35 ± 3 | γ, ce, γγ | 557.30 → 0 | -0.06 |
| 559.26 ± 0.08 | 12.3 ± 1.2 | 12.9 ± 1.2 | γ, ce, γγ | 559.21 → 0 | -0.05 |
| 560 | 0.07 ± 0.02 | | γγ | 740.20 → 180.01 | |
| 573.33 ± 0.10 | 0.49 ± 0.05 | | γ γγ | 712.07 → 138.892 | -0.15 |
| 598.1 ± 0.3 | 0.017 ± 0.008 | | γ γγ | 598.04 → 0 | -0.06 |
| 639.09 ± 0.10 | 0.19 ± 0.03 | | γ γγ | 712.07 → 73.012 | -0.03 |
| 668.3 ± 0.3 | 0.019 ± 0.009 | | γ γγ | probably 807.2 → 138.892 | |
| 695.12 ± 0.10 | 0.072 ± 0.014 | | γ | 695.06 → 0 | -0.06 |
| 709.93 ± 0.15 | 0.052 ± 0.013 | | γ γγ | 848.84 → 138.892 | +0.02 |
| 712.10 ± 0.10 | 0.39 ± 0.06 | | γ | 712.07 → 0 | -0.03 |
| 735.3 ± 0.3 | 0.027 ± 0.007 | | γ γγ | 874.36 → 138.892 | +0.17 |
| 775.9 ± 0.3 | 0.010 ± 0.005 | | γ | 848.84 → 73.012 | -0.07 |
| 778.48 ± 0.15 | 0.042 ± 0.009 | | γ γγ | 1077.8 → 299.32 | 0 |
| 784.2 ± 0.2 | 0.017 ± 0.004 | | γ γγ | 964.27 → 180.01 | +0.06 |

| Transition Energy (keV) | Relative Intensity | | Methods of Detection | | Classification | $E_{calc}-E_{obs}$ |
|---|---|---|---|---|---|---|
| | Photon | Total | | | | |
| 800.9 ± 0.3 | 0.008 ± 0.004 | | γ | | 874.36 → 73.012 | +0.45 |
| 848.85 ± 0.15 | 0.11 ± 0.02 | | γ | | 848.84 → 0 | -0.01 |
| 874.36 ± 0.15 | 0.48 ± 0.07 | | γ | | 874.36 → 0 | 0 |
| 891.26 ± 0.15 | 0.072 ± 0.011 | | γ | γγ | 964.27 → 73.012 | 0 |

[a] Not directly observed.

[b] The 80.19 keV transition depopulates the 11.9 day isomer at 80.19 keV.

[c] M1 transition assumed.

[d] At limit of detection.

to this cascade. The $\gamma$-$\gamma$ angular correlation functions for several of the stronger cascades have been determined (Avida et al (1968)) and were used to correct the $C_{ij}$ values expected from the decay scheme, whenever possible. These values are shown in brackets along with the uncorrected values. It is seen that the agreement between the expected values when corrected in this manner and the experimental values is much better.

Table 7.4 presents a summary of the transitions in $^{193}$Ir following the beta decay of $^{193}$Os. The first column shows the adopted energy values. The next two columns indicate the photon and total transition intensities. The latter were deduced from the conversion and photon data with due allowance for undetected conversion electron groups. The fourth column indicates the ways in which the transition was observed; i.e. whether in direct, internal conversion, or $\gamma$-$\gamma$ measurements. The final columns of the table give the classification of the line in the decay scheme and the differences in keV between the values calculated from the decay scheme and the experimental values.

## 7.5 The Coulomb Excitation Results

Coulomb excitation measurements were performed with a thin window Ortec detector of 16 mm diameter x 5.5 mm depth placed at an angle of 125° with respect to the beam direction. The target consisted of metallic iridium enriched to 98.0% in $^{193}$Ir which was compressed and mounted on a lead backing. Oxygen ions from the McMaster University

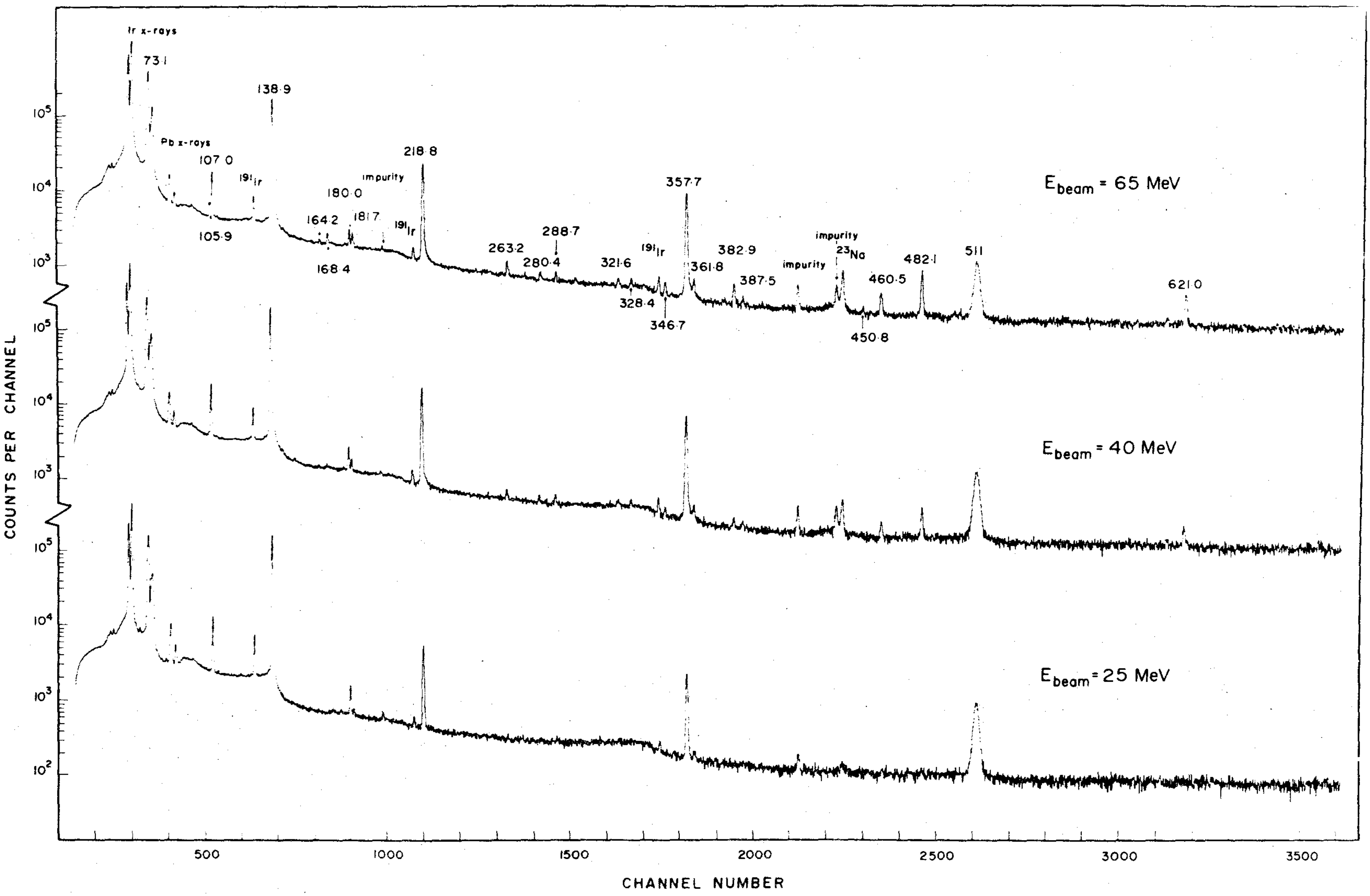

**Figure 7.12** Coulomb excitation spectrum of $^{193}$Ir obtained with 25, 40 and 65 MeV oxygen beams.

## TABLE 7.5

### Transitions Following Coulomb Excitation of $^{193}$Ir

| Transition Energy (keV) | | | |
|---|---|---|---|
| 25 MeV | 40 MeV | 65 MeV | Classification |
| 73.0 | 73.1 | 73.1 | 73.013→0 |
| 107.0 | 107.0 | 107.0 | 180.01 →73.012 |
| 138.9 | 138.9 | 138.9 | 138.892→0 |
| | | 164.2 | 521.8 →357.7 |
| 180.0 | 180.0 | 180.0 | 180.01 →0 |
| 181.8 | 181.7 | 181.7 | 361.81 →180.01 |
| 218.8 | 218.8 | 218.8 | 357.7 →138.892 |
| | 263.2 | 263.2 | 621.0 →357.7 |
| | 280.2 | 280.5 | 460.48 →180.01 |
| | 288.8 | 288.7 | 361.81 →73.012 |
| | 321.7 | 321.6 | 460.48 →138.892 |
| 357.8 | 357.7 | 357.7 | 357.7 →0 |
| 361.7 | 361.8 | 361.8 | 361.81 →0 |
| | 382.8 | 382.9 | 521.8 →138.892 |
| | 387.5 | 387.6 | 460.48 →73.012 |
| | 460.6 | 460.5 | 460.48 →0 |
| | 482.0 | 482.1 | 621.0 →138.892 |
| | 620.8 | 621.1 | 621.0 →0 |
| | | 105.9 | unclassified |
| | | 168.4 | |
| | 328.5 | 328.3 | |
| | 346.6 | 346.7 | |
| | | 450.8 | |

model FN tandem Van de Graaff accelerator were used to bombard the target using beam energies of 25, 40, 55 and 65 MeV.

The Coulomb excitation spectra recorded with the 25, 40 and 65 MeV bombarding energies are shown in Fig. 7.12. Transitions arising from the higher-lying levels are seen to increase in yield as the bombarding energy is increased. The results of the Coulomb excitation experiments are presented in table 7.5. The first three columns indicate those transitions observed using 25, 40 and 65 MeV oxygen beams while the remaining column gives the classification of the transition in the level scheme of $^{193}$Ir. Several lines of unknown origin are also included in table 7.5.

It is noticed that, although all the known positive parity levels below 500 keV are populated in the Coulomb excitation process, the 142 and 299 keV transitions are absent (the 219 keV transition being masked) from the spectra. This provides additional evidence that the 142-299-219 keV cascade decays into the $11/2^-$ 80 keV isomer.

## 7.6 The Level Structure of $^{193}$Ir

The results of the present measurements are summarized in the decay scheme of Fig. 7.13 which shows the transitions which are securely established. The dashed levels at 521.8 and 621.0 keV indicate levels which are populated only in the Coulomb excitation process. The energy and total intensity is shown for each transition and a dot used to indicate those transitions which produce observable coincidences. The beta intensities and log $f_ot$ values shown on the decay scheme have been deduced from the transition intensities assuming that the absolute

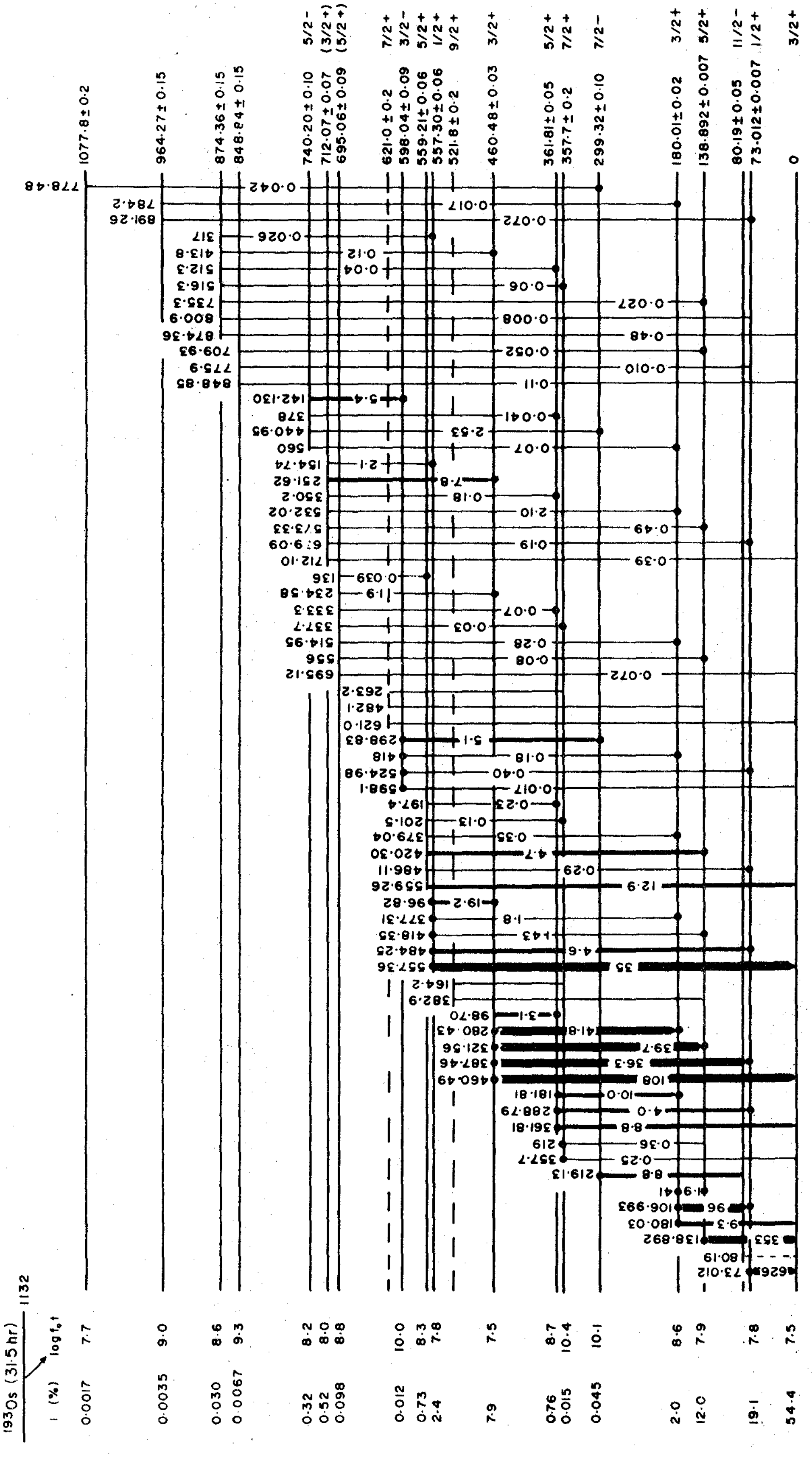

Figure 7.13 Level structure of $^{193}$Ir

intensity of the 460 keV gamma ray is 3.95% (Price et al (1969)) and that the total decay energy is 1132 keV (Nablo et al (1958)).

A discussion of the spins, parities and level assignments follows. Conclusions based upon the reaction data will be freely quoted whenever necessary although the evidence for these conclusions is deferred until chapter X.

The ground state of $^{193}$Ir has been measured to have spin $3/2^+$ (Marakawa and Suwa (1952)) and is generally assigned to either the $d_{3/2}$ shell state or the $3/2^+$ [402] orbital. The reaction data to be presented later indicate that the extreme single-particle model is not valid for the iridium isotopes; rather the shell model strength is fragmented into states which apparently obey a Nilsson description. These data establish the ground state as the $3/2^+$ [402] orbital with the $5/2^+$ and $7/2^+$ band members at 139 and 358 keV respectively. The $5/2^+$ and $7/2^+$ members of this ground state band are also observed in Coulomb excitation.

Mossbauer experiments (Atzmony et al (1967)) have conclusively established the spin of the 73 keV level to be $1/2^+$. The reaction data indicate that this state is a mixture of the $K = K_o - 2$ gamma vibration and the $1/2^+$ [400] orbital.

With the spins of the 0, 73 and 139 keV levels assigned the values of $3/2^+$, $1/2^+$ and $5/2^+$ respectively, the presence of strong first forbidden beta feeds to all these levels leads to a $3/2^-$ assignment for the ground state of $^{193}$Os. The Nilsson model suggests that it is the $3/2^-$ [512] state.

Population of the 522 keV state in Coulomb excitation indicates that its wave function strongly resembles the ground state wave function. Since the state exhibits branching only to the $5/2^+$ and $7/2^+$ members of the ground state band, it can be uniquely assigned as the $9/2^+$ member of the ground state band. This state, as well as the $11/2^+$ member, has recently been identified in inelastic deuteron scattering measurements (Norgaard et al (1971)).

The 362 keV state is found to have spin $5/2^+$ from the E2 radiation feeding the 73 keV $(1/2^+)$ level. Furthermore, the mixed character of the radiations in the 362 $(5/2^+) \rightarrow 180 \rightarrow 73$ $(1/2^+)$ cascade demands a $3/2^+$ spin assignment for the 180 keV level. The reaction data indicate that these states form the $3/2^+$ and $5/2^+$ members of the combined $K = K_o - 2$ gamma vibrational and $1/2^+$ [400] band. This interpretation is supported by the relatively large Coulomb excitation probabilities observed for these states.

The collective nature of the 621 keV state is established from Coulomb excitation with the spin of the state being restricted to values of $3/2^+$, $5/2^+$ or $7/2^+$. The $7/2^+$ spin value is highly favoured since this state would be populated in the beta decay process if either of the other spin choices were made. Moreover the state branches only to the $3/2^+$, $5/2^+$ and $7/2^+$ members of the $K = 3/2^+$ ground state band, with branching to the $1/2^+$ [400] $K = 1/2^+$ band conspicuously absent. Therefore the state receives a $K = 7/2^+$ assignment which, together with its collective nature, indicates that it forms the $K = K_o + 2$ gamma vibrational member of the ground state.

This state and a similar interpretation is obtained from the inelastic deuteron scattering measurements of Norgaard et al (1971).

The spin of the 460 keV level is confirmed to be $3/2^+$ by the observation of M1 + E2 transitions from this state deexciting to each of the 139 keV ($5/2^+$), 73 keV ($1/2^+$) and 0 keV ($3/2^+$) levels. The spin of the 557 keV level appears to be $1/2^+$ from the deexcitation pattern of the gamma rays since strong branching occurs to the 73 keV ($1/2^+$) and 0 keV ($3/2^+$) levels while the 139 keV ($5/2^+$) level is only weakly populated. This assignment is supported by the internal conversion data which indicate that the 418 keV transition feeding the 139 keV ($5/2^+$) level is E2 in character and that the 484 keV transition feeding the 73 keV ($1/2^+$) level possesses the pure M1 multipolarity required of $1/2 \rightarrow 1/2$ transitions. These levels are not populated in the reaction studies and it is suggested that the states are the $3/2^+$ and $1/2^+$ band members of the $1/2^+$ [411] hole state. This band is expected to show inverted level ordering and has been identified in the neighbouring rhenium isotopes. If the assignment is valid, then we may expect to observe the same pair of states at slightly higher excitation energy in $^{191}$Ir since this nucleus is somewhat more deformed and the position of the $1/2^+$ [411] orbital decreases with increasing deformation.

The 559 keV state is assigned a spin of $5/2^+$ since it exhibits intense branching to the 139 keV ($5/2^+$) and 0 keV ($3/2^+$) levels, but negligible branching to the 73 keV ($1/2^+$) level. Both the internal conversion and reaction data agree with this assignment, although these data cannot exclude the $3/2^+$ possibility. The reaction data indicate that this state is likely the $5/2^+$ [402] hole state.

Spins of $5/2^+$ and $3/2^+$ are tentatively assigned to the 695 and 712 keV levels based upon their observed modes of decay. The 695 keV level deexcites to all $3/2^+$, $5/2^+$ and $7/2^+$ low-lying states but not to the $1/2^+$ state. On the other hand, the 712 keV level is depopulated by fairly strong transitions to all the $1/2^+$, $3/2^+$ and $5/2^+$ low-lying states but not to the $7/2^+$ state.

The observed M4 multipolarity of the 80 keV transition makes a spin assignment of $11/2^-$ mandatory for the isomeric state (Boehm and Marmier (1957)). The reaction data indicate this state may be the $11/2^-$ [505] particle state.

The spin of the 299 keV level is required to be $7/2^-$ from the E2 character of the 219 keV radiation and this assignment is supported by the reaction data, which indicate that this level has $\ell = 3$ transfer. The E2 character of the 299 keV gamma ray then demands that the 598 keV level has spin $3/2^-$. Note that increasing the spin of this level by one unit would require an M2 transition to favourly compete with E1 transitions. The mixed character of the 142 and 441 keV transitions feeding these $3/2^-$ and $7/2^-$ states indicates a $5/2^-$ spin assignment for the 740 keV state. Therefore the spins for the sequence of levels at 299, 598 and 740 keV are uniquely determined to be $7/2^-$, $3/2^-$ and $5/2^-$ respectively.

It is interesting to notice that the negative parity states at 299, 598 and 740 keV, along with the 80 keV isomeric state, form an independent set of levels in which very little interaction is observed with the remainder of the decay scheme. It is also noticed in this connection that the log $f_o t$ value for the allowed beta feed to the 598 keV level is extremely large, being >10. These considerations suggest that the negative parity states exhibit some form of shape dependence which retards the beta transitions into these states and also the electromagnetic transitions from these to the positive parity states. These levels will be discussed in more detail in chapter X.

# CHAPTER VIII

# THE DECAY OF $^{191}$Pt

## 8.1 Previous and Concurrent Work

The present investigation of the decay of $^{191}$Pt→$^{191}$Ir was prompted by the interesting results obtained from studying the level structure of $^{193}$Ir. In particular, it was wondered if the peculiar subsystem of levels and the doublet structure of some of the levels observed in $^{193}$Ir would reappear in $^{191}$Ir which, possessing two less neutrons, is expected to be slightly more deformed.

Prior to the start of this work the results of several investigations of the $^{191}$Pt decay, carried out in the early days of Ge(Li) detectors, had been published (Harmatz et al (1962), Blichert-Toft et al (1966) and Schumacker et al (1966)). In addition, Schumacker and Langhoff (1967) had examined the 588 keV level by exciting it through nuclear resonance fluorescence.

Midway through the present investigation, work by the Swedish group of Malmskog et al (1970) appeared and removed many of the earlier conflicting assignments. The present work confirms the level scheme of $^{191}$Ir proposed by these authors, but extends it through the establishment of several new levels and the observation of many new transitions.

Late in 1970, the work of Backlin et al (1970) on the negative parity states in $^{189}$Ir, $^{191}$Ir and $^{193}$Ir appeared. The portion of this paper dealing with $^{193}$Ir has already been referred to. They limited their comments concerning $^{191}$Ir to the 268-220 keV cascade which is analogous to the 299-219 cascade in $^{193}$Ir discussed in the last chapter, and established that the intensity of the 171 keV isomeric transition in $^{191}$Ir is consistent with the assumption that the 268-219 keV cascade feeds the isomer. In addition, they employed the delayed electron-electron coincidence technique to show that the 268 keV transition precedes the 220 keV gamma ray in the cascade.

The gamma ray, $\gamma$-$\gamma$ coincidence and reaction data obtained in the present investigation support their conclusions and extend their conclusions concerning these negative parity states by showing that there is in reality a 141-268-220 triple cascade in complete analogy with the situation in $^{193}$Ir.

## 8.2 The Direct Gamma Ray Results

The direct gamma ray measurements presented in this section were obtained using the same equipment and procedures as used for the measurements of section 7.2. A spectrum taken with the thin window Ortec detector is shown in Fig. 8.1. The upper portion of the spectrum was recorded without abosrber using a source which had been enriched to 0.76% $^{190}$Pt. The x-rays and gamma rays from other platinum isotopes and their daughters are quite prominent. Also present is a substantial amount of $^{192}$Ir impurity. The remaining portions of the spectrum were taken with a 2 mm lead-cadmium-copper absorber using a source of lower (0.40% $^{190}$Pt) enrichment. The lower enrichment sources exhibit only slight traces of the $^{192}$Ir contaminent but contain appreciable $^{46}$Sc impurity which is responsible for the high energy Compton edge appearing in Fig. 8.1. A portion of the 129 keV line is due to the $^{195}$Pt decay and the quoted intensity of this line has been corrected accordingly. The 209 keV line is partly obscured by the $^{199}$Au 208 keV transition. Although a transition of 411 keV is assigned to the decay scheme, the weak line appearing at 412 keV likely results from the $^{198}$Au decay since its intensity apparently changes when sources of differing enrichments are used. The 511 keV peak arises from annihilation radiation associated with weak positron emission in either $^{191}$Pt or impurity nuclei. The weak peaks have been expanded and shown separately in the inserts.

Measurements were taken using various solid angles to insure that coincidence summing effects were not significant. These measurements indicated that only with the largest detector in the closest geometry were such effects observable, as evidenced by the occurence of a 488 keV peak resulting from the intense 268-220 keV cascade.

The results of the gamma ray energy measurements are displayed in table 8.1. The first column shows the energies obtained from the Chalk River $\pi\sqrt{2}$ spectrometer while the second column presents the weighted mean of the energies derived from various Ge(Li) detectors. Agreement between the two sets of measurements is excellent although each set has been obtained independently of the other.

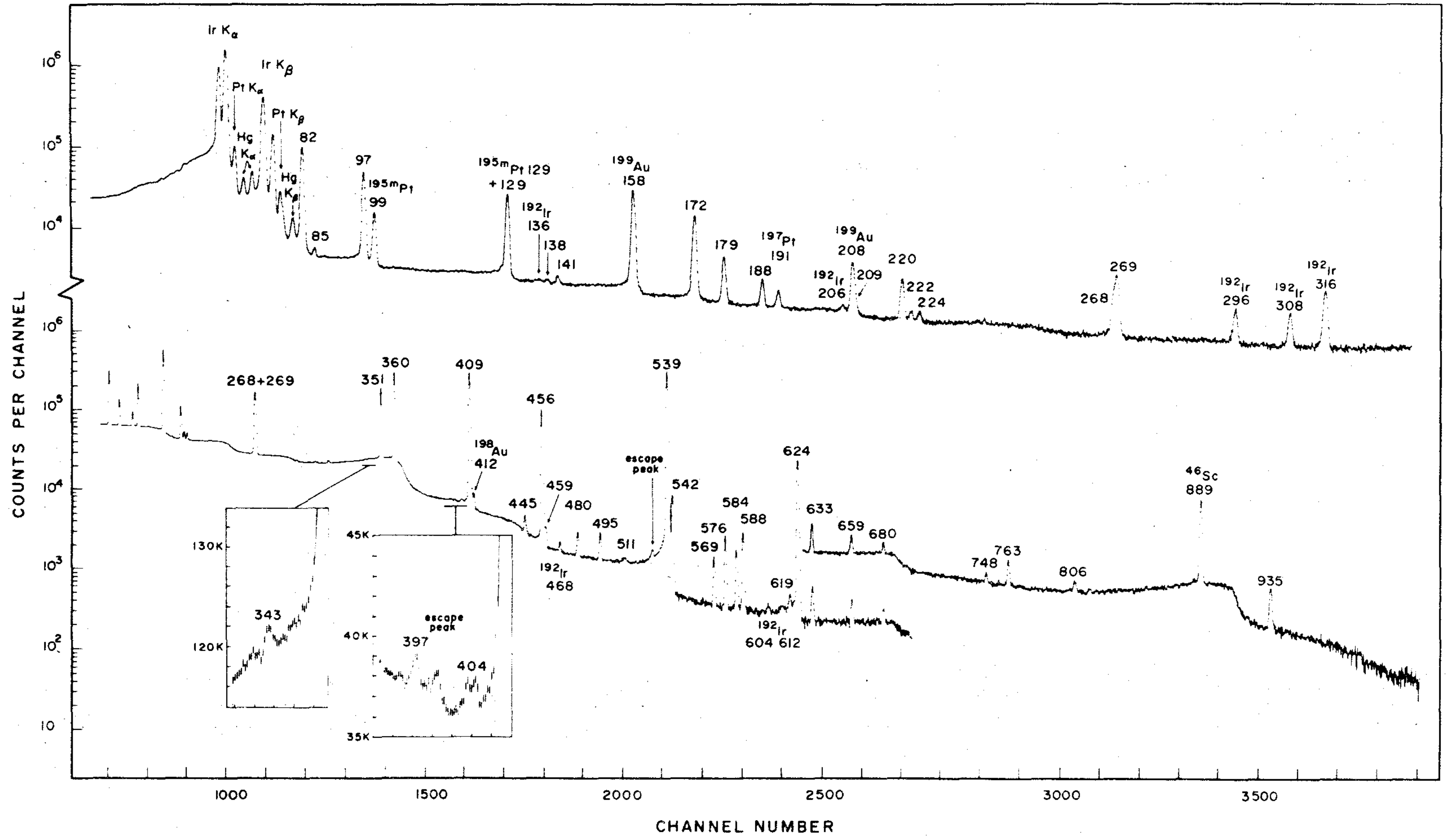

Figure 8.1 The gamma ray spectrum of $^{191}$Pt. The upper spectrum was recorded without absorber while the lower were taken with a 2 mm lead absorber.

## TABLE 8.1

## $^{191}$Ir Gamma Ray Energies

| $\pi\sqrt{2}$ Energy (keV) | Ge(Li) Energy (keV) |
|---|---|
| 82.398 ± 0.007 | 82.40 ± 0.05 |
| | 85.15 ± 0.08 |
| 96.517 ± 0.009 | 96.53 ± 0.05 |
| 129.400 ± 0.007 | 129.39 ± 0.04 |
| | 138.2 ± 0.2 |
| 140.884 ± 0.015 | 140.86 ± 0.08 |
| 172.19 ± 0.02 | 172.21 ± 0.05 |
| 178.96 ± 0.03 | 178.96 ± 0.05 |
| 187.68 ± 0.04 | 187.70 ± 0.05 |
| | 208.96 ± 0.15 |
| | 219.65 ± 0.05 |
| | 221.74 ± 0.08 |
| 223.65 ± 0.10 | 223.67 ± 0.08 |
| 267.91 ± 0.08 | 267.96 ± 0.10 |
| 268.68 ± 0.08 | 268.75 ± 0.08 |
| | 343.2 ± 0.2 |
| 351.17 ± 0.03 | 351.16 ± 0.05 |
| 359.88 ± 0.03 | 359.90 ± 0.05 |
| | 396.7 ± 0.2 |
| | 404.1 ± 0.3 |
| 409.42 ± 0.03 | 409.46 ± 0.02 |
| | 445.13 ± 0.08 |
| 456.44 ± 0.05 | 456.50 ± 0.05 |
| | 458.59 ± 0.15 |
| | 479.95 ± 0.07 |
| | 494.69 ± 0.07 |
| 538.86 ± 0.05 | 538.89 ± 0.05 |
| | 541.64 ± 0.10 |
| | 568.81 ± 0.08 |
| | 576.46 ± 0.08 |
| | 583.61 ± 0.08 |
| | 587.95 ± 0.08 |
| | 618.7 ± 0.4 |
| | 624.06 ± 0.06 |
| | 633.18 ± 0.10 |
| | 658.75 ± 0.15 |
| | 680.0 ± 0.2 |
| | 748.0 ± 0.2 |
| | 762.60 ± 0.15 |
| | 806.4 ± 0.3 |
| | 935.33 ± 0.15 |

The gamma ray intensities are presented in column 2 of table 8.4 and are normalized to a value of 100 for the 409 keV transition. The uncertainties in the energy and intensity measurements have been deduced in the same manner and with approximately the same precision as the results of section 7.2.

## 8.3 The Internal Conversion Results

Figs. 8.2, 8.3 and 8.4 show spectra obtained from a series of sources with the Chalk River $\pi\sqrt{2}$ spectrometer. The peaks recorded with each source were measured relative to either the K conversion line of the 409 keV transition or the L lines of the 97 keV transition.

Precise values of the mixing ratios were obtained for the 82, 97 and 172 keV transitions from the L subshell ratios. The relation between the photon and conversion electron intensity scales was established using the conversion coefficients derived from the mixing ratios of the 97 and 172 keV transitions.

A summary of the internal conversion results is shown in table 8.2. The first six columns denote the transition energy and present the measured photon and electron intensities. All values are relative to the 409 keV photon intensity. The errors associated with the electron intensities represent only the statistical uncertainties as discussed in section 7.3. The final columns of the table indicate the transition multipolarities and E2 admixtures.

Most of the transitions are observed to be predominantly M1

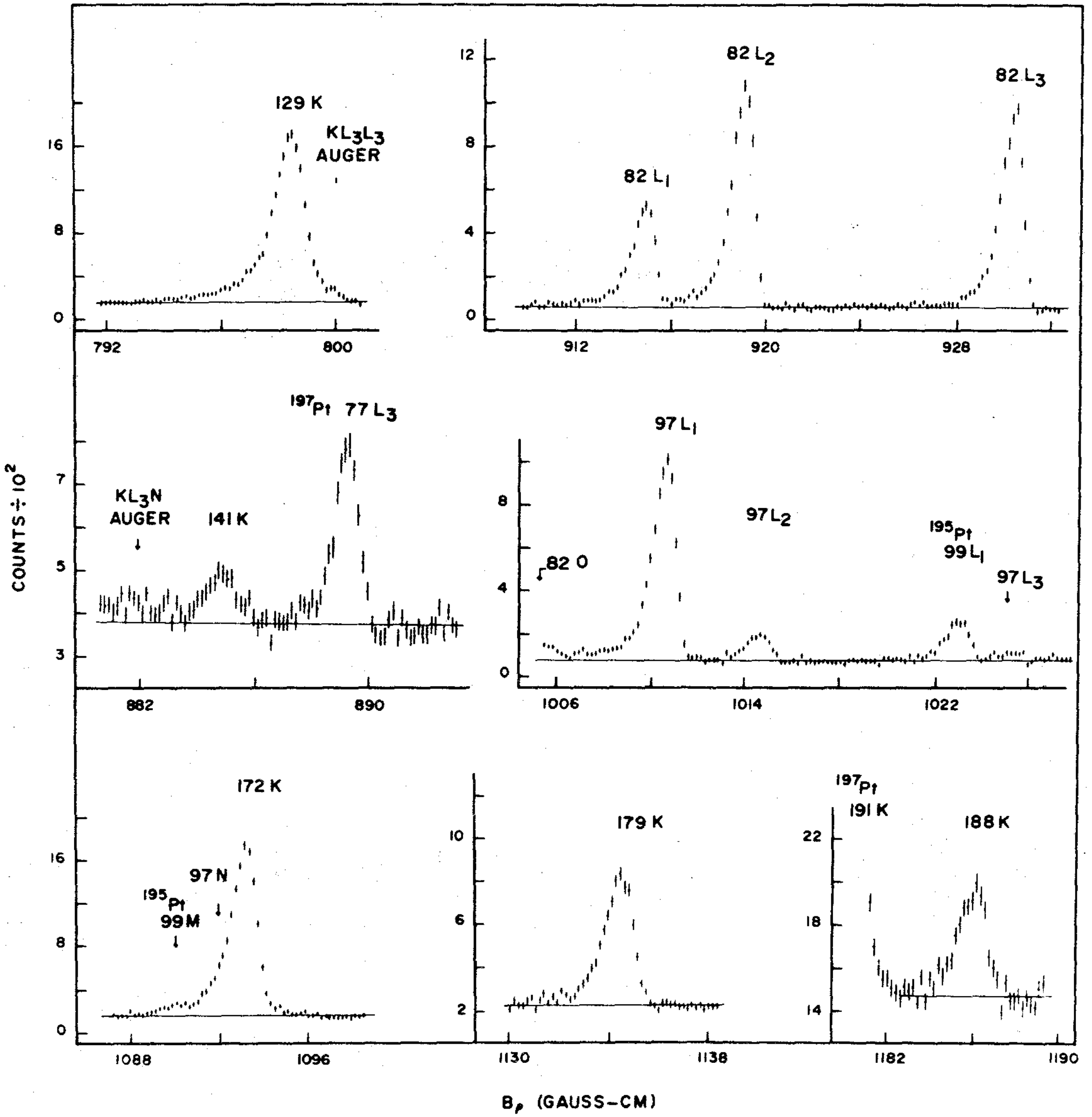

Figure 8.2 Portions of the internal conversion spectrum of $^{191}$Pt showing the momentum region below 1300 G cm.

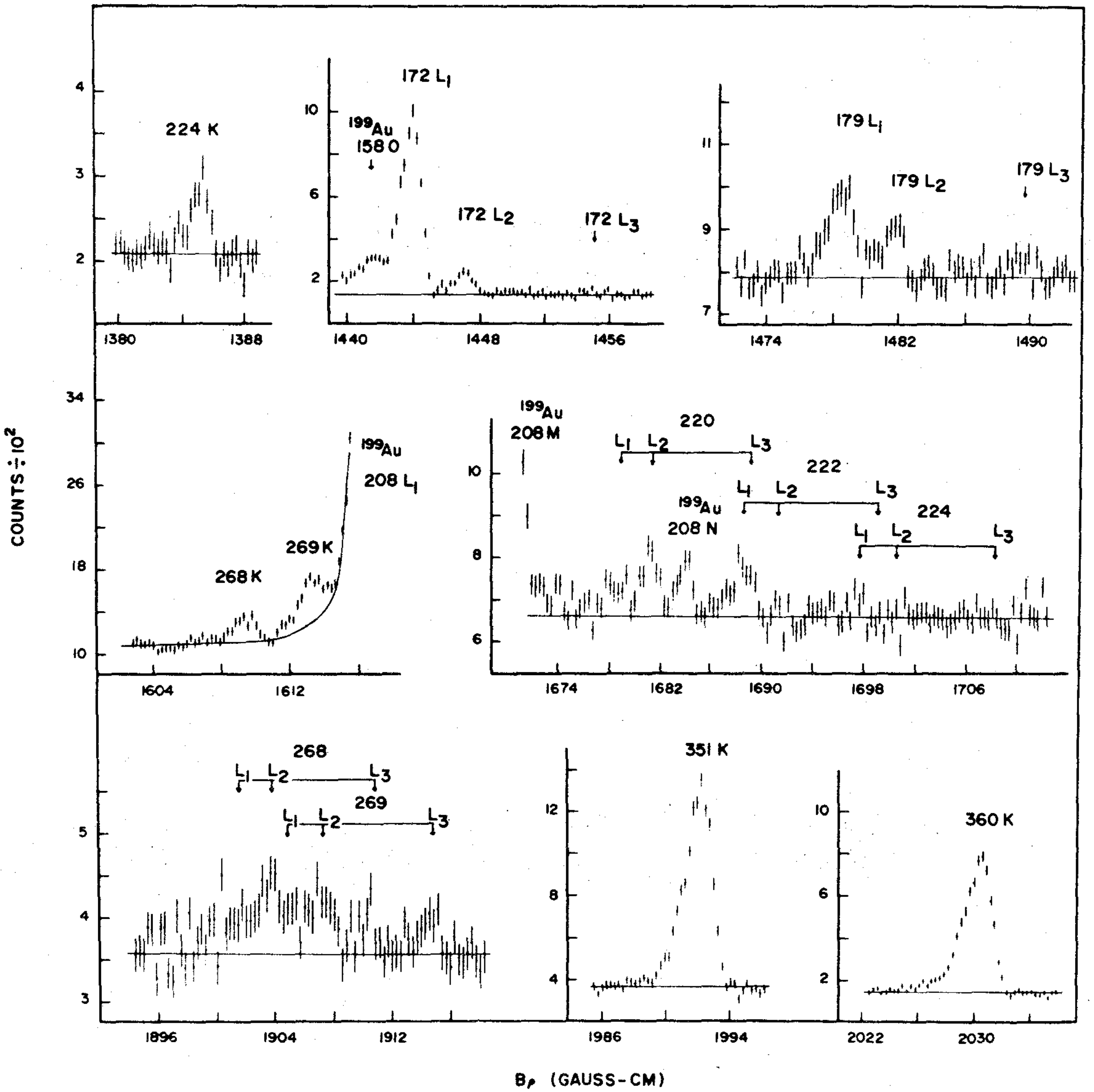

Figure 8.3 Portions of the internal conversion spectrum of $^{191}$Pt showing the momentum region between 1300 and 2100 G cm.

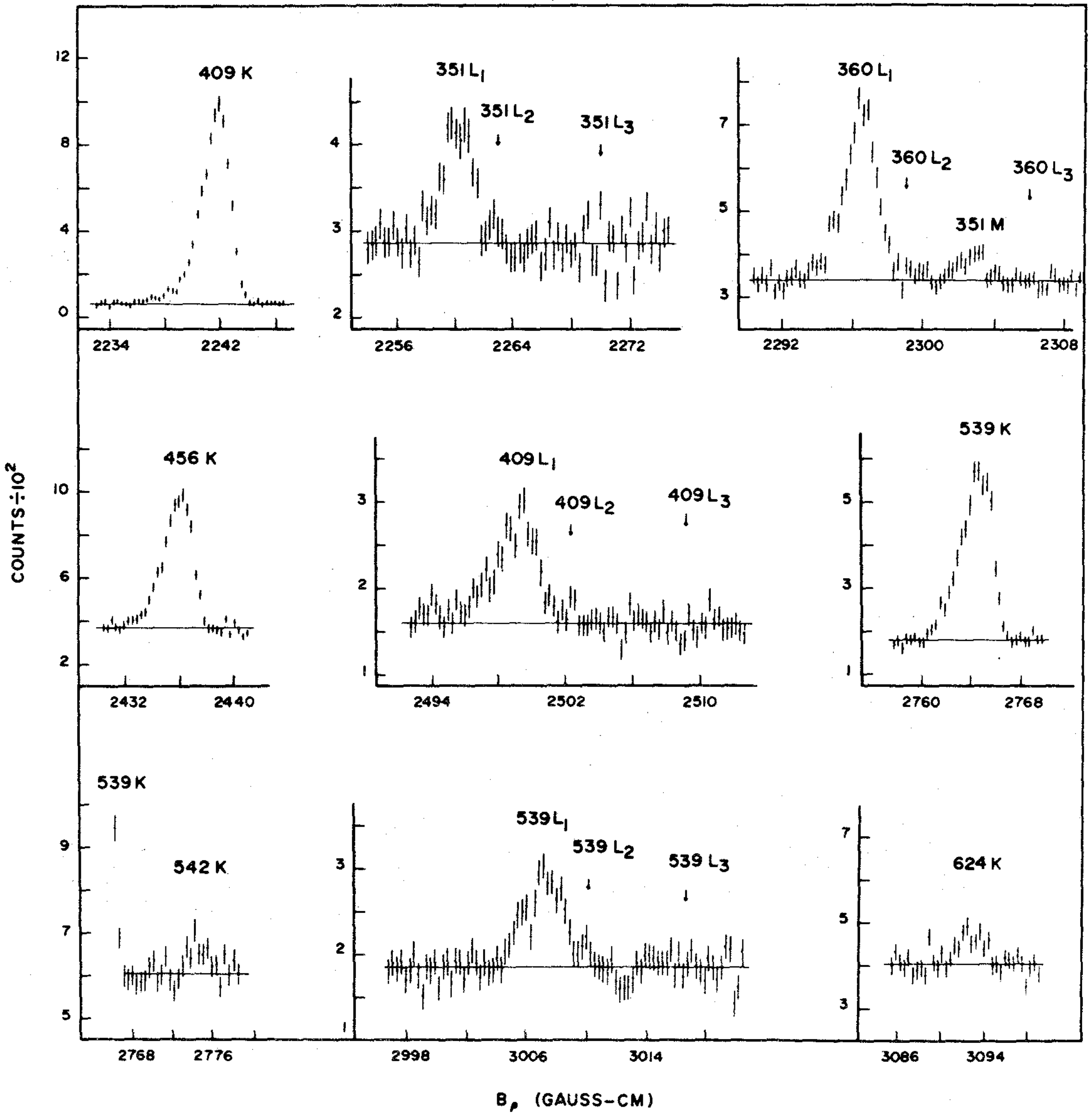

Figure 8.4 Portions of the internal conversion spectrum of $^{191}$Pt showing the momentum region above 2100 G cm.

TABLE 8.2

## $^{191}$Ir Internal Conversion Intensities and Multipole Assignments

| Transition (keV) | Intensity | | | | | Multipolarity | %E2 |
|---|---|---|---|---|---|---|---|
| | Photon | K | $L_1$ | $L_2$ | $L_3$ | | |
| 82 | 61 ± 6 | | 48.9 ± 1.4 | 96.7 ± 1.5 | 89.0 ± 1.4 | M1 + E2 | 41.3 ± 1.0 |
| 97 | 41 ± 2 | | 35.6 ± 0.5 | 4.7 ± 0.3 | 1.8 ± 0.2 | M1 + E2 | 1.7 ± 0.3 |
| 129 | 40 ± 4 | 83 ± 2 | | | | M1 + E2 | 19 ± 11 |
| 141 | 0.94 ± 0.14 | 1.6 ± 0.4 | | | | M1 + E2 | < 50 |
| 172 | 44 ± 2 | 46.6 ± 0.9 | 7.00 ± 0.11 | 0.68 ± 0.07 | 0.06 ± 0.05 | M1 + E2 | 0.5 ± 0.5 |
| 179 | 12.7 ± 0.6 | 8.6 ± 0.2 | 1.68 ± 0.14 | 0.75 ± 0.13 | 0.17 ± 0.13 | M1 + E2 | 37 ± 5 |
| 188 | 5.2 ± 0.3 | 3.6 ± 0.2 | 0.91 ± 0.18 | 0.31 ± 0.18 | | M1 + E2 | < 36 |
| 220 | 10.3 ± 0.5 | | 0.25 ± 0.05 | 0.39 ± 0.05 | 0.41 ± 0.07 | E2 | > 92 |
| 224 | 1.40 ± 0.15 | 0.63 ± 0.08 | 0.05 ± 0.04 | < 0.03 | < 0.03 | M1 + E2 | < 30 |
| 268 | 9.7 ± 1.0 | 0.93 ± 0.10 | 0.31 ± 0.15 | 0.27 ± 0.15 | 0.16 ± 0.06 | E2 | > 90 |
| 269 | 20.6 ± 2.0 | 1.8 ± 0.5 | 0.27 ± 0.15 | 0.39 ± 0.06 | 0.15 ± 0.06 | E2 | > 90 |
| 351 | 42 ± 2 | 6.79 ± 0.16 | 1.11 ± 0.08 | < 0.10 | < 0.03 | M1 + E2 | < 6 |
| 360 | 75 ± 4 | 12.9 ± 0.3 | 1.86 ± 0.05 | 0.10 ± 0.03 | < 0.03 | M1 + E2 | < 4 |
| 409 | 100 ± 5 | 11.24 ± 0.15 | 1.87 ± 0.12 | 0.19 ± 0.09 | < 0.04 | M1 + E2 | < 6 |
| 456 | 42 ± 2 | 2.93 ± 0.09 | 0.36 ± 0.09 | | | M1 + E2 | 15 ± 11 |
| 539 | 171 ± 9 | 7.2 ± 0.2 | 1.15 ± 0.09 | < 0.12 | < 0.12 | M1 + E2 | 20 ± 10 |
| 542 | 4.6 ± 0.5 | 0.21 ± 0.05 | | | | M1 + E2 | < 40 |
| 624 | 17.6 ± 0.9 | 0.46 ± 0.08 | | | | M1 + E2 | 35 ± 21 |

in character with small E2 admixtures. The 82 and 179 keV transitions seem to have abnormally large E2 mixtures, possibly indicating a highly collective character for these states. The 220, 268 and 269 keV transitions are apparently pure E2 in character.

## 8.4 The Gamma-Gamma Coincidence Results

The two-parameter gamma-gamma coincidence arrangement has already been discussed. For the present experiment, a thin layer of cadmium was placed in front of each detector to attenuate the intense x-ray radiation arising from the electron capture process. Samples containing an enrichment of 0.40% $^{190}$Pt were used and 9.12 x $10^6$ coincidence events accumulated with an average (true + chance)/chance rate of 39.9/1. Fig. 8.5 shows the projection of the coincidence events on the 1024 channel axis after removal of chance. The gates used for analysis of the data are indicated by the markings beneath the peak labels. A selection of the large amount of coincidence data is presented in Figs. 8.6 to 8.11 together with appropriate portions of the decay scheme. This selection will serve to justify the decay scheme proposed.

### The 82 keV Level

The 82 keV state is fed, either directly or indirectly, by the gamma rays which appear both in the spectrum and the insert of Fig. 8.6a. Confirmation of this portion of the decay scheme is to be found in the spectra in coincidence with the gates of Figs. 8.6c, 8.7a, 8.7d, 8.8d, 8.9d, 8.10e, 8.11e and 8.11f. In addition a gate set on the weak 680 keV gamma ray (Fig. 8.11d) indicates that this transition also feeds the 82 keV level.

## The 129 keV Level

The spectrum in coincidence with the 129 keV gating transition is shown in Fig. 8.6b. All of the gamma rays, with the exception of the 172 and 360 keV transitions, result from direct feeding into this level. The 172 and 360 keV transitions are connected to the 129 keV level by a 50 keV transition which cannot be directly observed in these experiments. The analogous situation was found to exist in the $^{193}$Ir level scheme. The presence of this transition is also indicated by the observation of strong 129 keV peaks in the 172 and 360 keV gates (Figs. 8.7d and 8.8d). From these coincidence data, a total intensity of 5.0 ± 1.0 is obtained for the 50 keV transition. The spectra in coincidence with gates set on the weak 619, 633 and 806 keV transitions (Figs. 8.11a, b and c) show that these gamma rays all feed the 129 keV state directly.

## The 179 keV Level

The 179 keV level is deexcited by strong 97 and 179 keV transitions and populated by the spectrum of transitions shown in Fig. 8.6c. Additional support for these observations is provided by the gates set on the higher energy gamma rays in Figs. 8.7d, 8.8d, 8.9c, 8.10c, 8.11e and 8.11f. Several of these spectra show 129 keV coincidences resulting from the 50 keV transition discussed above.

### The 343 keV Level

The 343 keV level is well-known from Coulomb excitation studies (McGowan and Stelson (1958)) but has not been previously observed in the electron decay process. The state is very weakly populated and this is reflected by the poor statistics in the coincidence spectrum associated with the 343 keV gate (Fig. 8.6d). This gate shows that the level is populated by weak transitions of energies 196, 245 and 404 keV. When gates are placed on these weak transitions, the 214 and 343 keV gamma rays which deexcite this level are observed (not shown).

### The 351 keV Level

The 351 keV state is fed by the 188, 397 and 411 keV transitions and depopulated by a number of gamma rays, as shown in the insert of Fig. 8.7. The gamma rays feeding this state are shown in Figs. 8.7c, 8.7d and 8.7e while those deexciting it appear in Figs. 8.7a and 8.7b. The peaks at 268 and 539 keV in Fig. 8.7c result from incomplete separation of the 222 keV gating transition from the 220 and 224 keV radiations.

### The 539 keV Level

The 539 keV state is deexcited by four intense gamma rays of energies 360, 409, 456 and 539 keV and populated by weak gamma rays of energy 85, 209 and 224 keV. The deexciting radiations are shown in Figs. 8.8a, b and c. The absence of peaks at 360 and 456 keV in Fig. 8.8a is caused by an oversubtraction of background involving the adjacent 82 keV radiation. Figs. 8.8d and 8.8e show the gamma rays feeding into the 539 keV level. The 82, 97, 129 and 179 keV radiations in Fig. 8.8d arise from the decay path of the 360 keV gating transition; the unobserved 50 keV transition accounting for the 129 keV gamma ray.

## The 588 keV Level

The 588 keV state is depopulated by the 459-129 and 245-343 keV cascades already discussed and by the 588 keV ground state transition. The spectrum in coincidence with the 588 keV gate (Fig. 8.9a) shows the $^{192}$Ir gamma rays resulting from coincidences with the $^{192}$Ir 589 keV transition which forms most of this gate. There is however an additional peak at 160 keV which represents the 160-588 keV cascade. The existence of this cascade is also indicated when a gate is set at 588 keV in the poor detector (not shown). It appears that about half the observed peak results from the Compton of the 296 keV transition while the other half is due to the 160-588 keV cascade. This complication precludes establishing the 160 keV transition with surety and it has not been included in the decay scheme of Fig. 8.13.

## The 624 keV Level

The 624 keV level is depopulated by gamma rays of energy 85, 445, 495, 542 and 624 keV and populated only by the weak 138 keV gamma ray. The strong gamma rays deexciting this level are shown in Fig. 8.9b and the weak 138 keV transition feeding this state is observed in two of the four gates shown in Figs. 8.9c, d, e and f. The statistics in the other two gates are too poor to reveal the 138 keV transition but these spectra do show the lower members of the cascades originating from the 624 keV level. The peak at 296 keV in Fig. 8.9f results from summing in the gating detector from the 308-296-316 keV cascade in $^{192}$Ir.

### The 391, 659 and 800 keV Levels

These states, together with the 171 keV isomeric state, decay mainly within themselves and form a subsystem of levels similar to that observed in the $^{193}$Ir level structure.

The spectra shown in Figs. 8.10a, b and d clearly indicate that the 141 and 268 keV transitions are in cascade, that the 409 keV radiation (masked in the direct spectrum) is a crossover, and that the 220 keV gamma ray is in coincidence with all three. The 129 keV peak occuring in Fig. 8.10d results from incomplete separation of the 220 keV gating transition from the adjacent 222 keV radiation. The ordering and positioning of the 141-268-220 keV cascade is established by the spectra in coincidence with the 480, 576 and 659 keV gates (Figs. 8.10c, e and f). These spectra show that the 141 keV gamma ray branches through the 480, 576 and 659 keV gamma rays, in addition to its main cascade. Therefore the 141 keV transition necessarily feeds a level at 659 keV while the 268-220 keV cascade populates the 171 keV isomeric state. Confirmation of these statements is provided by the spectrum of Fig. 8.10a which reveals the 480, 576 and 659 transitions depopulating the 659 keV level.

These arguments establish that the states at 800, 659 and 391 keV decay predominently by means of the 141-268-220 keV cascade into the 4.9 sec 171 keV isomeric state. Further direct evidence for the existence of these levels is provided by the reaction data presented in the following chapter.

### The 748, 763 and 935 keV Levels

These levels are securely established by the various coincidence gates already discussed and merit no further attention.

The results of the coincidence measurements are summarized in the form of the coincidence probabilities of table 8.3. The first two columns of the table indicate the gamma ray pairs for which coincidence probabilities are given, the following two columns give the experimental values of $C_{ij}$ and $C_{ji}$ corresponding to each pair, and the fifth column indicates the value of $C_{ij}$ expected from the decay scheme. As in the $^{193}$Os decay, angular correlation effects are significant and account for the rather large discrepancies between the measured and expected $C_{ij}$ values. The experimental $C_{ij}$ values were normalized to the expected values by means of the strong 268-220 keV stretched E2 cascade, after multiplying the expected value by $\omega(\theta) = 1.05$ (see section 7.4) to allow for angular correlation effects. Since $^{191}$Pt decays by electron capture, all gamma rays in the decay are in coincidence with the x-rays. These x-ray coincidences have not been included in table 8.3.

A summary of the transitions in $^{191}$Ir following the decay of $^{191}$Pt is presented in table 8.4. The first column shows the adopted

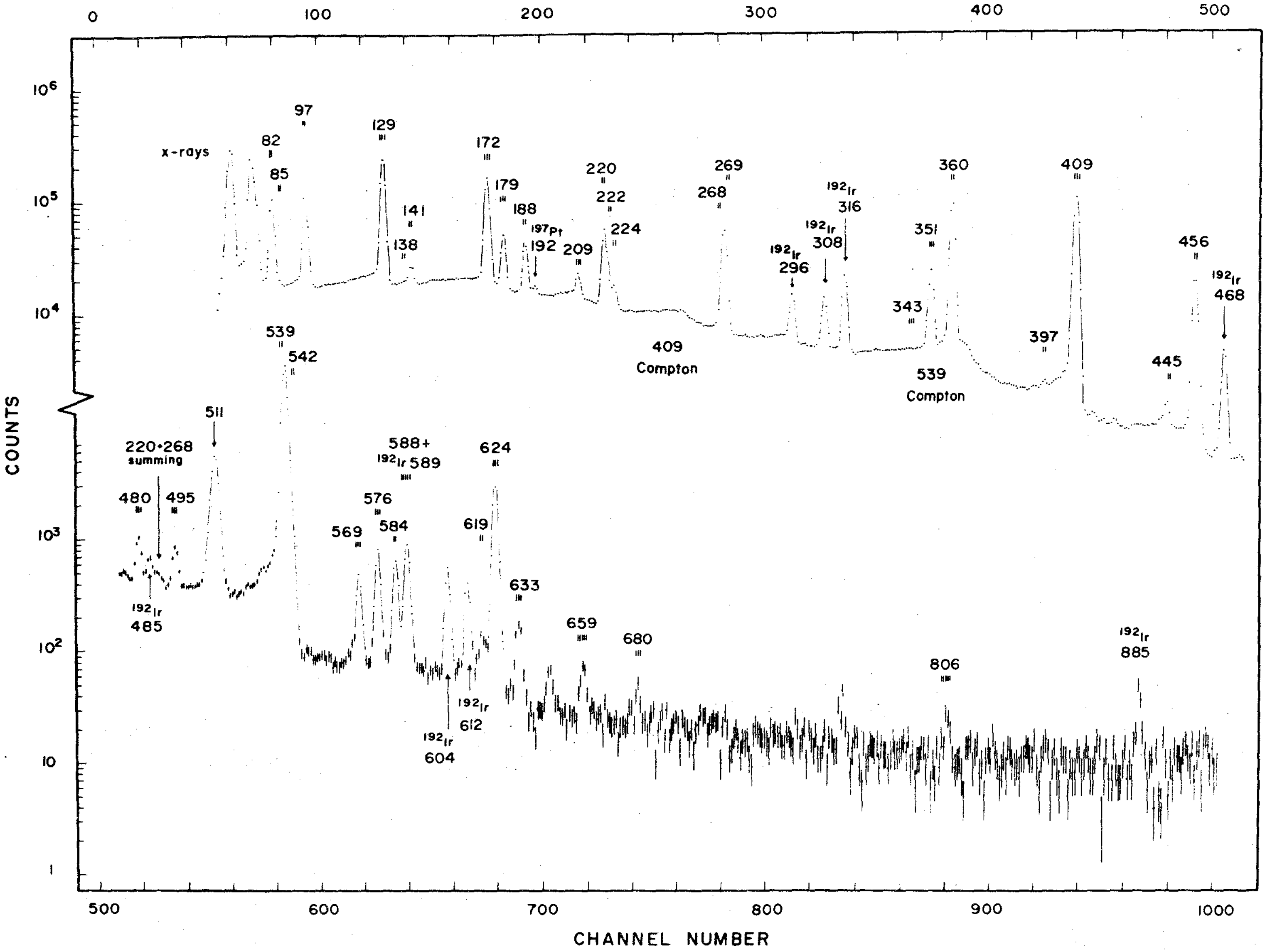

**Figure 8.5** The spectrum of $^{191}$Pt coincidence events projected onto the high resolution axis. The positions of the gates used in the analysis are indicated.

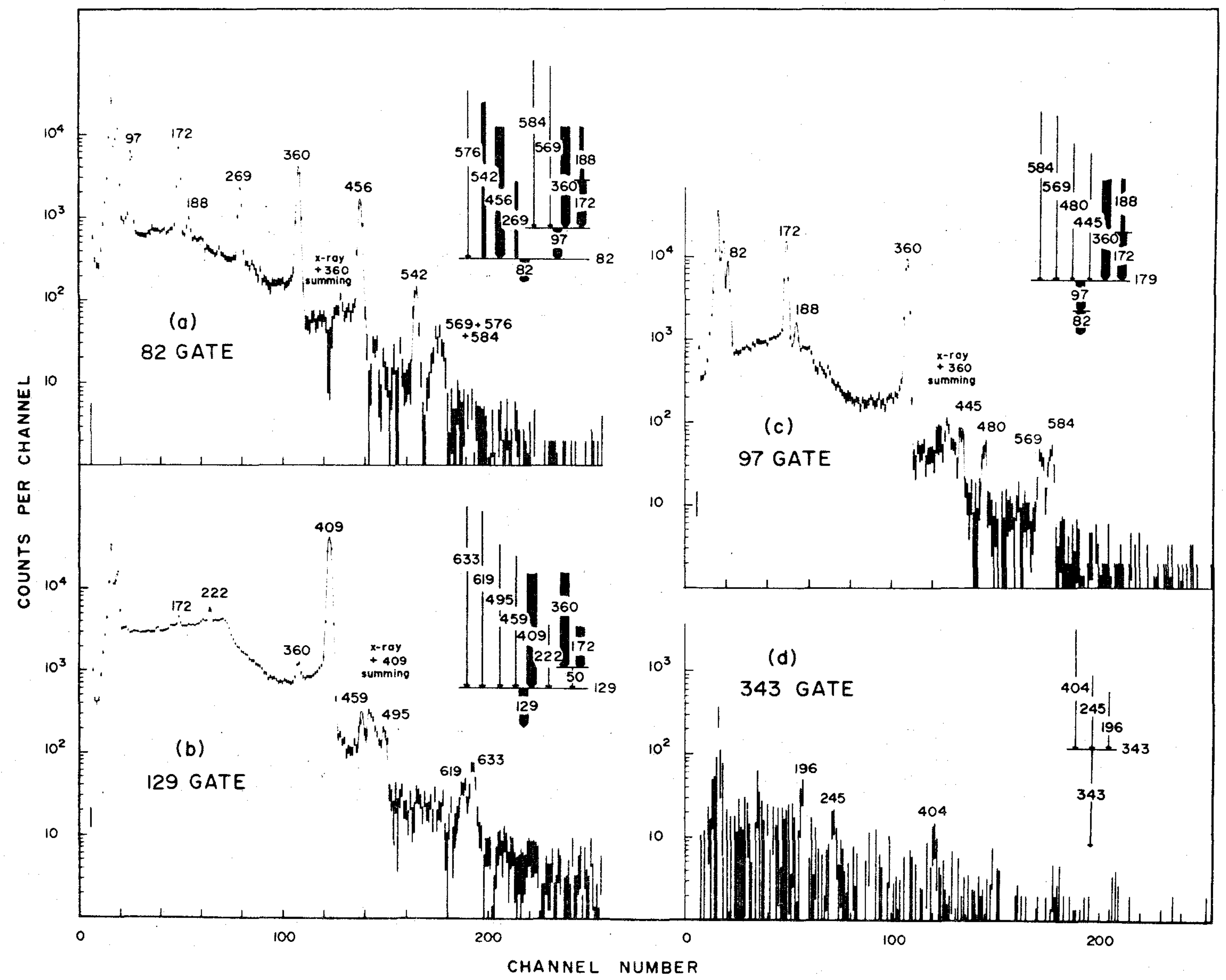

Figure 8.6 Coincidence data associated with the 82, 129, 179 and 343 keV levels.

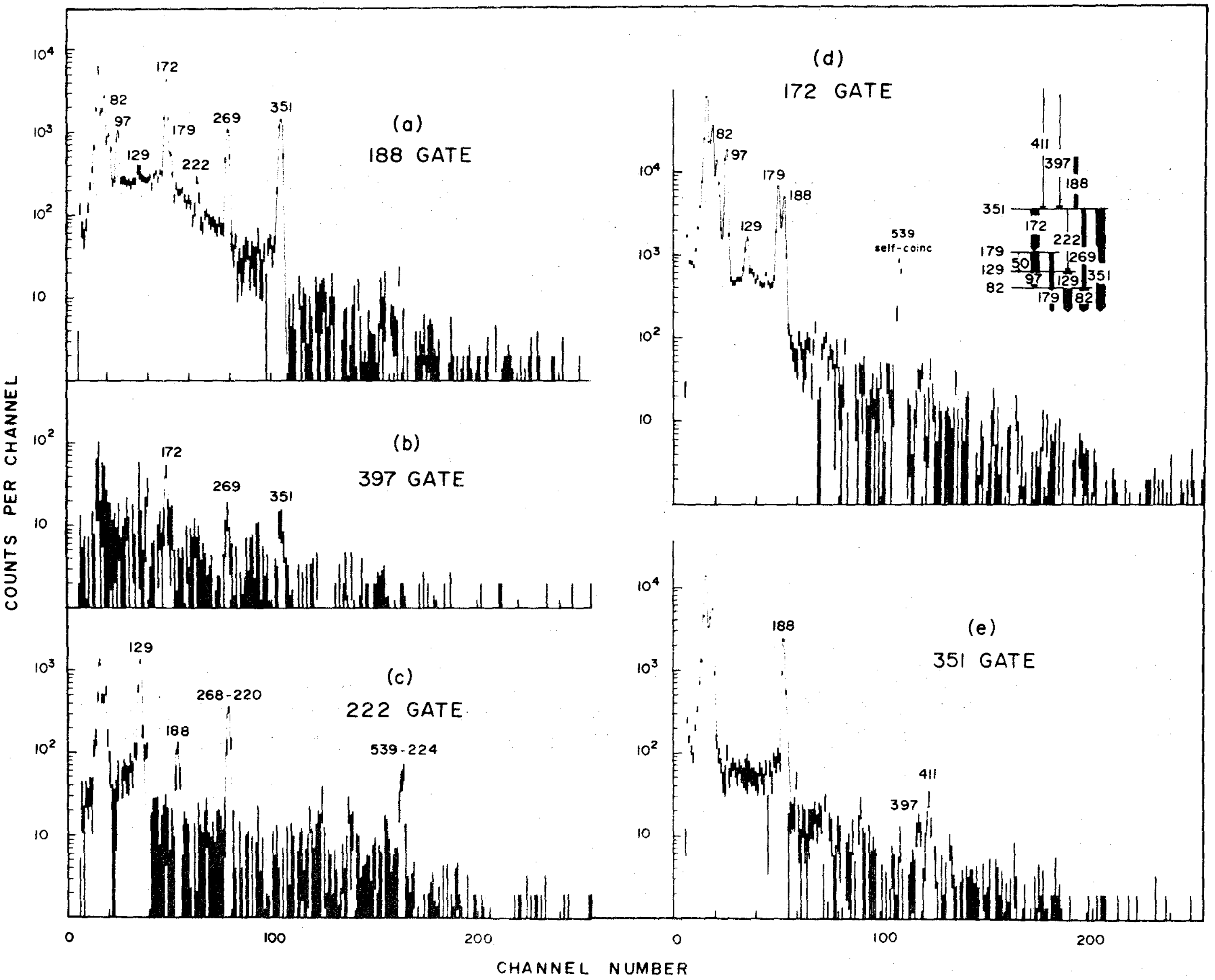

Figure 8.7 Coincidence data associated with the 351 keV level.

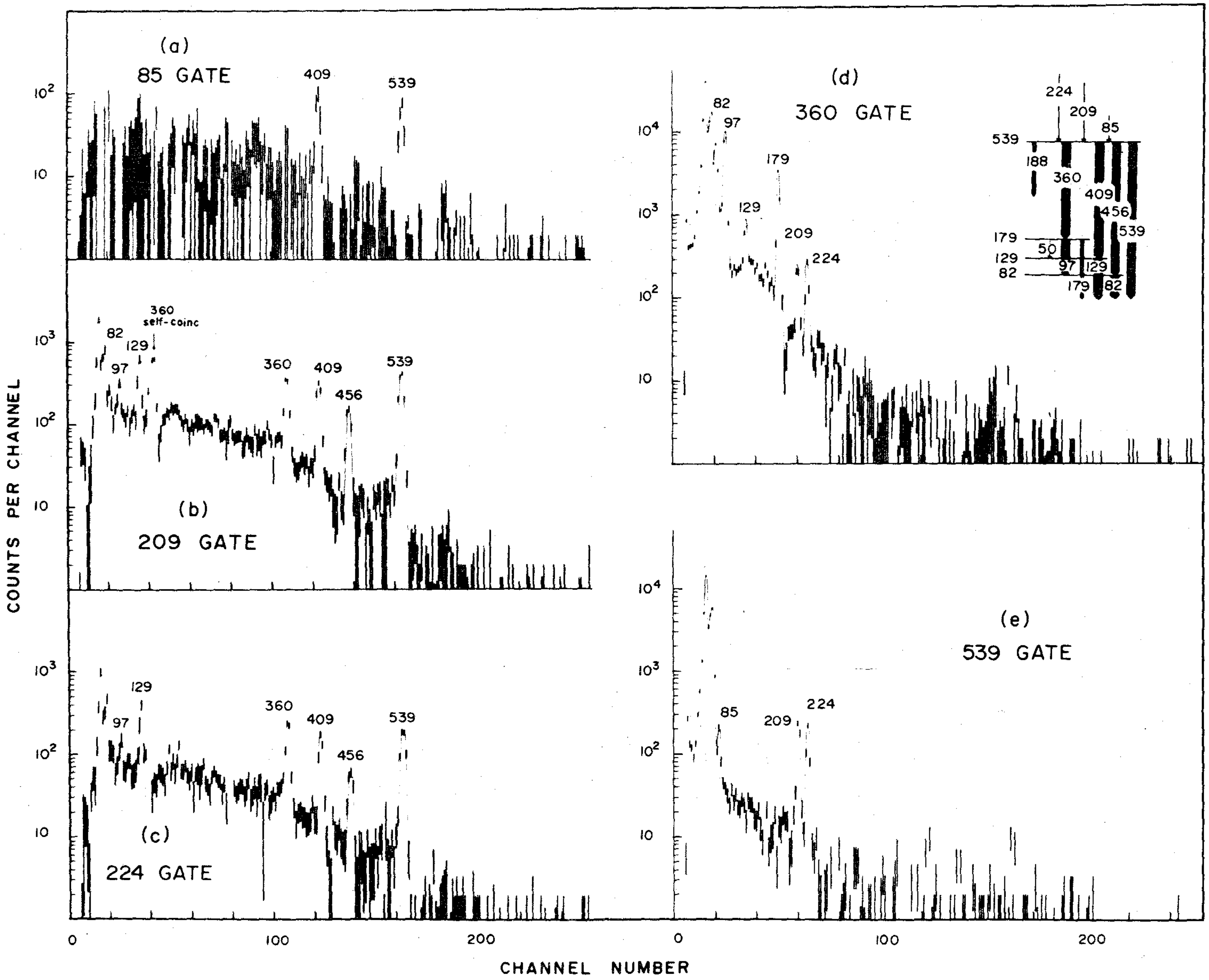

**Figure 8.8** Coincidence data associated with the 539 keV level.

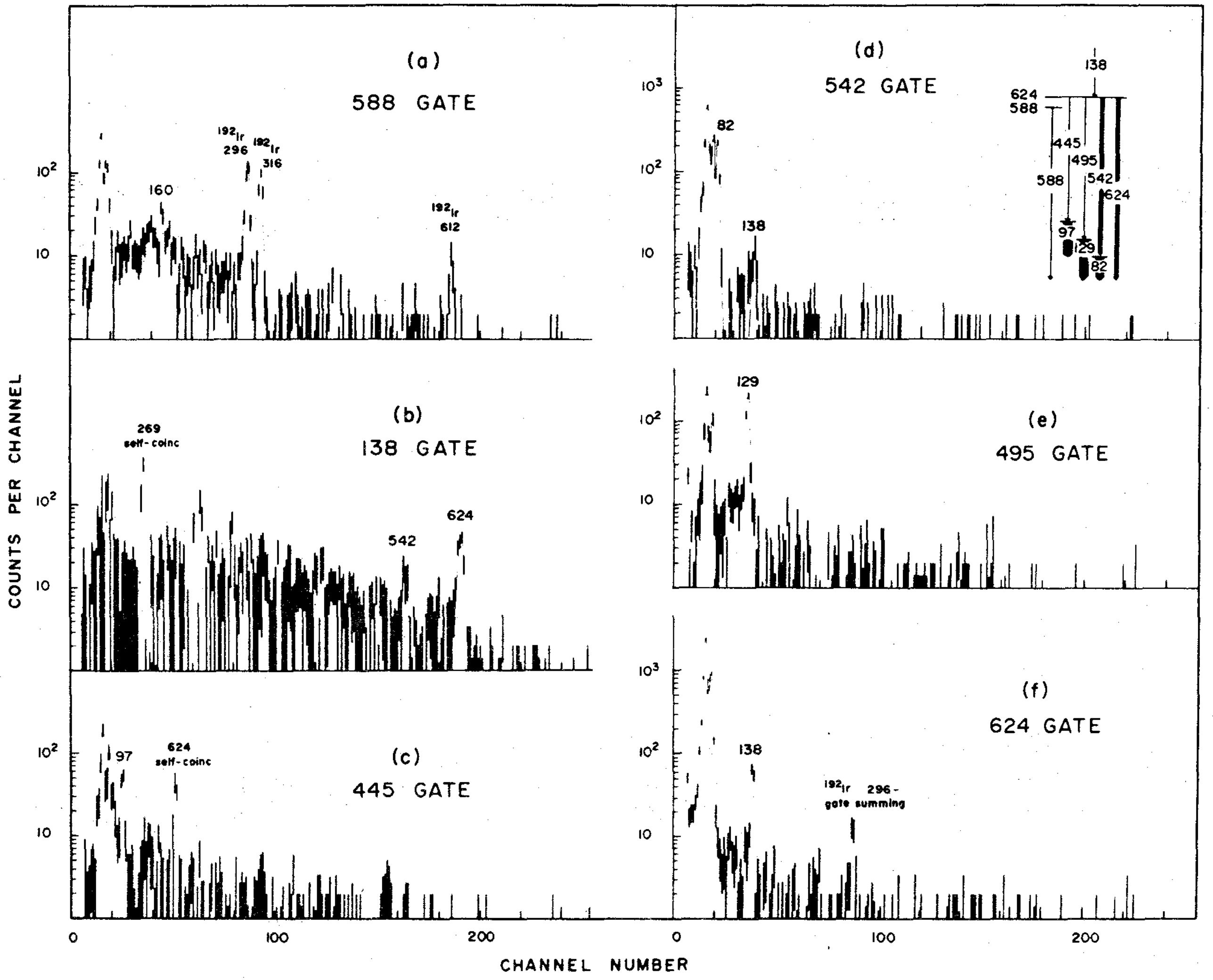

Figure 8.9 Coincidence data associated with the 588 and 624 keV levels.

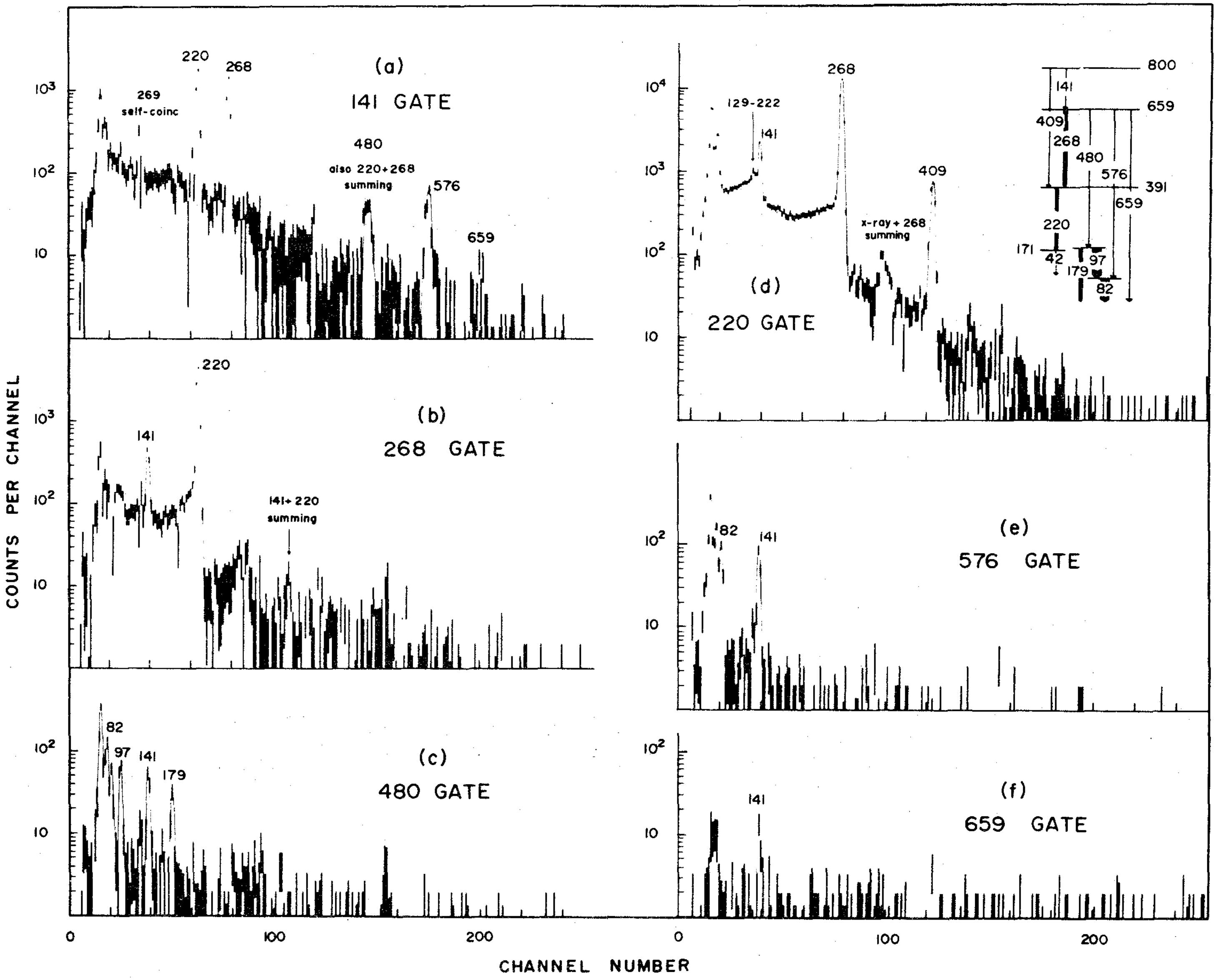

Figure 8.10 Coincidence data associated with the 171, 391, 659 and 800 keV levels.

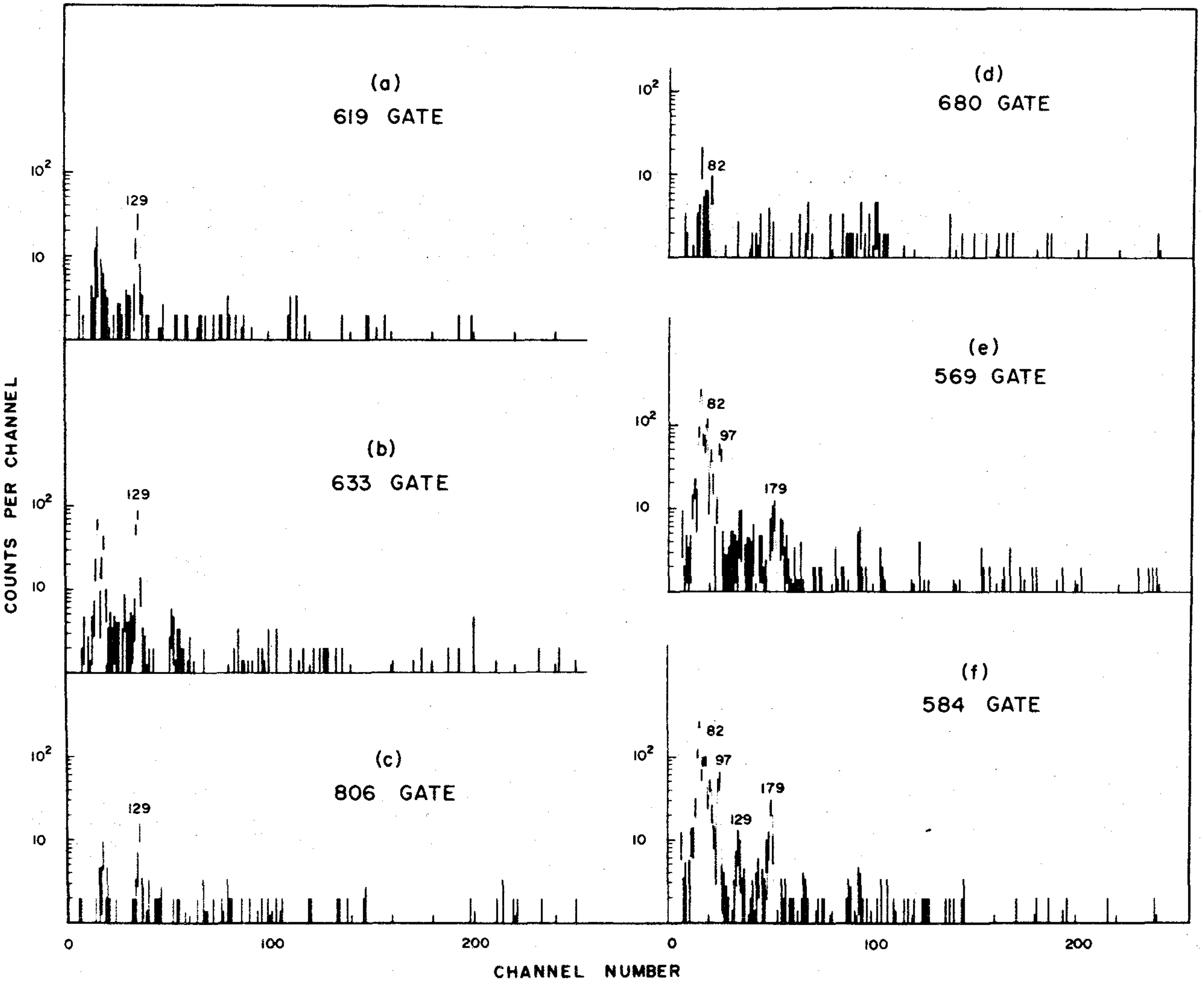

Figure 8.11 Coincidence data associated with various high energy transitions.

## TABLE 8.3

## $\gamma$-$\gamma$ Coincidence Probabilities in $^{191}$Ir

| $\gamma_i$ | $\gamma_j$ | $C_{ij}$ | $C_{ji}$ | $C_{expected}$ |
|---|---|---|---|---|
| 82 | 97 | 3.00 | 2.59 | 3.45 |
| | 141 | | 0.03 | 0.01 |
| | 172 | 3.20 | 3.21 | 3.35 |
| | 188 | 0.26 | 0.31 | 0.29 |
| | 209 | | 0.051 | 0.046 |
| | 224 | | 0.040 | 0.038 |
| | 269 | 1.80 | 1.76 | 1.73 |
| | 360 | 5.63 | 6.60 | 5.70 |
| | 445 | | 0.028 | 0.052 |
| | 456 | 3.30 | 3.40 | 3.52 |
| | 480 | | 0.054 | 0.054 |
| | 542 | 0.40 | 0.37 | 0.39 |
| | 569 | 0.066 | 0.051 | 0.052 |
| | 576 | 0.17 | 0.13 | 0.12 |
| | 584 | | 0.06 | 0.07 |
| | 680 | | 0.006 | 0.007 |
| 85 | 360 | 0.20 | | 0.13 |
| | 409 | 0.20 | | 0.17 |
| | 539 | 0.28 | 0.31 | 0.29 |
| 97 | 172 | 4.12 | 4.16 | 5.15 |
| | 188 | 0.22 | 0.21 | 0.35 |
| | 209 | | 0.040 | 0.040 |
| | 224 | 0.030 | 0.032 | 0.032 |
| | 360 | 7.00 | 7.42 | 8.79 |
| | 445 | 0.064 | 0.066 | 0.080 |
| | 480 | 0.061 | 0.060 | 0.080 |
| | 569 | 0.066 | 0.063 | 0.080 |
| | 584 | 0.081 | 0.082 | 0.11 |
| 129 | 172 | 0.17 | 0.18 | |
| | 188 | 0.024 | 0.032 | 0.030 |
| | 209 | 0.072 | 0.080 | 0.10 |
| | 214 | | 0.030 | |
| | 222 | 0.41 | 0.35 | 0.39 |
| | 360 | 0.27 | 0.32 | |
| | 409 | 31.4 | 32.7 | 27.2 |
| | 459 | 0.21 | 0.11 | 0.13 |
| | 480 | | 0.007 | |
| | 495 | 0.18 | 0.13 | 0.17 |

| $\gamma_i$ | $\gamma_j$ | $C_{ij}$ | $C_{ji}$ | $C_{expected}$ |
|---|---|---|---|---|
| 129 | 569 | | 0.005 | |
| | 584 | | 0.006 | |
| | 619 | 0.051 | 0.047 | 0.030 |
| | 633 | 0.092 | 0.091 | 0.067 |
| | 806 | | 0.013 | 0.010 |
| 138 | 542 | 0.020 | 0.021 | 0.042 |
| | 624 | 0.070 | 0.085 | 0.16 |
| 141 | 220 | 0.52 | 0.55 | 0.61 |
| | 268 | 0.56 | 0.60 | 0.68 |
| | 480 | 0.045 | 0.050 | 0.050 |
| | 576 | 0.084 | 0.090 | 0.10 |
| | 659 | 0.014 | 0.013 | 0.014 |
| 160 | 588 | 0.016 | 0.020 | |
| 172 | 179 | 1.49 | 1.39 | 1.59 |
| | 188 | 1.17 | 1.13 | 1.29 |
| | 397 | 0.036 | 0.028 | 0.035 |
| | 411 | 0.024 | 0.025 | |
| 179 | 188 | 0.078 | 0.073 | 0.11 |
| | 209 | | 0.02 | 0.012 |
| | 360 | 2.11 | 2.30 | 2.72 |
| | 445 | 0.034 | 0.036 | 0.025 |
| | 480 | 0.026 | 0.025 | 0.025 |
| 179 | 569 | 0.018 | 0.014 | 0.025 |
| | 584 | 0.032 | 0.045 | 0.034 |
| 188 | 209 | 0.023 | 0.020 | 0.020 |
| | 222 | 0.068 | 0.039 | 0.043 |
| | 224 | | 0.018 | 0.017 |
| | 269 | 0.52 | 0.56 | 0.61 |
| | 351 | 1.21 | 1.24 | 1.23 |
| 196 | 214 | 0.013 | | |
| | 343 | 0.013 | 0.021 | |
| 209 | 360 | 0.25 | 0.19 | 0.29 |
| | 409 | 0.30 | 0.50 | 0.39 |
| | 456 | 0.15 | 0.18 | 0.16 |
| | 539 | 0.57 | 0.60 | 0.66 |
| 214 | 245 | | 0.009 | |
| | 404 | | 0.020 | |
| 220 | 268 | 7.95a) | 8.33a) | 7.75 (8.14) |
| | 409 | 0.96 | 0.99 | |
| 224 | 360 | 0.25 | 0.19 | 0.24 |
| | 409 | 0.20 | | 0.32 |
| | 456 | 0.084 | 0.10 | 0.13 |
| | 539 | 0.41 | 0.55 | 0.56 |

| $\gamma_i$ | $\gamma_j$ | $C_{ij}$ | $C_{ji}$ | $C_{expected}$ | $\gamma_i$ | $\gamma_j$ | $C_{ij}$ | $C_{ji}$ | $C_{expected}$ |
|---|---|---|---|---|---|---|---|---|---|
| 245 | 343 | 0.017 | 0.019 | | | | | | |
| 269 | 397 | 0.019 | 0.022 | 0.015 | | | | | |
| | 411 | 0.014 | 0.010 | | | | | | |
| 343 | 404 | 0.024 | 0.044 | 0.064 | | | | | |
| 351 | 397 | 0.023 | 0.028 | 0.030 | | | | | |
| | 411 | 0.043 | 0.029 | | | | | | |

[a] Mean value of $C_{ij}$ and $C_{ji}$ normalized to $C_{expected}$ after correcting for angular corrleation effects.

TABLE 8.4

Transitions in $^{191}$Ir Following the Decay of $^{191}$Pt

| Transition Energy (keV) | Relative Intensity |  | Methods of Detection | Classification | $E_{calc}-E_{obs}$ |
|---|---|---|---|---|---|
|  | Photon | Total |  |  |  |
| 63.29 ± 0.05 | 488 ± 61 |  | γ | $K_{\alpha_2}$ |  |
| 64.93 ± 0.05 | 840 ± 105 |  | γ | $K_{\alpha_1}$ |  |
| 73.42 ± 0.05 | 259 ± 32 |  | γ | $K_{\beta_1} + K_{\beta_3}$ |  |
| 75.59 ± 0.05 | 74 ± 9 |  | γ | $K_{\beta_2} + K_{\beta_4}$ |  |
| 41.92a) |  |  |  | 171.32 → 129.400 |  |
| 50b) |  | 5.0 ± 1.0 | γγ | 178.93 → 129.400 |  |
| 82.398 ± 0.007 | 61 ± 6 | 725 ± 66 | γ, ce, γγ | 82.398 → 0 | 0 |
| 85.15 ± 0.08 | 0.75 ± 0.09 | 8.2c) | γ γγ | 624.06 → 538.85 | +0.06 |
| 96.517 ± 0.009 | 41 ± 2 | 316 ± 14 | γ, ce, γγ | 178.93 → 82.398 | +0.01 |
| 129.400 ± 0.007 | 40 ± 4 | 147 ± 18 | γ, ce, γγ | 129.400 → 0 | 0 |
| 138.2 ± 0.2 | 0.3 ± 0.2 | 1.0c) | γ γγ | 762.56 → 624.06 | +0.30 |
| 140.884 ± 0.015 | 0.94 ± 0.14 | 2.8 ± 0.6 | γ, ce, γγ | 799.75 → 658.87 | 0 |
| 160 | 0.02d) |  | γγ | 747.74 → 587.95 |  |
| 172.19 ± 0.02 | 44 ± 2 | 101 ± 4 | γ, ce, γγ | 351.15 → 178.93 | +0.03 |
| 178.96 ± 0.03 | 12.7 ± 0.6 | 24.5 ± 1.1 | γ, ce, γγ | 178.93 → 0 | −0.03 |
| 187.69 ± 0.04 | 5.2 ± 0.3 | 9.9 ± 0.9 | γ, ce, γγ | 538.85 → 351.15 | +0.01 |
| 196 | 0.04 ± 0.01 |  | γγ | 538.85 → 343.2 |  |
| 208.96 ± 0.15 | 1.7 ± 0.3 | 3.0c) | γ γγ | 747.74 → 538.85 | −0.07 |
| 214 | 0.11 ± 0.03 | 0.19c) | γγ | 343.2 → 129.400 |  |
| 219.65 ± 0.05 | 10.3 ± 0.5 | 12.9 ± 0.5 | γ, ce, γγ | 390.97 → 171.32 | 0 |
| 221.74 ± 0.08 | 1.45 ± 0.15 | 2.4c) | γ γγ | 351.15 → 129.400 | +0.01 |
| 223.67 ± 0.08 | 1.40 ± 0.15 | 2.2 ± 0.2 | γ, ce, γγ | 762.56 → 538.85 | +0.04 |

| Transition Energy (keV) | Relative Intensity Photon | Relative Intensity Total | Methods of Detection | Classification | $E_{calc}-E_{obs}$ |
|---|---|---|---|---|---|
| 245 | 0.04 ± 0.01 | 0.06c) | γγ | 587.95 → 343.2 | |
| 267.92 ± 0.08 | 9.7 ± 1.0 | 11.0 ± 1.0 | γ, ce, γγ | 658.87 → 390.97 | −0.02 |
| 268.71 ± 0.08 | 20.6 ± 2.0 | 23.6 ± 2.0 | γ, ce, γγ | 351.15 → 82.398 | +0.04 |
| 343.2 ± 0.2 | 0.16 ± 0.05 | | γ γγ | 343.2 → 0 | 0 |
| 351.17 ± 0.03 | 42 ± 2 | 50 ± 2 | γ, ce, γγ | 351.15 → 0 | −0.02 |
| 359.88 ± 0.03 | 75 ± 4 | 88 ± 4 | γ, ce, γγ | 538.85 → 178.93 | +0.04 |
| 396.7 ± 0.2 | 0.13 ± 0.04 | | γ γγ | 747.74 → 351.15 | −0.11 |
| 404.1 ± 0.3 | 0.14 ± 0.07 | | γ γγ | 747.74 → 343.2 | +0.44 |
| 409 | 1.2 ± 0.2 | | γγ | 799.75 → 390.97 | |
| 409.44 ± 0.02 | 100 ± 5 | 112 ± 5 | γ, ce, γγ | 538.85 → 129.400 | +0.01 |
| 411 | 0.12 ± 0.03 | | γγ | 762.56 → 351.15 | |
| 445.13 ± 0.08 | 0.68 ± 0.07 | | γ γγ | 624.06 → 178.93 | 0 |
| 456.47 ± 0.05 | 42 ± 2 | 46 ± 2 | γ, ce, γγ | 538.85 → 82.398 | −0.02 |
| 458.59 ± 0.15 | 0.54 ± 0.10 | | γ γγ | 587.95 → 129.400 | −0.04 |
| 479.95 ± 0.07 | 0.71 ± 0.07 | | γ γγ | 658.87 → 178.93 | −0.01 |
| 494.69 ± 0.07 | 0.75 ± 0.07 | | γ γγ | 624.06 → 129.400 | −0.03 |
| 538.87 ± 0.05 | 171 ± 9 | 180 ± 9 | γ, ce, γγ | 538.85 → 0 | −0.02 |
| 541.64 ± 0.10 | 4.6 ± 0.5 | 4.8 ± 0.5 | γ, ce, γγ | 624.06 → 82.398 | +0.02 |
| 568.81 ± 0.08 | 0.66 ± 0.05 | | γ γγ | 747.74 → 178.93 | 0 |
| 576.46 ± 0.08 | 1.47 ± 0.11 | | γ γγ | 658.87 → 82.398 | +0.01 |
| 583.61 ± 0.08 | 0.95 ± 0.07 | | γ γγ | 762.56 → 178.93 | +0.02 |
| 587.95 ± 0.08 | 1.70 ± 0.13 | | γ γγ | 587.95 → 0 | 0 |
| 618.7 ± 0.4 | 0.11 ± 0.04 | | γ γγ | 747.74 → 129.400 | −0.36 |

| Transition Energy (keV) | Relative Intensity | | Methods of Detection | Classification | $E_{calc}-E_{obs}$ |
|---|---|---|---|---|---|
| | Photon | Total | | | |
| 624.06 ± 0.06 | 17.6 ± 0.9 | 18.1 ± 0.9 | γ, ce, γγ | 624.06 → 0 | 0 |
| 633.18 ± 0.10 | 0.30 ± 0.03 | | γ γγ | 762.56 → 129.400 | -0.02 |
| 658.75 ± 0.15 | 0.19 ± 0.02 | | γ γγ | 658.87 → 0 | +0.12 |
| 680.0 ± 0.2 | 0.086 ± 0.017 | | γ γγ | 762.56 → 82.398 | +0.16 |
| 748.0 ± 0.2 | 0.052 ± 0.010 | | γ | 747.74 → 0 | -0.26 |
| 762.60 ± 0.15 | 0.15 ± 0.02 | | γ | 762.56 → 0 | -0.04 |
| 806.4 ± 0.3 | 0.047 ± 0.009 | | γ γγ | 935.33 → 129.400 | -0.47 |
| 935.33 ± 0.15 | 0.15 ± 0.02 | | γ | 935.33 → 0 | 0 |

[a] The 41.92 keV transition depopulates the 4.9 sec isomer at 171.32 keV.

[b] Not directly observed.

[c] M1 transition assumed.

[d] At limit of detection.

energy values. The next two columns indicate the photon and total transition intensities while the fourth column lists the various ways in which the transition has been detected. The final columns of the table give the classification of the line in the decay scheme and the energy differences between the values calculated from the decay scheme and the experimental values.

## 8.5 The Coulomb Excitation Results

The Coulomb excitation results were obtained with the McMaster University model FN accelerator under the experimental conditions described in section 7.5. Oxygen beams of 25, 40, 55 and 65 MeV were used to bombard a thick target consisting of compressed metallic iridium, enriched to 89.6% in $^{191}$Ir.

The spectra recorded with the 25, 40 and 65 MeV oxygen beams are shown in Fig. 8.12 and the corresponding results presented in table 8.5. The first three columns indicate the transitions observed at these beam energies while the last column gives the classification of the transition in the level scheme of $^{191}$Ir. No attempt has been made to extract relative B(E2) values from the present measurements. Several unclassified lines whose origin has not been established are included in table 8.5.

Although all the low-lying positive parity levels are populated in these experiments, no members of the 141-268-220 keV cascade were observed. This is consistent with other evidence indicating that these transitions feed the $11/2^-$ 171 keV isomeric state.

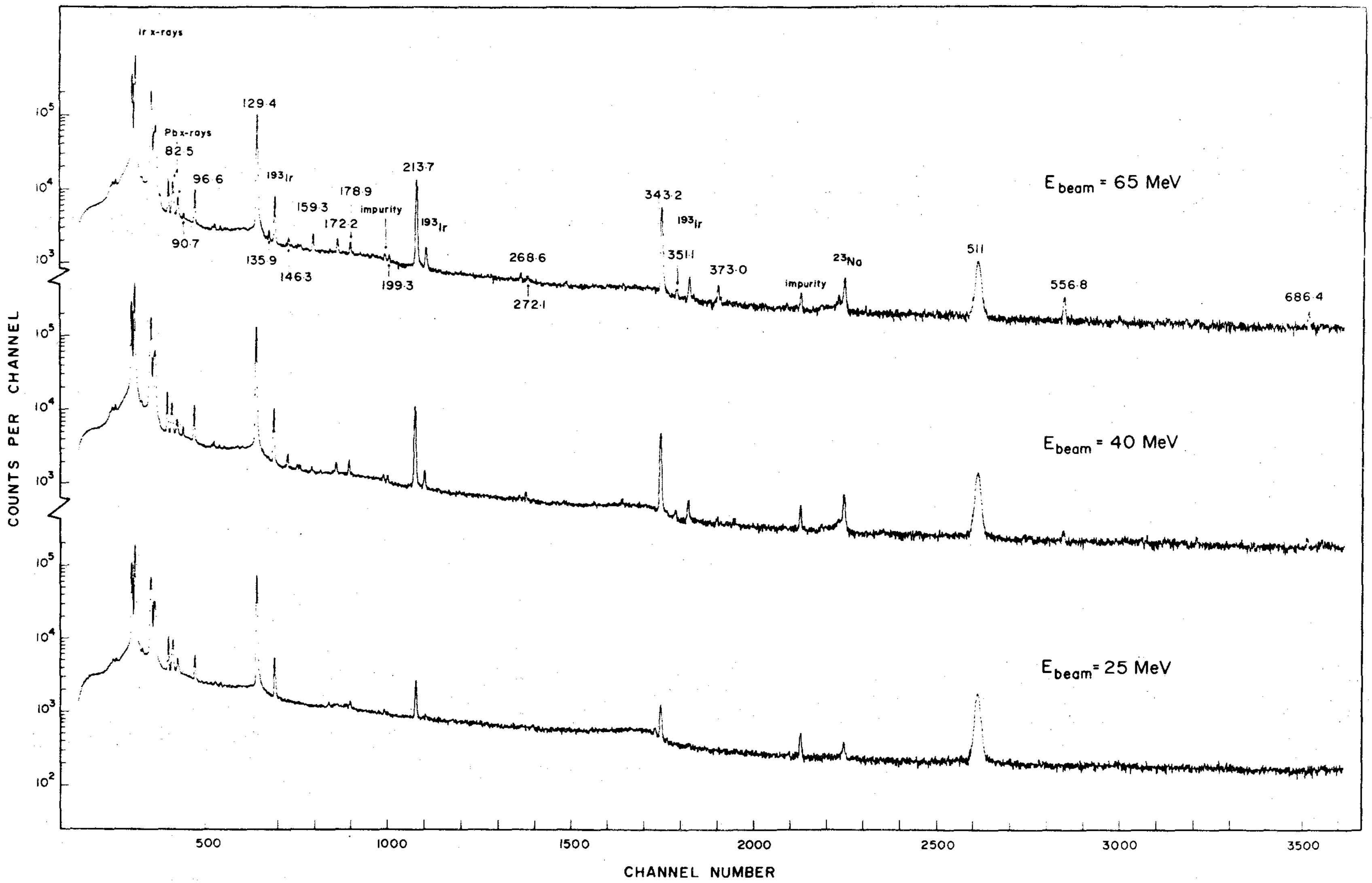

**Figure 8.12** Coulomb excitation spectrum of $^{191}$Ir obtained with 25, 40 and 65 MeV oxygen beams.

## TABLE 8.5

## Transitions Following Coulomb Excitation of $^{191}$Ir

| Transition Energy (keV) | | | |
|---|---|---|---|
| 25 MeV | 40 MeV | 65 MeV | Classification |
| 82.5 | 82.5 | 82.5 | 82.398→0 |
| 96.6 | 96.6 | 96.6 | 178.93 →82.398 |
| 129.4 | 129.4 | 129.4 | 129.400→0 |
| | 159.3 | 159.3 | 502.5 →343.2 |
| | 172.2 | 172.2 | 351.15 →178.93 |
| | 178.9 | 178.9 | 178.93 →0 |
| 213.7 | 213.7 | 213.7 | 343.2 →129.400 |
| | 268.7 | 268.5 | 351.15 →82.398 |
| 343.2 | 343.2 | 343.1 | 343.2 →0 |
| | 351.1 | 351.0 | 351.15 →0 |
| | 373.0 | 373.0 | 502.5 →129.400 |
| | 556.9 | 556.8 | 686.3 →129.400 |
| | 686.2 | 686.6 | 686.3 →0 |
| | 90.7 | 90.7 | |
| | | 135.9 | |
| | 146.3 | 146.3 | Unclassified |
| | 199.3 | 199.3 | |
| | 272.1 | 272.1 | |

## 8.6 The Level Structure of $^{191}$Ir

The results of these experiments are summarized in the level scheme of Fig. 8.13 which shows the securely established transitions in $^{191}$Ir. The levels at 503 and 686 keV are dashed to indicate that they are populated only in Coulomb excitation. The energies and total intensities are shown for each transition and dots marked on those transitions for which coincidence information was obtained. The electron capture intensities and log $f_o t$ values have been deduced from the transition intensities assuming 50% feeding to the ground state. A total decay energy of 1000 keV is estimated from beta decay systematics and this value has been used in obtaining the log $f_o t$ values.

The ground state of $^{191}$Ir is measured to have spin $3/2^+$ (Marakawa and Suwa (1952)) and the reaction data to be presented establish this as the $3/2^+$ [402] Nilsson orbital. The $5/2^+$ and $7/2^+$ rotational band members are known from Coulomb excitation to be the 129 and 343 keV states respectively, with these assignments confirmed by the reaction data.

The spin of the 82 keV state is expected to be $1/2^+$ from nuclear systematics. This state is clearly populated by an $\ell = 0$ transition in the reaction data, thus establishing its spin with certainty. Moreover the reaction data establish that this state is composed of the $K = K_o - 2$ gamma vibration together with the $1/2^+$ [400] orbital.

Strong first forbidden electron capture transitions to each of

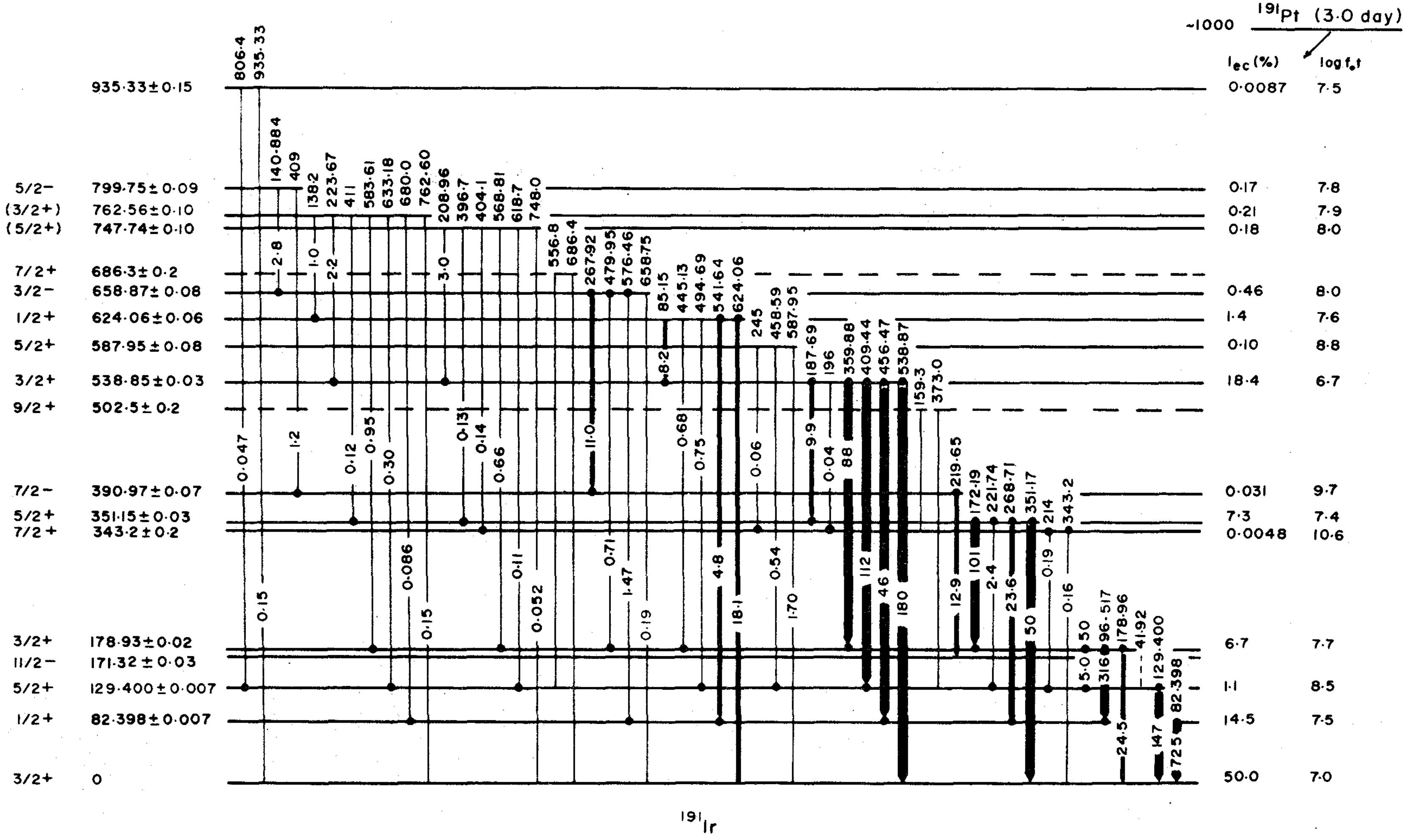

Figure 8.13 Level structure of $^{191}$Ir.

the 0 $(3/2^+)$, 82 $(1/2^+)$ and 129 $(5/2^+)$ levels suggest a $3/2^-$ assignment for the ground state of $^{191}$Pt. The Nilsson model indicates this to be the $3/2^-$ [512] state.

The 503 keV state is populated in Coulomb excitation. This state branches to the $7/2^+$ and $5/2^+$ members of the ground state band and, accordingly, is assigned as the $9/2^+$ member of the ground state band. This state, along with the $11/2^+$ member, has recently been observed in inelastic deuteron scattering (Norgaard et al (1971)) but with much poorer energy resolution than afforded by the present Ge(Li) measurements.

The 351 keV state receives a spin assignment of $5/2^+$ because of the pure E2 radiation feeding the 82 keV $(1/2^+)$ level. The mixed character of the radiations in the 351 $(5/2^+)\rightarrow 179 \rightarrow 82$ $(1/2^+)$ cascade requires that the 179 keV level have spin $3/2^+$. The reaction data show that these states make up the $3/2^+$ and $5/2^+$ members of the combined $K = K_o - 2$ gamma vibrational and $1/2^+$ [400] band. The observation of relatively large Coulomb excitation probabilities for these states supports this interpretation.

The Coulomb excitation results indicate that the 686 keV state is highly collective in nature. Since this state is not populated in the decay process, it likely has a spin $7/2^+$. Furthermore a $K = 7/2^+$ value is suggested by the decay mode of this state which exhibits branching only to the $K = 3/2^+$ band and none to the $K = 1/2^+$ band. These arguments indicate that the 686 keV state forms the $K = K_o + 2$ gamma vibrational member of the ground state. The inelastic deuteron scattering measurements of Norgaard et al (1971) provides a similar interpretation.

The spin of the 539 keV level is determined to be $3/2^+$ from the observed M1 + E2 character of the transition deexciting to each of the 129 keV ($5/2^+$), 82 keV ($1/2^+$) and 0 keV ($3/2^+$) states. The 624 keV level exhibits strong branching to the 82 keV ($1/2^+$) and 0 keV ($3/2^+$) states but very little branching to the 129 keV ($5/2^+$) state and consequently receives a spin assignment of $1/2^+$. This assignment is supported by the conversion data and also agrees with that determined for the analogous state in $^{193}$Ir. The 539 and 624 keV levels are not populated in the reaction work and it seems probable that these states form the $3/2^+$ and $1/2^+$ band members of the $1/2^+$ [411] hole state, which is known to exhibit inverted level ordering. Since the position of the $1/2^+$ [411] Nilsson orbital decreases with increasing deformation, this state is expected to occur at higher excitation energy in $^{191}$Ir than in $^{193}$Ir. The present results clearly show this effect. Whereas corresponding members of the $3/2^+$ [402] and $1/2^+$ [400] states are all located within a few keV of each other, the $1/2^+$ [411] members in $^{191}$Ir are upshifted in energy by ∿75 keV relative to those in $^{193}$Ir.

The 588 keV state is assigned a spin of $5/2^+$ since it exhibits significant branching to the 129 keV ($5/2^+$) and 0 keV ($3/2^+$) levels, but none to the 82 keV ($1/2^+$) level. In the reaction data, this state is populated with $\ell = 2$ transfer which accords with the $5/2^+$ assignment. The reaction data indicate that this state is likely the $5/2^+$ [402]

hole state.

The 748 and 763 keV levels are tentatively assigned spins of $5/2^+$ and $3/2^+$ respectively. The assignments are based upon the observed gamma ray branching from these levels. The levels branch to all the low-lying $1/2^+$, $3/2^+$, $5/2^+$ and $7/2^+$ states, with the exceptions that the 748 keV level does not populate the $1/2^+$ state and the 763 keV level does not decay to the $7/2^+$ state.

The 171 keV isomeric state is found to have spin $11/2^-$ from the observed E3 multipolarity of the deexciting radiation (Nablo et al (1958)) and the reaction data show this state may be the $11/2^-$ [505] particle state.

The spin of the 391 keV level is established as $7/2^-$ by the E2 character of the 220 keV radiation and the $\ell = 3$ transfer observed for this state in the reaction data. The E2 character of the 268 keV gamma ray then demands a spin assignment of $3/2^-$ for the 659 keV level. A higher spin value for this state would require an M2 transition to favourably compete with E1 transitions. The 141 keV transition is measured to be M1 + E2 and by analogy with $^{193}$Ir, the 409 keV radiation is expected to be of similar character. Thus a $5/2^-$ spin assignment is indicated for the 800 keV state. The sequence of levels at 391, 659 and 800 keV accordingly receive spin assignments of $7/2^-$, $3/2^-$ and $5/2^-$ respectively.

These states, together with the 171 keV isomeric state, from a subsystem of negative parity states similar to that observed in $^{193}$Ir. However it is noticed that this subsystem is not isolated from the other states to the same degree as observed for the $^{193}$Ir case. The log $f_o t$ value for electron capture to the $3/2^-$ state is not as severely hindered and the electromagnetic transitions from this state to the positive parity states are more prominent than observed in $^{193}$Ir.

# CHAPTER IX

# ($^3$He,d) AND ($\alpha$,t) REACTIONS ON $^{190}$Os AND $^{192}$Os

## 9.1 The Energy and Cross Section Results

The present experiments were performed using beams of 28 MeV $^3$He and $^4$He particles obtained from the model MP tandem Van de Graaff accelerator at the University of Rochester Nuclear Structure Research Laboratory. The reaction products were magnetically analyzed and detected by means of nuclear emulsions as described in section 6.4. Targets of thickness $\sim$ 100 $\mu$g/cm$^2$ were prepared by vacuum evaporating osmium metal, isotopically enriched to 95.5% for the $^{190}$Os targets and 98.7% for the $^{192}$Os targets, onto 50 $\mu$g/cm$^2$ carbon backings. Typical exposure times were 6 hr for the deuteron spectra and 4 hr for the triton spectra, using beam currents of 1 to 2 $\mu$A.

For the ($^3$He,d) reactions, spectra were taken at two different angles in the regions of 30-35° and 55-60°. Different angles were chosen for each target in order to eliminate from the region of interest, spurious reaction peaks due to the carbon backings. Figures 9.1 and 9.2 show the ($^3$He,d) spectra obtained with the $^{190}$Os and $^{192}$Os targets. The deuteron peak widths are typically 16-17 keV. No contaminants, other than the carbon backings, were observed in the spectra and the isotopic enrichments were high enough that the different isotopes did

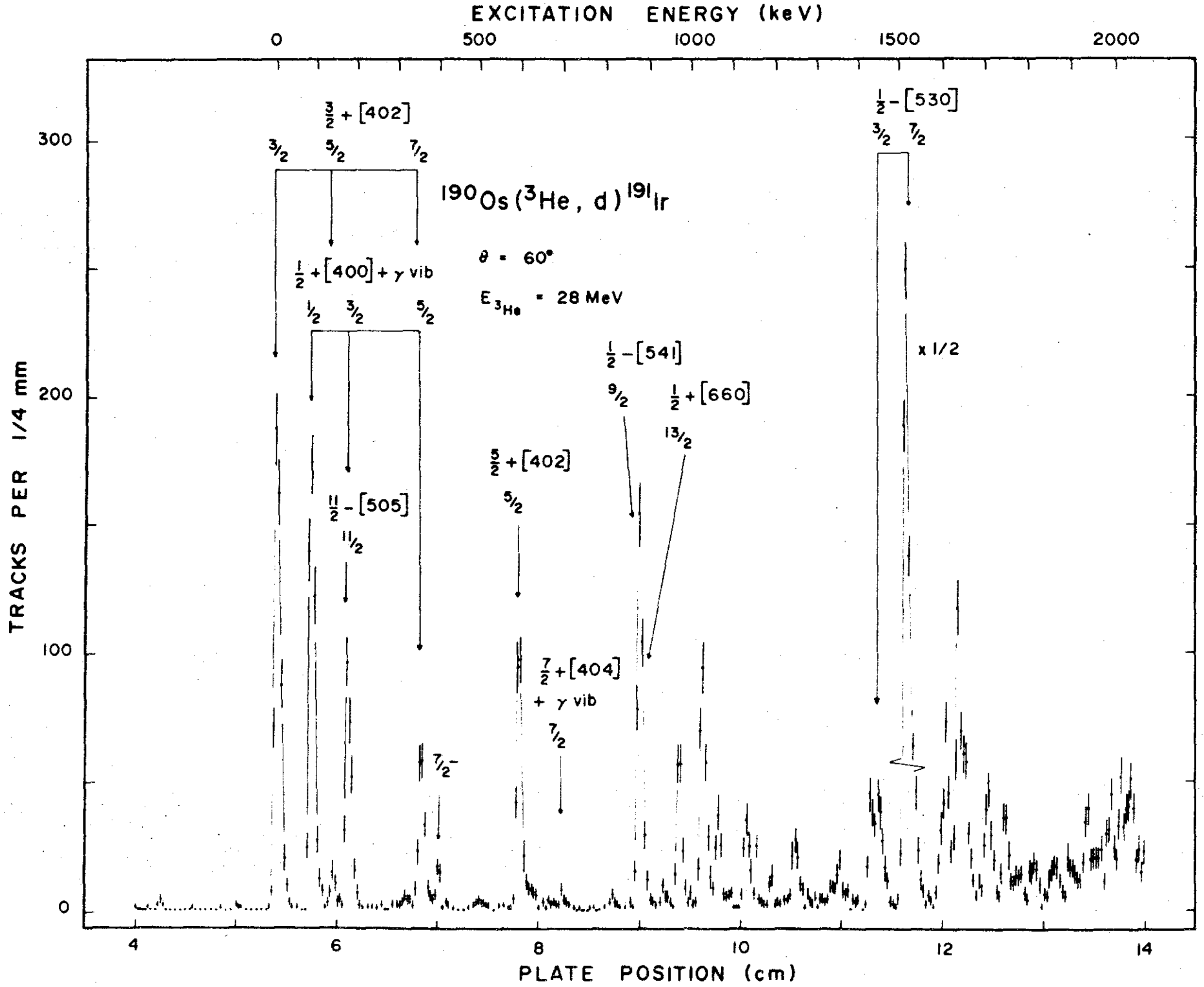

Figure 9.1 $^{190}$Os($^3$He,d)$^{191}$Ir deuteron spectrum.

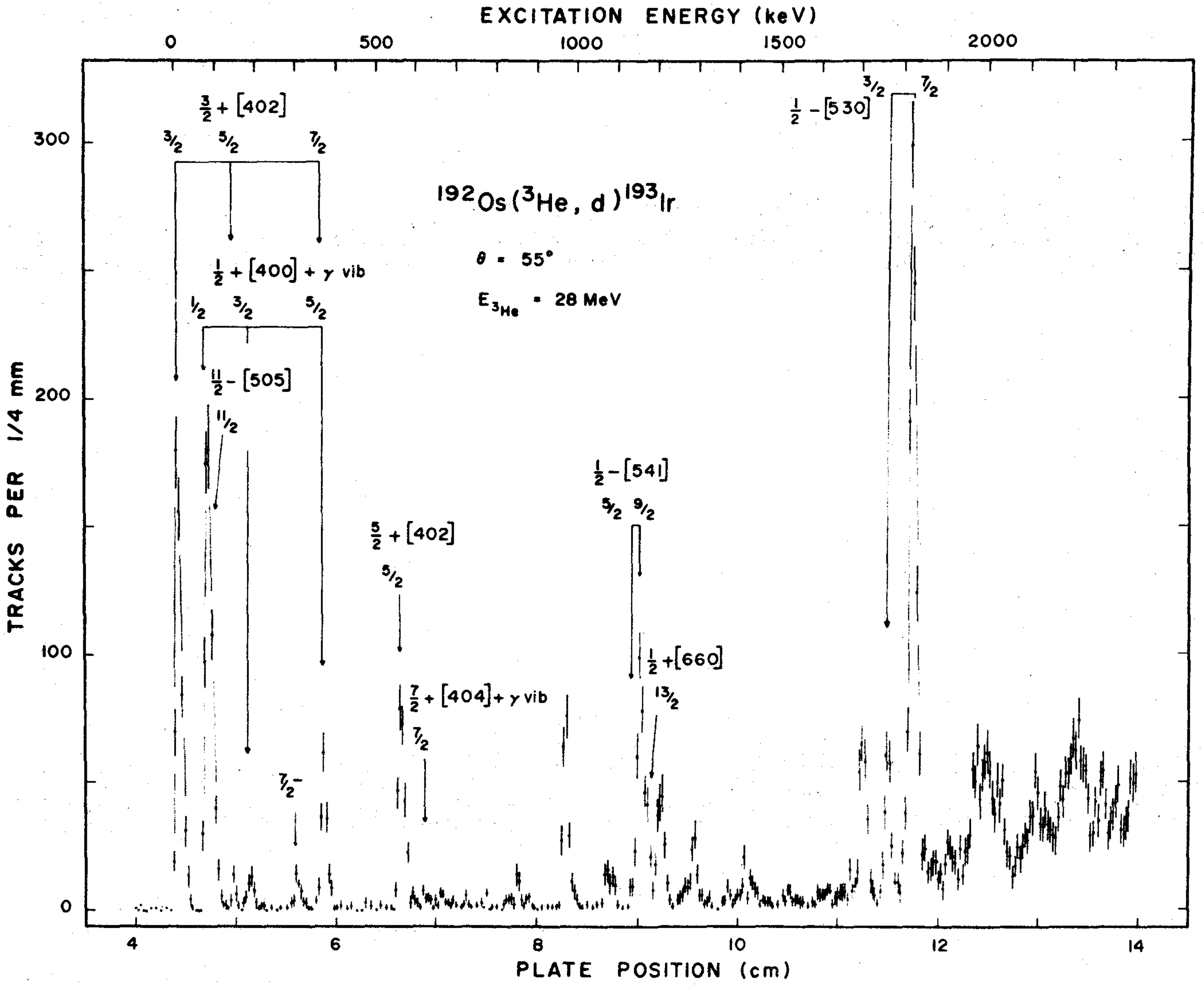

Figure 9.2 $^{192}$Os($^3$He,d)$^{193}$Ir deuteron spectrum.

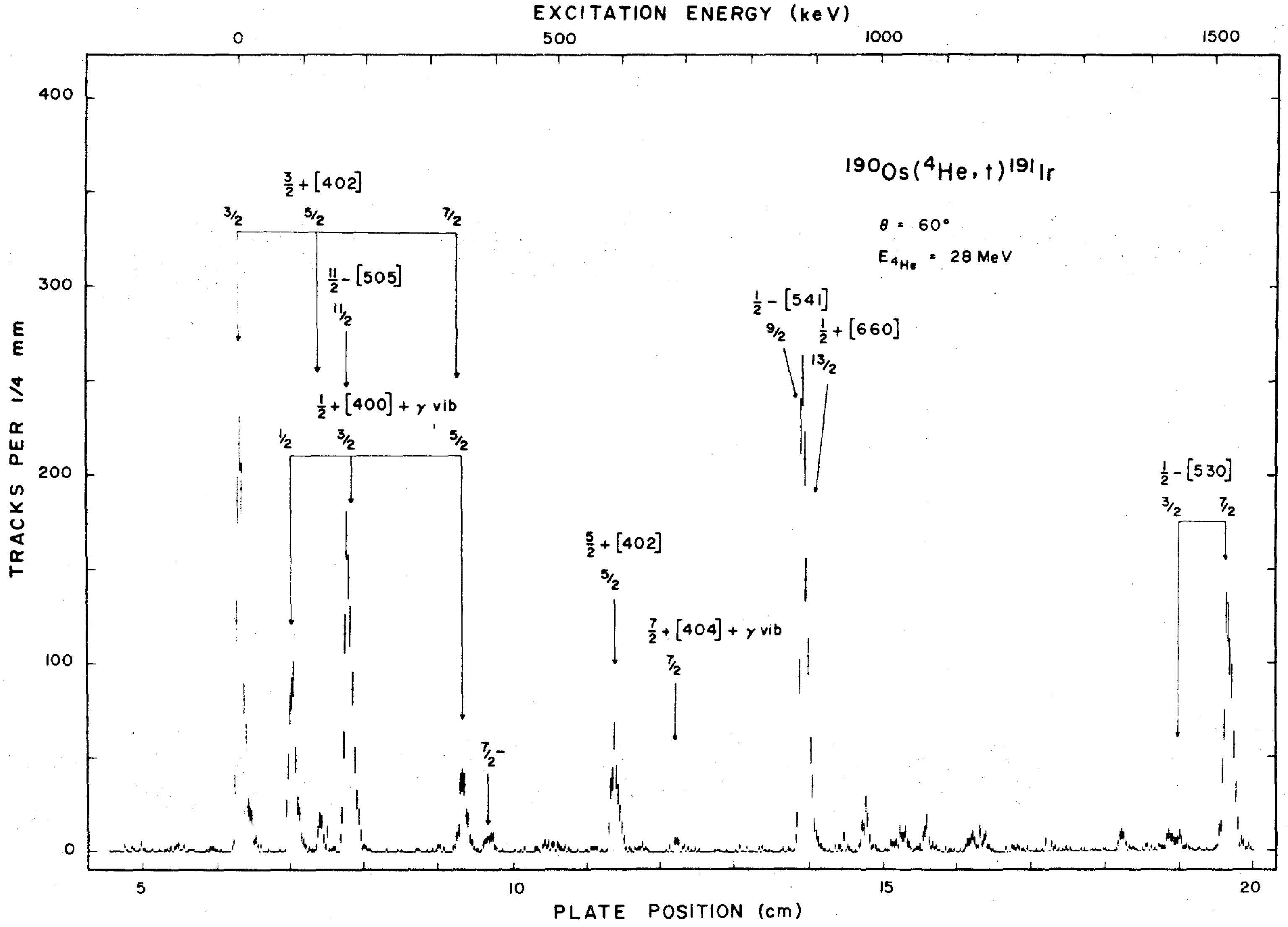

Figure 9.3 $^{190}$Os(α,t)$^{191}$Ir triton spectrum.

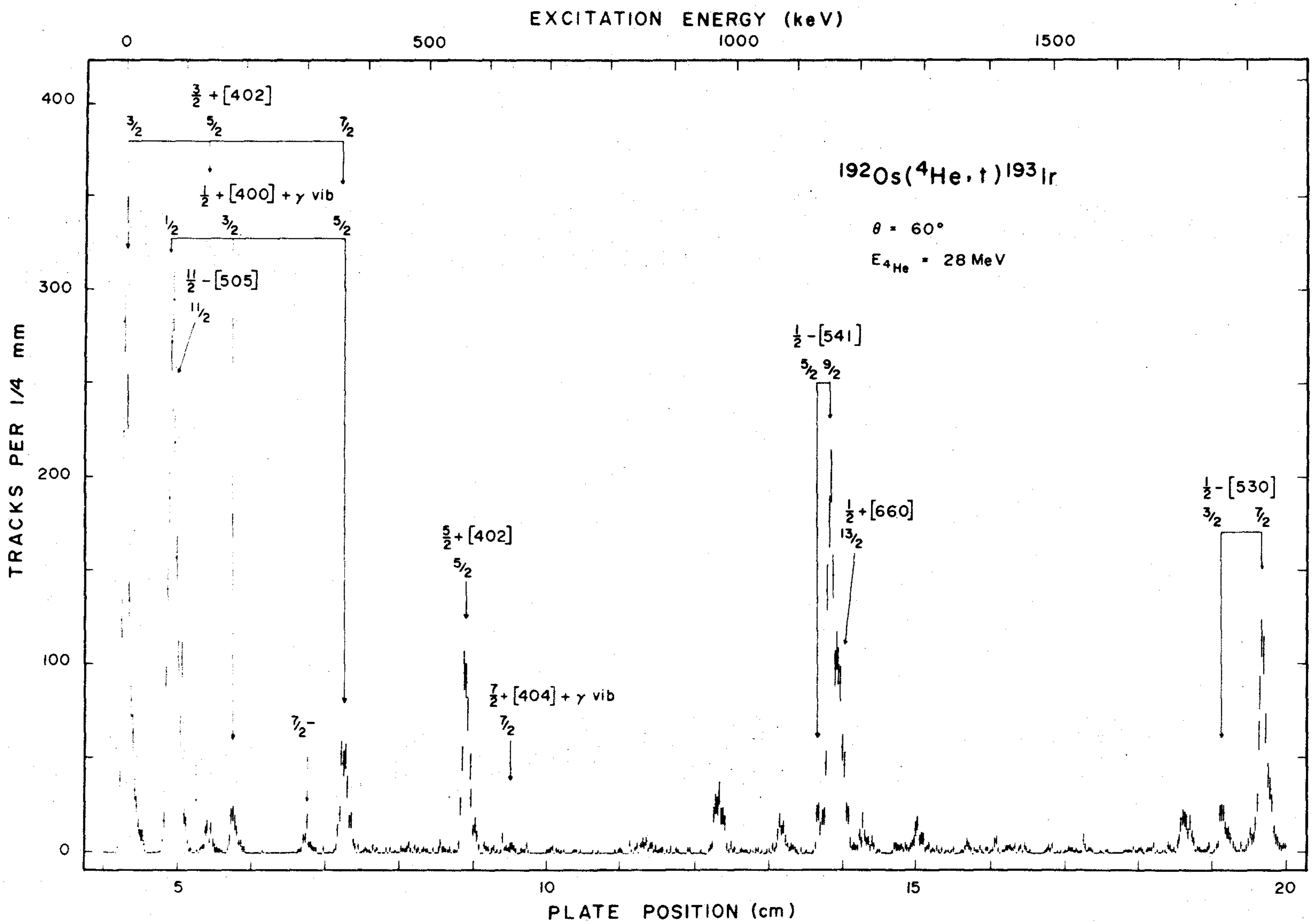

Figure 9.4 $^{192}$Os(α,t)$^{193}$Ir triton spectrum.

not interfere with each other. The triton spectra from the ($\alpha$,t) reactions were recorded at angles of $\theta = 45°$ and $\theta = 60°$ for each target. Typical ($\alpha$,t) spectra for the $^{190}$Os and $^{192}$Os targets are shown in Figs. 9.3 and 9.4 with an observed triton resolution of 12 keV.

The assignments indicated in the figures are discussed in detail in the following chapter. The 392 keV peak in the $^{191}$Ir spectra and the 299 keV peak in the $^{193}$Ir spectra represent the $7/2^-$ members of the negative parity level sequence observed in the decay studies. These states are particularly interesting since their presence may provide evidence of non-axial symmetry in the $^{191}$Ir and $^{193}$Ir nuclei.

The reaction cross sections were calculated by comparing the number of reaction events to the number of events elastically scattered from the osmium targets. This procedure has already been described in section 6.4. The elastic scattering at the $\theta = 45°$ monitor angle was taken to be 89% of the Rutherford value for 28 MeV $^3$He and 104% of the Rutherford value for 28 MeV $^4$He, as predicted by the DWBA calculations.

The average excitation energies from each reaction together with the observed ($^3$He,d) and ($\alpha$,t) cross sections are presented in tables 9.1 and 9.2 for levels in $^{191}$Ir and $^{193}$Ir respectively. For strongly populated states the uncertainties are about 3 keV in the excitation energies and 10% in the relative intensities. The uncertainties in the absolute values of the cross sections are estimated to be of the order of 25% due to difficulties in establishing the

TABLE 9.1

Levels Populated in $^{191}$Ir

| Level Energy keV | | Reaction Cross Sections σ(μb/sr) | | | |
|---|---|---|---|---|---|
| | | ($^3$He,d) | | (α,t) | |
| ($^3$He,d) | (α,t) | θ = 35° | θ = 60° | θ = 45° | θ = 60° |
| 0 | 0 | 52 | 38 | 55 | 72 |
| 83 | 83 | 61 | 33 | 18 | 32 |
| 130 | 129 | 2.2 | 2.8 | 2.5 | 4.8 |
| 174 | 173 | 20 | 19 | 49 | 61 |
| 353 | 353 | 17 | 13 | 7.5 | 13 |
| 392 | 392 | 2.2 | 2.6 | 3.0 | 3.5 |
| 591 | 591 | 26 | 18 | 14 | 20 |
| 694 | 687 | <2 | 1.0 | 1.2 | 1.0 |
| 883 | 881 | 20 | 27 | 78 | 87 |
| 978 | 977 | 16 | 11 | 3.8 | 6.3 |
| 1034 | 1033 | 33 | 19 | 1.2 | 3.5 |
| 1071 | 1068 | 8.8 | 6.9 | 2.1 | 3.5 |
| 1139 | 1136 | 12 | 6.9 | 1.6 | 2.9 |
| 1254 | | 5.2 | 5.9 | <1 | <1 |
| 1357 | 1360 | 2.6 | 2.9 | 3.0 | 2.6 |
| 1435 | 1431 | 7.3 | 8.3 | 3.9 | 3.0 |
| 1452 | 1445 | 21 | 8.3 | <2 | 2.3 |
| 1522 | 1518 | 135 | 104 | 30 | 51 |
| 1613 | | 20 | 16 | | |
| 1642 | | 33 | 20 | | |
| 1660 | | 13 | 10 | | |
| 1711 | | 16 | 10 | | |

TABLE 9.2

Levels Populated in $^{193}$Ir

| Level Energy keV | | Reaction Cross Sections $\sigma$($\mu$b/sr) | | | |
|---|---|---|---|---|---|
| | | ($^3$He,d) | | ($\alpha$,t) | |
| ($^3$He,d) | ($\alpha$,t) | $\theta$ = 30° | $\theta$ = 55° | $\theta$ = 45° | $\theta$ = 60° |
| 0 | 0 | 52 | 36 | 84 | 91 |
| 76 | 78 | 52 | 43 | 99 | 117 |
| 139 | 140 | 3.9 | 1.5 | 4.4 | 4.0 |
| 180 | 182 | 4.1 | 2.8 | 4.0 | 6.4 |
| 298 | 301 | 3.9 | 2.5 | 6.0 | 3.3 |
| 364 | 364 | 13 | 11 | 13 | 19 |
| 562 | 563 | 24 | 18 | 22 | 32 |
| 621 | 622 | <2 | 1.1 | 1.2 | 1.0 |
| 851 | 852 | 1.7 | 1.7 | 1.0 | 2.1 |
| 969 | 969 | 20 | 13 | 4.6 | 12 |
| 1072 | 1070 | 6.0 | 3.2 | 1.7 | 5.6 |
| | 1133 | | | 6.7 | 5.7 |
| 1151 | 1150 | 19 | 19 | 60 | 65 |
| 1165 | 1162 | 3.7 | 5.5 | 31 | 26 |
| 1202 | 1200 | 13 | 11 | 2.7 | 4.4 |
| 1286 | 1287 | 6.1 | 5.2 | 4.4 | 4.5 |
| 1406 | 1408 | <4 | 2.2 | 1.7 | 1.1 |
| 1698 | 1698 | 19 | 14 | 5.7 | 8.8 |
| 1760 | 1759 | 14 | 12 | 4.9 | 7.5 |
| 1821 | 1820 | 85 | 66 | 36 | 43 |
| 1970 | | | 11 | | |
| 1999 | | | 11 | | |
| 2029 | | | 7 | | |

absolute area of the elastic peak and the spectrograph and monitor solid angles.

## 9.2 The Reaction Q-Value Measurements

During each of the $(\alpha,t)$ exposures, the accompanying $(\alpha,\alpha')$ spectrum was recorded on an adjacent photographic plate. The positions of the elastic peak in this spectrum and the ground state peak in the $(\alpha,t)$ spectrum were subsequently used to determine the Q-value for the corresponding reaction.

Since the spectrograph calibration is known, the position of the elastic peak provides a measure of the effective beam energy. This value may then be combined with the position of the ground state triton peak to obtain the reaction Q-value. By using this procedure, errors in the spectrograph calibration are cancelled to a large degree through the introduction of an effective beam energy whose value need not necessarily coincide with the true beam energy.

The mean Q-value obtained for the $^{190}$Os $(\alpha,t)$ $^{191}$Ir reaction from the above procedure was found to be -14.569 ± 0.008 MeV. Similarly, the $^{192}$Os$(\alpha,t)^{193}$Ir reaction Q-value was determined as -13.923 ± 0.008 MeV. These values result in the following mass differences

$$^{191}\text{Ir} - {}^{190}\text{Os} = 2.044 \pm 0.008 \text{ MeV} + 1 \text{ amu}$$
$$^{193}\text{Ir} - {}^{192}\text{Os} = 1.398 \pm 0.008 \text{ MeV} + 1 \text{ amu.}$$

## 9.3 The DWBA Calculations

It was shown in section 4.5 that the reaction cross section for a single particle stripping reaction on an even-even target nucleus is given by

$$\frac{d\sigma}{d\Omega} = (2j + 1)\ \phi_{\ell}(\theta)\ U^2 \qquad \text{for spherical nuclei} \qquad 9.1$$

$$\frac{d\sigma}{d\Omega} = 2c^2_{j\ell}\ \phi_{\ell}(\theta)\ U^2 \qquad \text{for deformed nuclei} \qquad 9.2$$

where $\phi_{\ell}(\theta)$ is the DWBA cross section.

A series of DWBA calculations were carried out using the computer code DWUCK, developed by Kunz at the University of Alberta. The optical model parameters used for these calculations are shown in table 9.3. The parameters are similar to those found by Lu and Alford (1970) as giving reasonable fits to observed angular distributions in the odd-A rhenium isotopes. A local, zero-range potential and a lower cut-off of 9.6 fm were used in all the calculations since this cut-off was observed to be particularly important in the rhenium ($^3$He,d) studies.

The calculated ($^3$He,d) cross sections were multiplied by the appropriate zero-range renormalization factor of N = 4.42. Some of the calculated ($^3$He,d) angular distributions are displayed in Fig 9.5. For the ($\alpha$,t) calculations, a zero-range renormalization factor of N = 46 was assumed although this value is subject to considerable uncertainty (Hering et al (1970)). Typical ($\alpha$,t) angular distributions are presented in Fig. 9.6.

## 9.4 Determination of $\ell$-Values

In the rhenium studies mentioned above, it was observed that

## TABLE 9.3

### Optical Model Parameters Used in DWBA Calculations

| | | $V_o$ MeV | $r_o$ fm | a fm | $W_o$ MeV | $W_D$ MeV | $r_o'$ fm | a' fm | $V_{s_o}$ factor | $r_{oc}$ fm | $a_c$ fm |
|---|---|---|---|---|---|---|---|---|---|---|---|
| | $^3$He | -175 | 1.14 | 0.723 | -17.5 | 0 | 1.60 | 0.810 | 0 | 1.40 | 0.723 |
| ($^3$He,d) | d | -111 | 1.05 | 0.859 | 0 | +70.8 | 1.24 | 0.794 | 0 | 1.25 | 0.859 |
| | bound state proton | adjusted to reproduce separation energy | 1.25 | 0.650 | 0 | 0 | 0 | 0 | 8 | 1.25 | 0.650 |
| | α | -200 | 1.40 | 0.60 | -20 | 0 | 1.40 | 0.60 | 0 | 1.30 | 0 |
| (α,t) | t | -200 | 1.40 | 0.60 | -50 | 0 | 1.40 | 0.60 | 0 | 1.30 | 0 |
| | bound state proton | adjusted to reproduce separation energy | 1.25 | 0.65 | 0 | 0 | 0 | 0 | 8 | 1.25 | 0.65 |

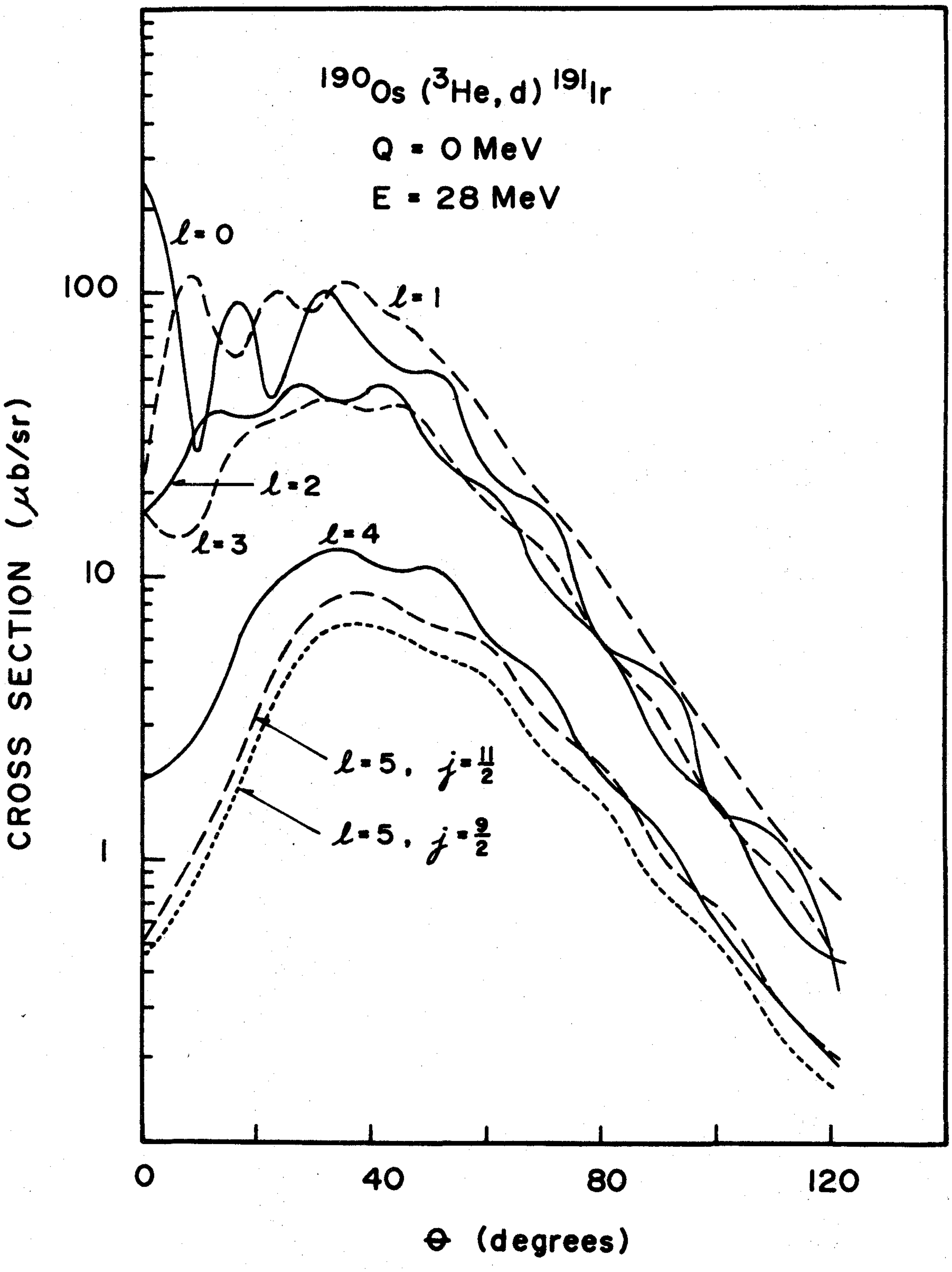

Figure 9.5 DWBA calculations for the $^{190}$Os($^3$He,d)$^{191}$Ir reaction at 28 MeV and Q = 0 MeV.

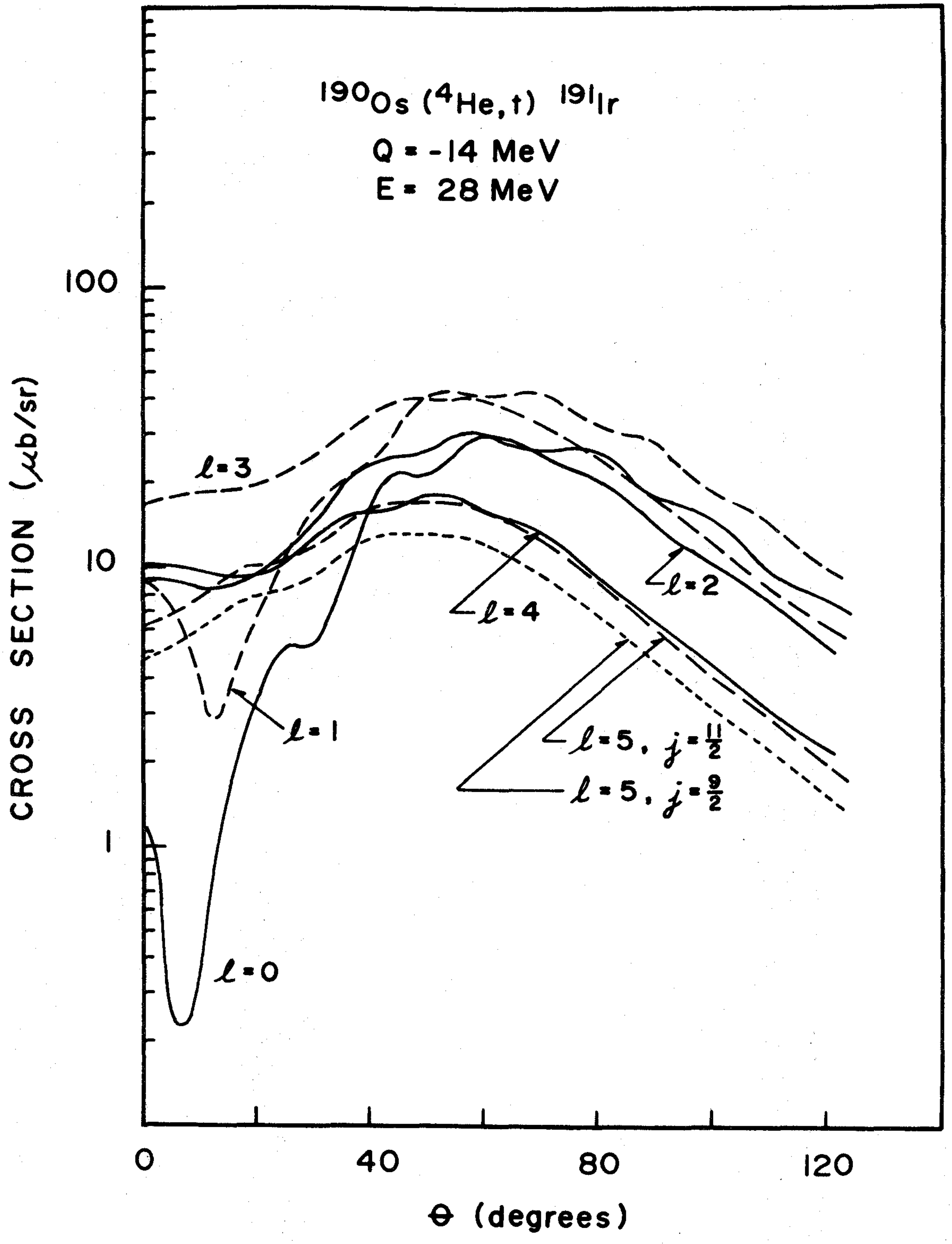

Figure 9.6 DWBA calculations for the $^{190}$Os(α,t)$^{191}$Ir reaction at 28 MeV and Q = -14 MeV.

the ratio of ($^3$He,d) to ($\alpha$,t) cross sections can be a useful indicator of $\ell$-value. The basis of this behaviour is demonstrated in Figs. 9.5 and 9.6 which reveal an $\ell$ dependence for the DWBA cross sections which is quite different in the two reactions. Consequently this ratio can be a fairly good indicator of $\ell$-value, particularly at forward angles.

The ($^3$He,d) to ($\alpha$,t) cross section ratios for various $\ell$-values have been calculated from the DWBA cross sections. Although the individual cross sections exhibit a slight j dependence, the calculated ratios are found to be quite insensitive to j-value. Figs. 9.7 and 9.8 show these ratios as a function of excitation energy for $^{191}$Ir and $^{193}$Ir respectively. Since the DWBA calculations of the ($\alpha$,t) cross section are subject to considerable uncertainty for absolute cross sections, the calculated ratios have been normalized to the measured ratios for the $\ell = 2$, $j = 3/2$ transition to the ground states of $^{191}$Ir and $^{193}$Ir. A single normalizing factor has been applied to both isotopes. The experimental ratios, together with their statistical uncertainties, are shown on the normalized curves of Figs. 9.7 and 9.8 for those states whose $\ell$-value is known. Agreement between the calculated and measured ratios is quite satisfactory and often is sufficient to uniquely define the $\ell$-value.

By using this comparison procedure, it has been possible to assign $\ell$-values to most of the states observed in the present work. The experimental and calculated cross section ratios, together with the deduced $\ell$-values, are shown in tables 10.2 and 10.3 of the following chapter.

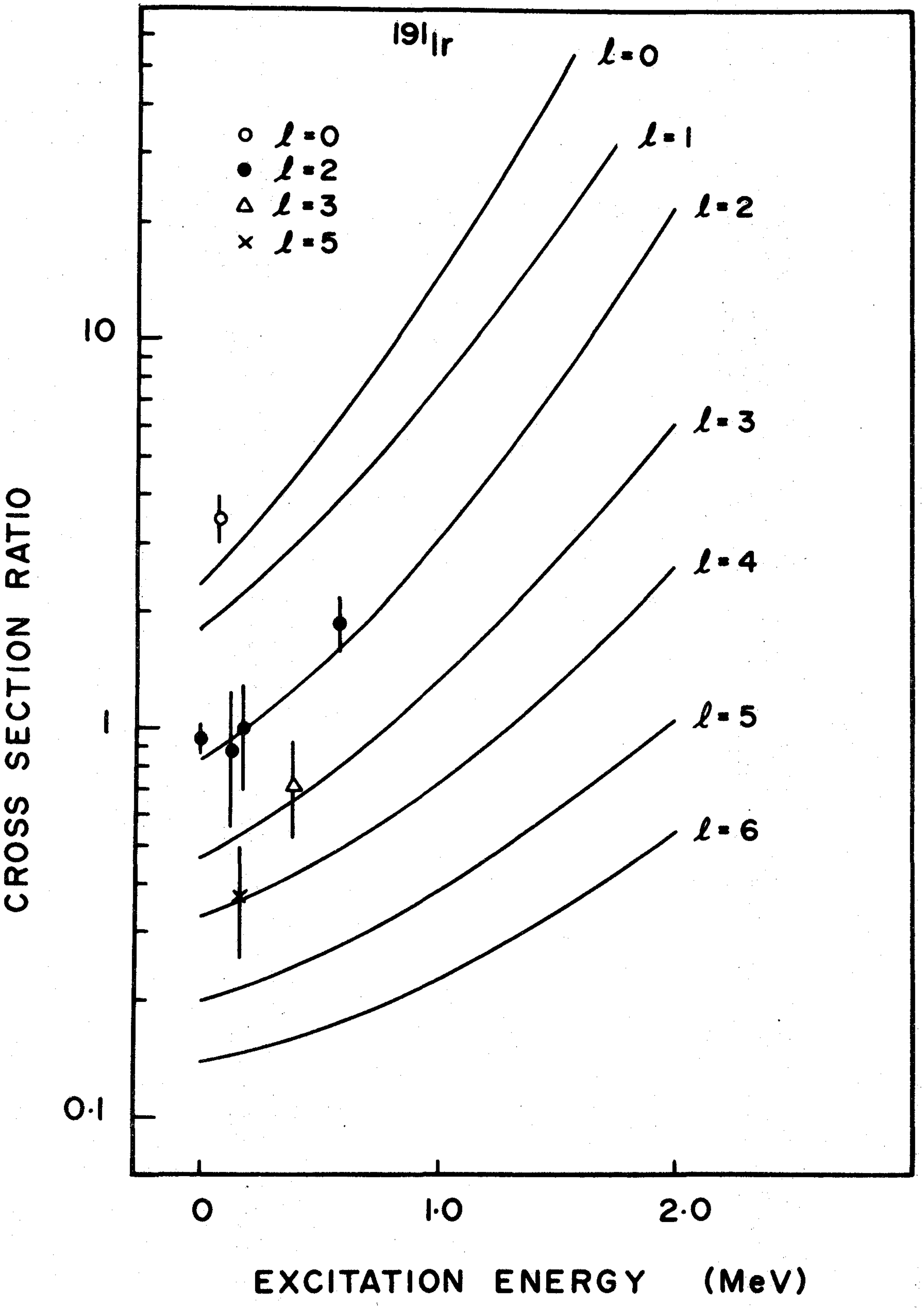

**Figure 9.7** Ratio of ($^3$He,d) to ($\alpha$,t) cross sections as a function of excitation energy for $^{191}$Ir.

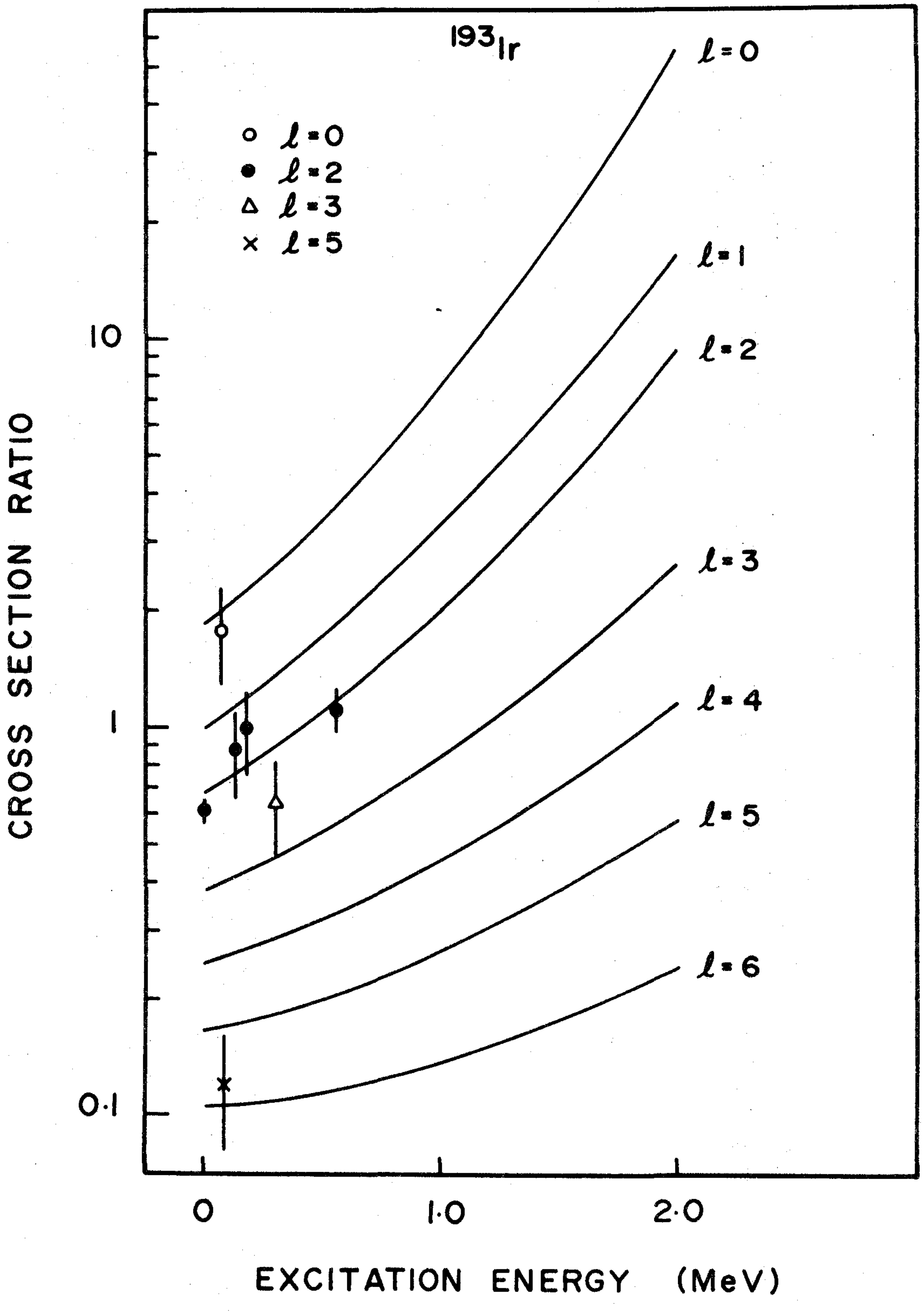

Figure 9.8 Ratio of ($^{3}$He,d) to (α,t) cross sections as a function of excitation energy for $^{193}$Ir.

## 9.5 Extraction of the Spectroscopic Factors

It is common practice to extract spectroscopic factors from the data by normalizing to a prominent state in the spectrum whose spectroscopic factor is thought to be known from a nuclear model. For the present work, such a procedure is to be avoided since the iridium nuclei lie in a region where neither the Nilsson model nor the shell model is expected to work well. In fact, one of the principal aims of this investigation is to determine whether a spherical or deformed description of these nuclei is most appropriate.

The ($^3$He,d) zero-range renormalization factor of N = 4.42 is expected to be accurate to within 20%. This expectation is verified by several recent works. Lu and Alford (1970) have found from the odd-A rhenium studies that this factor needs to be multiplied by 1.08 - 1.2 to agree with their normalized values while O'Neil et al (1971) obtain a multiplying factor of 0.78 from studies of the lutetium isotopes. Both results confirm the expected value to within the experimental uncertainties and consequently this value of N = 4.42 has been used to extract spectroscopic factors from the present ($^3$He,d) measurements.

Since the zero-range renormalization factor for the ($\alpha$,t) calculations is subject to considerable uncertainty, the ($\alpha$,t) spectroscopic factors have been obtained by normalizing to the ground state spectroscopic factors obtained from the ($^3$He,d) measurements with a single normalizing factor used for all the data. In order to achieve this normalization, it was necessary to multiply the DWBA cross sections for the ($\alpha$,t) reaction by a factor of N = 118, rather than the expected value of $N = 46$.

## 9.6 Shell Model Versus Nilsson Model for the Iridium Isotopes

Equations 9.1 and 9.2 show that a comparison between the experimental and calculated cross section provides a measure of the effective spectroscopic factor $(2j + 1)\ U^2$ or $2c^2_{j\ell}\ U^2$, depending on whether the shell model or Nilsson model is applicable. Since $U^2$ is approximately unity for unoccupied states, stripping into such states may be used to determine whether the states are best described in terms of a spherical or deformed nuclear model. If the spherical description is valid, then values greater than 2 should be observed, whereas values less than 2 are expected if the deformed description applies. Table 9.4 shows the values of these effective spectroscopic factors for states of known spin and parity in $^{191}$Ir and $^{193}$Ir. It is immediately noticed that none of the values are larger than 2 and it is concluded that the shell model states are severely fragmented in the iridium nuclei. It will be shown in the next chapter that this fragmentation apparently obeys a Nilsson description.

TABLE 9.4

Spectroscopic Factors for States of Known Spin in $^{191}$Ir and $^{193}$Ir

| | Energy | Spin | Observed Spectroscopic Factor $(2j+1)\,U^2$ from ($^3$He,d) | or | $2c_{j\ell}^2\,U^2$ from ($\alpha$,t) |
|---|---|---|---|---|---|
| $^{191}$Ir | 0 | $3/2^+$ | 1.39 | | 1.39[a)] |
| | 82 | $1/2^+$ | 0.80 | | 0.61 |
| | 129 | $5/2^+$ | 0.07 | | 0.07 |
| | 171 | $11/2^-$ | 1.73 | | 1.41 |
| | 179 | $3/2^+$ | 0.11 | | 0.11 |
| | 391 | $7/2^-$ | 0.07 | | 0.06 |
| | 588 | $5/2^+$ | 0.50 | | 0.52 |
| $^{193}$Ir | 0 | $3/2^+$ | 1.34 | | 1.34[a)] |
| | 73 | $1/2^+$ | 0.50 | | 0.48 |
| | 80 | $11/2^-$ | 1.43 | | 1.78 |
| | 139 | $5/2^+$ | 0.07 | | 0.07 |
| | 180 | $3/2^+$ | 0.09 | | 0.09 |
| | 299 | $7/2^-$ | 0.08 | | 0.05 |
| | 559 | $5/2^+$ | 0.49 | | 0.51 |

a) Normalized to ($^3$He,d) value using a normalizing factor 2.56 obtained from average of $^{191}$Ir and $^{193}$Ir.

# CHAPTER X

# DISCUSSION OF RESULTS

## 10.1 Nilsson and Coriolis Mixing Calculations

The identification of Nilsson states is often based upon the characteristic distribution of reaction strength among the rotational band members, as described by the coefficients $c^2_{j\ell}$. For many of the proton states in the iridium mass region, the value of $c^2_{j\ell}$ is nearly unity for one particular band member with the result that only a single strong peak occurs in the rotational spectrum. In these cases, identification of the band relies upon the observed $\ell$ transfer and transition strength and, in addition, upon the predictions of the Nilsson model as to the location of the state.

In order to estimate the relative positions of the Nilsson states, calculations were performed using a Nilsson program due originally to Chi (1967), but modified in the manner prescribed by Lamm (1969). The recommended well parameters of $\kappa = 0.0637$ and $\mu = 0.600$ were used for all the single proton orbitals. A deformation of $\delta = 0.125$ was assumed for both $^{191}$Ir and $^{193}$Ir, corresponding to the average value obtained for these nuclei from measurements of B(E2) values in the ground state bands (Norgaard et al (1971)).

The calculations were carried out for all states expected in the region of the 77th proton and are shown in Fig. 10.1 with energies defined relative to the $3/2^+$ [402] ground state. In this region, a variety of states arise from the N = 5 and N = 6 shells as well as from the N = 4 shell. Since the Nilsson calculation is only expected to yield reliable energy spacings within any particular shell, a realistic result may require shifting the N = 5 and N = 6 states relative to those of the N = 4 shell. Unfortunately, there is a scarcity of experimental evidence to indicate the appropriate shifts required. However for the odd-A rhenium nuclei, it has been experimentally determined that the $9/2^-$ [514] orbital occurs below the $5/2^+$ [402] state (Lu and Alford (1970)). To reproduce this observed behaviour, all of the states arising from the $h_{11/2}$ shell have been depressed by 700 keV as indicated by the dashed lines in Fig. 10.1. It is emphasized that these shifts are introduced only to make the calculation as realistic as possible since the $9/2^-$ and $7/2^-$ members of the $h_{11/2}$ shell are not likely to be populated in the present experiments.

There is one remaining adjustment to the calculations of Fig. 10.1 which is necessary in order to reproduce the observed $3/2^+$ ground state for $^{191}$Ir and $^{193}$Ir. From the general Nilsson diagram presented in chapter I it is observed that the $11/2^-$ [505] orbital is expected to form the ground state for the iridium isotopes. However this orbital is not observed as a ground state in any known nucleus, presumably as a result of strong pairing interactions involving the state. In an attempt to compensate for this pairing, the effective position of the $11/2^-$ [505] state has been elevated by $2\Delta$ = 1900 keV.

The pairing formalism discussed in section 2.1 has been used to obtain the emptiness factor $U^2$ and the single-quasi-particle energies. A gap parameter of $\Delta = 950$ keV is indicated from the odd-even mass differences and this value was used in the calculations. The Fermi surface, which represents the only free parameter of the pairing calculations, was placed 400 keV below the unperturbed $3/2^+$ [402] band head. The emptiness factor $U^2$ obtained from these calculations is shown as a function of the single-particle energy in Fig. 10.1.

An average rotational parameter of $\frac{\hbar^2}{2\mathcal{J}} = 35$ keV is observed for the even-even osmium isotopes and this value has been used to form the rotational structure in $^{191}$Ir and $^{193}$Ir. The rather large value of this inertial parameter indicates that these transitional nuclei do not exhibit large deformations. The spectrum obtained from the Nilsson plus pairing calculations is shown in Fig. 10.2a, while the corresponding spectroscopic factors are given in column two of table 10.1.

Since Coriolis interactions may be important in this mass region, band mixing calculations were carried out using the Coriolis matrix elements of section 2.3. The following positive parity orbitals were included in the calculation: $7/2^+$ [404], $5/2^+$ [402], $1/2^+$ [411], $3/2^+$ [402] and $1/2^+$ [400]. The results indicate that only slight mixing occurs for these states, producing rather minor changes in their properties. The negative parity orbitals considered in the mixing calculation were: $9/2^-$ [514], $11/2^-$ [505], $1/2^-$ [541],

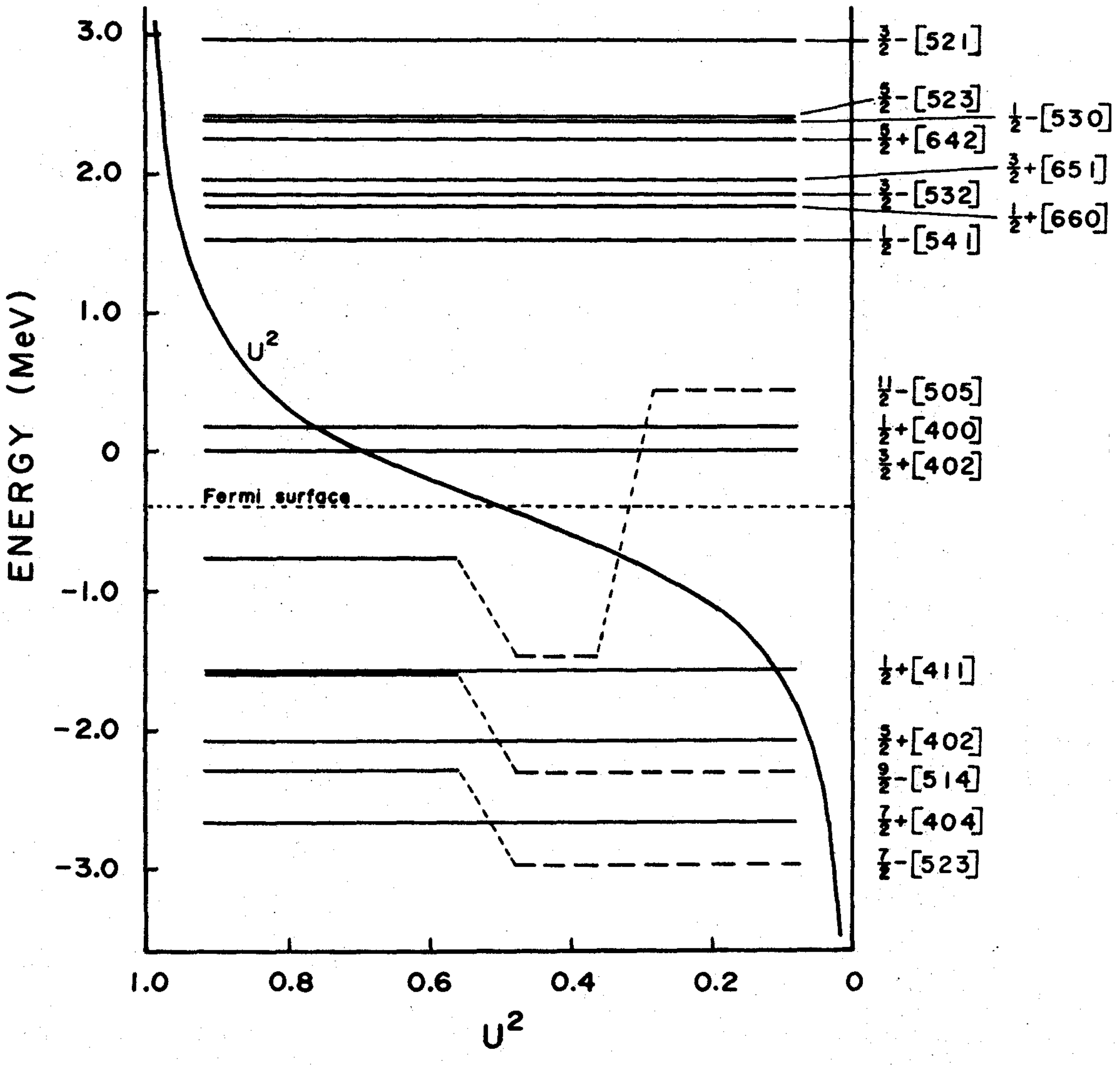

**Figure 10.1** Single-particle levels obtained from the Nilsson calculation using $\kappa = 0.0637$, $\mu = 0.600$, $\delta = 0.125$. The dashed levels have been shifted as discussed in the text. Also shown are the results of the pairing calculation using $\Delta = -400$ keV.

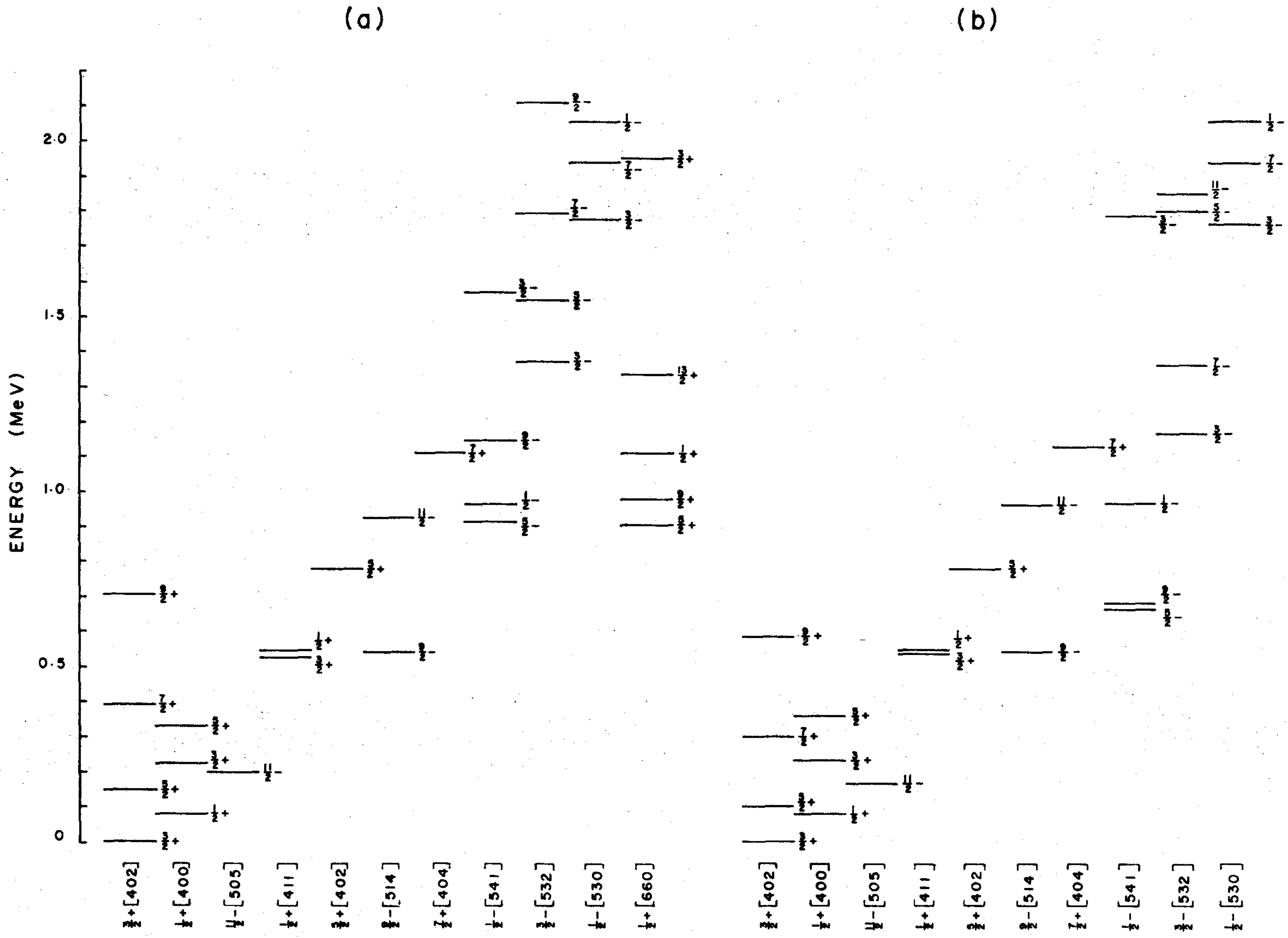

Figure 10.2 The spectrum obtained from Nilsson and pairing calculations assuming an inertial parameter of 35 keV with a) no band mixing b) full strength band mixing included.

## TABLE 10.1

Predicted Spectroscopic Factors With and Without the Inclusion of Coriolis Coupling

| State | Unperturbed $c_{j\ell}^2\ U^2$ | Perturbed[a] $c_{j\ell}^2\ U^2$ |
|---|---|---|
| 7/2 $7/2^+$ [404] | 0.04 | 0.03 |
| 9/2 | <0.01 | <0.01 |
| 9/2 $9/2^-$ [514] | <0.01 | <0.01 |
| 11/2 | 0.05 | <0.01 |
| 5/2 $5/2^+$ [402] | 0.062 | 0.06 |
| 7/2 | 0.002 | 0.01 |
| 9/2 | <0.001 | <0.01 |
| 1/2 $1/2^+$ [411] | 0.02 | 0.02 |
| 3/2 | 0.07 | 0.02 |
| 5/2 | <0.01 | <0.01 |
| 7/2 | <0.01 | <0.01 |
| 9/2 | <0.01 | <0.01 |
| 3/2 $3/2^+$ [402] | 0.66 | 0.81 |
| 5/2 | 0.02 | <0.01 |
| 7/2 | 0.02 | 0.03 |
| 9/2 | <0.01 | <0.01 |
| 1/2 $1/2^+$ [400] | 0.55 | 0.55 |
| 3/2 | 0.17 | 0.07 |
| 5/2 | 0.03 | 0.05 |
| 7/2 | <0.01 | <0.01 |
| 9/2 | <0.01 | <0.01 |
| 11/2 $11/2^-$ [505] | 0.83 | 0.87 |
| 1/2 $1/2^-$ [541] | <0.01 | <0.01 |
| 3/2 | <0.01 | 0.05 |
| 5/2 | 0.06 | 0.09 |
| 7/2 | 0.01 | <0.01 |
| 9/2 | 0.87 | 1.64 |
| 11/2 | <0.01 | <0.01 |
| 3/2 $3/2^-$ [532] | <0.01 | <0.01 |
| 5/2 | 0.04 | <0.01 |
| 7/2 | 0.03 | 0.04 |
| 9/2 | 0.89 | 0.12 |
| 11/2 | <0.01 | <0.01 |
| 1/2 $1/2^-$ [530] | <0.01 | <0.01 |
| 3/2 | 0.10 | 0.04 |
| 5/2 | <0.01 | <0.01 |
| 7/2 | 0.82 | 0.83 |
| 9/2 | 0.02 | 0.02 |
| 11/2 | 0.03 | 0.03 |
| 1/2 $1/2^+$ [660] | <0.01 | |
| 3/2 | <0.01 | |
| 5/2 | <0.01 | |
| 7/2 | <0.01 | |
| 9/2 | 0.02 | |
| 11/2 | <0.01 | |
| 13/2 | 0.93 | |

[a] Values obtained using full strength band mixing.

## TABLE 10.2

### Spectroscopic Information for $^{191}$Ir

| State | Energy (keV) | Experimental ($^3$He,d) to ($\alpha$,t) cross Section Ratio | Assigned $\ell$ | Calculated Cross Section Ratio for Assigned $\ell$ | $c_{j\ell}^2 U^2$ | | |
|---|---|---|---|---|---|---|---|
| | | | | | From ($^3$He,d) | From ($\alpha$,t) | Predicted[a)] |
| 3/2 3/2$^+$ [402] | 0 | 0.95 | 2 | 0.83 | 0.70 | 0.70[b)] | 0.75 |
| 1/2 1/2$^+$ [400] | 83 | 3.48 | 0 | 2.63 | 0.40 | 0.31 | 0.55 |
| 5/2 3/2$^+$ [402] | 129 | 0.88 | 2 | 0.94 | 0.04 | 0.04 | 0.01 |
| 11/2 11/2$^-$ [505] | 171 | 0.38 | 5 | 0.22 | 0.87 | 0.71 | 0.85 |
| 3/2 1/2$^+$ [400] | 179 | 1.00 | 2 | 0.99 | 0.06 | 0.06 | 0.12 |
| 7/2 3/2$^+$ [402] | 353 | 2.29 | 4 | 0.41 | 0.79[c)] | 0.21[c)] | 0.02 |
| 5/2 1/2$^+$ [400] | | | 2 | 1.20 | 0.19[c)] | 0.13[c)] | 0.04 |
| 5/2 5/2$^+$ [402] | 591 | 1.89 | 2 | 1.64 | 0.25 | 0.26 | 0.06 |
| 7/2 7/2$^+$ [404] | 690 | | 4 | 0.54 | 0.03 | 0.03 | 0.03 |
| 9/2 1/2$^-$ [541] | 882 | 0.26 | 5 | 0.35 | 1.46[c)] | 2.08[c)] | 1.44 |
| 13/2 1/2$^+$ [660] | | | 6 | 0.21 | 1.66[c)] | 1.65[c)] | 0.93 |
| 3/2 1/2$^-$ [530] | 1449 | 10.4 | 1 | 17.3 | 0.06 | 0.09 | 0.10 |
| 7/2 1/2$^-$ [530] | 1520 | 4.46 | 3 | 2.81 | 1.13 | 0.85 | 0.82 |
| I = 7/2 | 392 | 0.73 | 3 | 0.66 | 0.04 | 0.03 | |
| | 978 | 4.11 | 2 | | | | |
| | 1034 | 27.2 | 0 | | | | |
| | 1070 | 4.19 | 2 | | | | |
| | 1138 | 7.50 | 1 or 2 | | | | |
| | 1359 | 0.87 | 4 or 5 | | | | |
| | 1433 | 1.87 | 3 or 4 | | | | |

a) Values obtained using an attenuation factor of 0.5 for the Coriolis matrix elements.

b) Normalized to ($^3$He,d) value using a normalizing factor 2.56 obtained from average of $^{191}$Ir and $^{193}$Ir.

c) Spectroscopic factor obtained when the entire cross section is assumed to be of the assigned $\ell$.

## TABLE 10.3

### Spectroscopic Information for $^{193}$Ir

| State | Energy (keV) | Experimental ($^3$He,d) to ($\alpha$,t) cross Section Ratio | Assigned $\ell$ | Calculated Cross Section Ratio for Assigned $\ell$ | $c^2_{j\ell}\ U^2$ | | |
|---|---|---|---|---|---|---|---|
| | | | | | From ($^3$He,d) | From ($\alpha$,t) | Predicted[a)] |
| 3/2 $3/2^+$ [402] | 0 | 0.61 | 2 | 0.68 | 0.67 | 0.67[b)] | 0.75 |
| 1/2 $1/2^+$ [400] | 73 | 1.79 | 0 | 2.00 | 0.25 | 0.24 | 0.55 |
| 11/2 $11/2^-$ [505] | 80 | 0.12 | 5 | 0.17 | 0.72 | 0.89 | 0.85 |
| 5/2 $3/2^+$ [402] | 139 | 0.89 | 2 | 0.77 | 0.04 | 0.04 | 0.01 |
| 3/2 $1/2^+$ [400] | 181 | 1.03 | 2 | 0.80 | 0.05 | 0.05 | 0.12 |
| 7/2 $3/2^+$ [402] | 364 | 1.03 | 4 | 0.30 | 0.64[c)] | 0.25[c)] | 0.02 |
| 5/2 $1/2^+$ [400] | | | 2 | 0.95 | 0.15[c)] | 0.13[c)] | 0.04 |
| 5/2 $5/2^+$ [402] | 562 | 1.12 | 2 | 1.18 | 0.25 | 0.26 | 0.06 |
| 7/2 $7/2^+$ [404] | 621 | | 4 | 0.35 | 0.03 | 0.02 | 0.03 |
| 5/2 $1/2^-$ [541] | 1133 | | 3 | 0.97 | | 0.06 | 0.09 |
| 9/2 $1/2^-$ [541] | 1150 | 0.32 | 5 | 0.30 | 1.33 | 1.31 | 1.44 |
| 13/2 $1/2^+$ [660] | 1163 | 0.12 | 6 | 0.15 | 0.44 | 0.50 | 0.93 |
| 3/2 $1/2^-$ [530] | 1760 | 2.88 | 1 | 10.7 | 0.05 | 0.15 | 0.10 |
| 7/2 $1/2^-$ [530] | 1821 | 2.37 | 3 | 2.10 | 0.72 | 0.61 | 0.82 |
| I = 7/2 | 299 | 0.65 | 3 | 0.47 | 0.04 | 0.03 | |
| | 969 | 4.39 | 0 or 1 | | | | |
| | 1071 | 3.53 | 1 or 2 | | | | |
| | 1201 | 4.85 | 1 | | | | |
| | 1286 | | 3 | | | | |
| | 1698 | 3.40 | 2 or 3 | | | | |

[a)] Values obtained using an attenuation factor of 0.5 for the Coriolis matrix elements.

[b)] Normalized to ($^3$He,d) value using a normalizing factor 2.56 obtained from average of $^{191}$Ir and $^{193}$Ir.

[c)] Spectroscopic factor obtained when the entire cross section is assumed to be of the assigned $\ell$.

$3/2^-$ [532] and $1/2^-$ [530]. The $1/2^-$ [541] and $3/2^-$ [532] orbitals undergo particularly strong mixing, which is manifest in rather dramatic changes to the energies and spectroscopic factors for these states. The $5/2^-$ [523] and $3/2^-$ [521] states, which are expected to occur at high excitation energy, have been excluded from the calculation since a better description is obtained when these states are not present. The absence of coupling effects involving the $3/2^-$ [521] orbital probably indicates that at high excitations, this state ceases to exist in a form capable of treatment by the Nilsson description.

The mixing calculations have been performed using various attenuating factors for the Coriolis matrix elements. The results obtained using full strength Coriolis interactions are shown in the form of the energy spectrum of Fig. 10.2b and the corresponding spectroscopic factors listed in column three of table 10.1.

A comparison of the experimental spectroscopic factors with the model calculations clearly shows that band mixing must be included in the Nilsson description if the observed properties are to be successfully reproduced. The magnitude of the required mixing is found to be approximately half that of the full strength interaction and consequently the predicted spectroscopic factors of tables 10.2 and 10.3 have been obtained using an attenuation factor of 0.5 for the Coriolis matrix elements.

## 10.2 Interpretation of the Results

In recent works, the low-lying states in the iridium isotopes have been described either in terms of core excitations based upon the $d_{3/2}$ shell model state (Avida et al (1968)) or in terms of a Nilsson description (Berg et al (1970)). Success has been claimed for both models and it therefore has remained an open question as to whether the ground state should be attributed to the $d_{3/2}$ shell state or the $3/2^+$ [402] Nilsson orbital. In section 9.6 it was concluded that the extreme single-particle model is not applicable to the iridium isotopes. In the present section it will be shown that the Nilsson model provides a surprisingly good description for many of the states in these nuclei.

### The $3/2^+$ [402] Orbital

This orbital is found as the ground state of the $^{191}$Ir and $^{193}$Ir isotopes. The only rotational member of this orbital which exhibits a large spectroscopic factor is the I = 3/2 band head, for which $c_{j\ell}^2 = 0.95$. The values of $c_{j\ell}^2 U^2$ deduced from the measured cross sections are found in tables 10.2 and 10.3, and for the ground states of $^{191}$Ir and $^{193}$Ir are observed to be 0.70 and 0.67 respectively. These values were extracted from the ($^3$He,d) measurements and have been used in normalizing the ($\alpha$,t) values, as discussed previously. Since the values are larger than one-half of $c_{j\ell}^2$, the Fermi level must be located below the $3/2^+$ [402] orbital.

The $5/2^+$ and $7/2^+$ members of the $3/2^+$ [402] rotational band have been established in the radioactive decay and Coulomb excitation studies, and are expected to have values of $c_{j\ell}^2 U^2 \sim 0.02$. The $5/2^+$ member is observed in both nuclei with experimental $c_{j\ell}^2 U^2$ values of 0.04 which, considering the small cross sections involved, are in good agreement with expectation. The $7/2^+$ member cannot be resolved from the 5/2 $1/2^+$ [400] state in either nucleus. The $9/2^+$ member of the band has a negligible value of $c^2_{j\ell}\ U^2$ and consequently these states are not observed in the reaction studies, although their positions are known from the Coulomb excitation experiments reported in sections 7.5 and 8.5. The present results establish with certainty the $3/2^+$ [402] assignment for the $^{191}$Ir and $^{193}$Ir ground state bands.

## The $1/2^+$ [400] Orbital and ($K_o$-2) Gamma Vibration

In the radioactive decay studies, states are established at 82 and 73 keV in $^{191}$Ir and $^{193}$Ir respectively, which may be attributed to the $1/2^+$ [400] orbital. The cross section to these I = 1/2 band heads is expected to be reasonably large since their $c^2_{j\ell}\ U^2$ value is predicted to be 0.55. These states are observed in the present reaction data with $c^2_{j\ell}\ U^2$ values of 0.40 and 0.31 in $^{191}$Ir and 0.25 and 0.24 in $^{193}$Ir. As the experimental values are only about half that expected for a pure $1/2^+$ [400] band, it is concluded that in each nucleus the states are composed of the $1/2^+$ [400] orbital together with an equal contribution of the ($K_o$-2) gamma vibration built upon the ground state. This conclusion is supported by the internal conversion data which reveals abnormally large E2 admixtures in the 82 and 73 keV transitions and by the Coulomb excitation data in which the members of this band are rather strongly populated. From recent inelastic deuteron scattering measurements, Norgaard et al (1971) have similarly identified the ($K_o$-2) gamma vibration with the $1/2^+$ [400] state.

Although no calculations are available for the iridium isotopes, Soloviev and Vogel (1967) have performed microscopic quasi-particle calculations which include the interaction of quasi-particles with phonons. This leads to vibrational admixtures in the one-quasi-particle states, in addition to the predominently collective phonon states. In most cases the vibrational admixtures are small and the results reduce to those of the usual independent quasi-particle model (i.e Nilsson model with pairing). However in other cases the vibrational components may be quite large. For the rhenium isotopes, the calculations predict an appreciable vibrational admixture in the $1/2^+$ [400] one-quasi-particle state. Presumably the calculations would also predict similar mixtures for the $1/2^+$ [400] band in the iridium isotopes.

The $3/2^+$ member of the $1/2^+$ [400] band appears at 179 and 180 keV in $^{191}$Ir and $^{193}$Ir respectively. Although these states are predicted to have a $c_{j\ell}^2 U^2$ value of 0.12, the observed values are expected to be somewhat smaller because of the vibrational admixtures. The experimental values of 0.06 for $^{191}$Ir and 0.05 for $^{193}$Ir are in good agreement with these expectations.

The $5/2^+$ member of the $1/2^+$ [400] band and the $7/2^+$ member of the $3/2^+$ [402] band form an unresolved doublet in the reaction data, whose respective component energies of 351 and 343 keV in $^{191}$Ir and 362 and 358 keV in $^{193}$Ir are precisely established from the decay studies. In each case, the observed centroid of the doublet corresponds to the upper member, suggesting that most of the cross section is associated with the 5/2 $1/2^+$ [400] state. However, it is observed that regardless of how the strength is divided, the combined strength to these states is several times larger than expected. The source of this discrepancy, which persists for both $^{191}$Ir and $^{193}$Ir, is unknown. The remaining members of the $1/2^+$ [400] band are predicted to have very small cross sections and have not been observed.

## The $11/2^-$ [505] Orbital

From conversion electron studies, the $11/2^-$ [505] state is observed to form isomers at 171 keV in $^{191}$Ir and 80 keV in $^{193}$Ir. It has already been remarked that in the absence of pairing, this state would be expected to be the ground state of the iridium isotopes. To simulate this effect in the calculations, the $11/2^-$ [505] orbital has been somewhat arbitrarily lifted above the $3/2^+$ [402] state, which is observed to form the true ground state. Although this shift was performed in order to reproduce the observed level ordering, the resulting calculation of the spectroscopic factor gives a value in good agreement with the values extracted from the experiments. The value of $c_{j\ell}^2\ U^2$ is calculated to be 0.85 as compared to experimental values of 0.71 and 0.87 for $^{191}$Ir and 0.72 and 0.89 for $^{193}$Ir. The $11/2^-$ [505] isomer assignments are thus verified by the present work.

## The $5/2^+$ [402] Orbital

A $5/2^+$ state is identified at 588 keV in $^{191}$Ir and 559 keV in $^{193}$Ir from the radioactive decay work. These states are also populated in the present reaction studies with $c_{j\ell}^2\ U^2$ values of 0.25 and 0.26

for both nuclei. The only available $5/2^+$ state in this region is the $5/2^+$ [402] band head which forms the ground state of the rhenium isotopes and consequently is expected to appear as a hole state in the iridium isotopes. Since the calculated value of $c_{j\ell}^2$ for this band head is 0.96 and the observed values of $c_{j\ell}^2 U^2$ are less than one-half of this value, the observed levels may be assigned to the 5/2 $5/2^+$ [402] hole state.

From the model calculations we find $c_{j\ell}^2 U^2$ to be 0.06 which is considerably smaller than the observed values. This might suggest that the $5/2^+$ [402] state is located closer to the Fermi surface than predicted by the calculations. Although a small shift in this direction also causes some improvement in the predicted position of the state, a shift of the magnetude necessary to produce agreement between the spectroscopic factors lowers the calculated energy so far as to create a serious disagreement with experiment. A more realistic explanation may be provided by the pairing interactions involving the $11/2^-$ [505] state. It has already been seen that a rather arbitrary elevation of this state is necessary to account for its observed properties. If it is supposed that there is an appreciable probability that, in their ground states, the iridium nuclei have the $11/2^-$ [505] orbital occupied by a pair of protons at the expense of leaving the nearby $5/2^+$ [402] orbital empty, then one can not only explain the enhanced spectroscopic factor for the $5/2^+$ [402] orbital but also the observed $3/2^+$ ground state since the odd proton would then be deposited into the $3/2^+$ [402] orbital. One might object that if the spectroscopic factor for the $5/2^+$ [402] orbital is enhanced, then that of the $11/2^-$ [505]

orbital should be similarly retarded. However the $9/2^-$ [514] orbital, which is expected to occur in this region, will have nearly all of its strength drained into the $11/2^-$ [505] orbital due to strong Coriolis coupling. Because of this depletion of strength, the $9/2^-$ [514] orbital will not be located in these studies and any compensating effect that it might have on the $11/2^-$ [505] orbital cannot be determined.

Only negligible spectroscopic strength is expected in the higher spin members of the $5/2^+$ [402] band, and these states are not observed. On the basis of the arguments presented above, it is concluded that the $5/2^+$ [402] hole state is identified in both $^{191}$Ir and $^{193}$Ir.

### The $1/2^+$ [411] Orbital

The $1/2^+$ [411] orbital is expected to appear as a hole state with the I = 1/2 and I = 3/2 members inverted. According to the calculations, the spectroscopic factors for all members of this band should be less than 0.04 resulting in very small reaction cross sections. It is tempting to attribute the $3/2^+$ and $1/2^+$ states observed at 539 and 624 keV in $^{191}$Ir and at 460 and 557 keV in $^{193}$Ir to this band. These levels are well established from the decay studies but are not populated in the reaction data. The observations appear to be consistent with the proposed assignment, although weak peaks should have been observed in the reaction spectra corresponding to the I = 3/2 and I = 1/2 members. These considerations allow only a tentative assignment for the $1/2^+$ [411] orbital.

## The $7/2^+$ [404] Orbital and ($K_o$+2) Gamma Vibration

States at 686 keV in $^{191}$Ir and 621 keV in $^{193}$Ir are observed in Coulomb excitation and identified as the ($K_o$+2) gamma vibrational state built upon the ground state. This assignment is also indicated by the inelastic deuteron scattering measurements of Norgaard et al (1971). These states are weakly observed in the present reaction data. Although the states are barely detectable they are found in all the spectra with $c_{j\ell}^2\ U^2$ values of 0.03 for $^{191}$Ir and 0.02 and 0.03 for $^{193}$Ir. The model calculations reveal that the $7/2^+$ [404] bandhead, with a $c_{j\ell}^2$ of 1.00, is expected to form a hole state in this energy region which has a predicted $c_{j\ell}^2\ U^2$ of 0.04. It thus appears that the vibrational states contain a sizeable fraction of single-particle strength which can be identified with the $7/2^+$ [404] orbital. From these observations, it is concluded that these $7/2^+$ states are composed of the $7/2^+$ [404] orbital together with the ($K_o$+2) gamma vibration based upon the ground state.

This particular gamma vibration is not expected to appear in any of the nearby nuclei for which microscopic calculations have been performed. If such calculations become available for the transition region, it will be of interest to see if they predict vibrational admixtures in the $7/2^+$ [404] orbital.

## The $1/2^-$ [541] Orbital

The $1/2^-$ [541] orbital is expected to occur at excitation energies of about 1 MeV in the iridium isotopes, as seen from the calculated energy spectra of Fig. 10.2. This band is particularly interesting because Coriolis interactions involving the $3/2^-$ [532] orbital are expected to strongly perturb its structure. Since both the $1/2^-$ [541] and $3/2^-$ [532] orbitals arise from the $h_{9/2}$ shell model state, most of the cross section is concentrated in the I = 9/2 band members as evidenced by the $c_{j\ell}^2\ U^2$ values of $\sim$0.88 predicted for these states when band mixing is neglected. When full strength mixing is included, much of the strength of the higher-lying 9/2 $3/2^-$ [532] state is drained into the 9/2 $1/2^-$ [541] state, dramatically increasing its $c_{j\ell}^2\ U^2$ value to 1.64. The 9/2 $1/2^-$ [541] state can therefore be used to provide a reliable indication of the amount of Coriolis mixing present in the iridium isotopes.

In $^{193}$Ir, candidates for the 9/2 $1/2^-$ [541] state are provided by the 1150-1163 keV doublet which is strongly populated in both the ($^3$He,d) and ($\alpha$,t) spectra. The ($^3$He,d) to ($\alpha$,t) cross section ratios indicate that the stronger 1150 keV component has $\ell = 5$ structure whereas the 1165 keV peak is of $\ell = 6$ character. The $\ell = 6$ transition is thought to provide evidence for the $1/2^+$ [660] orbital as discussed in a following subsection. The $\ell = 5$ transition may then be identified with the 9/2 $1/2^-$ [541] state. Values of $c_{j\ell}^2\ U^2$ of 1.33 and 1.31 are obtained for this state from the ($^3$He,d) and ($\alpha$,t) measurements, respectively. These values are greater than unity which indicates that an appreciable amount of band mixing is present. Mixing calculations, in which the Coriolis interactions are reduced to 0.5 of their full strength, provide a value $c_{j\ell}^2\ U^2$ of 1.44, in good agreement with the experimental values. The uncertainties preclude a more accurate determination of the attenuation coefficient and, accordingly, the value of 0.5 has been used for the model calculations.

The only other member of the $1/2^-$ [541] band which is likely to be observed in the reaction experiments is the I = 5/2 band member, for which $c_{j\ell}^2 U^2$ is predicted to be 0.09. A transition is observed at 1133 keV in the $(\alpha,t)$ spectra whose strength is consistent with an $\ell = 3$ transition. Although the state cannot be resolved in the $(^3He,d)$ data from the much stronger 1150 keV state, the value of $c_{j\ell}^2 U^2$ extracted from the $(\alpha,t)$ measurements is 0.06, in good agreement with the value expected for the I = 5/2 band member.

In $^{191}Ir$, the only candidate for the 9/2 $1/2^-$ [541] state is the intense transition at 882 keV. The cross section ratios for this state fall between values expected for an $\ell = 5$ and an $\ell = 6$ transition. Assuming this peak is due entirely to the I = 9/2 member of the $1/2^-$ [541] band, $c_{j\ell}^2 U^2$ values of 1.46 and 2.08 are extracted from the $(^3He,d)$ and $(\alpha,t)$ measurements, respectively. It is significant that the value obtained from the $(\alpha,t)$ data is the larger since any $\ell = 6$ contribution in the peak will tend to enhance that value. In addition, these spectroscopic factors are noticeably greater than the values obtained for the corresponding state in $^{193}Ir$. These observations, together with the fact that an $\ell = 6$ transition is observed close in energy to the 9/2 $1/2^-$ [541] state in $^{193}Ir$, indicate that the 882 keV state is an unresolved doublet consisting of an $\ell = 6$ component together with a larger $\ell = 5$ contribution. A qualitative estimate of the relative intensities of these components allows the

$c^2_{ij}$ $U^2$ values for the 9/2 1/2⁻ [541] state to be brought into good agreement with the values observed for $^{193}$Ir.

The I = 5/2 band member of the 1/2⁻ [541] orbital, for which $c^2_{j\ell}$ $U^2$ is predicted to be 0.09, has not been located in $^{191}$Ir. The band mixing calculations indicate that the I = 5/2 and 9/2 members will be located close in energy, as experimentally observed in the $^{193}$Ir case. The weakly populated I = 5/2 member of the band may therefore be masked by the I = 9/2 member in $^{191}$Ir.

The observation of intense I = 9/2 states in both iridium isotopes is regarded as strong evidence for the assignment of the 1/2⁻ [541] orbital to these nuclei. It is observed that the excitation energy of this orbital decreases significantly in going from $^{193}$Ir to $^{191}$Ir. This behavior is characteristic of orbitals arising from the $h_{9/2}$ and $i_{13/2}$ shells since these orbitals undergo a rapid decrease in energy as the deformation increases. The observed positions of the 9/2 1/2⁻ [541] state in $^{191}$Ir and $^{193}$Ir indicate that $^{191}$Ir has the larger deformation, with the deformation difference between the two nuclei being $\Delta\delta = 0.017$. Physically, it is expected that the isotope with fewer neutrons will exhibit the larger deformation since shell model effects become less important as the shells are emptied.

## The 3/2⁻ [532] Orbital

The presence of the 3/2⁻ [532] orbital is indicated by the rather dramatic Coriolis coupling effects observed for the 1/2⁻ [541] band. This coupling removes much of the strength from the 3/2⁻ [532]

band, resulting in predicted $c^2_{j\ell}\ U^2$ values of 0.01, 0.04 and 0.31 for the respective I = 5/2, 7/2 and 9/2 band members. The calculations also show that the energy of the prominent I = 9/2 member is raised above 2200 keV. The experimental data accords with these calculations since the $3/2^-$ [532] band is not observed among the low-lying states.

## The $1/2^-$ [530] Orbital

The model calculations show that the $1/2^-$ [530] orbital should be found at an energy of ∿ 1800 keV, with nearly all of its strength concentrated in the I = 7/2 member since $c^2_{j\ell}\ U^2$ is predicted to be 0.82 for this member. Intense $\ell = 3$ peaks are observed at 1520 keV in $^{191}$Ir and 1821 keV $^{193}$Ir which almost certainly represent the 7/2 $1/2^-$ [530] state. The measured values of $c^2_{j\ell}\ U^2$ are 0.85 and 1.13 for the state in $^{191}$Ir and 0.61 and 0.72 for the corresponding state in $^{193}$Ir, in decent agreement with the expected value.

The only other member of the $1/2^-$ [530] band which is likely to be populated in these experiments is the I = 3/2 member, for which $c^2_{j\ell}\ U^2$ is 0.10. In $^{191}$Ir, a state is observed at 1449 keV having $\ell = 1$ or 2. The measurements reveal a $c^2_{j\ell}\ U^2$ value of 0.06 and 0.09 for this state and accordingly it is identified with the I = 3/2 member. In $^{193}$Ir, the I = 3/2 member is tentatively identified with the 1760 keV state although its cross section ratios are more indicative of an $\ell = 2$ transition. The measured $c^2_{j\ell}\ U^2$ values for this peak are 0.05 and 0.15.

Additional evidence for the $1/2^-$ [530] orbital assignment is provided by the characteristic energy shift observed for the proposed states. In going from $^{193}$Ir to $^{191}$Ir, the energies of the states are downshifted by ∿ 300 keV, in agreement with the shift expected on the basis of the behaviour observed for the $1/2^-$ [541] orbital. These arguments establish the $1/2^-$ [530] band assignment in both $^{191}$Ir and $^{193}$Ir. No coupling effects are found between this band and the $3/2^-$ [521] orbital which, had it been present, would have appreciably perturbed the observed energies and spectroscopic factors. It may be that at high excitation energies the $3/2^-$ [521] orbital becomes fragmented to such a high degree that its identity is lost.

## The $1/2^+$ [660] Orbital

The N = 6 states, of which the $1/2^+$ [660] orbital is the lowest, have yet to be located with certainty in the odd-proton nuclei. The evidence has already been discussed which indicates that $\ell = 6$ transitions occur at 882 keV in $^{191}$Ir and 1163 keV in $^{193}$Ir. Unfortunately the transition in $^{191}$Ir is not resolved from the 9/2 $1/2^-$ [541] state so that quantitative estimates of its strength cannot be reliably established.

For states arising from the $i_{13/2}$ shell, almost all of the spectroscopic strength is concentrated into the I = 13/2 band member. Thus the identification of these states relies mainly upon the observation of intense $\ell = 6$ transitions. In addition, these states are expected to display strong Coriolis coupling which will further enhance the I = 13/2 member of the $1/2^+$ [660] band at the expense of the other higher lying N = 6 states. One therefore expects to observe $c_{j\ell}^2\ U^2$ values greater than unity for the 13/2 $1/2^+$ [660] state.

In the present work, values of $c_{j\ell}^2$ $U^2$ of 0.44 and 0.50 are observed for the $\ell = 6$ transition in $^{193}$Ir and a qualitative estimate indicates similar values are reasonable for the proposed $\ell = 6$ transition in $^{191}$Ir. Although these values are clearly at variance with the results expected for the 13/2 $1/2^+$ [660] state, no other state is capable of explaining the large $\ell = 6$ cross sections observed in the spectra. Another argument is provided by the observed positions of the $1/2^+$ [660] and $1/2^-$ [541] states in the data. Since these states exhibit the same slope on a Nilsson diagram, they are expected to maintain their relative positions in both iridium isotopes; a feature which is strikingly apparent in the data. These considerations are thought to provide good evidence for the assignment of the $1/2^+$ [660] states in both $^{191}$Ir and $^{193}$Ir. It is concluded that the $1/2^+$ [660] states are fragmented in both nuclei to values of about half their unperturbed strength.

## 10.3 Possible Evidence for the Existence of Asymmetry in the Iridium Isotopes

In chapters VII and VIII, a sequence of negative parity states having spins $7/2^-$, $3/2^-$ and $5/2^-$ were found to be based upon the $11/2^-$ [505] state in both $^{191}$Ir and $^{193}$Ir. These states apparently form a separate subsystem of levels for which the beta transitions into these states and also the electromagnetic transitions from these to the positive parity states is highly hindered. It was suggested that these hindrances are the result of changes in nuclear shape. Such changes in shape may not be unreasonable since the calculations of Kumar and Baranger (1968) indicate that the potential energy minimum is rather shallow in the region of the even osmium nuclei.

Backlin et al (1970) have attributed the $7/2^-$ state to the coupling of the $h_{11/2}$ shell model state, which they emphasize to be spherical, with a phonon excitation. However the present reaction studies indicate that the $11/2^-$ state likely obeys a Nilsson description rather than the spherical description. In addition, the $7/2^-$ state is clearly populated by both the ($^3$He,d) and ($\alpha$,t) reactions indicating single-particle structure for this state. In fact, the sequence of negative parity states appears to have the properties of an anomolously ordered rotational band. Hecht and Satchler (1962) have shown that the rotational levels of an asymmetric nucleus may be ordered quite differently from those in the corresponding symmetric case. In an asymmetric description, the lowest member of the $11/2^-$ [505] orbital (denoted level 75 by Hecht and Satchler) may take on any of the spin values from $11/2^-$ to $1/2^-$ depending upon the deformation and asymmetry parameters used. As a concrete example, for $\beta = -0.2$, $\gamma = 15°$ the spin sequence of this band becomes $7/2^-$, $11/2^-$, $3/2^-$ $9/2^-$, $5/2^-$. Unfortunately, the particle wave functions for an asymmetric nucleus, which are required to calculate the rotational spectrum as well as the spectroscopic factors, are not at our disposal. If the observed properties of this proposed band can be reproduced using an asymmetric rotor description, this would provide direct evidence for the existence of non-axial symmetry as no other description seems able to reproduce these properties. It is realized that an asymmetric description, which by its very nature introduces K admixtures into the problem, also provides an alternative description of Coriolis mixing.

## 10.4 Summary

A variety of experiments have been performed in order to establish and identify the states in $^{191}$Ir and $^{193}$Ir. The states observed in the present experiments are shown in Figs. 10.3 and 10.4. Solid dots indicate the levels observed in radioactive decay, open cirlces show those observed in Coulomb excitation and crosses specify the states found in the ($^3$He,d) and ($\alpha$,t) reaction studies.

From the decay studies, the gamma ray and internal conversion energies and intensities have been measured with high precision. These measurements establish the transition multipolarities and mixing ratios for many of the gamma rays and have been used to uniquely determine the spins and parities for all the states observed in the low energy spectrum of $^{191}$Ir and $^{193}$Ir. A series of $\gamma$-$\gamma$ coincidence experiments was performed. Decay schemes, thought to be free of ambiguities, have been constructed from the data and are presented in chapters VII and VIII.

The reaction data reveals that the extreme single-particle shell model is not valid in the iridium region, whereas the Nilsson model is surprisingly successful. It has been shown that band mixing must be included in the model, with Coriolis matrix elements of half strength providing good agreement with experiment.

The $3/2^+$ [402], $11/2^-$ [505], $5/2^+$ [402], $1/2^-$ [541] and $1/2^-$ [530] Nilsson orbitals have been established and evidence is obtained which indicates that the $3/2^-$ [532] band is present, although unidentified. The $1/2^+$ [411] orbital is tentatively assigned. The $(K_o-2)$ and $(K_o+2)$ gamma vibrations based upon the ground state are found to be mixed with the $1/2^+$ [400] and $7/2^+$ [404] orbitals respectively. The $1/2^+$ [660] orbital has been located, albeit with appreciable fragmentation of its strength.

Several interesting negative parity states have been found to decay strongly to the $11/2^-$ [505] state, and it is suggested that these states provide evidence of non-axial symmetry in the iridium isotopes.

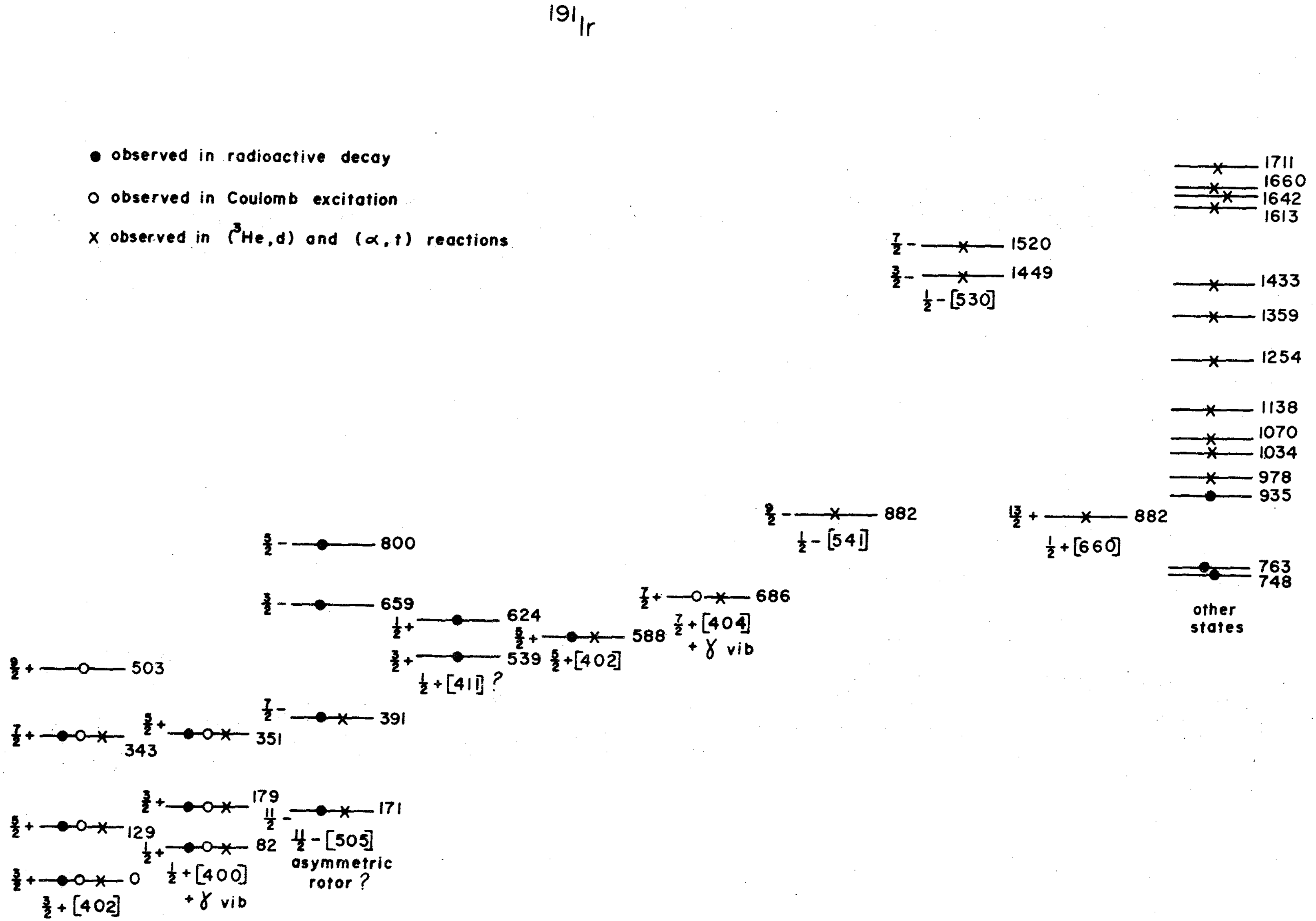

Figure 10.3 States observed in $^{191}$Ir from the present experiments.

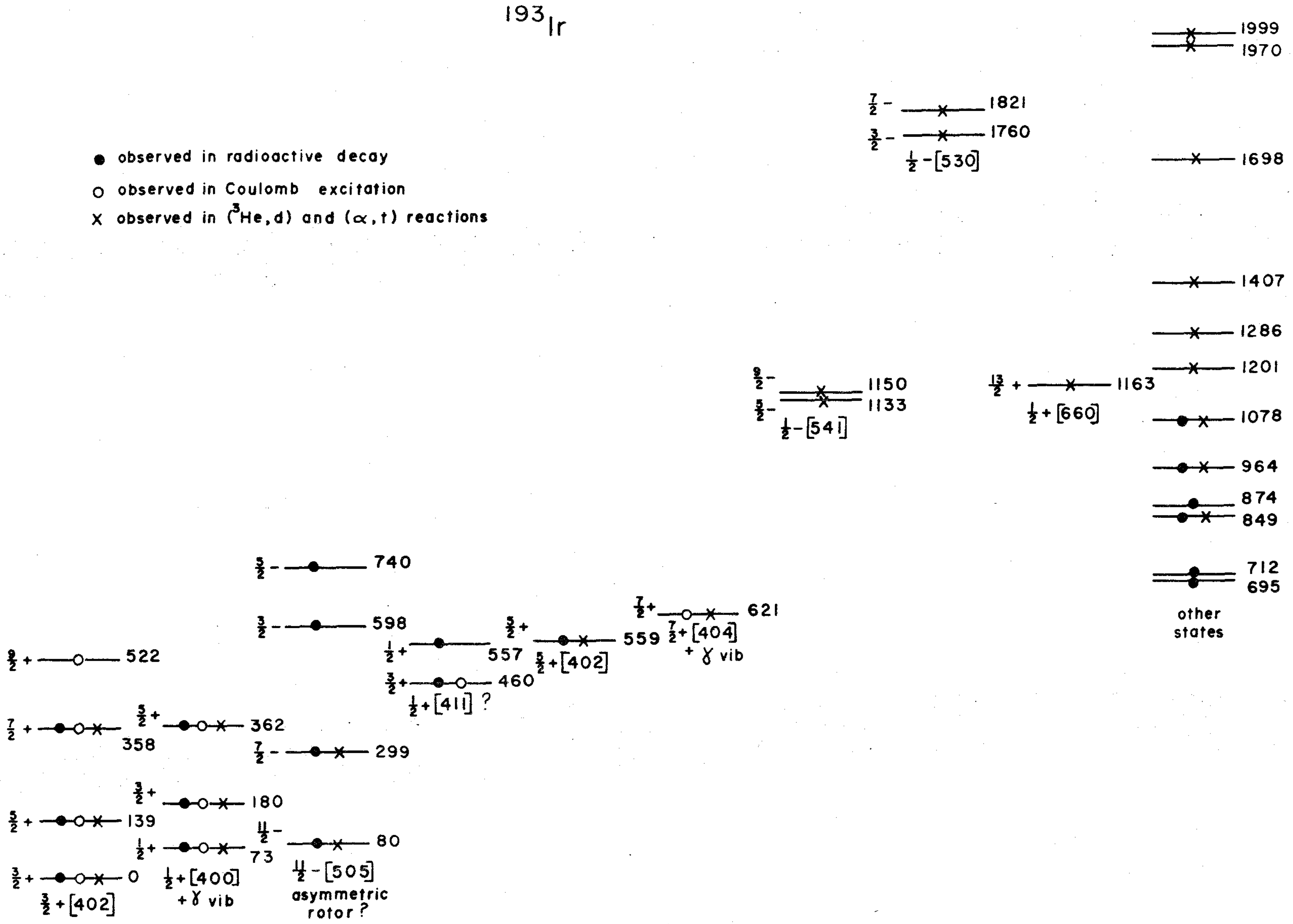

Figure 10.4 States observed in $^{193}$Ir from the present experiments.

# REFERENCES

Agin, G. P., Clark, G. E., Mandeville, C. E. and Potnis, V. R. (1967). Phys. Rev. 164, 1495.

Alder, K., Bohr, N., Huus, T., Mottelson, B. and Winther, A. (1956). Rev. Mod. Phys. 28, 432.

Alexander, P. and Ryde, H. (1967). Bull. Am. Phys. Soc. II. 12, 597.

Andersen, B. L. (1968). Nucl. Phys. A112, 443.

Atzmony, U., Bauminger, E. R., Lebenbaum, D., Mustachi, A., Ofer, S. and Wernick, J. H. (1967). Phys. Rev. 163, 314.

Avida, R., Burde, J. Molchadzki, A. and Berant, Z. (1968). Nucl. Phys. A114, 365.

Avida, R., Burde, J. and Molchadzki, A. (1968). Nucl. Phys. A115, 405.

Backlin, A., Berg, V. and Malmskog, S. G. (1970). Nucl. Phys. A156, 647.

Bardeen, J., Cooper, L. N. and Schrieffer, J. R. (1957). Phys. Rev. 108, 1175.

Bassel, R. H., Drisko, R. M. and Satchler, G. R. (1962). ORNL Report 3240.

Berg, V., Malmskog, S. G. and Backlin, A. (1970). Nucl. Phys. A143, 177.

Bisgaard, K. M. and Hanson, R. J. (1969). Nucl. Phys. A125, 305.

Blichert-Toft, P. H., Funk, E. G. and Mihelich, J. W. (1966). Nucl. Phys. 77, 513.

Boehm, F. and Marmier, P. (1957). Phys. Rev. 105, 974.

Bogoliubov, N. N. (1958). Nuovo Cimento 7, 794.

Bohr, A. (1952). K. Danske Vidensk. Selsk. Mat.-Fys. Medd. 26, No. 14.

Bohr, A. and Mottelson, B. R. (1953). K. Danske Vidensk. Selsk. Mat.-Fys. Medd. 27, No. 16.

Bohr, A., Mottelson, B. R. and Pines, D. (1958). Phys. Rev. 110, 936.

Børggreen, J., Løvhøiden, G. and Waddington, J. C. (1969). Nucl. Phys. A131, 241.

Burke, D. G., Zeidman, B., Elbek, B., Herskind, B. and Olesen, M. (1966). K. Danske Vidensk. Selsk. Mat.-Fys. Medd. 35, No. 2.

Camp, D. C. (1967). UCRL Report 50156.

Chi, B. E. (1967). State Univ. of New York (Albany) Publication.

Choudhury, D. C. (1954). K. Danske Vidensk. Selsk. Mat.-Fys. Medd. 28, No. 4.

Davydov, A. S. and Fillipov, G. F. (1958). Nucl. Phys. 8, 237.

de-Shalit, A. (1961). Phys. Rev. 122, 1530.

de-Shalit, Amos and Talmi, Igal. (1963). "Nuclear Shell Theory", Academic Press Inc., New York.

Enge, H. A. (1964). Nucl. Instr. and Meth. 28, 126.

Fano, U. (1947). Phys. Rev. 72, 26.

Feenberg, E. and Trigg, G. (1950). Rev. Mod. Phys. 22, 399.

French, J. B. and Raz, B. J. (1956). Phys. Rev. 104, 1411.

Goldhaber, M., Grodzins, L. and Sunyar, A. W. (1958). Phys. Rev. 109, 1015.

Graham, R. L., Ewan, G. T. and Geiger, J. S. (1960). Nucl. Instr. and Meth. 9, 245.

Gustafsson, S., Johansson, K., Karlsson, E., Norlin, L. O. and Svensson, A. G. (1967). Ark. Fys. 34, 169.

Hagar, R. S. and Seltzer, E. C. (1968). "Nuclear Data", Section A Vol. 4, Academic Press Inc., New York.

Hagar, R. S. and Seltzer, E. C. (1969). "Nuclear Data", Section A Vol. 6, Academic Press Inc., New York.

Harmatz, B., Handley, T. H. and Mihelich, J. W. (1962). Phys. Rev. 128, 1186.

Haxel, O., Jensen, J. H. D. and Suess, H. E. (1949). Phys. Rev. 75, 1766.

Haxel, O., Jensen, J. H. D. and Suess, H. E. (1950). Z. Physik 128, 295.

Hecht, K. T. and Satchler, G. R. (1962). Nucl. Phys. 32, 286.

Hering, W. R., Becker, H., Wiedner, C. A. and Thompson, W. J. (1970). Nucl. Phys. A151, 33.

Kerman, A. K. (1956). K. Danske Vidensk. Selsk. Mat.-Fys. Medd. 30, No. 15.

Kisslinger, L. S. and Sorensen, R. A. (1963). Rev. Mod. Phys. 35, 853.

Kumar, K. and Baranger, M. (1968). Nucl. Phys. A122, 273.

Lamm, I. L. (1969). Nucl. Phys. A125, 504.

Løvhøiden, G., Waddington, J. C., Hagemann, K. A., Hjørth, S. A. and Ryde, H. (1970). Nucl. Phys. A148, 657.

Lu, M. T. and Alford, W. P. (1970). UC-NSRL Report 34.

Macfarlane, M. H. and French, J. B. (1960). Rev. Mod. Phys. 32, 567.

Malmskog, S. G., Berg, V., Backlin, A. and Hedin, G. (1970). Nucl. Phys. A143, 160.

Mayer, M. G. (1949). Phys. Rev. 75, 1969.

Mayer, M. G. (1950). Phys. Rev. 78, 16.

Mayer, M. G. and Jensen, J. H. D. (1966). "Alpha, Beta and Gamma Ray Spectroscopy" edited by K. Siegbahn, Vol. 1, North-Holland Publishing Co., Amsterdam.

McGowan, F. K. and Stelson, P. H. (1958). Phys. Rev. 109, 901.

Metzger, F. R. (1967). Phys. Rev. 161, 1249.

Murakawa, K. and Suwa, S. (1952). Phys. Rev. 87, 1048.

Murray, G., Graham, R. L. and Geiger, J. S. (1965). Nucl. Phys. 63, 353.

Nablo, S. V., Johns, M. W., Artna, A. and Goodman, R. H. (1958). Can. J. Phys. 36, 1409.

Nathan, O. and Nilsson, S. G. (1966). "Alpha, Beta and Gamma Ray Spectroscopy" edited by K. Siegbahn, Vol. 1, North-Holland Publishing Co., Amsterdam.

Newton, T. D. (1960). Can. J. Phys. 38, 700.

Nilsson, S. G. (1955). K. Danske Vidensk. Selsk. Mat.-Fys. Medd. 29, No. 16.

Norgaard, P., Bisgaard, K. M., Gregersen, K. and Morgen, P. (1971). To be published in Nucl. Phys.

O'Neil, R. A., Burke, D. G. and Alford, W. P. (1971). To be published in Nucl. Phys.

Perry, F. C. and Smith Murphy, Jr., E. (1967). Nucl. Phys. A99, 497.

Plajner, Z., Brabec, V., Maly, L. and Vejs, M. (1967). Nucl. Phys. A121, 367.

Preston, M. A. (1962). "Physics of the Nucleus", Addison-Wesley Publishing Co., Reading, Mass.

Price, R. H., Johns, M. W., Ahmed, N. M. and Habib, E. E. (1969). Can. J. Phys. 47, 727.

Rotenberg, M., Bivins, R., Metropolis, N. and Wooten, Jr., J. K. (1959). "The 3-j and 6-j Symbols", Technology Press, MIT, Cambridge, Mass.

Satchler, G. R. (1958). Ann. Phys. 3, 275.

Schumacher, M., Schoneberg, R. and Flammersfeld, A. (1966). Z. Physik 191, 343.

Schumacher, M. and Langhoff, H. (1967). Phys. Rev. 162, 1153.

Spencer, J. E. and Enge, H. A. (1967). Nucl. Instr. and Meth. 49, 181.

Soloviev, V. G. and Vogel, P. (1967). Nucl. Phys. A92, 449.

Tjom, P. O. and Elbek, B. (1967). K. Danske Vidensk. Selsk. Mat.-Fys. Medd. 36, No. 8.

Ungrin, J. and Johns, M. W. (1969). Nucl. Instr. and Meth. 70, 112.

Valatin, J. G. (1958). Nuovo Cimento 7, 843.

Wu, C. S., Ambler, E., Hayward, R. W., Hoppes, D. D. and Hudson, R. P. (1957). Phys. Rev. 105, 1413.